NUMERICAL ANALYSIS AND SIMULATIONS IN BONE REMODELING MODELS

Rebeca Martínez Fernández

Departamento de Matemática Aplicada

Universidade de Santiago de Compostela

Ph.D. Dissertation

November 2010

ISBN 978-84-9887-632-1 (Edición digital PDF)

Don Juan Manuel Viaño Rey, catedrático del Departamento de Matemática Aplicada de la Universidade de Santiago de Compostela, y Don José Ramón Fernández García, profesor Contratado Doutor del Departamento de Matemática Aplicada I de la Universidade de Vigo, informan que la memoria titulada:

NUMERICAL ANALYSIS AND SIMULATIONS IN BONE REMODELING MODELS

fue realizada bajo su dirección por Doña Rebeca Martínez Fernández, estimando que la interesada se encuentra en condiciones de optar al grado de Doctor en Ciencias Matemáticas, por lo que solicitan que sea admitida a trámite para su lectura y defensa pública.

En Santiago de Compostela, a 10 de Noviembre de 2010.

Los directores:

Prof. Dr. Juan M. Viaño Rey Prof. Dr. José R. Fernández García

La doctoranda: Rebeca Martínez Fernández

Agradecimientos

En primer lugar, me gustaría agradecerle a mis directores, Juan M. Viaño y José R. Fernández, el haberme dado la oportunidad de comenzar en el mundo de la investigación. Sin su trabajo y dedicación no habría sido posible finalizar esta tesis. Al profesor J. Manuel García-Aznar no sólo el tiempo y esfuerzo dedicados en el último año y medio, también el apoyo recibido, día tras día, en los momentos más difíciles. A la profesora Isabel Figueiredo por su trabajo y hospitalidad en las estancias realizadas en el Centro de Matemáticas de la Universidad de Coimbra y al profesor G.E. Stavroulakis la aportunidad de trabajar con él en la estancia realizada en la Universidad Técnica de Creta.

A lo largo de estos años, he compartido muy buenos momentos (y no tan buenos) con mis compañeros de la facultad. Marta, Andrés, Rafa, Rosa... a todos ellos me gustaría darles las gracias, en especial a Tere, que me ha ayudado desde que empecé a hacer mis primeras simulaciones hasta el final de esta tesis, y a Laura, por la ayuda prestada cuando todo parecía dificilísimo. A Manu, porque no puedo evitar sonreir cuando recuerdo todas las tardes que pasamos en la sala. Y, por supuesto, a la gente que empezó este camino conmigo en los cursos de doctorado y master: Marcos, Chor, Javier, Cesar y Dani, pero sobre todo a María y a Diana, con las que compartí cursos, despacho, viajes... y a las que siempre agradeceré su apoyo y su amistad.

Me gustaría agradecerle a mis compañeros en Coimbra y en Creta los momentos compartidos durante mis estancias. Gracias a vosotros, nunca olvidaré estos meses.

Por último, agradecerle a mi familia el apoyo recibido a lo largo de estos años, en especial a mi madre y a mi abuela, porque sin ellas no habría sido posible llegar hasta aquí.

Moitas gracias!

Contents

Resumen

El aumento de la esperanza de vida ha conllevado el desarrollo de nuevas tecnologías médicas. Técnicas quirúrgicas, más eficientes y menos invasivas, o fármacos de diseño son ejemplos de gran importancia hoy en día. Estos avances conducen a nuevas demandas en investigación y, especialmente, a un nuevo perfil profesional que combine aspectos de ingeniería y medicina para consolidar una nueva disciplina: la Bioingeniería.

La Bioingeniería agrupa campos como la Tecnología Biomédica, Biomateriales o Biomecánica. Centrándonos en esta última, la biomecánica es la aplicación de los principios de la mecánica a los sistemas vivos. Utilizando las leyes y conceptos de la física, los mecanismos y estructuras biomecánicos pueden ser estudiados y simulados. La biomecánica ayuda a entender el comportamiento de los organismos, la respuesta de los órganos y tejidos desde el punto de vista mecánico, a predecir cambios debidos a alteraciones en su entorno y a proponer métodos artificiales de intervención. Por tanto, el diagnóstico, la cirugía y el diseño de prótesis están directamente relacionados con la biomecánica.

Muchos investigadores han tratado de estudiar la relación entre la estructura del hueso y las fuerzas mecánicas que actúan sobre él desde, al menos, el siglo XVII. En el siglo XIX, se describió la relación entre la forma del hueso y su función. El cirujano alemán Julius Wolff estableció que no sólo existe una relación entre la estructura del hueso y las cargas a las que es sometido, sino que además el hueso vivo se adapta a las alteraciones en estas cargas cambiando su estructura interna. Este proceso es

denominado remodelación ósea y esta afirmación es conocida como la ley de Wolff. La investigación experimental ha confirmado a lo largo de los años la veracidad de esta suposición, mostrando que incluso en la edad adulta el hueso puede adaptar su estructura en respuesta a las cargas a las que está siendo sometido.

El principal objetivo de esta tesis es realizar la simulación numérica y desarrollar el análisis matemático de algunos modelos de remodelación ósea, con los cuales somos capaces de predecir el comportamiento del tejido óseo y su capacidad de adaptarse a las cargas aplicadas. Estos modelos son utilizados habitualmente para predecir la respuesta del hueso cuando se implanta una prótesis y se aplican cargas inusuales o para diseñar mejores implantes cambiando la geometría, el material o incluso la localización.

En lo que sigue, realizamos un resumen de los cuatro capítulos que forman esta memoria de tesis, resultado de la investigación llevada a cabo durante los últimos cinco años en el Departamento de Matemática Aplicada de la Universidad de Santiago de Compostela bajo la dirección de los profesores José Ramón Fernández García y Juan Manuel Viaño Rey.

Capítulo 1: El tejido óseo y su comportamiento.
En este capítulo se explica como es la estructura interna de un hueso y como se produce el proceso de remodelación ósea, centrándonos en aquellos aspectos que serán relevantes para entender los modelos que se plantean en los siguientes capítulos.

El hueso es un órgano rígido que forma el esqueleto de los vertebrados. Cumple funciones tan esenciales como proteger los órganos vitales del cuerpo humano o aportar la estructura necesaria al sistema muscular. Cada hueso tiene una forma diferente y una compleja estructura interna y externa. Los huesos son livianos aunque muy resistentes y duros. En su interior podemos encontrar diferentes tejidos, como sangre, nervios, venas, cartílagos, médula ósea o tejido óseo.

Existen dos clases de tejido óseo: el cortical y el esponjoso. Los dos tejidos tienen la misma estructura y composición pero el cortical es más denso. Este tejido es el que recubre los huesos, proporcionándoles un aspecto sólido y continuo.

En el interior del órgano encontramos el hueso esponjoso o trabecular. Este tejido se caracteriza por tener una densidad muy baja. Consiste en una estructura esponjosa en cuyos huecos se encuentra la médula ósea y pequeños vasos sanguíneos. El 80% de la masa ósea de un esqueleto adulto es hueso cortical pero, el volumen que ocupa el hueso esponjoso es diez veces mayor.

El fluido en el cual se encuentra embolsado el hueso esponjoso está en contacto con el plasma sanguíneo. En el plasma es donde se encuentran las células óseas, que son las encargadas de regular las reacciones químicas que provocan la adición o pérdida de masa del hueso trabecular, también denominado matriz ósea.

Dependiendo de la función que realicen, las células pueden ser clasificadas en cuatro tipos: osteoblastos, osteoclastos, células de borde y osteocitos.

Las células generadoras de hueso son los osteoblastos. Cuando el hueso se está formando rápidamente, como en la infancia o en la cura de una fractura, los osteoblastos son predominantes y su forma es oval o cúbica. En los adultos encontramos menos osteoblastos y con una forma alargada.

Las células de borde forman una capa que cubre la superficie de la matriz ósea. Son osteoblastos inactivos y su forma es plana. Cuando son activados, como respuesta a algún estímulo, se convierten en una capa de osteoblastos.

Los osteocitos son las células óseas más abundantes en el esqueleto adulto, más del

90%, y su forma es estrellada. Estas células son osteoblastos que se han quedado atrapados en la matriz ósea que han secretado y tienen la capacidad de secretar o reabsorber la matriz ósea que las rodea.

Los osteoclastos son las células responsables de la reabsorción del tejido óseo. Cuando son activados, se agrupan formando células multinucleadas y una vez terminada la absorción del hueso se dividen en células mononucleadas.

Estos cuatro tipos de células son las responsables de realizar el proceso de remodelado óseo. Es un proceso lento que ocurre durante toda la vida del ser humano, aunque con más rapidez en la infancia. Normalmente, la formación y reabsorción del hueso se mantienen en equilibrio, conservando la integridad y fuerza del esqueleto. En la reabsorción, los osteoclastos erosionan la superficie del hueso trabecular creando pequeñas cavidades. Después, los osteoblastos reparan la superficie, generando hueso nuevo, y una capa de células de borde cubren la nueva superficie. La transición entre la actividad de los osteoblastos y los osteoclastos no es inmediata, en el ser humano puede durar alrededor de treinta días, mientras que la fase de creación de hueso necesita alrededor de 10 días. En el primer año de vida de un ser humano, casi el 100% del esqueleto es renovado por este proceso. En los adultos, cada año se renueva alrededor del 10% del hueso.
Existen dos tipos de remodelación ósea: la interna y la externa. En la remodelación ósea externa, la forma del hueso cambia, mientras que en la interna se mantiene la geometría y las propiedades varían. En esta tesis nos centraremos en el segundo tipo.

Capítulo 2: Un modelo de remodelación ósea en elasticidad adaptativa.
Cuando se intenta estudiar desde el punto de vista mecánico el comportamiento de un hueso, es imposible modelar la estructura trabecular. Es por ello que se definen propiedades continuas que nos permiten evitar trabajar con las propiedades reales del hueso. Esto supone considerar el hueso como un material continuo. Sin embargo,

cuando lo que nos interesa conocer es el comportamiento del hueso en una zona, y no en un punto concreto, esta hipótesis no supone ninguna restricción. Habitualmente, los modelos de remodelación ósea, como los estudiados en esta tesis, incorporan una función que mide la porosidad de la matriz ósea.

En la primera sección de este capítulo se explica el primer modelo matemático para un problema de remodelación ósea planteado en 1976 por Cowin y Hegedus (véanse [15, 46]). Para obtener este modelo se hacen las siguientes hipótesis:

- Las propiedades mecánicas del hueso son esencialmente las mismas que las de la matriz ósea.
- La porosidad de la matriz ósea cambia con la adición o pérdida de masa. Esta transferencia de masa ocurre como resultado de una reacción química regulada por las células óseas.
- Las proporciones de estas reacciones químicas dependen de la deformación y son muy lentas. Se estima que el tiempo característico de estas reacciones es del orden de meses. Por este motivo el modelo de remodelación ósea será considerado cuasiestático.
- El hecho de que el hueso esté embolsado en un organismo vivo, se refleja en el modelo considerando la estructura porosa en un baño de fluido perfusante. Cuando sea necesario, se asumirá que el baño perfusante es una reserva de calor isoterma.
- Cuando la porosidad de la matriz ósea cambia, el área de la superficie de contacto entre la matriz y el perfusante, en el que se encuentran las células óseas, se modifica. Puesto que no hay una relación directa entre la porosidad y esta área, se consideran sólo cambios de porosidad y no se introduce el área de la superficie de contacto como variable del modelo.

Aplicando estas hipótesis, Cowin y Hegedus obtuvieron las ecuaciones de equilibrio para la masa, el momento y la energía y la desigualdad de entropía, estableciendo la

siguiente ley constitutiva para el tensor de tensiones:

$$\boldsymbol{\sigma} = (\xi_0 + e)\mathcal{C}(e)\boldsymbol{\varepsilon}(\boldsymbol{u}),$$

donde ε denota el tensor de deformación y $\mathcal{C}(e)$ caracteriza las propiedades mecánicas del hueso. La función e mide el cambio en la porosidad de la matriz ósea. Esta función se define como $e = \xi - \xi_0$, donde ξ es la fracción volúmica de material presente en la matriz ósea y ξ_0 es la fracción volúmica de referencia.

Para controlar el proceso de remodelado óseo, Cowin y Hegedus obtuvieron la ecuación diferencial ordinaria:

$$\dot{e} = a(e) + \mathcal{A}(e) \, : \, \boldsymbol{\varepsilon}(\boldsymbol{u}),$$

donde $a(e)$ y $\mathcal{A}(e)$ son los coeficientes de remodelación. Esta ecuación determina la tasa de cambio en la porosidad del hueso como una función dependiente de la fracción volúmica y la deformación.

Cuando la tasa de cambio en la fracción volúmica es cero y la fracción volúmica de referencia es uno, le ecuación constitutiva para el tensor de tensiones coincide con la ley de Hooke. Sin embargo, en elasticidad adaptativa los coeficientes de proporcionalidad entre la tensión y la deformación dependen de la fracción volúmica de material presente en el hueso.

En la segunda sección de este capítulo se obtiene la formulación variacional de este problema. Aplicando el método de Euler para discretizar las derivadas temporales y el método de elementos finitos para aproximar la variable espacial, se obtiene el problema discretizado. A continuación, se prueba un resultado de estimación de error que, bajo ciertas condiciones de regularidad adicional, nos permite deducir la convergencia lineal del esquema. Por último, se describe el algoritmo numérico que hemos utilizado para resolver el problema discreto, consistente en una ecuación variacional discreta que resolvemos aplicando el método de Cholesky y una ecuación en diferencias, y se presentan algunas simulaciones numéricas en una, dos y tres dimensiones.

En la tercera sección se supone que el hueso puede entrar en contacto con un sólido rígido o deformable.

Cuando suponemos que el obstáculo es rígido, se utiliza la condición de Signorini para modelar su comportamiento, es decir

$$u_\nu \leq s, \quad \sigma_\nu \leq 0, \quad (u_\nu - s)\sigma_\nu = 0,$$

donde u_ν denota el desplazamiento normal, σ_ν la tensión normal y s la distancia entre el hueso y el obstáculo, medida en la dirección de la normal exterior a la frontera del hueso.

Para modelar el comportamiento del obstáculo deformable hemos utilizado la condición de respuesta normal; la tensión normal en la frontera del hueso que entra en contacto con el obstáculo está dada por

$$-\sigma_\nu = p_\nu(u_\nu - s),$$

donde la función p_ν debe ser nula cuando los dos cuerpos no están en contacto. Tomando

$$p_\nu(r) = \frac{1}{\mu}\, r_+,$$

siendo μ el coeficiente de deformabilidad del obstáculo, se prueba la convergencia de la solución del problema de contacto con respuesta normal a la solución del problema de Signorini cuando el coeficiente de deformabilidad tiende a cero.

Aplicando el esquema de Euler para discretizar las derivadas temporales y el método de los elementos finitos para aproximar la variable espacial, se obtienen los problemas discretizados y las estimaciones del error que nos permiten establecer la convergencia lineal del algoritmo. Por último se describe el algoritmo numérico que hemos utilizado para obtener las simulaciones numéricas en una y dos dimensiones. Este algoritmo consiste en resolver una ecuación variacional no lineal, en el caso de contacto con un

sólido deformable, o una inecuación variacional elíptica para el problema de Signorini. Ambas ecuaciones son resueltas aplicando un algoritmo de tipo penalización-dualidad.

Los resultados presentados en este capítulo han sido publicados en [20, 26, 27, 28].

Capítulo 3: Remodelación ósea inducida por un estímulo local.
En este capítulo se analiza, desde el punto de vista numérico, el modelo estudiado en [66] por Weinans, Huiskes y Grootenboer en 1992. Este modelo se basa en el principio de que la remodelación ósea es inducida por una señal mecánica local que activa las células reguladoras (osteoblastos y osteoclastos); es decir, el hueso tiene sensores que detectan el estimulo mecánico y, dependiendo de su magnitud, causan adaptaciones locales en el hueso. La idea principal de este modelo es utilizar la densidad aparente ρ como caracterización de la morfología interna del hueso.

Weinans et al. consideran el hueso como un material elástico, donde el coeficiente de Poisson es constante y el módulo de Young depende de la densidad aparente del hueso:

$$E = M\rho^{\gamma},$$

donde M y γ son constantes positivas que caracterizan las propiedades mecánicas del hueso.

En el modelo considerado en el capítulo anterior, el cambio en la densidad ósea se regía por las desviaciones producidas en el tensor de deformación. Sin embargo, las ideas de Wolff implicaban que la remodelación no sólo se producía en respuesta a la deformación y, por ello, en este modelo se considera como estímulo mecánico la densidad de energía de deformación:

$$U(\boldsymbol{\sigma}(\boldsymbol{u}), \boldsymbol{\varepsilon}(\boldsymbol{u})) = \frac{1}{2}\boldsymbol{\sigma}(\boldsymbol{u}) \,:\, \boldsymbol{\varepsilon}(\boldsymbol{u}).$$

Puesto que el hueso trabecular es una estructura porosa, la densidad de energía de deformación para la matriz ósea es aproximada por U/ρ, que representa la energía de deformación por unidad de masa. Por lo tanto, la variación en la densidad aparente del hueso viene determinada por la siguiente ecuación diferencial ordinaria de primer orden, no lineal:

$$\dot{\rho} = B\left(\frac{U(\boldsymbol{\sigma}(\boldsymbol{u}), \boldsymbol{\varepsilon}(\boldsymbol{u}))}{\rho} - S_r\right), \quad \rho_a \leq \rho \leq \rho_b,$$

donde B y S_r son constantes que regulan el proceso de remodelación ósea. Además, se impone que los valores de la densidad aparente no sobrepasen el valor ρ_b, correspondiente a la densidad del hueso cortical, ni sean menores que la densidad mínima permitida, ρ_a, correspondiente al hueso reabsorbido. Esta ecuación implica que en los puntos en los cuales la densidad alcanza el valor máximo o mínimo, el proceso de remodelación se detiene. En los otros puntos, el sistema está en equilibrio cuando el estímulo alcanza el valor de referencia S_r.

La formulación variacional de este modelo consiste en una ecuación variacional para el cálculo del campo de desplazamientos, y una inecuación variacional para el cálculo de la densidad ósea. Esta inecuación se obtiene haciendo uso de las propiedades de la subdiferencial de la función indicatriz del intervalo $[\rho_a, \rho_b]$, lo que nos permite garantizar que la solución que buscamos pertenece al intervalo.

Una vez obtenida la formulación variacional del problema, aplicando el esquema de Euler y el método de los elementos finitos hemos obtenido un problema discretizado y las estimaciones del error para el campo de desplazamientos y la densidad ósea. Además, bajo ciertas hipótesis adicionales de regularidad, hemos obtenido la convergencia lineal del algoritmo propuesto. Por último, se describe el algoritmo numérico que ha sido implementado y se muestran las simulaciones numéricas realizadas en una y dos dimensiones. La ecuación variacional para obtener el campo de desplazamientos la resolvemos aplicando el método de Cholesky y la inecuación variacional para cal-

cular la densidad ósea mediante el algoritmo de tipo penalización-dualidad utilizado en el capítulo anterior. La principal ventaja del método propuesto es que nos permite obtener el campo de desplazamientos y la densidad ósea resolviendo dos problemas desacoplados.

Los resultados correspondientes a este capítulo pueden ser consultados en [23].

Capítulo 4: Un modelo de remodelación ósea en piezoelectricidad.
Es un hecho aceptado en remodelación ósea que el hueso adapta su estructura interna a las cargas mecánicas a las que está sujeto. Como ya hemos comentado, este proceso de adaptación es realizado por las células óseas. Sin embargo, no está claro como estas células son capaces de controlar la reabsorción y formación de hueso en función de las condiciones mecánicas.

Fukada y Yasuda probaron en 1957 que el hueso es un material piezoeléctrico en el sentido clásico, es decir, las cargas mecánicas aplicadas producían una polarización en el hueso. Además, poco después se verificó el efecto inverso: la aplicación de un potencial eléctrico producía una deformación (véanse [38, 39]). Desde entonces, las propiedades eléctricas de los huesos han sido ampliamente estudiadas y se cree que las señales eléctricas en el tejido óseo juegan un papel importante en el proceso de remodelado óseo (véanse [2, 42, 43]). Sin embargo, apenas existen modelos matemáticos que justifiquen la remodelación ósea basada en el efecto piezoeléctrico ([61, 62, 63]).

En este capítulo se propone utilizar el modelo analizado en el capítulo anterior para caracterizar las propiedades elásticas del hueso y considerar las leyes constitutivas clásicas para materiales piezoeléctricos, con una pequeña variación en su acoplamiento. Para regular la relación entre el campo eléctrico y el mecánico se introduce la función $\alpha(\rho) = \rho^\gamma$ dependiente de la densidad ósea. Esta función garantiza que el campo eléctrico aumenta con la densidad del hueso. Por tanto, las ecuaciones constitutivas

que consideraremos para el tensor de tensiones σ y el desplazamiento eléctrico $\mathbf{D}$ son las siguientes:

$$\boldsymbol{\sigma} = 2\,\mu(\rho)\boldsymbol{\varepsilon}(\boldsymbol{u}) + \lambda(\rho)\mathrm{Div}\,(\boldsymbol{u})\mathcal{I} - \alpha(\rho)\mathcal{E}^*\mathbf{E}(\varphi),$$

$$\mathbf{D} = \mathbf{D}_{\boldsymbol{\varepsilon}} + \mathbf{D}_{\mathbf{E}} = \alpha(\rho)\mathcal{E}\boldsymbol{\varepsilon}(\boldsymbol{u}) + \alpha(\rho)\beta\mathbf{E}(\varphi),$$

donde $\mathbf{E}(\varphi) = (E_i(\varphi))_{i=1}^d$ es el campo eléctrico, $\mathcal{E}^* = (e^*_{ijk})_{i,j,k=1}^d$ denota el adjunto del tensor piezoeléctrico $\mathcal{E} = (e_{ijk})_{i,j,k=1}^d$ y β es el tensor de permitividad eléctrica.

Siguiendo los trabajos de Gjelsvik (véanse [42, 43]) trataremos de demostrar que el modelo propuesto predice la formación y reabsorción de hueso, y que esta está regulada por los valores del desplamiento eléctrico debidos a las cargas mecánicas ($\mathbf{D}_{\boldsymbol{\varepsilon}}$).

El problema variacional para el modelo propuesto se escribe como un sistema acoplado formado por dos ecuaciones variacionales no lineales para el campo de desplazamientos y el potencial eléctrico y una inecuación variacional parabólica no lineal para la densidad aparente.

Una vez obtenida la formulación variacional, aplicando el método de los elementos finitos para aproximar la variable espacial y el esquema de Euler explícito para discretizar la variable temporal, obtenemos un esquema discretizado y las estimaciones del error para el campo de desplazamientos, el potencial eléctrico y la densidad aparente. Además, bajo ciertas condiciones de regularidad adicional, deducimos la convergencia lineal del algoritmo. Por último, se describe el algoritmo utilizado para resolver el esquema discretizado. En este algoritmo se resuelve el sistema formado por las ecuaciones variacionales lineales para el campo de desplazamientos y el potencial eléctrico. Este problema se escribe como un sistema lineal cuya matriz no es simétrica y, por ello, lo resolvemos aplicando la factorización LU a la matriz del sistema. A continuación, se resuelve la inecuación variacional para obtener la densidad aparente aplicando un algoritmo de tipo penalización dualidad. Por último, se presentan algunas simulaciones

numéricas en una, dos y tres dimensiones.

Conclusiones.

A lo largo de esta tesis se han presentado distintos modelos de remodelación ósea y se han realizado simulaciones numéricas utilizando el método de los elementos finitos para mostrar su comportamiento.

Los dos primeros modelos, estudiados en los capítulos dos y tres, tienen como característica principal el considerar el hueso como un material elástico. Se ha realizado el análisis numérico de estos dos modelos clásicos y se han propuesto algoritmos numéricos para su resolución. Además se han implementado estos algoritmos en una, dos y tres dimensiones.

En el último capítulo de la tesis, se propone un modelo en el que el hueso es modelado como un material piezoeléctrico. Hemos realizado el análisis numérico y propuesto un algoritmo para su resolución que hemos implementado en una, dos y tres dimensiones, mostrando que los resultados numéricos son acordes con las teorías de otros autores.

En todos los modelos estudiados, la existencia y unicidad de solución para el problema variacional es un problema abierto. Si bien es cierto que existen resultados para problemas similares, en lo que respecta al modelo de Cowin y Hegedus, las condiciones de regularidad necesarias son muy restrictivas. Otros trabajos más recientes abordan este estudio para el modelo propuesto por Weinans, Huiskes y Grootemboer, obteniendo el resultado de existencia y unicidad de solución para un problema regularizado.

Agradecimientos:

Este trabajo fue parcialmente financiado por MCYT-España “Contacto de materiales viscoplásticos y viscoelásticos: formulación matemática y análisis numérico” (Proyecto BFM2003-05357, Investigador Principal: Juan M. Viaño) y MEC-Spain “Análisis matemático y simulación numérica de modelos avanzados de comportamiento de materiales: aplicaciones en la industria, biomecánica y ortodoncia” (Proyecto MTM2006-13981, In-

vestigador Principal: Juan M. Viaño). Además, durante los últimos tres años recibí financiación por parte del Ministerio de Educación y Ciencia (España) a través de la beca predoctoral de Formación de Personal Investigador BES-2007-16164.

Summary

The increase in life expectancy causes the medical technologies development. The new technical surgery, more efficient and less invading, as laser surgery, and designed medicines are examples of great importance nowadays. These advances lead to new demands in research and, specially, a new professional profile, combining medical and engineering aspects to consolidate a new discipline: the Bioengineering.

Bioengineering gathers fields like Biomedical technology, Biomaterials or Biomechanics. We focus our attention in the last one: Biomechanics is the application of mechanical principles to living organisms. By using the laws and concepts of physics, biomechanical mechanisms and structures can be simulated and studied. Biomechanics helps to understand how the organism works, to characterize the behavior of alive organs and tissues from the mechanical point of view, to predict the changes that are due to alterations and to propose artificial intervention methods. Hence, diagnosis, surgery and prothesis design are directly related to Biomechanics.

Investigators have been studying the relationship between the structure of the bone and mechanical forces since at least the seventeenth century. In the nineteenth century, a number of authors described the relationships between the form and function of bones in greater detail, and Julius Wolff made the critical observation that not only there is a clear relationship between bone structure and loading but also living bone adapts to alterations in loads by changing its structure in accordance to mathematical laws. This is called bone remodeling. Experimental research verifies the existence of

Wolff's law, showing that as consequence of bone remodeling the bone can adapt its structure to changes in the loads even in the adult age.

The main objective in this Ph.D. Thesis is to perform the numerical simulation and to develop the mathematical analysis of some bone remodeling models, which are able to predict the behavior of bone tissue and its capacity to adapt itself to applied loads. These models are used to predict the response of the bone when a prothesis is implanted, unusual loads are applied or to design better implants changing the geometry, the material or even the location.

In the following, we summarize the four chapters that comprise this Ph.D. Thesis. This work has been developed during the last five years in the Department of Applied Mathematics Universidad de Santiago de Compostela under the supervision of Professors José Ramón Fernández García and Juan Manuel Viaño Rey.

Chapter 1: The bone tissue and its behavior.
In this chapter we explain how is the internal morphology of a bone and what is the bone remodeling. We will focus our attention in those components that are the responsible of regulating the process, to understand the bone remodeling models that we introduce in the next chapters.

Bones are rigid organs that form the skeleton of vertebrates. They are the responsible of vital functions as to protect the organs of the body or to provide a frame to keep the body supported. Each bone has a different shape and a complex internal and external structure. Although they are lightweight, they are strong and hard. Making the bone up, we can find different tissues like marrow, endosteum and periosteum, nerves, blood vessels, cartilage and bone tissue.

There are two major classes of bone tissue: cancellous and cortical bone. Both have

the same structure and composition, but cortical bone is more dense. This tissue gives bones their smooth, white and solid appearance.

Filling the interior of the organ is the trabecular bone. It is a type of osseous tissue with a low density and strength but very high surface area, that fills the inner cavity of long bones. It consists of a network of hard, interconnected filaments interspersed with marrow and a large number of small blood vessels. It accounts for the 20% of total bone mass, but it has nearly ten times the surface area of compact bone.

The bone matrix (also called spongy, cancellous or trabecullar bone) is encased in the extracellular fluid, which is always in contact with the blood plasma. Within the plasma we can find the bone cells, which are responsible for regulating the chemical reactions which imply the addition or loss of bone mass, causing a change in the porosity of bone matrix.

The bone cells can be classified in four types, depending on their function: osteoblasts, osteoclasts, bone lining cells and osteocytes.

The bone generating cells are the osteoblasts. When the bone is forming quickly, like in the growth or in the cure of a fracture, the osteoblasts are predominant and their shape is oval or cubic. In adult bones we can find less osteoblasts and with an elongated or flat shape.

Bone lining cells form a thin layer which covers all of the available bone surface on the bone matrix. They are essentially inactive osteoblasts and their form is plane. Usually they are inactive waiting to be stimulated and to become a layer of osteoblasts.

Osteocytes are the most abundant cells found in adult skeleton, more than 90%. An osteocyte is a star-shaped cell. When osteoblasts become trapped in the matrix they

secrete, they become osteocytes.

An osteoclast is the bone cell that removes bone tissue. When osteoclasts are stimulated they merge together and form big osteoclasts with several nuclei. Once they complete the absorption, they are divided into mono nuclei cells and in the future they can be stimulated forming new multinucleated osteoclasts.

The bone cells are the responsible of develop the bone remodeling process. Bone remodeling is a slow, lifelong process in which old bone is removed from the skeleton and new bone is added. Usually, the removal and formation of bone are in balance and maintain skeletal strength and integrity. During the resorption, the osteoclasts break down bone to create small cavities in the surface of the bone matrix. Then, osteoblasts repair the surface generating new bone and finally, the bone surface is covered by a layer of lining cells which protect the new surface. The transition between the activity of osteoblasts and osteoclasts is not immediate, in the human being this time is approximately 30 days. The activity of osteoclasts takes around 10 days. In the first year of life, almost 100% of the skeleton is replaced. In adults, remodeling proceeds at about 10% per year.
There are two kinds of bone remodeling: external, in which the geometry of the bone changes along the time, and internal, in which the properties of the bone change without modifying its form. In this thesis we will focus on the second one.

Chapter 2: A strain adaptive bone remodeling model.

When we try to study, from the mechanical point of view, the structure of a bone it is impossible to model each trabecular structure. Because of that, we need to define continuous properties and to avoid using real properties of bone tissue. This implies to consider bone tissue as a continuum material. This hypothesis is justified because we are interested on the bone response in a large enough area to obtain results about

the properties of this area. Most bone remodeling theories are exposed in a similar way, by using a continuous formulation. In fact, almost all models characterize the surrounding of a point employing the apparent density, which is a mean value of the real density in that point.

In the first section of this chapter, we introduce a bone remodeling model proposed by Cowin and Hegedus in 1976 (see [15, 46]). To obtain this model, they make the following assumptions:

- The mechanical properties of the whole bone are essentially the same as the bone matrix.

- The porosity of the bone matrix is changed by the addition or the removal of mass from the bone matrix. This mass transfer occurs as a result of a chemical reaction which is mediated by the bone cells.

- The rates of these chemical reactions depend upon the strain and are very slow (on the order of months). This justifies that the bone remodeling process is considered quasistatic.

- The fact that living bone matrix is encased in a living organism is reflected in the model by setting the porous structure in a bath of perfusant. We will assume the perfusant bath to be an isothermal heat reservoir.

- As the porosity of the bone matrix changes, the area of the interface between the porous structure and the fluid will also in general change. There is not a direct relation between the porosity and the area of the interface. We will consider that only porosity changes and we will not introduce the area of the interface into the model as a variable.

Applying these hypotheses, Cowin and Hegedus obtained the equilibrium equations for mass, momentum and energy and the entropy inequality, establishing the following

constitutive law for the stress tensor:

$$\boldsymbol{\sigma} = (\xi_0 + e)\mathcal{C}(e)\boldsymbol{\varepsilon}(\boldsymbol{u}),$$

where ε denotes the strain tensor and $\mathcal{C}(e)$ characterizes the mechanical properties of the bone. The function e measures the change in the porosity of the bone and it is defined as $e = \xi - \xi_0$, where ξ is the volume fraction of material present in the bone and ξ_0 is a volume fraction of reference.

In order to control the bone remodeling process, Cowin and Hegedus obtained a first-order ordinary differential equation:

$$\dot{e} = a(e) + \mathcal{A}(e) \, : \, \boldsymbol{\varepsilon}(\boldsymbol{u}),$$

where $a(e)$ and $\mathcal{A}(e)$ are the remodeling coefficients dependent upon the change in volume fraction of the adaptive elastic material from the reference volume fraction. This remodeling rate equation specifies the rate of change of the volume fraction as a function of the volume fraction and strain.

When the change in volume fraction vanishes and the reference volume fraction is one, the constitutive equation for the stress tensor coincides with the classical Hooke's law. In the theory of adaptive elasticity, however, the coefficients of proportionality between stress and strain depend upon the volume fraction of elastic material.

In the second section of this chapter, we obtain a variational formulation for this problem. Applying the Euler scheme to discretize the time derivatives and the finite element method to approximate the spatial variable, we obtain a fully discrete scheme. Next, we prove a main error estimates result and, under suitable regularity conditions, we deduce the linear convergence of the algorithm. Finally, we describe a numerical algorithm to solve the discrete problem and we perform some numerical simulations in one, two and three dimensions.

In the third section, we assume that the bone can come into contact with a rigid or deformable obstacle.

When we assume that the contact is produced with a rigid obstacle the classical Signorini contact conditions are employed; that is,

$$u_\nu \leq s, \quad \sigma_\nu \leq 0, \quad (u_\nu - s)\sigma_\nu = 0,$$

where u_ν denotes the normal displacement, σ_ν the normal stress and s the distance between the bone and the obstacle, measured along the outward unit normal vector ν.

When we assume that the contact is produced with a deformable obstacle, the well-known normal compliance contact condition is employed; that is, the normal stress on the part of the boundary that can come into contact with the obstacle is given by

$$-\sigma_\nu = p_\nu(u_\nu - s),$$

where the function p_ν must be zero if the two bodies are in contact. As an example, one may consider

$$p_\nu(r) = \frac{1}{\mu}\, r_+,$$

where μ is a deformability constant. We establish the convergence of the solution to the contact problem with a deformable obstacle, when the deformability coefficient tends to zero, to the solution to the Signorini's problem.

Applying the Euler scheme to discretize the time derivatives and the finite element method to approximate the spatial variable, we obtain the variational formulations and some error estimates results. Finally, the linear convergence of the proposed algorithm is deduced and numerical simulations in one and two dimensions are performed. This algorithm consists in solving a nonlinear variational equation, for the problem with a deformable obstacle, or an elliptic variational inequality for the Signorini's problem. Both equations are solved with a penalty-duality algorithm.

The results presented in this chapter have been recently published in [20, 26, 27, 28].

Chapter 3: Bone remodeling induced by a local stimulus.
In this chapter we analyze, from the numerical point of view, the model studied in [66] by Weinans, Huiskes and Grootenboer in 1992. This model is based on the principle that bone remodeling is induced by a local mechanical signal which activates the regulating cells (osteoblasts and osteoclasts); that is, the bone has sensors, which can detect a mechanical stimulus, and, depending on its magnitude, cause local bone adaptations. The main idea of this model is to use the apparent density as the characterization of the internal morphology.

Weinans et al. consider the bone as an elastic material, in which the Poisson's modulus and Young's ratio depend on the apparent density:

$$E = M\rho^{\gamma},$$

where M and γ are positive constants which characterize the bone behavior.

In the previous chapter it was assumed a relationship in which the adaptation of the bone was coupled directly to deviations of the strain tensor. However, the original ideas of Wolff implied more issues than just this notion of bone remodeling due to deviations in its normal stress environment. Hence, in this model, they consider as mechanical stimulus the Strain Energy Deformation:

$$U(\boldsymbol{\sigma}(\boldsymbol{u}), \boldsymbol{\varepsilon}(\boldsymbol{u})) = \frac{1}{2}\boldsymbol{\sigma}(\boldsymbol{u}) \,:\, \boldsymbol{\varepsilon}(\boldsymbol{u}).$$

The strain energy deformation is approximated by U/ρ, which represents the strain energy per unit of bone mass. Hence, the variation in the bone density is given by the

following nonlinear first-order ordinary differential equation:

$$\dot{\rho} = B\left(\frac{U(\boldsymbol{\sigma}(\boldsymbol{u}), \boldsymbol{\varepsilon}(\boldsymbol{u}))}{\rho} - S_r\right), \quad \rho_a \leq \rho \leq \rho_b,$$

where B and S_r are constants that regulate the bone remodeling process. Moreover, the bone density can not exceed the value ρ_b, corresponding to the density of the cortical bone, or being smaller than the minimal density allowed, ρ_a, corresponding to the reabsorved bone. This equation means that the points in which the density reaches the minimum or maximum value, the remodeling process stops. On the other points, the system is in equilibrium when the stimulus reaches the reference value S_r.

The variational formulation of this model consists in a variational equation for the displacement field and a variational inequality for the bone density. This equation is obtained applying the properties of the subdiferential of the indicator function of the interval $[\rho_a, \rho_b]$, which guarantees that the solution belongs to the interval

Applying the Euler scheme and the finite element method we obtain a discrete problem and the error estimates for the displacement field and the bone density. Moreover, under suitable regularity assumptions, the linear convergence of the algorithm is established. Finally, we describe the numerical algorithm which is implemented and show the numerical simulations performed in one and two dimensions. The variational equation for the displacement field is solved applying the Cholesky method and the variational inequality for the bone density by using the penalty-duality algorithm already used in the previous chapter. The main advantage of this algorithm is to obtain the displacement field and the bone density solving two uncoupled problems.

The results corresponding to this chapter have been published in [23].

Chapter 4: A piezoelectric bone remodeling model.

It is widely accepted in bone remodeling that the bone adapts its internal structure to the mechanical loads and this adaptation process is developed by the bone cells. However, it is unclear how actuator cells, osteoclasts and osteoblasts, are able to control bone resorption and formation as a function of mechanical conditions.

Fukada and Yasuda showed in 1957 that dry bone is piezoelectric in the classic sense, that is, mechanical stress produces polarization (direct effect) and application of an electric field produces strain (converse effect) (see [38, 39]). Since then, the electrical properties of bone tissue have been widely investigated. It is believed that electric signals play an important role in the bone remodeling process (see [2, 42, 43]). However, it has not been normally used to understand bone remodeling and, currently, there are not many models that justify bone remodeling based on bone piezoelectricity (see [61, 62, 63]).

In this chapter, our aim is to use the bone remodeling model analyzed in the previous chapter to characterize the elastic properties of the bone and extend the classical electro-mechanical dependence adding a function $\alpha(\rho) = \rho^\gamma$ which regulates the coupling between the mechanical and electric field. This function guarantees that the electric field increases with the density of the bone. Hence, as a first approach, the constitutive law for the stress tensor σ and the electric displacement $\mathbf{D}$ are the following:

$$\boldsymbol{\sigma} = 2\,\mu(\rho)\boldsymbol{\varepsilon}(\boldsymbol{u}) + \lambda(\rho)\mathrm{Div}\,(\boldsymbol{u})\mathcal{I} - \alpha(\rho)\mathcal{E}^*\mathbf{E}(\varphi),$$

$$\mathbf{D} = \mathbf{D}_{\boldsymbol{\mathcal{E}}} + \mathbf{D}_{\mathbf{E}} = \alpha(\rho)\mathcal{E}\boldsymbol{\varepsilon}(\boldsymbol{u}) + \alpha(\rho)\beta\mathbf{E}(\varphi),$$

where $\mathbf{E}(\varphi) = (E_i(\varphi))_{i=1}^d$ is the electric field, $\mathcal{E}^* = (e^*_{ijk})_{i,j,k=1}^d$ represents the transpose of the third-order piezoelectric tensor $\mathcal{E} = (e_{ijk})_{i,j,k=1}^d$ and β is the electric permittivity tensor.

Following the works of Gjelsvik (see [42, 43]) we try to numerically show that bone formation and resorption may be related to electrical charges in the bone surfaces due to contributions produced by mechanical loading ($\mathbf{D}_{\boldsymbol{\varepsilon}}$).

The variational problem for the proposed model is written as a coupled system of two nonlinear variational equations for the displacement and the electric potential fields, and a parabolic variational inequality for the apparent density.

Then, applying the finite element method to approximate the spatial variable and the Euler scheme to discretize the time derivatives, we obtain a discrete scheme and error estimates for the displacement field, the electric potential field and the apparent density. Moreover, under suitable regularity conditions, we deduce the linear convergence of the algorithm. Finally, we describe the algorithm applied to solve the discrete scheme. In this algorithm the system composed by the linear variational equations for the displacement field and the electric potential field is solved. This problem is written as a linear system which matrix is not symmetric. Hence, we solve it using the LU factorization. Then, the variational inequality to obtain the apparent density is solved applying a penalty-duality algorithm. Finally, we perform some numerical simulations in one, two and three dimensions.

Conclusions.

In the course of this Ph.D. thesis we studied several bone remodeling models and numerical simulations have been performed to show its behavior.

The first two models, studied in chapters two and three, have in common to consider the bone as an elastic material. We have developed the numerical analysis of these classical models and numerical algorithms have been proposed to their resolution. Moreover, these algorithms have been implemented in one, two and three dimensions.

In the last chapter, we proposed a new bone remodeling model in which we consi-

dered the bone as an piezoelectric material. We developed the numerical analysis, we proposed an algorithm to its resolution and we have implemented this algorithm in one, two and three dimensions, showing that the numerical results are according to the theories proposed by other authors.

The existence and uniqueness of weak solutions for the discrete problems were obtained by using classical results on linear variational equations or elliptic variational inequalities. However, we remark that the existence and uniqueness results of weak solutions for the continuous variational formulations are open problems. In the Cowin and Hegedus model, this result was obtained for a similar variational formulation in which stronger assumptions were made over the data. Recently, Fernández and Kuttler dealt with the model proposed by Weinans, Huiskes and Grootenboer obtaining an existence and uniqueness result for a regularized problem.

Acknowledgement:
This work was partially supported by MCYT-Spain "Contacto de materiales viscoplásticos y viscoelásticos: formulación matemática y análisis numérico" (Project BFM2003-05357, Head of the project: Juan M. Viaño) and MEC-Spain "Análisis matemático y simulación numérica de modelos avanzados de comportamiento de materiales: aplicaciones en la industria, biomecánica y ortodoncia" (Project MTM2006-13981, Head of the project: Juan M. Viaño). Furthermore, during the past three years I have been funded by Ministerio de Educación y Ciencia (Spain) through Grant Number BES-2007-16164 of FPI program.

Introduction

The increase in life expectancy causes the medical technologies development. The new technical surgery more efficient and less invading, as laser surgery, and designed medicines are examples of great importance nowadays. These advances lead to new demands in research and, specially, a new professional profile, combining medical and engineering aspects to consolidate a new discipline: the Bioengineering.

Bioengineering is the application of engineering principles to the full spectrum of living systems. This is achieved using existing methodologies in such fields as molecular biology, biochemistry, microbiology, pharmacology, immunology or neuroscience and applying them to the design of medical devices, diagnostic equipment, biocompatible materials and other important medical needs.

Bioengineering gathers fields like Biomedical technology, Biomaterials or Biomechanics. We focus our attention in the last one: Biomechanics is the application of mechanical principles to living organisms. By applying the laws and concepts of physics, biomechanical mechanisms and structures can be simulated and studied.

Biomechanics helps to understand how the organism works, to characterize the behavior of alive organs and tissues from the mechanical point of view, to predict the changes that are due to alterations and to propose artificial intervention methods. Hence, diagnosis, surgery and prothesis design are directly related to biomechanics.

Investigators have been studying the relationship between the structure of the bone and mechanical forces since at least the seventeenth century. In the nineteenth century, a number of authors described the relationships between the form and function of bones in greater detail, and Julius Wolff made the critical observation that not only there is a clear relationship between bone structure and loading but also living bone adapts to alterations in loads by changing its structure in accordance with mathematical laws. This is called bone remodeling. Experimental research verifies the existence of Wolff's law, showing that as consequence of bone remodeling the bone can adapt its structure to changes in the loads even in the adult age.

The main objective in this Ph.D. Thesis is to perform the numerical simulation and to develop the mathematical analysis of some bone remodeling models, which are able to predict the behavior of bone tissue and its capacity to adapt itself to applied loads. These models are used to predict the response of the bone when a prothesis is implanted, unusual loads are applied or to design better implants changing the geometry, the material or even the location.

This work is structured as follows. In the first Chapter, in order to understand the mathematical models that we analyze in this thesis, we explain how is the internal structure of a bone and how a bone remodeling process occurs, and we make a brief introduction to the models considered.

In Chapter 2 we study the first continuous mathematical formulation of a bone remodeling process already considered by Cowin et al (see [15, 16, 46]). We propose and analyze a numerical method to solve the model and perform some numerical simulations. In the second part of this chapter, we assume that the bone is in contact with an obstacle, which can be deformable or rigid. We numerically study both problems and establish a convergence result. Finally, we perform some numerical simulations in one, two and three dimensions.

In Chapter 3 we analyze, from the numerical point of view, the model proposed by Weinans, Huiskes and Grootenboer (see [66]). The main characteristic of this model is that, in spite of considering the bone as an isotropic material and model its behavior with a continuous formulation, we can predict the discontinuities in the internal morphology of the bone. We propose an algorithm to solve it, we analyze it and we perform some numerical simulations.

In Chapter 4 we propose a bone remodeling model in which the bone is considered as a piezoelectric material and a numerical method to solve it. We provide its numerical analysis and we perform some numerical simulations which demonstrate that its behavior is in agreement with the theoretical knowledge about bone remodeling.

Acknowledgement

This work was partially supported by MCYT-Spain "Contacto de materiales viscoplásticos y viscoelásticos: formulación matemática y análisis numérico" (Project BFM2003-05357, Head of the project: Juan M. Viaño) and MEC-Spain "Análisis matemático y simulación numérica de modelos avanzados de comportamiento de materiales: aplicaciones en la industria, biomecánica y ortodoncia" (Project MTM2006-13981, Head of the project: Juan M. Viaño). Furthermore, during the past three years I have been funded by Ministerio de Educación y Ciencia (Spain) through Grant Number BES-2007-16164 of FPI program.

Chapter 1

The bone tissue and its behavior

In this chapter we explain how is the internal morphology of a bone, the different tissues that make up these organs and how they work (see [10], [11] and [41]). In order to understand the bone remodeling models that we introduce in the next chapters, we will focus our attention in those components that are the responsible of regulating the bone remodeling process.

1.1 Bone morphology

Bones are rigid organs that form the skeleton of vertebrates. Their function is to move, to support, and to protect the organs of the body, to produce red and white blood cells and to store minerals. Each bone has a different shape and a complex internal and external structure. Although they are lightweight, they are strong and hard. Making the bone up, we can find different tissues like marrow, endosteum and periosteum, nerves, blood vessels, cartilage and bone tissue.

Bones have several essential functions:

- Some bones protect internal organs, such as the skull protects the brain or the ribs protect the heart and lungs.
- They provide a frame to keep the body supported.

- Bones, skeletal muscles, tendons, ligaments and joints function together to generate and to transfer forces so that individual body parts or the whole body can be manipulated.
- They are important in the mechanical aspect of hearing.
- The marrow, located within the medullary cavity of long bones and interstices of cancellous bone, produces blood cells.
- Bones act as reserve of minerals important for the body, most notably calcium and phosphorus.

Bone tissue is an alive tissue which consist of three basic components: the bone cells, extracellular fluid and the solid extracellular material which is called the bone matrix. The bone matrix is a solid structure with interconnected pores (see Figure 1.1). This bone matrix (also called spongy, cancellous or trabecullar bone) is encased in the extracellular fluid, which is always in contact with the blood plasma. Within the plasma we can find the bone cells, which are the responsible of regulating the chemical reactions which cause the addition or loss of bone mass, causing a change in the porosity of bone matrix. These cells, which we describe in the following with more detail, are osteoblasts, osteoclasts and osteocytes. Wrapping the bone matrix is the cortical or compact bone. This bone tissue provides the bone its smooth and solid appearance.

Attending to its shape we can classify the bones in three types: long, short and flat.

- The long bones are those that are longer than they are wide, and grow primarily by elongation of the diaphysis, with an epiphysis at the ends of the growing bone (see Figure 1.2). The ends of epiphyses are covered with a hyaline cartilage. The long bones include the femurs, tibias, the humeri, radii, metacarpals and metatarsals of the hands and feet, and the phalanges of the fingers and toes. Additionally, the outer shell of the long bone is compact bone. The interior part of the long bone is the medullary cavity with the inner core of the bone cavity being composed (in adults) of yellow marrow.

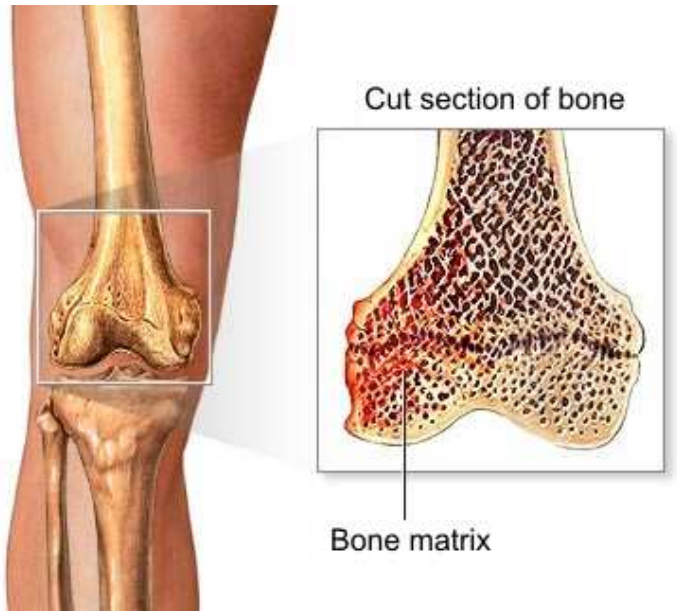

Figure 1.1: Bone matrix.

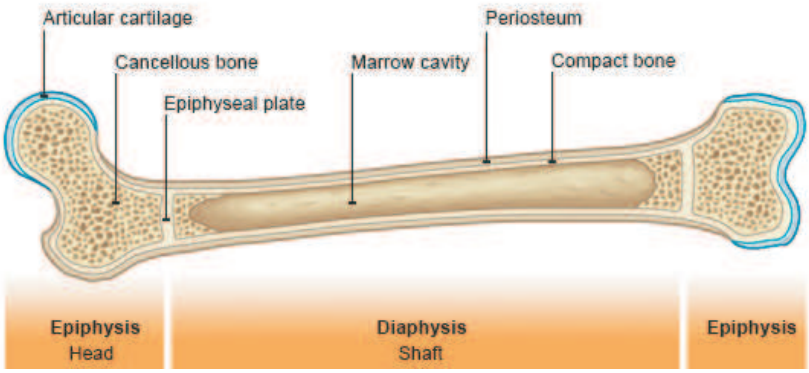

Figure 1.2: Anatomy of a long bone.

- Short bones are defined as being approximately as wide as they are tall. These consist of cancellous tissue enclosed within a thin layer of compact bone. To this group belong the carpals (bones of hands and wrists) and tarsus (bones of feet and ankles).

- Flat bones are those bones which are found where the principal requirement is either extensive protection or the provision of broad surfaces for muscular attachment, the bones are expanded into broad, flat plates, as in the skull, the

pelvis, sternum, rib cage, and the scapula. These bones are composed of two thin layers of compact tissue enclosing between them a variable quantity of cancellous tissue, which is the location of red bone marrow.

As we said previously, there are two major classes of bone tissue which significantly contribute to the structural strength of the skeletal system. They are called cancellous and cortical bone. Both of them have the same structure and composition, but cortical bone is more dense (see Figure 1.3).

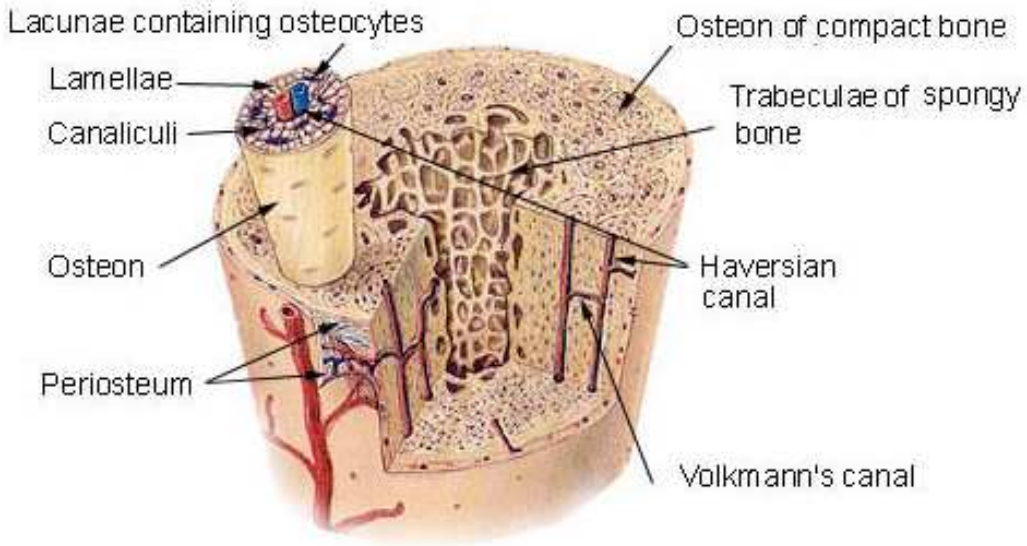

Figure 1.3: Compact and cancellous bone.

The hard outer layer of bones is composed of cortical or compact bone tissue, so-called due to its minimal gaps and spaces. This tissue gives bones their smooth, white and solid appearance, and accounts for 80% of the total bone mass of an adult skeleton. It is extremely hard, formed of multiple stacked layers with few gaps and its blood vessels are microscopically small. Its main function is to support the body, to protect organs and to store minerals.

Filling the interior of the organ is the trabecular bone. It is a type of osseous tissue with a low density and strength but very high surface area, that fills the inner cavity of long bones. It consists of a network of hard, interconnected filaments interspersed with marrow and a large number of small blood vessels. This tissue runs mostly parallel to the long axis of the bone. The blood vessels lie in their own channels called Haversian canals and bone is concentrically layered around each canal. Collectively, the concentric layers of bone and the canal form a unit called a Haversian system or osteon (see Figure 1.4). Between each concentric layer, or lamellae, a ring of dark elliptical spots called lacunae is present where, normally, osteocytes are embedded. The canaliculi are small channels that interconnect adjacent osteocytes. Each lamellae is composed of collagen fibers with a high directionality. The fibers and adjoint lamellas goes in different directions. The fibers of collagen are normally interconnected between them and with other lamellas, increasing the resistance of the bone. Cancellous bone is also where most of the arteries and veins of bone organs are found. It accounts for the remaining 20% of total bone mass, but it has nearly ten times the surface area of compact bone.

Periosteum is a membrane that lines the outer surface of all bones, except at the joints of long bones. The cells that are in periosteum are able to remove or create bone tissue as response to stimulus. The periosteum consist in two layers: the internal layer contains cells that can become in osteoblast and the external one contains less cells and more collagen. Periosteum is attached to bone by strong collagenous fibers. It also provides an attachment for muscles and tendons.

The endosteum is a thin layer of connective tissue which lines the surface of the bone tissue that forms the medullary cavity of long bones. This endosteal surface is usually resorbed during long periods of malnutrition resulting in less cortical thickness.

To develop the several functions of a bone, the bone cells show different morphology, function and location. There are four kinds of cells: osteoblast, osteoclast, bone lining

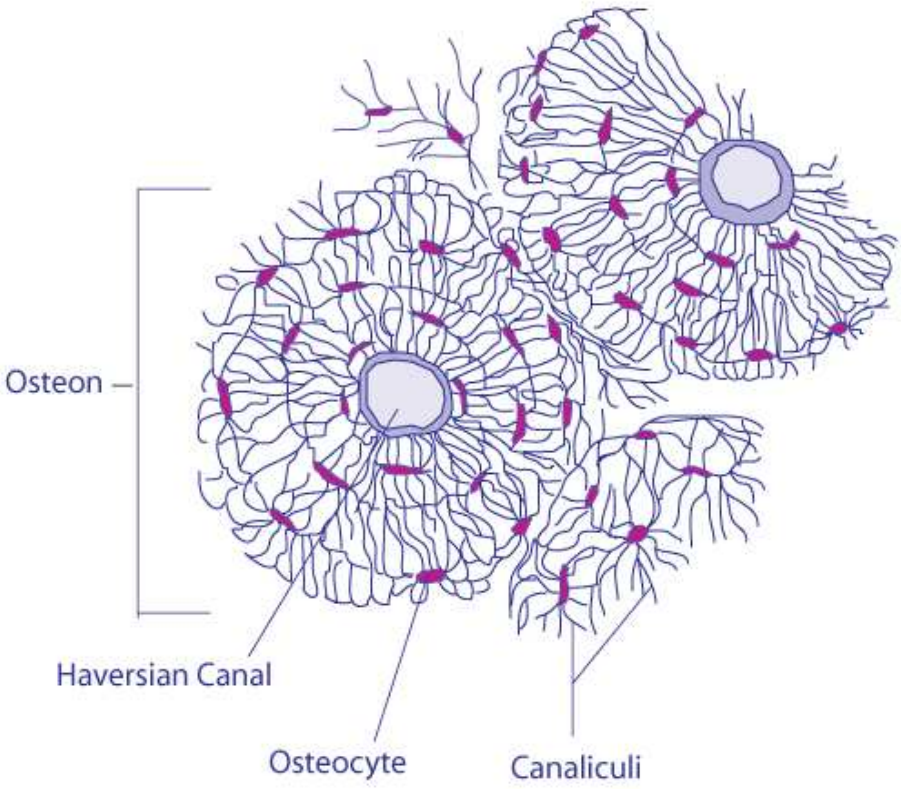

Figure 1.4: Osteon or Haversian system.

cells and osteocytes.

The bone generating cells are the osteoblasts (see Figure 1.5). Their main function is to synthesize and to secrete the bone matrix. When the bone is forming quickly, like in the growth or in the cure of a fracture, the osteoblasts are predominant and their shape is oval or cubic. In adult bones we can find less osteoblasts and with an elongated or flat shape.

Bone lining cells form a thin layer which cover all of the available bone surface (see Figure 1.6). They are essentially inactive osteoblasts. Its form is plane. Usually they are inactive waiting to be stimulated and to become a layer of osteoblasts.

Osteocytes are the most abundant cells found in adult skeleton, more than 90%. An osteocyte is a star-shaped cell. When osteoblasts become trapped in the matrix they secrete, they become osteocytes. Osteocytes are networked to each other via long cytoplasmic extensions that occupy tiny canals called canaliculi, which are used for exchange of nutrients and waste. The space that an osteocyte occupies is called a lacuna. Although osteocytes have reduced synthetic activity and, like osteoblasts are not capable of mitotic division, they are actively involved in the routine turnover of bone matrix.

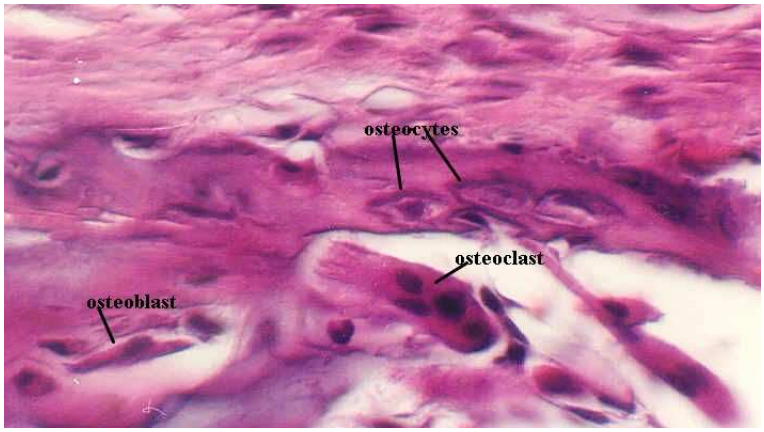

Figure 1.5: Osteocytes, osteoblast and osteoclasts with several nuclei.

An osteoclast is the bone cell that removes bone tissue. When osteoclasts are stimulated they merge together and form big osteoclasts with several nuclei. Usually, osteoclasts have between three and twenty nuclei. They eliminate bone tissue by removing its mineralized matrix. Once osteoclasts complete the absorption, they are divided into mono nuclei cells and in the future they can be stimulated forming new multinucleated osteoclasts.

Located in the canal are the osteoblasts. As we explained before, they are the bone generating cells. They deposit a sequence of layers of lamellar bone on the inner wall of the osteon, forming the lamellae sequentially, from the most external inward towards

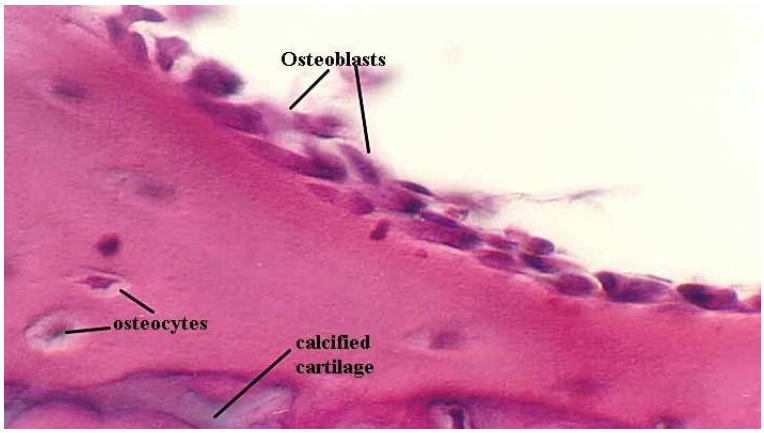

Figure 1.6: Layer of osteoblasts. When they are inactive are called bone lining cells.

the Haversian canal.

The cells in the cancellous bone remain between lamellas or over the surface of trabecullas, where they can be affected by the cells in the bone marrow. However, the most bone cells in cortical bone are surrounded by bone matrix. Maybe, because of this difference in the organization in each class of bone, the remodeling process is produced more quickly in cancellous bone. This difference can be observed, for example, in the X-rays of long bones for a immobilized leg. In this situation, the density in the cancellous bone diminishes, as a consequence of the absorption in the trabecullae, earlier than in the cortical bone.

Bone tissue (cortical and cancellous) could be made of plexiform bone or laminar bone. Plexiform bone forms the embryo of the skeleton and when it is growing up, this tissue is replaced by laminar bone. The callus that appear in a fracture are made in the same way. Small amount of plexiform bone can be part of tendons and ligaments. Except in these cases, plexiform bone does not appear in the human skeleton after four or five years old.

Plexiform and laminar bone are differentiated in its formation, composition, organi-

zation and mechanical properties. In the plexiform bone, the resorption and formation are produced with high velocity, whereas the laminar bone is not so active. Comparing both types of tissue, plexiform bone does not present a stable relation of minerals to collagen (in fact, it could be observed a huge variation in its mineral density) and contains around four times more osteocites per volume unit. These osteocites are of different sizes, orientation and distribution. Nevertheless, in laminar bone they are of uniform size and their principal axis is oriented parallel to collagen fibers forming bone matrix. The mineralization in plexiform bone is produced in a irregular way, creating an irregular appearance. On the other hand, in the laminar bone the diameter of the fibers of collagen varies less and it remains parallel, forming the lamellas with a uniform distribution. This organization gives an homogeneous aspect. Owe to this organization, plexiform bone is more flexible and weaker than laminar bone. The irregular structure in plexiform bone implies that the mechanical properties do not depend on the applied loads, and it imposes an isotropic behavior. On the contrary, laminar bone is anisotropic and its mechanical properties depend on the orientation of the loads.

1.2 The bone remodeling process

Bone remodeling is a dynamic, lifelong process in which old bone is removed from the skeleton and new bone is added. There are two kinds of bone remodeling: external, in which the geometry of the bone changes along the time, and internal, in which the properties of the bone change without modifying its form. In this thesis we will focus on the second one.

Bone remodeling consists of two distinct stages, resorption and formation, which involve the activity of osteoclasts and osteoblasts. Usually, the removal and formation of bone are in balance and maintain skeletal strength and integrity. Remodeling responds to functional demands and muscle attachments. As a result, bone is added where needed and removed where it is not required. These changes are produced in

the internal surface of bone matrix.

The remodeling process takes place in the following phases:

- Bone resorption: In this phase, the osteoclasts break down bone acting on the cancellous bone surface to erode the mineral and matrix. This process is known as bone resorption. Through a chemical process osteoblast reduce the ph from a value of 7 to 4. This acid ph dissolves the mineral bone and diminishes the organic part of bone matrix. Bone resorption is complete when small cavities are created in the surface of the bone matrix (bone has been removed)(see Figure 1.7).

- Bone formation: Osteoblasts form new bone. They work to repair the surface and fill the eroded cavities with new bone that then has to be mineralized (this phase needs about 10 days). The transition between the activity of osteoclasts and osteoblasts is not immediate. In the human being this time is approximately 30 days.

- Completion: The bone surface is restored and covered by a layer of lining cells which protect the bone (see Figure 1.8). The new bone is calcified and the remodeling process is completed.

The three phases described previously occur in a specific place and are developed by a group of cells called Basic Multicellular Units (BMU). A BMU is a group of osteoblasts and osteoclasts which act in an specific place to develop a bone remodeling cycle. There are several BMU acting in different parts of bone. The Bone Structural Units (BSU) are the areas of new bone created by a BMU. Each BMU has a finite lifetime, so new units are continuously forming as old units are finishing.

In the first year of life, almost 100% of the skeleton is replaced. In adults, remodeling proceeds at about 10% per year. During childhood, bone formation exceeds resorption,

but as the aging process occurs, resorption exceeds formation.

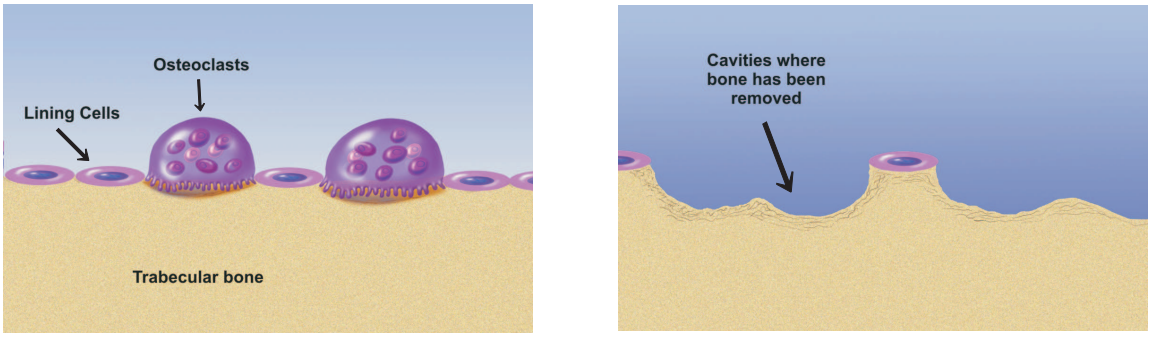

Figure 1.7: Bone resorption.

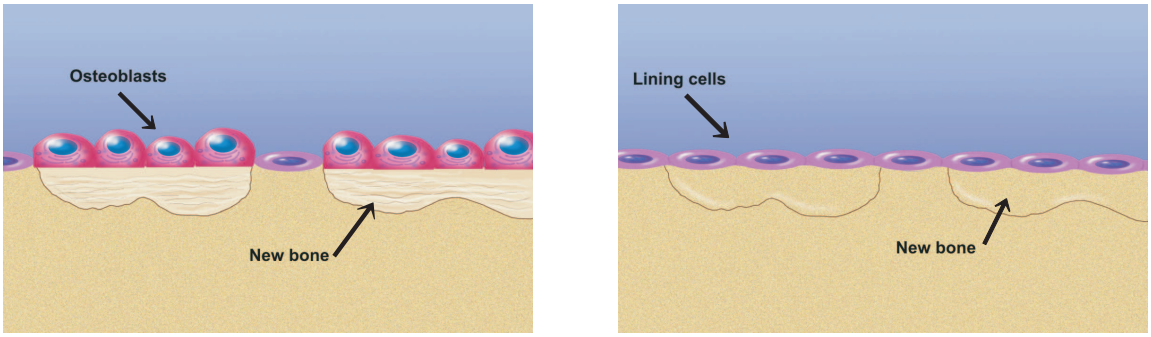

Figure 1.8: Bone formation.

The remodeling process is caused essentially by two regulating process. The first one is a hormonal regulating process and the second one depends on the mechanical charges that act on the body.

- In the hormonal mechanism takes part the parathormona: this hormone is secreted by the parathyroid glands. It acts to decrease the concentration of calcium in the blood. This hormone stimulates the osteoclasts, which accelerate the bone resorption. As a consequence, it produces a release of calcium from the blood and bone matrix. The equilibrium is recovered and it finishes the release of parathormone. In the case of an increase of blood calcium, calcitonin is secreted

to inhibit bone resorption by the osteoclasts and it causes that calcium is accumulated in bone matrix, reducing the concentration of calcium in blood. This hormonal regulation is orientated to conserve the hemostatic equilibrium, keeping the calcium concentration in blood, more than to preserve the bone resistance.

- In the second mechanism, a change in the forces acting on the body leads to the adaptation of the bone tissue, which suffers morphology changes. Thus, bone mass is added in the places with a strong charge and resorbed where the charge is smaller. In spite of the minimum intensity and type or charge necessary to keep the normal density of the bone have not been determined yet, experimental research shows that a decrease in the charge leads to a decrease in the resistance and in the bone mass. The opposite effect is known as well, that is, an increase in the charge leads to an increase in the resistance of the bone.

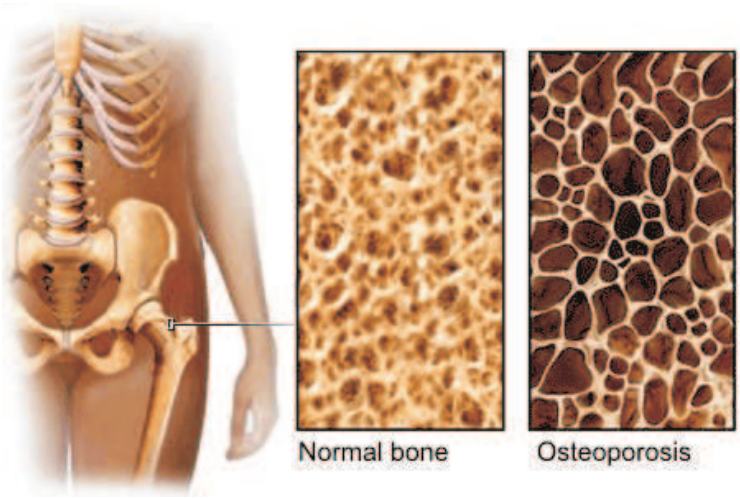

Figure 1.9: Density of bone matrix.

These adaptation factors, unlike the first one, have a tendency to keep an optimum skeleton for locomotion. In Figure 1.9 we can observe the bone matrix in a healthy bone and in a bone which suffers from osteoporosis. In the second one, the porosity is bigger than in the healthy bone, which produces the bone become weaker. This is an

example in where the hormonal factor has an important role, but usually the second factor is predominant over the first one. Because of this, the bone remodeling models that we discuss in the next chapters only take into account the response of the bone to the mechanical loads.

Finally, we introduce two important parameters to understand the internal structure of a bone: the porosity and the specific surface. The porosity is defined as the empty volume per unit of volume in the bone, or the proportional part of the bone occupied by the bone marrow. The specific surface is the internal surface area per volume unit in the bone. The importance of these values is evident, because the mechanical properties of the bone depend on the porosity. As we said, the bone is an alive tissue that is changing its internal structure along the time. These changes are regulated by physiological process that always take place in the internal surface of the bone matrix (see Figure 1.10). Only in these walls can be added or removed bone tissue and then, the velocity of change in the porosity is affected by the amount of internal surface available to the physiological activity.

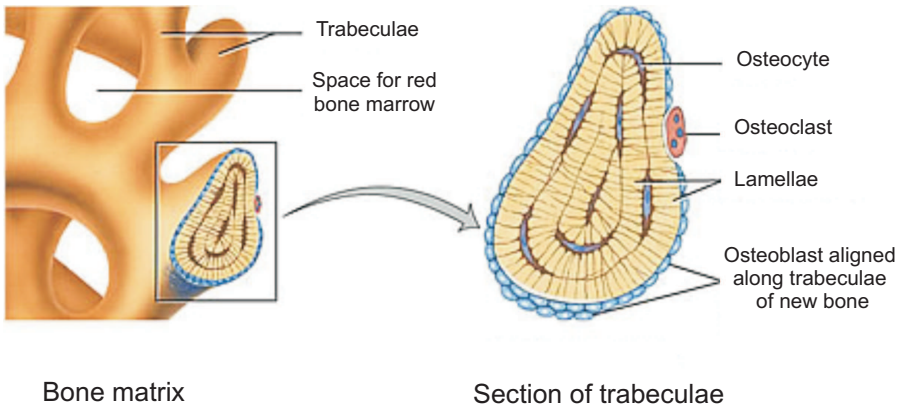

Figure 1.10: The remodeling process takes place in the surface of the trabeculae.

1.3 Modeling the bone tissue

When we try to study, from the mechanical point of view, the structure of a bone it is impossible to model each trabecular structure. Because of that, we need to define continuous properties and to avoid using real properties of bone tissue. This implies to consider bone tissue as a continuum material. This hypothesis is justified because we are interested on the bone response in a large enough area to obtain results about the properties of this area. Most bone remodeling theories are exposed in a similar way, by using a continuous formulation. In fact, almost all models characterize the surrounding of a point employing the apparent density, which is a mean value of the real density in that point.

In the late 19th century, Julius Wolff proposed in [67] that trabecular bone oriented itself in a direction that aligned with the principle stress experienced by the bone. While Dr. Wolff largely focused on trabecular bone, the idea that bone is a dynamic organ adaptive to its mechanical environment has been generalized, over time, to the whole bone including compact portion of bone. This generalization has largely been accepted by clinicians. For instance, they recognize that astronauts return with weaker bone after a long mission, while weightlifters possess increased bone density in response to their training.

Cowin and Hegedus proposed in 1976 the first continuous mathematical formulation of bone remodeling (see [15, 46]). They considered the bone matrix as a porous elastic solid encased in the extracellular fluid. The bone remodeling appears as a consequence of chemical reactions between bone matrix and the extracellular fluid. In this model, the evolution of bone remodeling process is characterized by using a function which measures the changes in the porosity, assuming that the bone has an equilibrium state in which there is not bone remodeling. As in many other models, Cowin and Hegedus proposed to consider that the bone matrix is an anisotropic and elastic material. However, to develop the numerical simulations, they assume as other authors, that the

anisotropic behavior of the bone is not relevant and therefore, they consider the bone to be orthotropic or even isotropic. The values of the constants needed for the adaptive elastic model have been studied by many authors and we can find the values of Young modulus and Poisson's ratio for different bones (see [41]). However, each model incorporates other constants to determine the remodeling rate. In [34], the remodeling rate coefficients for Cowin and Hegedus model was determined for a cylindrical body inhomogeneous along the axis of the cylinder, but homogenous in each transverse plane of the cylinder. During the last ten years, some papers dealt with mathematical issues of this bone remodeling model as the existence and uniqueness of weak solutions under some quite strong assumptions (see, e.g., [57, 64]) or the analysis of an asymptotic rod model (see [30, 31, 32, 33]). In the second chapter of this thesis we analyze this model from the mathematical and numerical points of view, and we provide some numerical results.

After this model, many authors tried to propose more complete models to reproduce the behavior of bone tissue, most of them based on considering that the bone has sensors, which can detect a mechanical stimulus, and, depending on its magnitude, cause local bone adaptations. In the third chapter we analyze the model introduced in [66] which is based on that theory. These models characterize the mechanical behavior of the bone using the aparent density. The variation of density can be described by using an objective function which depends on the strain energy and some bone remodeling parameters, described there with more detail. The main restriction of this model is that we consider the bone as an isotropic material.

How the bone is capable of responding to mechanical environment and specifically how osteocytes and osteoblasts can perceive forces remain unanswered. In the 1960s, collagen piezoelectricity was invoked as a potential mechanism by which osteocytes could detect areas of greater stress. According to this theory, applied stress generated local potential gradients along the collagen fiber and thus provided a local stimulus for

bone-generating cells.

Currently, a renovated interest has appeared to show the importance of bone piezoelectricity in bone responsiveness to mechanical environment (see [2, 63]). Two different mechanisms are responsible for bone piezoelectricity: extracellular matrix piezoelectricity, mainly due to the molecular asymmetry of collagen, and streaming potentials generated by the flow of a liquid across charged surfaces. Hence, in the fourth chapter we propose a hypothesis in which we demonstrate, through a computational approach, that only bone matrix piezoelectricity is able to explain how bone is selectively deposited or removed at different periosteal surfaces. Moreover, such bone remodeling piezoelectric model is numerically analyzed and several simulations are provided.

Chapter 2

A strain adaptive bone remodeling model

In this chapter we present the results obtained in the study of a bone remodeling model introduced in [15]. They have been recently published in [20, 26, 27, 28].

2.1 The model

In this section, we introduce a bone remodeling model proposed by Cowin and Hegedus, following the original works [15], [16] and [46] (see also the recent review [14]). Our aim is to model the bone as a porous elastic solid and to simulate the mechanical adaptation process like if the rate of mass added or removed was controlled by the deformation.

In the previous chapter, we described the biological aspects of a bone remodeling process. We turn now to present only the aspects that we take into account to obtain the mathematical model:

- The mechanical properties of the whole bone are essentially the same as the bone matrix, which is considered to be a porous elastic solid containing a fluid in its pores.

- The porosity of the bone matrix is changed by the addition or the removal of mass from the bone matrix. This mass transfer occurs as a result of a chemical reaction which is mediated by the bone cells. The rates of these chemical reactions depend upon the strain and are very slow (on the order of months). This justifies that the bone remodeling process is considered quasistatic.

- As the porosity of the bone matrix changes, the area of the interface between the porous structure and the fluid will also in general change. There is not a direct relation between the porosity and the area of the interface. We will consider only porosity changes and we will not introduce the area of the interface into the model as a variable.

- The fact that living bone matrix is encased in a living organism is reflected in the model by setting the porous structure in a bath of perfusant. We will assume the perfusant bath to be an isothermal heat reservoir.

- It is important to enhance that the equations in the model are applied only over the porous matrix structure without perfusant. The effect of the internal perfusant is accounted for by transfer terms in each equilibrium equations.

Applying these hypotheses, Cowin and Hegedus obtained in 1976 the first bone remodeling model. In [16] and [46] they derived, as usual in continuum mechanics, the equilibrium equations for mass, momentum and energy and the entropy inequality, establishing the following constitutive law for the stress tensor:

$$\boldsymbol{\sigma} = (\xi_0 + e)\mathcal{C}(e)\boldsymbol{\varepsilon}(\boldsymbol{u}),$$

where $\boldsymbol{\varepsilon}$ denotes the strain tensor (see the next section for more details) and $\mathcal{C}(e)$ characterizes the mechanical properties of the bone. The function e measures the change in the porosity of the bone and it is defined as $e = \xi - \xi_0$, where ξ is the volume fraction of material present in the bone and ξ_0 is a volume fraction of reference. By definition,

e only has to verify $-\xi_0 < e < 1 - \xi_0$, being $0 < \xi_0 < 1$. It seems reasonable to assume that for healthy bone we can choose ξ such that $|e| < 1$; however, in some pathological situations $|e|$ can exceed this value.

In order to control the bone remodeling process, Cowin and Hegedus obtained a first-order ordinary differential equation:

$$\dot{e} = a(e) + \mathcal{A}(e) \, : \, \boldsymbol{\varepsilon}(\boldsymbol{u}),$$

where $a(e)$ and $A(e)$ are the remodeling coefficients dependent upon the change in volume fraction of the adaptive elastic material from the reference volume fraction. This remodeling rate equation specifies the rate of change of the volume fraction as a function of the volume fraction and strain. A positive value of $\dot{e}$ means the volume fraction of elastic material is increasing while a negative value means the volume fraction is decreasing.

When the change in volume fraction e vanishes and the reference volume fraction ξ_0 is one, the constitutive equation for the stress tensor coincides with the classical Hooke's law. In the theory of adaptive elasticity, however, the coefficients of proportionality between stress and strain depend upon the volume fraction of elastic material.

This theory involves the functions $a(e)$, $A_{ij}(e)$ and $C_{ijkl}(e)$ which characterize the material properties. Because of the lack of experimental data about these functions, Firoozbakhsh and Cowin (see [34]) proposed to consider approximations using Taylor's developments:

$$\begin{aligned} a(e) &= a_0 + a_1 e + a_2 e^2, \\ A_{ij}(e) &= A^0_{ij} + A^1_{ij} e, \\ C_{ijkl}(e) &= \frac{1}{\xi_0 + e}(\xi_0 C^0_{ijkl} + C^1_{ijkl} e), \end{aligned}$$

where a_0, a_1, a_2, A^0_{ij}, A^1_{ij}, C^0_{ijkl} and C^1_{ijkl} are constants which represent the properties of the bone. These parameters were determined considering an inhomogeneous cylindrical body that is loaded by a steady uniform stress directed along the cylindrical axis. With this example, the values of the remodeling rate coefficients were estimated by physical arguments, assuming that the time of remodeling increases along with the compressive stress as well as the final homogeneous volume fraction. The elasticity coefficients, which determine the mechanical properties of the bone, were estimated by Cowin and Buskirk in [17]. These values can be seen in Section 2.2.3. Moreover, Firoobakhsh and Cowin proved in [34] that the bone remodeling function e tends to an homogeneous state. In the numerical simulations that we perform in this chapter we can observe that this property is achieved.

2.2 Analysis of the bone remodeling model

Our aim in this section is propose and analyze a numerical method to solve the bone remodeling model introduced in the previous section.

First, we introduce the mathematical problem which we are going to study and we derive its variational formulation. Then, applying the Euler scheme to discretize the time derivatives and the finite element method to approximate the spatial variable we obtain a fully discrete scheme. Next, we prove a main error estimates result and, under suitable regularity conditions, we deduce the linear convergence of the algorithm. Finally, we describe a numerical algorithm to solve the discrete problem and we perform some numerical simulations which demonstrate its accuracy and its behavior.

2.2.1 The mathematical problem and its variational formulation

Let us denote by $\cdot$ the euclidean inner product in $\mathbb{R}^d$ and its corresponding norm by $|\cdot|$. Let $\mathbb{S}^d$ be the space of second order symmetric tensors on $\mathbb{R}^d$ or, equivalently, the space of symmetric matrices of order d, and let : be its inner product and $|\cdot|$ its norm. Denote by $\Omega \subset \mathbb{R}^d$, $d = 1, 2, 3$, an open bounded domain and denote by $\Gamma = \partial\Omega$ its outer surface which is assumed to be Lipschitz continuous and it is divided into two disjoint parts Γ_D and Γ_N. We denote by $\boldsymbol{x} = (x_i)_{i=1}^d$ a generic point of $\overline{\Omega} = \Omega \cup \Gamma$, and for $\boldsymbol{x} \in \Gamma$, $\boldsymbol{\nu}(\boldsymbol{x}) = (\nu_i(\boldsymbol{x}))_{i=1}^d$ denotes the outward unit vector, normal to Γ at point $\boldsymbol{x}$ (see Figure 2.1).

The bone occupying the volume $\overline{\Omega}$ is being acted upon by a volume force of density $\boldsymbol{f}$, it is clamped on Γ_D and surface tractions with density $\boldsymbol{g}$ act on Γ_N. Finally, let $[0, T]$, $T > 0$, be the time interval of interest and $t \in [0, T]$ any instant in this time interval.

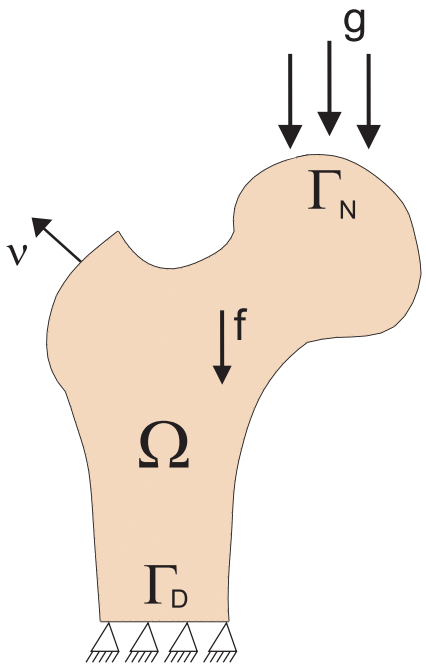

Figure 2.1: A bone remodeling problem.

Let $\boldsymbol{u} : (\boldsymbol{x}, t) \in \overline{\Omega} \times (0, T) \to \boldsymbol{u}(\boldsymbol{x}, t) = (u_i(\boldsymbol{x}, t)) \in \mathbb{R}^d$ be the displacement field, $\boldsymbol{\sigma} : (\boldsymbol{x}, t) \in \overline{\Omega} \times (0, T) \to \boldsymbol{\sigma}(\boldsymbol{x}, t) = (\sigma_{ij}(\boldsymbol{x}, t)) \in \mathbb{S}^d$ the stress field and $\boldsymbol{\varepsilon}(\boldsymbol{u}) : (\boldsymbol{x}, t) \in$

$\overline{\Omega} \times [0,T] \to \boldsymbol{\varepsilon}(\boldsymbol{u}(\boldsymbol{x},t)) = (\varepsilon_{ij}(\boldsymbol{u}(\boldsymbol{x},t)))_{i,j=1}^{d} \in \mathbb{S}^d$ the strain tensor given by

$$\varepsilon_{ij}(\boldsymbol{u}(\boldsymbol{x},t)) = \frac{1}{2}\left(\frac{\partial u_i}{\partial x_j}(\boldsymbol{x},t) + \frac{\partial u_j}{\partial x_i}(\boldsymbol{x},t)\right), \quad i,j = 1...d, \quad \boldsymbol{x} \in \overline{\Omega}.$$

To measure the change in volume fraction from a reference configuration we introduce a function $e : (\boldsymbol{x},t) \in \overline{\Omega} \times [0,T] \to e(\boldsymbol{x},t) \in \mathbb{R}$, which we will name as *bone remodeling* function.

As noticed in the previous section, according to [15, 46], the bone is assumed elastic and the constitutive law is written as follows,

$$\boldsymbol{\sigma} = (\xi_0 + e)\mathcal{C}(e)\boldsymbol{\varepsilon}(\boldsymbol{u}) \quad in \quad \overline{\Omega} \times [0,T],$$

where ξ_0 represents the reference volume fraction and $\mathcal{C}(e) = (C_{ijkl}(e))_{i,j,k,l=1}^{d}$ is a constitutive tensor depending on the bone properties.

The evolution of the bone remodeling function is obtained from the following first-order ordinary differential equation (see [15, 46]),

$$\dot{e} = a(e) + \mathcal{A}(e) \,:\, \boldsymbol{\varepsilon}(\boldsymbol{u}) \quad in \quad \overline{\Omega} \times [0,T],$$

where $a(e)$ is a constitutive function and $\mathcal{A}(e) = (A_{ij}(e))_{i,j=1}^{d}$ denote the bone remodeling rate coefficients. A dot above a function denotes the time derivative of this function.

For a given constant $L > 0$, let us define the truncation operator $\Phi_L : \mathbb{R} \to [-L, L]$ by

$$\Phi_L(r) = \begin{cases} -L & \text{if} \quad -L \leq r, \\ r & \text{if} \quad -L \leq r \leq L, \\ L & \text{if} \quad r \geq L. \end{cases}$$

Finally, the process is assumed quasistatic and therefore, the inertia effects are ne-

glected. Moreover, let e_0 denote the initial bone remodeling function.

The mechanical problem derived from the continuum mechanics law in the framework of small displacements theory, is the following.

Problem P1. *Find the displacement field* $\boldsymbol{u} : \overline{\Omega} \times [0,T] \to \mathbb{R}^d$*, the stress field* $\boldsymbol{\sigma} : \overline{\Omega}\times[0,T] \to \mathbb{S}^d$ *and the bone remodeling function* $e : \overline{\Omega}\times[0,T] \to \mathbb{R}$ *such that* $e(\cdot,0) = e_0$ *and*

$$\boldsymbol{\sigma} = (\xi_0 + e)\mathcal{C}(e)\boldsymbol{\varepsilon}(\boldsymbol{u}) \quad in \quad \Omega \times (0,T), \tag{2.1}$$

$$\dot{e} = a(e) + \mathcal{A}(e) \,:\, \boldsymbol{\varepsilon}(\boldsymbol{u}) \quad in \quad \Omega \times (0,T), \tag{2.2}$$

$$-\mathrm{Div}\,\boldsymbol{\sigma} = \gamma(\xi_0 + \Phi_L(e))\boldsymbol{f} \quad in \quad \Omega \times (0,T), \tag{2.3}$$

$$\boldsymbol{u} = \boldsymbol{0} \quad on \quad \Gamma_D \times (0,T), \tag{2.4}$$

$$\boldsymbol{\sigma\nu} = \boldsymbol{g} \quad on \quad \Gamma_N \times (0,T). \tag{2.5}$$

Here, $\gamma > 0$ is the density of the full elastic material which is assumed constant for the sake of simplicity.

We turn now to obtain a variational formulation of Problem P1. We use the classical spaces $L^2(\Omega)$ and $H^1(\Omega)$ equipped with the classical norms (see [1]):

$$L^2(\Omega) = \{v : \Omega \to \mathbb{R};\, v \,\text{measurable},\, \int_\Omega v^2 d\boldsymbol{x} < \infty\},$$

and

$$H^1(\Omega) = \{v \in L^2(\Omega);\, \frac{\partial v}{\partial x_i} \in L^2(\Omega),\, 1 \le i \le d\},$$

where $\dfrac{\partial v}{\partial x_i}\,(1 \le i \le d)$ denotes the distributional derivatives of v with respect to the variable x_i.

Let us denote by $Y = L^2(\Omega)$ and $H = [L^2(\Omega)]^d$, and define the following spaces

equipped with the product norms:

$$
\begin{aligned}
&V = \{\boldsymbol{w} = (w_i)_{i=1}^d \in [H^1(\Omega)]^d \ ; \ \boldsymbol{w} = \boldsymbol{0} \quad \text{on} \quad \Gamma_D\},\\
&Q = \{\boldsymbol{\tau} = (\tau_{ij})_{i,j=1}^d \in [L^2(\Omega)]^{d\times d} \ ; \ \tau_{ij} = \tau_{ji}, \quad 1 \le i,j \le d\},\\
&(\boldsymbol{u},\boldsymbol{v})_H = \sum_{i=1}^d \int_\Omega u_i v_i d\boldsymbol{x}, \qquad (\boldsymbol{\sigma},\boldsymbol{\tau})_Q = \sum_{i,j=1}^d \int_\Omega \sigma_{ij}\tau_{ij} d\boldsymbol{x},\\
&(\boldsymbol{u},\boldsymbol{v})_V = (\boldsymbol{u},\boldsymbol{v})_H + (\boldsymbol{\varepsilon}(\boldsymbol{u}),\boldsymbol{\varepsilon}(\boldsymbol{v}))_Q,
\end{aligned}
$$

and the associated norms $\|\boldsymbol{v}\|_V = (\boldsymbol{v},\boldsymbol{v})_V^{1/2}$ and $\|\boldsymbol{\tau}\|_Q = (\boldsymbol{\tau},\boldsymbol{\tau})_Q^{1/2}$.

We note that, since $meas(\Gamma_D) > 0$, it follows from Korn's inequality that there exists a positive constant C such that $|\boldsymbol{\varepsilon}(\boldsymbol{u})|_Q \ge C\|\boldsymbol{v}\|_V$. Thus, $\|\cdot\|_V$ and $\|\cdot\|_{[H^1(\Omega)]^d}$ are equivalent norms on V.

In order to obtain an existence and uniqueness result (see [57]) the following assumptions are done on the problem data.

The elasticity coefficients C_{ijkl} are assumed to satisfy the following properties:

$$
\begin{aligned}
&\text{(a) There exists } L_{\mathcal{C}} > 0 \text{ such that}\\
&\qquad |(\xi_0 + r_1)C_{ijkl}(r_1) - (\xi_0 + r_2)C_{ijkl}(r_2)| \le L_{\mathcal{C}}|r_1 - r_2|, \quad \forall r_1, r_2 \in \mathbb{R}.\\
&\text{(b) There exists } M_{\mathcal{C}} > 0 \text{ such that } |(\xi_0 + r)C_{ijkl}(r)| \le M_{\mathcal{C}}, \quad \forall r \in \mathbb{R}.\\
&\text{(c) } C_{ijkl}(r) = C_{jikl}(r) = C_{klij}(r) \text{ for } i,j,k,l = 1,\dots,d, \quad \forall r \in \mathbb{R}.\\
&\text{(d) There exists } m_{\mathcal{C}} > 0 \text{ such that}\\
&\qquad (\xi_0 + r)\mathcal{C}(r)\boldsymbol{\tau} : \boldsymbol{\tau} \ge m_{\mathcal{C}}|\boldsymbol{\tau}|^2, \quad \forall \boldsymbol{\tau} \in \mathbb{S}^d, \quad \forall r \in \mathbb{R}.
\end{aligned}
\tag{2.6}
$$

The constitutive function a and the bone remodeling rate coefficients A_{ij} are Lips-

chitz and bounded functions in $\mathbb{R}$; that is, there exist L_a, $L_{\mathcal{A}}$, M_a and $M_{\mathcal{A}}$ such that:

$$\begin{aligned} &\text{(a) } |a(r_1)-a(r_2)| \le L_a|r_1-r_2|, \quad |a(r)| \le M_a, \quad \forall r_1, r_2, r \in \mathbb{R}, \\ &\text{(b) } |\mathcal{A}(r_1)-\mathcal{A}(r_2)| \le L_{\mathcal{A}}|r_1-r_2|, \quad |\mathcal{A}(r)| \le M_{\mathcal{A}}, \quad \forall r_1, r_2, r \in \mathbb{R}. \end{aligned} \tag{2.7}$$

The reference volume fraction ξ_0 satisfies the following conditions for some value $0 < \xi_0^m < 1$,

$$\xi_0 \in C(\overline{\Omega}), \quad 0 < \xi_0^m \le \xi_0(\boldsymbol{x}) \le 1 \text{ for all } \boldsymbol{x} \in \overline{\Omega}. \tag{2.8}$$

The density forces have the regularity,

$$\boldsymbol{f} \in C([0,T]; [C(\overline{\Omega})]^d), \quad \boldsymbol{g} \in C([0,T]; [C(\overline{\Gamma_N})]^d), \tag{2.9}$$

and the initial value of the bone remodeling function e_0 verifies that

$$e_0 \in C(\overline{\Omega}). \tag{2.10}$$

For every $e \in L^\infty(\Omega)$, let us define the bilinear form $c(e;\cdot,\cdot) : V \times V \to \mathbb{R}$,

$$c(e;\boldsymbol{u},\boldsymbol{v}) = \int_\Omega (\xi_0 + e)\mathcal{C}(e)\boldsymbol{\varepsilon}(\boldsymbol{u}) \,:\, \boldsymbol{\varepsilon}(\boldsymbol{v})\, d\boldsymbol{x}, \quad \forall \boldsymbol{u}, \boldsymbol{v} \in V,$$

and the linear form $L(e;\cdot) : V \to \mathbb{R}$ given by

$$L(e;\boldsymbol{v}) = \int_\Omega \gamma(\xi_0 + \Phi_L(e))\boldsymbol{f} \cdot \boldsymbol{v}\, d\boldsymbol{x} + \int_{\Gamma_N} \boldsymbol{g} \cdot \boldsymbol{v}\, d\Gamma, \quad \forall \boldsymbol{v} \in V.$$

Throughout this work we systematically use the following identification

$$s(\boldsymbol{x}, t) \equiv s(t)(\boldsymbol{x})$$

for every function $s : \overline{\Omega} \times [0,T] \to \mathbb{R}$. With this notation, applying the Green's formula,

$$(\boldsymbol{\sigma}\boldsymbol{\nu}, \boldsymbol{v})_{[L^2(\Gamma)]^d} = (\boldsymbol{\sigma}, \boldsymbol{\varepsilon}(\boldsymbol{v}))_Q + (\operatorname{Div}\boldsymbol{\sigma}, \boldsymbol{v})_H \qquad \forall \boldsymbol{v} \in V,$$

we derive the following variational formulation for the mechanical problem P1.

Problem VP1. *Find a displacement field* $\boldsymbol{u} : [0,T] \to V$ *and the bone remodeling function* $e : [0,T] \to L^\infty(\Omega)$ *such that* $e(0) = e_0$ *and,*

$$c(e(t); \boldsymbol{u}(t), \boldsymbol{v}) = L(e(t); \boldsymbol{v}) \quad \forall \boldsymbol{v} \in V, \quad a.e.\ t \in (0,T), \tag{2.11}$$

$$\dot{e}(t) = a(e(t)) + \mathcal{A}(e(t)) : \boldsymbol{\varepsilon}(\boldsymbol{u}(t)) \quad in \quad \mathcal{D}'(0,T; L^2(\Omega)), \tag{2.12}$$

$$e(0) = e_0, \tag{2.13}$$

where $\mathcal{D}'(0,T; L^2(\Omega))$ is the space of distributions valued on $L^2(\Omega)$ (see [1]).

The following result, which states the existence of a unique weak solution to Problem VP1, can be obtained proceeding as in [57].

Theorem 2.1 *Let the assumptions (2.6)-(2.10) hold. Assume that, for any given function* $e \in C^1([0,T]; C(\overline{\Omega}))$*, the unique solution to the following problem:*

$$\boldsymbol{u}(t) \in V, \quad c(e(t); \boldsymbol{u}(t), \boldsymbol{v}) = L(e(t); \boldsymbol{v}) \quad \forall \boldsymbol{v} \in V,$$

has the regularity $\boldsymbol{u} \in C([0,T]; [H^3(\Omega)]^d)$ *for* $d = 2, 3$ *or* $u \in C([0,T]; H^2(\Omega))$ *for* $d = 1$*. Then, there exists a unique solution to Problem* VP1 *with the following regularity:*

$$\boldsymbol{u} \in C([0,T]; [C^1(\overline{\Omega})]^d), \quad e \in C^1([0,T]; C(\overline{\Omega})).$$

In [57], the existence and uniqueness of a weak solution was proved for a regularized problem in which the elasticity coefficients were defined using truncation and mollification operators. The main idea of the proof is based on the application of the Cauchy-Lipschitz-Picard theorem and Schauder lemma. In order to do this, a priori estimates were obtained for problems (2.11) and (2.12), using the regularized coefficients and stronger hypothesis over the data. All these conditions were used to prove an additional regularity result for the solution of the problem:

Given $e \in L^\infty(\Omega)$, find $\boldsymbol{u} \in V$ such that

$$c(e; \boldsymbol{u}, \boldsymbol{v}) = L(e; \boldsymbol{v}) \qquad \forall \boldsymbol{v} \in V. \tag{2.14}$$

In particular, it is needed to prove that

$$\boldsymbol{u} \in [H^3(\Omega)]^d. \tag{2.15}$$

The existence and uniqueness of solution to Problem VP1 is an open problem. In particular, it is necessary to study the conditions over the data to obtain a unique solution for the variational problem (2.14) with regularity (2.15).

2.2.2 Numerical analysis of a fully discrete scheme

We now introduce a finite differences scheme and a finite element algorithm for approximating solutions to Problem VP1 and we proof an error estimates result.

First, we consider two finite dimensional spaces $V^h \subset V$ and $B^h \subset L^\infty(\Omega) \subset Y$, approximating the spaces V and $L^\infty(\Omega)$, respectively. Here, $h > 0$ denotes the spatial discretization parameter.

Secondly, the time derivatives are discretized by using a uniform partition of the time interval $[0, T]$, denoted by $0 = t_0 < t_1 < \ldots < t_N = T$, where $t_j = jk$, k being the time step size defined as $k = T/N$ and $N \geq 1$. Moreover, for a continuous function $S(t)$ we let $S_n = S(t_n)$.

In this section, C denotes a positive constant which depends on the problem data and the continuous solution, but it is independent of the discretization parameters h and k.

Remark 2.1 *In the numerical simulations presented in the next section, V^h and B^h consist of continuous and piecewise affine functions and piecewise constant functions,*

respectively; that is,

$$V^h = \{\boldsymbol{w}^h \in [C(\overline{\Omega})]^d \,;\, \boldsymbol{w}^h_{|_{Tr}} \in [P_1(Tr)]^d,\ Tr \in \mathcal{T}^h, \quad \boldsymbol{w}^h = \boldsymbol{0} \ \text{ on } \ \Gamma_D\}, \quad (2.16)$$

$$B^h = \{\xi^h \in L^\infty(\Omega) \,;\, \xi^h_{|_{Tr}} \in P_0(Tr), \quad Tr \in \mathcal{T}^h\}, \quad (2.17)$$

where Ω is assumed to be a polygonal domain, $\mathcal{T}^h$ denotes a finite element triangulation of $\overline{\Omega}$ composed by d-symplex denoted by Tr, and $P_q(Tr)$, $q = 0, 1$, represents the space of polynomials of total degree less or equal to q in Tr.

Using the forward Euler scheme, we propose the following fully discrete approximation of Problem VP1:

Problem VP1^{hk}. *Find a discrete displacement field $\boldsymbol{u}^{hk} = \{\boldsymbol{u}^{hk}_n\}_{n=0}^N \in (V^h)^{N+1}$ and a discrete bone remodeling function $e^{hk} = \{e^{hk}_n\}_{n=0}^N \in (B^h)^{N+1}$ such that*

$$c(e^{hk}_n; \boldsymbol{u}^{hk}_n, \boldsymbol{v}^h) = L(e^{hk}_n; \boldsymbol{v}^h), \quad \forall \boldsymbol{v}^h \in V^h \quad (n = 0, 1, 2, \ldots, N), \quad (2.18)$$

$$\frac{e^{hk}_n - e^{hk}_{n-1}}{k} = a(e^{hk}_{n-1}) + \mathcal{A}(e^{hk}_{n-1}) \,:\, \boldsymbol{\varepsilon}(\boldsymbol{u}^{hk}_{n-1}) \quad (n = 1, 2, \ldots, N), \quad (2.19)$$

where $e^{hk}_0 \in B^h$ is an appropriate approximation of the initial condition e_0.

In the following theorem we state the existence and uniqueness of the discrete solution.

Theorem 2.2 *Let the assumptions (2.6)-(2.10) hold. Therefore, Problem* VP1^{hk} *has a unique solution $(\boldsymbol{u}^{hk}, e^{hk}) \in (V^h \times B^h)^{N+1}$.*

Its proof is directly obtained applying the well-known Lax-Milgram lemma (see [44]), keeping in mind assumptions (2.6).

Below we focus our attention on deriving error estimates for the numerical errors $\|\boldsymbol{u}_n - \boldsymbol{u}^{hk}_n\|_V$ and $\|e_n - e^{hk}_n\|_Y$. The following theorem is the main result of this section.

Theorem 2.3 *Let the assumptions of Theorem 2.1 hold and denote by* $(\boldsymbol{u}, e)$ *and* $(\boldsymbol{u}^{hk}, e^{hk})$ *the respective solutions to problems* VP1 *and* VP1^{hk}. *Then, we have, for all* $\{\boldsymbol{v}_n^h\}_{n=0}^N \in (V^h)^{N+1}$*:*

$$\begin{aligned}\max_{0\le n\le N}\big\{\|e_n - e_n^{hk}\|_Y^2 + \|\boldsymbol{u}_n - \boldsymbol{u}_n^{hk}\|_V^2\big\}\\ \le C\Big(\|e_0 - e_0^{hk}\|_Y^2 + k\sum_{j=1}^{N}\Big[\|\dot e_j - \delta e_j\|_Y^2 + \|\boldsymbol{u}_j - \boldsymbol{u}_{j-1}\|_V^2\Big]\\ + k^2 + \max_{0\le n\le N}\|\boldsymbol{u}_n - \boldsymbol{v}_n^h\|_V^2 + \|\boldsymbol{u}_0 - \boldsymbol{u}_0^{hk}\|_V^2\Big),\end{aligned} \tag{2.20}$$

where we use the notation $\delta e_j = (e_j - e_{j-1})/k$ *for* $j = 1, \ldots, N$.

Proof First, let us obtain an error estimates on the bone remodeling function e. By subtraction of equation (2.12) at time $t = t_n$ and equation (2.19) we find that

$$\dot e_n - \frac{e_n^{hk} - e_{n-1}^{hk}}{k} = a(e_n) - a(e_{n-1}^{hk}) + \mathcal{A}(e_n) : \boldsymbol{\varepsilon}(\boldsymbol{u}_n) - \mathcal{A}(e_{n-1}^{hk}) : \boldsymbol{\varepsilon}(\boldsymbol{u}_{n-1}^{hk}).$$

Integrating in Ω and using the norm in Y, we have,

$$\begin{aligned}\|e_n - e_n^{hk}\|_Y \le \ & \|e_{n-1} - e_{n-1}^{hk}\|_Y + k\Big(\|a(e_n) - a(e_{n-1}^{hk})\|_Y + \|\dot e_n - \delta e_n\|_Y\\ & + \|\mathcal{A}(e_n) : \boldsymbol{\varepsilon}(\boldsymbol{u}_n) - \mathcal{A}(e_{n-1}^{hk}) : \boldsymbol{\varepsilon}(\boldsymbol{u}_{n-1}^{hk})\|_Y\Big).\end{aligned}$$

Now, using (2.7) we get

$$\begin{aligned}&\|\mathcal{A}(e_n) : \boldsymbol{\varepsilon}(\boldsymbol{u}_n) - \mathcal{A}(e_{n-1}^{hk}) : \boldsymbol{\varepsilon}(\boldsymbol{u}_{n-1}^{hk})\|_Y\\ &\quad = \|\mathcal{A}(e_n) : \boldsymbol{\varepsilon}(\boldsymbol{u}_n) - \mathcal{A}(e_{n-1}^{hk}) : \boldsymbol{\varepsilon}(\boldsymbol{u}_n) + \mathcal{A}(e_{n-1}^{hk}) : \boldsymbol{\varepsilon}(\boldsymbol{u}_n) - \mathcal{A}(e_{n-1}^{hk}) : \boldsymbol{\varepsilon}(\boldsymbol{u}_{n-1}^{hk})\|_Y\\ &\quad \le C(\|\boldsymbol{u}_n\|_{[C^1(\overline\Omega)]^d}\|e_n - e_{n-1}^{hk}\|_Y + M_{\mathcal{A}}\|\boldsymbol{u}_n - \boldsymbol{u}_{n-1}^{hk}\|_V),\end{aligned}$$

and

$$\|a(e_n) - a(e_{n-1}^{hk})\|_Y \le C(\|e_n - e_{n-1}\|_Y + \|e_{n-1} - e_{n-1}^{hk}\|_Y).$$

Taking into account the regularity $e \in C^1([0,T]; C(\overline\Omega)) \subset C^1([0,T]; Y)$ and applying the mean value theorem we have $\|e_n - e_{n-1}\|_Y \le k\|\dot e\|_{C([0,T];Y)}$.

Now, by an induction argument we conclude the following estimates on the bone remodeling function e,

$$\begin{aligned}\|e_n - e_n^{hk}\|_Y \leq \quad & \|e_0 - e_0^{hk}\|_Y + Ck + Ck\sum_{j=1}^{n}\Big[\|e_{j-1} - e_{j-1}^{hk}\|_Y \\ & + \|\dot{e}_j - \delta e_j\|_Y + \|\boldsymbol{u}_{j-1} - \boldsymbol{u}_{j-1}^{hk}\|_V + \|\boldsymbol{u}_j - \boldsymbol{u}_{j-1}\|_V\Big].\end{aligned} \tag{2.21}$$

Next, let us estimate the numerical errors on the displacement field. Thus, we write equation (2.11) for all $\boldsymbol{v} = \boldsymbol{v}^h \in V^h \subset V$ and we subtract it to equation (2.18) to obtain,

$$c(e_n; \boldsymbol{u}_n, \boldsymbol{v}^h) - L(e_n; \boldsymbol{v}^h) - c(e_n^{hk}; \boldsymbol{u}_n^{hk}, \boldsymbol{v}^h) + L(e_n^{hk}; \boldsymbol{v}^h) = 0.$$

Therefore, we have, for all $\boldsymbol{v}^h \in V^h$,

$$\begin{aligned}& c(e_n; \boldsymbol{u}_n, \boldsymbol{u}_n - \boldsymbol{u}_n^{hk}) - L(e_n; \boldsymbol{u}_n - \boldsymbol{u}_n^{hk}) - c(e_n^{hk}; \boldsymbol{u}_n^{hk}, \boldsymbol{u}_n - \boldsymbol{u}_n^{hk}) + L(e_n^{hk}; \boldsymbol{u}_n - \boldsymbol{u}_n^{hk}) \\ & = c(e_n; \boldsymbol{u}_n, \boldsymbol{u}_n - \boldsymbol{v}^h) - L(e_n; \boldsymbol{u}_n - \boldsymbol{v}^h) - c(e_n^{hk}; \boldsymbol{u}_n^{hk}, \boldsymbol{u}_n - \boldsymbol{v}^h) + L(e_n^{hk}; \boldsymbol{u}_n - \boldsymbol{v}^h).\end{aligned}$$

Keeping in mind that

$$\begin{aligned}& c(e_n; \boldsymbol{u}_n, \boldsymbol{u}_n - \boldsymbol{v}^h) - c(e_n^{hk}; \boldsymbol{u}_n^{hk}, \boldsymbol{u}_n - \boldsymbol{v}^h) = c(e_n^{hk}; \boldsymbol{u}_n - \boldsymbol{u}_n^{hk}, \boldsymbol{u}_n - \boldsymbol{v}^h) \\ & \quad + c(e_n; \boldsymbol{u}_n, \boldsymbol{u}_n - \boldsymbol{v}^h) - c(e_n^{hk}; \boldsymbol{u}_n, \boldsymbol{u}_n - \boldsymbol{v}^h) \quad \forall \boldsymbol{v}^h \in V^h, \\ & c(e_n; \boldsymbol{u}_n, \boldsymbol{u}_n - \boldsymbol{u}_n^{hk}) - c(e_n^{hk}; \boldsymbol{u}_n^{hk}, \boldsymbol{u}_n - \boldsymbol{u}_n^{hk}) = c(e_n^{hk}; \boldsymbol{u}_n - \boldsymbol{u}_n^{hk}, \boldsymbol{u}_n - \boldsymbol{u}_n^{hk}) \\ & \quad + c(e_n; \boldsymbol{u}_n, \boldsymbol{u}_n - \boldsymbol{u}_n^{hk}) - c(e_n^{hk}; \boldsymbol{u}_n, \boldsymbol{u}_n - \boldsymbol{u}_n^{hk}),\end{aligned}$$

we can write the previous equation as

$$\begin{aligned}& c(e_n^{hk}; \boldsymbol{u}_n - \boldsymbol{u}_n^{hk}, \boldsymbol{u}_n - \boldsymbol{u}_n^{hk}) + c(e_n; \boldsymbol{u}_n, \boldsymbol{u}_n - \boldsymbol{u}_n^{hk}) - c(e_n^{hk}; \boldsymbol{u}_n, \boldsymbol{u}_n - \boldsymbol{u}_n^{hk}) \\ & \qquad - L(e_n; \boldsymbol{u}_n - \boldsymbol{u}_n^{hk}) + L(e_n^{hk}; \boldsymbol{u}_n - \boldsymbol{u}_n^{hk}) \\ & \quad = c(e_n^{hk}; \boldsymbol{u}_n - \boldsymbol{u}_n^{hk}, \boldsymbol{u}_n - \boldsymbol{v}^h) + c(e_n; \boldsymbol{u}_n, \boldsymbol{u}_n - \boldsymbol{v}^h) \\ & \qquad - c(e_n^{hk}; \boldsymbol{u}_n, \boldsymbol{u}_n - \boldsymbol{v}^h) - L(e_n; \boldsymbol{u}_n - \boldsymbol{v}^h) + L(e_n^{hk}; \boldsymbol{u}_n - \boldsymbol{v}^h).\end{aligned}$$

Using (2.6)(d), we have

$$c(e_n^{hk}; \boldsymbol{u}_n - \boldsymbol{u}_n^{hk}, \boldsymbol{u}_n - \boldsymbol{u}_n^{hk}) \geq m_{\mathcal{C}} \|\boldsymbol{u}_n - \boldsymbol{u}_n^{hk}\|_V^2.$$

Then, we obtain the next inequality,

$$\begin{aligned}
&m_{\mathcal{C}} \|\boldsymbol{u}_n - \boldsymbol{u}_n^{hk}\|_V^2 \\
&\quad \leq L(e_n; \boldsymbol{u}_n - \boldsymbol{u}_n^{hk}) - L(e_n^{hk}; \boldsymbol{u}_n - \boldsymbol{u}_n^{hk}) + c(e_n^{hk}; \boldsymbol{u}_n, \boldsymbol{u}_n - \boldsymbol{u}_n^{hk}) \\
&\qquad -c(e_n; \boldsymbol{u}_n, \boldsymbol{u}_n - \boldsymbol{u}_n^{hk}) + c(e_n^{hk}; \boldsymbol{u}_n - \boldsymbol{u}_n^{hk}, \boldsymbol{u}_n - \boldsymbol{v}^h) + c(e_n; \boldsymbol{u}_n, \boldsymbol{u}_n - \boldsymbol{v}^h) \\
&\qquad\quad -c(e_n^{hk}; \boldsymbol{u}_n, \boldsymbol{u}_n - \boldsymbol{v}^h) - L(e_n; \boldsymbol{u}_n - \boldsymbol{v}^h) + L(e_n^{hk}; \boldsymbol{u}_n - \boldsymbol{v}^h).
\end{aligned}$$

From properties (2.6) and (2.9) it follows that

$$\begin{aligned}
&L(e_n; \boldsymbol{u}_n - \boldsymbol{v}^h) - L(e_n^{hk}; \boldsymbol{u}_n - \boldsymbol{v}^h) \\
&\qquad = \int_\Omega \gamma(\Phi_L(e_n) - \Phi_L(e_n^{hk})) \boldsymbol{f}_n \cdot (\boldsymbol{u}_n - \boldsymbol{v}^h) d\boldsymbol{x} \\
&\qquad \leq C \|\boldsymbol{f}_n\|_{[C(\overline{\Omega})]^d} \|e_n - e_n^{hk}\|_Y \|\boldsymbol{u}_n - \boldsymbol{v}^h\|_V \quad \forall \boldsymbol{v}^h \in V^h, \\
&c(e_n^{hk}; \boldsymbol{u}_n, \boldsymbol{u}_n - \boldsymbol{u}_n^{hk}) - c(e_n; \boldsymbol{u}_n, \boldsymbol{u}_n - \boldsymbol{u}_n^{hk}) \\
&\qquad \leq C \|\boldsymbol{u}_n\|_{[C^1(\overline{\Omega})]^d} \|e_n - e_n^{hk}\|_Y \|\boldsymbol{u}_n - \boldsymbol{u}_n^{hk}\|_V, \\
&c(e_n^{hk}; \boldsymbol{u}_n - \boldsymbol{u}_n^{hk}, \boldsymbol{u}_n - \boldsymbol{v}^h) \leq C \|\boldsymbol{u}_n - \boldsymbol{u}_n^{hk}\|_V \|\boldsymbol{u}_n - \boldsymbol{v}^h\|_V, \\
&c(e_n; \boldsymbol{u}_n, \boldsymbol{u}_n - \boldsymbol{v}^h) - c(e_n^{hk}; \boldsymbol{u}_n, \boldsymbol{u}_n - \boldsymbol{v}^h) \\
&\qquad \leq C \|\boldsymbol{u}_n\|_{[C^1(\overline{\Omega})]^d} \|e_n - e_n^{hk}\|_Y \|\boldsymbol{u}_n - \boldsymbol{v}^h\|_V,
\end{aligned}$$

and therefore we can deduce that,

$$\begin{aligned}
&\|\boldsymbol{u}_n - \boldsymbol{u}_n^{hk}\|_V^2 \\
&\quad \leq C \|\boldsymbol{f}_n\|_{[C(\overline{\Omega})]^d} \|e_n - e_n^{hk}\|_Y \|\boldsymbol{u}_n - \boldsymbol{u}_n^{hk}\|_V \\
&\qquad + C \|\boldsymbol{u}_n\|_{[C^1(\overline{\Omega})]^d} \|e_n - e_n^{hk}\|_Y \|\boldsymbol{u}_n - \boldsymbol{u}_n^{hk}\|_V + C \|\boldsymbol{u}_n - \boldsymbol{u}_n^{hk}\|_V \|\boldsymbol{u}_n - \boldsymbol{v}^h\|_V \\
&\qquad + C \|\boldsymbol{u}_n\|_{[C^1(\overline{\Omega})]^d} \|e_n - e_n^{hk}\|_Y \|\boldsymbol{u}_n - \boldsymbol{v}^h\|_V \\
&\qquad + C \|\boldsymbol{f}_n\|_{[C(\overline{\Omega})]^d} \|e_n - e_n^{hk}\|_Y \|\boldsymbol{u}_n - \boldsymbol{v}^h\|_V \quad \forall \boldsymbol{v}^h \in V^h.
\end{aligned}$$

Using several times the inequality,

$$ab \leq \epsilon a^2 + (1/4\epsilon)b^2, \quad a, b, \epsilon \in \mathbb{R},\ \epsilon > 0, \tag{2.22}$$

taking ϵ small enough we find, for all $\boldsymbol{v}^h \in V^h$,

$$\|\boldsymbol{u}_n - \boldsymbol{u}_n^{hk}\|_V^2 \leq C\left(\|e_n - e_n^{hk}\|_Y^2 + \|\boldsymbol{u}_n - \boldsymbol{v}^h\|_V^2\right) \quad n = 0, 1, \ldots, N. \tag{2.23}$$

Combining (2.21) and (2.23), we have

$$\begin{aligned}
&\|e_n - e_n^{hk}\|_Y^2 + \|\boldsymbol{u}_n - \boldsymbol{u}_n^{hk}\|_V^2 \\
&\quad \leq C\|e_0 - e_0^{hk}\|_Y^2 + Ck^2 + Ck\sum_{j=1}^{n}\Big[\|e_{j-1} - e_{j-1}^{hk}\|_Y^2 \\
&\qquad + \|\dot{e}_j - \delta e_j\|_Y^2 + \|\boldsymbol{u}_{j-1} - \boldsymbol{u}_{j-1}^{hk}\|_V^2 + \|\boldsymbol{u}_j - \boldsymbol{u}_{j-1}\|_V^2\Big] + C\|\boldsymbol{u}_n - \boldsymbol{v}_n^h\|_V^2,
\end{aligned}$$

for all $\boldsymbol{v}_n^h \in V^h$.

Let us define the following quantities for $n = 1, \ldots, N$:

$$E_n = ||\boldsymbol{u}_n - \boldsymbol{u}_n^{hk}||_V^2 + ||e_n - e_n^{hk}||_Y^2,$$

$$g_n = ||e_0 - e_0^{hk}||_Y^2 + k^2 + k\sum_{j=1}^{n}[||\dot{e}_j - \delta e_j||_Y^2 + ||\boldsymbol{u}_j - \boldsymbol{u}_{j-1}||_V^2] + ||\boldsymbol{u}_n - \boldsymbol{v}_n^h||_V^2,$$

and let us denote $E_0 = g_0 = ||\boldsymbol{u}_0 - \boldsymbol{u}_0^{hk}||_V^2 + ||e_0 - e_0^{hk}||_Y^2$.
From the previous inequality we obtain

$$\begin{aligned}
&E_0 \leq g_0, \\
&E_n \leq Cg_n + Ck\sum_{j=1}^{n} E_{j-1}.
\end{aligned} \tag{2.24}$$

Han and Sofonea proved in [45] the following lemma which constitutes a discrete version of Gronwall's lemma.

Lemma 2.1 *Assume that* $\{g_n\}_{n=0}^N$ *and* $\{e_n\}_{n=0}^N$ *are two sequences of nonnegative real numbers satisfying*

$$\begin{aligned} &e_0 \leq C g_0, \\ &e_n \leq C g_n + C \sum_{j=1}^{n} k_j e_{j-1}, \quad n = 1, 2, \ldots, N. \end{aligned}$$

where $\{k_j\}_{j=1}^N$ *is a sequence of positive numbers. Then,*

$$\max_{0 \leq n \leq N} e_n \leq d \max_{0 \leq n \leq N} g_n,$$

where $d = C(1 + CTe^{CT})$ *with* $T = \sum_{j=1}^{N} k_j$.

Finally, applying this result to the estimates (2.24) it leads to (2.20). □

Error estimates (2.20) are the basis for the analysis of the convergence rate of the algorithm, presented below by using the finite element method.

Let Ω be a polyhedral domain and denote by $\mathcal{T}^h$ a finite element triangulation of $\overline{\Omega}$ compatible with the partition of the boundary $\Gamma = \partial\Omega$ into Γ_D and Γ_N. Let V^h and B^h be defined by (2.16) and (2.17), respectively, and assume that the discrete initial condition e_0^{hk} is given by $e_0^{hk} = \pi^h e_0$, where $\pi^h : C(\overline{\Omega}) \to B^h$ is the standard finite element interpolation operator (see, e.g., [13]).

Assume the following additional regularity conditions on the continuous solution:

$$\begin{aligned} &\boldsymbol{u} \in C^1([0,T]; V) \cap C([0,T]; [H^2(\Omega)]^d), \\ &e \in C([0,T]; H^1(\Omega)) \cap H^2(0,T; Y). \end{aligned} \tag{2.25}$$

The next result follows from estimates (2.20).

Corollary 2.1 *Let the assumptions of Theorem* 2.3 *hold. Under the additional regularity conditions (2.25), the fully discrete scheme is linearly convergent; that is, there*

exists a positive constant C, independent of h and k, such that

$$\max_{0\leq n\leq N}\left\{\|\boldsymbol{u}_n-\boldsymbol{u}_n^{hk}\|_V+\|e_n-e_n^{hk}\|_Y\right\}\leq C(h+k). \tag{2.26}$$

Proof First, proceeding as in the proof of Theorem 2.3, we obtain the following:

$$\|\boldsymbol{u}_0-\boldsymbol{u}_0^{hk}\|_V^2\leq C(\|e_0-e_0^{hk}\|_Y^2+\|\boldsymbol{u}_0-\boldsymbol{v}^h\|_V^2)\quad\forall\boldsymbol{v}^h\in V^h. \tag{2.27}$$

From the definition of the interpolation operator π^h we have (see [13]),

$$\|e_0-e_0^{hk}\|_Y\leq Ch\|e\|_{C([0,T];H^1(\Omega))}. \tag{2.28}$$

Using the well-known approximation property of the finite element space V^h, it follows that (see again [13]),

$$\inf_{v_n^h\in V^h}\|\boldsymbol{u}_n-\boldsymbol{v}_n^h\|_V^2\leq Ch^2\|\boldsymbol{u}\|^2_{C([0,T];[H^2(\Omega)]^d)},\quad n=0,1,\ldots,N. \tag{2.29}$$

Taking into account that $\boldsymbol{u}_0=\boldsymbol{u}(0)\in[H^2(\Omega)]^d$, we find that

$$\inf_{v_0^h\in V^h}\|\boldsymbol{u}_0-\boldsymbol{v}_0^h\|_V^2\leq Ch^2\|\boldsymbol{u}\|^2_{C([0,T];[H^2(\Omega)]^d)}.$$

Then, from (2.27) and (2.28) we have:

$$\|\boldsymbol{u}_0-\boldsymbol{u}_0^{hk}\|_V^2\leq Ch^2. \tag{2.30}$$

Using the mean value theorem, it is easy to check that

$$k\sum_{j=1}^{N}\left[\|\dot{e}_j-\delta e_j\|_Y^2+\|\boldsymbol{u}_j-\boldsymbol{u}_{j-1}\|_V^2\right]\leq Ck^2\left(\|e\|^2_{H^2(0,T;Y)}+\|\boldsymbol{u}\|^2_{C^1([0,T];V)}\right). \tag{2.31}$$

The estimate (2.26) is now concluded from (2.20) using (2.28), (2.29), (2.30) and (2.31). □

2.2.3 Numerical results

In this section we first describe shortly the numerical scheme implemented, and then we present some numerical examples to exhibit its performance in one-, two- and three-dimensional examples.

Numerical scheme

To approximate the spaces V and $L^\infty(\Omega)$ we use the finite element spaces V^h and B^h defined by (2.16) and (2.17), respectively.

First, the discrete displacement field $\boldsymbol{u}_n^{hk}$ is obtained solving problem (2.18):

$$\boldsymbol{u}_n^{hk} \in V^h, \quad c(e_n^{hk}; \boldsymbol{u}_n^{hk}, \boldsymbol{v}^h) = L(e_n^{hk}; \boldsymbol{v}^h) \quad \forall \boldsymbol{v}^h \in V^h.$$

This is a linear problem equivalent to a linear system which is solved by using Cholesky's method.

Next, let $n \in \{1, \ldots, N\}$ and suppose that $\boldsymbol{u}_{n-1}^{hk}$ and e_{n-1}^{hk} are known. The discrete bone remodeling function e_n^{hk} is calculated from equation (2.19) as:

$$e_n^{hk} = e_{n-1}^{hk} + ka(e_{n-1}^{hk}) + k\mathcal{A}(e_{n-1}^{hk}) \, : \, \boldsymbol{\varepsilon}(\boldsymbol{u}_{n-1}^{hk}).$$

The numerical scheme was implemented on a 3.2Ghz PC using MATLAB, and a typical 1D run ($h = k = 0.001$) took about 3.5 seconds of CPU time. A run for the 2D example spent about 6 seconds for each time iteration and for the 3D example took about 2 minutes for each time iteration. In order to detect a stationary state (the final time) we have introduced in the programs for two and three dimensions a test which is activated when the maximum value between two consecutive bone remodeling functions is smaller than 10^{-7} or 10^{-5}, respectively.

A one-dimensional example: the numerical convergence

As a one-dimensional example, the following problem is considered.

Problem P1-1D. *Find a displacement field* $u : [0,1] \times [0,1] \to \mathbb{R}$ *and a bone remodeling function* $e : [0,1] \times [0,1] \to \mathbb{R}$ *such that*

$$
\begin{aligned}
&-\frac{\partial}{\partial x}\left(e\frac{\partial u}{\partial x}\right)(x,t) = 1740\,(\frac{1}{2}+e(x,t)) \\
&\qquad\qquad \times\frac{-4xt\,e^{2t}-2e^{2t}(2xt+1)}{870+1740e^{t}(2xt+1)} \quad x\in(0,1),\ t\in(0,1),\\
&\dot{e}(x,t) = e(x,t)+\frac{\partial u}{\partial x}(x,t) \quad x\in[0,1],\ t\in[0,1],\\
&u(0,t) = 0 \quad t\in(0,1),\\
&e(1,t)\frac{\partial u}{\partial x}(1,t) = 2\,e^{2t}(2t+1) \quad t\in(0,1),\\
&e(x,0) = 1 \quad x\in[0,1].
\end{aligned}
$$

Problem **P1-1D** corresponds to Problem P1 with the following data, keeping in mind that the area of the cross-section is $A = 1m^2$:

$$
\begin{aligned}
&\Omega = (0,1), \quad T = 1\,day, \quad \xi_0 = \frac{1}{2}, \quad \gamma = 1740\,Kg/m^3,\\
&a(e) = e\,(\text{days})^{-1}, \quad \mathcal{A}(e) = 1\,(\text{days})^{-1}, \quad \mathcal{C}(e) = \frac{e}{\xi_0+e}N/m^2,\\
&f(x,t) = 1740\,(\frac{1}{2}+e(x,t))\frac{-4xt\,e^{2t}-2e^{2t}(2xt+1)}{870+1740e^{t}(2xt+1)}\,N/m \quad x\in[0,1],\ t\in[0,1],\\
&g(x,t) = 2\,e^{2t}(2t+1)\,N \quad \text{for} \quad x\in[0,1],\ t\in[0,1].
\end{aligned}
$$

The exact solution to Problem **P1-1D** is:

$$
u(x,t) = x^2e^t, \quad e(x,t) = e^t(2xt+1) \quad \text{for} \quad x\in[0,1],\ t\in[0,1].
$$

We observe that functions $\mathcal{C}(e)$ and $a(e)$ do not satisfy the boundedness assumptions presented in (2.6) and (2.7). However, it is easily solved by using the truncation function Φ_L. Anyway, we use value $L = 10^6$, so it is large enough and we can assume that this truncation does not modify the results.

Since the exact solution is known, we can plot the pointwise errors for the displacement and bone remodeling fields. Using the discretization parameters $h = k = 0.001$, these errors are ploted in Figure 2.2 at several times. As it can be seen, the highest pointwise errors are concentrated near the right end. In Figure 2.3, the evolution in time of the errors of the displacement and bone remodeling fields at point $x = 1$ is shown. As it was expected, the errors increase with respect to the time.

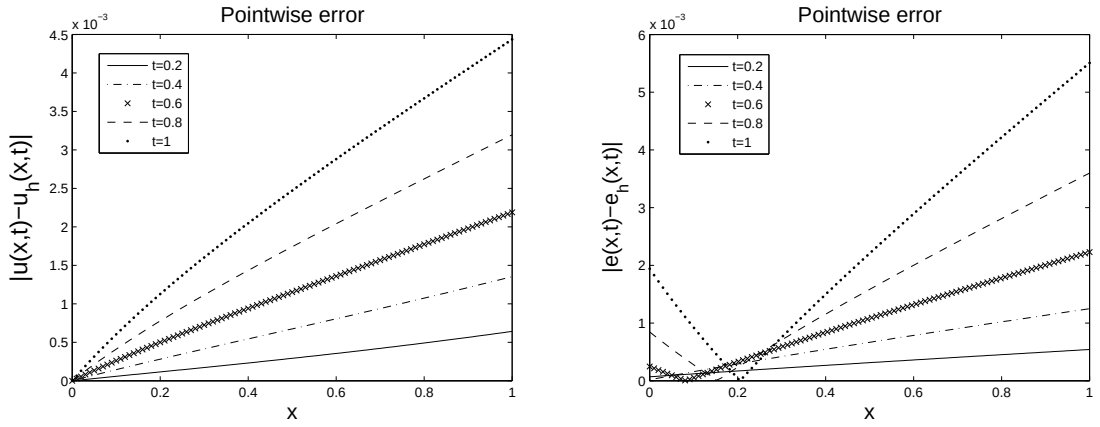

Figure 2.2: Example **P1-1D**: Pointwise errors of the displacements and bone remodeling fields at several times ($h = k = 0.001$).

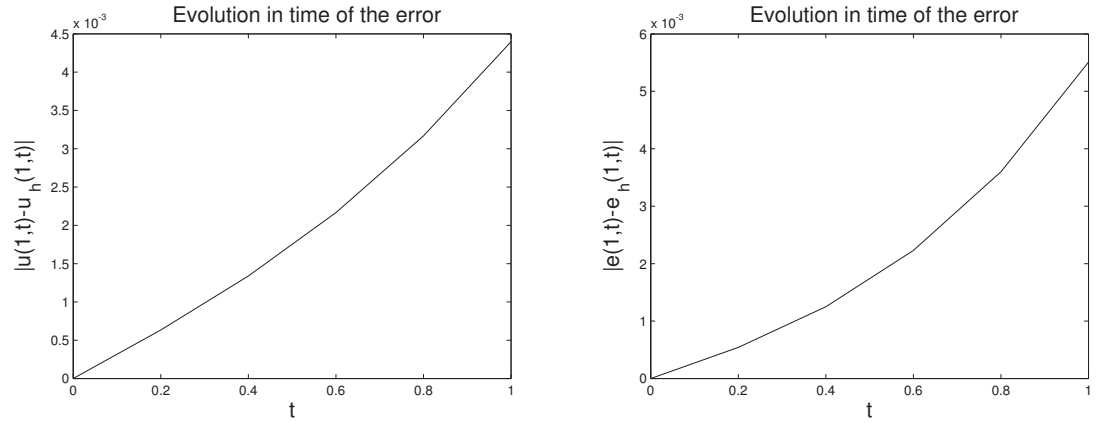

Figure 2.3: Example **P1-1D**: Evolution in time of the error of the displacement and bone remodeling fields at point $x = 1$.

$h \downarrow k \rightarrow$	0.1	0.05	0.01	0.005	0.001	0.0005	0.0001
0.1	1.200893	0.662375	0.339569	0.322338	0.315245	0.314803	0.314522
0.05	1.157869	0.592076	0.195785	0.168233	0.157710	0.157261	0.157046
0.01	1.143769	0.567737	0.117164	0.064651	0.033413	0.031921	0.031415
0.001	1.143326	0.566960	0.113821	0.058506	0.019353	0.016692	0.015738
0.001	1.143184	0.566711	0.112730	0.056395	0.011689	0.006449	0.003336
0.0005	1.143180	0.566703	0.112695	0.056330	0.011365	0.005844	0.001933
0.0001	1.143178	0.566700	0.112684	0.056306	0.011260	0.005636	0.001169

Table 2.1: Example **P1-1D**: Exact errors for some k and h.

The numerical errors, given by

$$E^{hk} = \max_{0 \leq n \leq N} \left\{ \|\boldsymbol{u}_n - \boldsymbol{u}_n^{hk}\|_V + \|e_n - e_n^{hk}\|_Y \right\}$$

and obtained for different discretization parameters h and k, are depicted in Table 2.1. Moreover, the evolution of the error depending on the parameter $h + k$ is plotted in Figure 2.4. We notice that the numerical convergence is clearly observed and the linear convergence, stated in Corollary 2.1, is achieved.

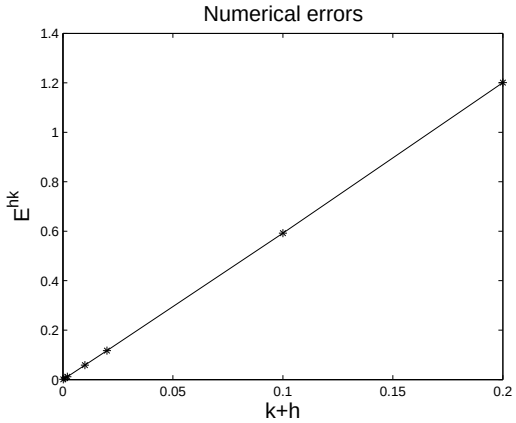

Figure 2.4: Example **P1-1D**: Asymptotic constant error.

Numerical results for two-dimensional problems

First two-dimensional example: a linearly increasing compression force

As a first two-dimensional example, we consider a domain $\Omega = (0, 1.2) \times (0, 6)$ which is being acted by a linearly increasing compression force with respect to x on the boundary part $[0, 1.2] \times \{6\}$. Its maximum magnitude is $50\, N/m$. The lower horizontal boundary remains clamped and no volume forces are given in Ω (see Figure 2.5). The

Figure 2.5: Example **P1-2D-1**: Physical setting.

following data have been employed in this example:

$$
\begin{aligned}
&T = 105\,\text{days}, \quad \mathcal{C}(e) = \frac{1}{\xi_0 + e}(\mathcal{C}^0 + \mathcal{C}^1 e), \quad a(e) = a_0 + a_1 e + a_2 e^2,\\
&\mathcal{A}(e) = \mathcal{A}^0 + \mathcal{A}^1 e, \quad \xi_0 = 0.892, \quad \gamma = 1740\, Kg/m^3, \quad \boldsymbol{f} = \mathbf{0}\, N/m^2,\\
&a_0 = 1296 \times 10^{-4}\,(100\ \text{days})^{-1}, \quad a_1 = -1296 \times 10^{-2}\,(100\ \text{days})^{-1},\\
&a_2 = 216 \times 10^{-2}\,(100\ \text{days})^{-1},
\end{aligned}
$$

where the fourth-order tensors $\mathcal{C}^0 = (C^0_{ijkl})^2_{i,j,k,l=1}$ and $\mathcal{C}^1 = (C^1_{ijkl})^2_{i,j,k,l=1}$ and the second-order tensors $\mathcal{A}^0 = (A^0_{ij})^2_{i,j=1}$ and $\mathcal{A}^1 = (A^1_{ij})^2_{i,j=1}$ have the following components

(see [17]):

$$
\begin{aligned}
&C^0_{1111} = 48\,GPa, \quad C^0_{2211} = 40\,GPa, \quad C^0_{2222} = 54\,GPa,\\
&C^0_{1211} = C^0_{1222} = 0\,GPa, \quad C^0_{1212} = 7\,GPa,\\
&C^1_{1111} = 90.816\,GPa, \quad C^1_{2211} = 75.68\,GPa, \quad C^1_{2222} = 102.17\,GPa,\\
&C^1_{1211} = C^1_{1222} = 0\,GPa, \quad C^1_{1212} = 13.244\,GPa,\\
&A^0_{11} = 216\,(100\text{days})^{-1}, \quad A^0_{22} = -216\,(100\text{days})^{-1}, \quad A^0_{12} = A^0_{21} = 0,\\
&A^1_{11} = 216\,(100\text{days})^{-1}, \quad A^1_{22} = -216\,(100\text{days})^{-1}, \quad A^1_{12} = A^1_{21} = 0.
\end{aligned}
$$

The initial bone remodeling function has the form,

$$e_0(x, y) = 0.01 \sin \frac{\pi\, y}{3} \quad \text{for} \quad (x, y) \in [0, 1.2] \times [0, 6].$$

Using the time discretization parameter $k = 0.01$, in Figure 2.6 the displacements are shown at initial time (left) and after 106 days (right). As can be observed, the displacements decrease since the bone remodeling function is positive and so the stiffness increases (see Figure 2.7). We have plotted the bone remodeling function at inicial time, after one iteration and at final time. As can be also seen in the next examples, after a few iterations the bone remodeling function takes a distribution similar to the

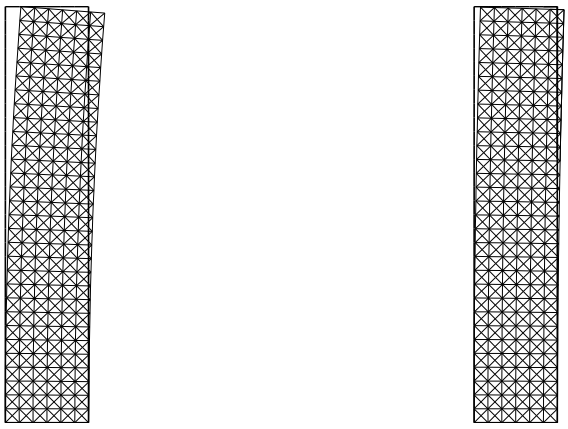

Figure 2.6: Example **P1-2D-1**: Initial configuration and displacements at initial time (left) and after 106 days (right).

last one.

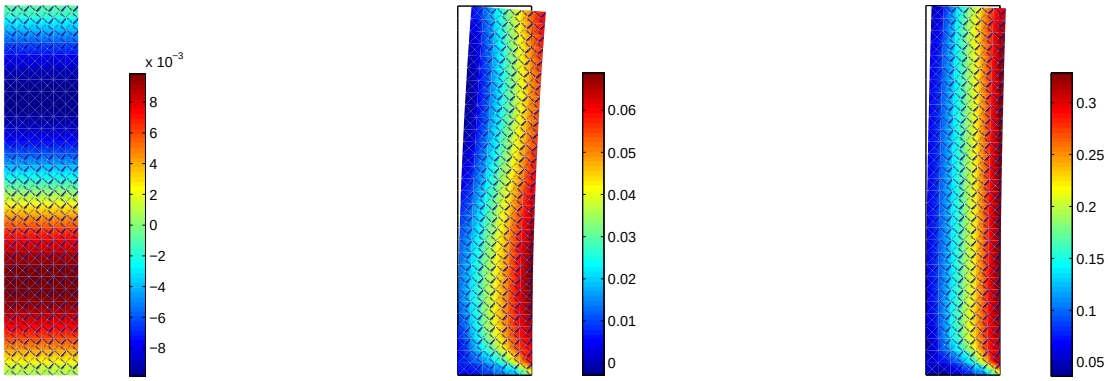

Figure 2.7: Example **P1-2D-1**: Bone remodeling function at initial time (left), after one iteration, t=0.01, and after 106 days (right).

Second two-dimensional example: compression and extension loads

As a second two-dimensional example we consider a similar setting than in the previous case (see Figure 2.8). The unique differences are: there is not initial bone remodeling ($e_0 = 0$), the final time is now $T = 100$ days and the compression force is supposed to be linearly increasing with respect to x with the following form:

$$\boldsymbol{g}(x, y, t) = (0, \frac{-10}{6}\, x + 10)\, N/m \quad if \quad y = 6.$$

This means that now, the right part of the bone is under compression loads and the left part is subjected to a traction charge with the same intensity.

Taking $k = 0.01$ as the time discretization parameter, the displacements fields (multiplied by 10), at initial time and at final time, and the bone remodeling function after one iteration and at final time are plotted in Figures 2.9 and 2.10, respectively. As we can see, the body bends but there is not a recuperation along the time in the displacements. However, the bone remodeling function is positive on the right part since the

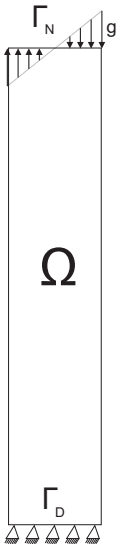

Figure 2.8: Example **P1-2D-2**: Physical setting.

body is compressed there. Hence, the bone is more dense on the right part in order to support the load over the time, but not stronger enough to reduce the displacements. Moreover, on the left part the bone remodeling function is negative which means that the bone is weaker in this area.

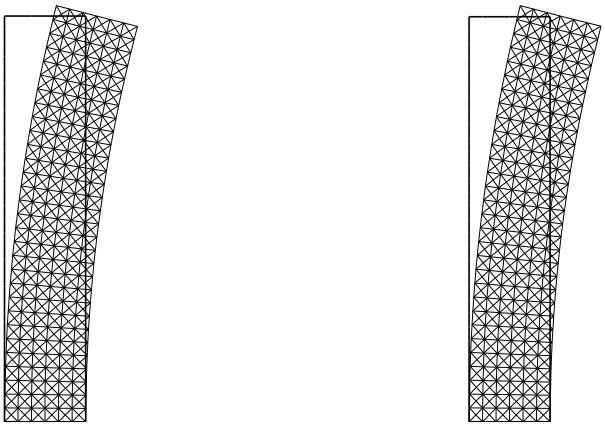

Figure 2.9: Example **P1-2D-2**: Initial configuration and displacements ($\times 10$) at initial time (left) and after 100 days (right).

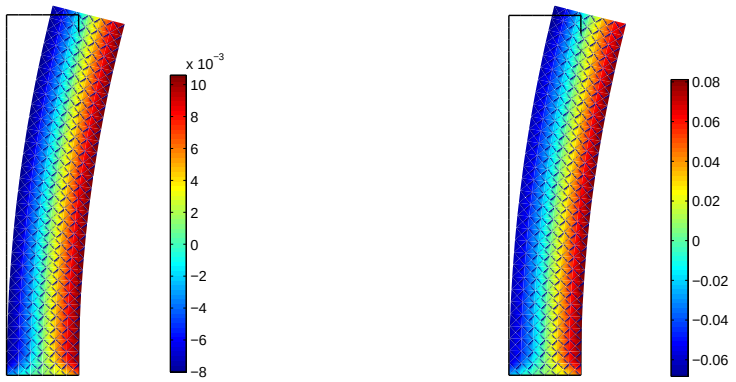

Figure 2.10: Example **P1-2D-2**: Bone remodeling function after one iteration, t=0.01, and after 100 days (right).

Third two-dimensional example: a compression force

As a final two-dimensional example, we consider a constant compression load of $10MPa$ acting on the upper boundary and that the lower horizontal boundary remains clamped (see Figure 2.11). We assume that the final time is now $T = 80$ days and the initial bone remodeling function is $e_0 = 0$.

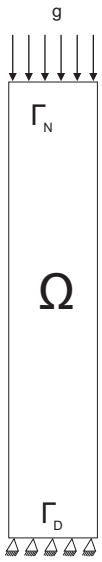

Figure 2.11: Example **P1-2D-3**: Physical setting.

Using the time discretization parameter $k = 0.01$, in Figures 2.12 and 2.13 the

displacements (multiplied by 10), at initial time and after 80 days, and the bone remodeling function at final time are shown. We can observe that there is a decrease in the displacements because of the bone remodeling which is constant in almost the whole bone because it is under a compressive load. The minimum values, reached on the lower boundary, are a consequence of the Dirichlet condition.

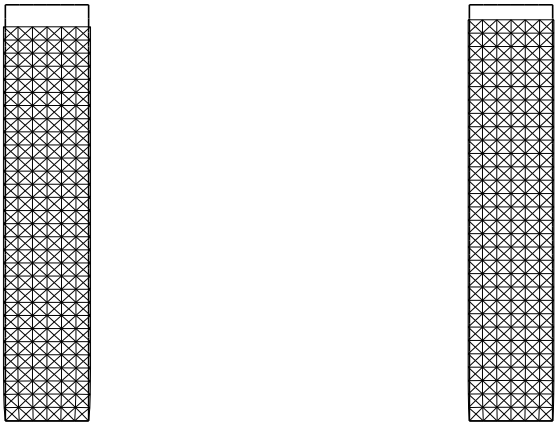

Figure 2.12: Example **P1-2D-3**: Initial configuration and displacements (×10) at initial time (left) and after 80 days (right).

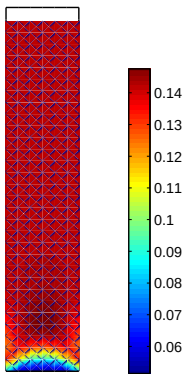

Figure 2.13: Example **P1-2D-3**: Bone remodeling function at final time.

A three-dimensional example: a linearly compression force

As a first three-dimensional example, we consider the domain $\Omega = (0, 1.2) \times (0, 1.2) \times (0, 6)$ which is clamped on its lower boundary $[0, 1.2] \times [0, 1.2] \times \{0\}$ and acted upon by a linearly increasing force on the boundary $[0, 1.2] \times [0, 1.2] \times \{6\}$ with maximum intensity $P = 30Pa$ (see Figure 2.14). No volume forces act in the body and we assume that the initial bone remodeling function is $e_0 = 0$.

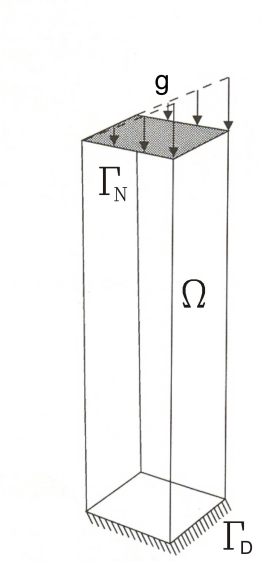

Figure 2.14: Example **P1-3D-1**: Physical setting.

The following data were employed in this example:

$$T = 114\,\text{days}, \quad \mathcal{C}(e) = \frac{1}{\xi_0 + e}(\mathcal{C}^0 + \mathcal{C}^1 e) N/m^2, \quad a(e) = a_0 + a_1 e + a_2 e^2 (\text{days})^{-1},$$
$$\boldsymbol{f} = \mathbf{0} N/m^3, \quad \boldsymbol{g}(x, y, z, t) = (0, 0, y) N/m^2, \quad \mathcal{A}(e) = \mathcal{A}^0 + \mathcal{A}^1 e (\text{days})^{-1},$$
$$\xi_0 = 0.892, \quad \gamma = 1740\, Kg/m^3, \quad a_0 = 1296 \times 10^{-4}\,(100 \text{ days})^{-1},$$
$$a_1 = -1296 \times 10^{-3}\,(100 \text{ days})^{-1}, \quad a_2 = 216 \times 10^{-2}\,(100 \text{ days})^{-1},$$

where the fourth-order tensors $\mathcal{C}^0 = (C^0_{ijkl})^3_{i,j,k,l=1}$ and $\mathcal{C}^1 = (C^1_{ijkl})^3_{i,j,k,l=1}$ and the second-order tensors $\mathcal{A}^0 = (A^0_{ij})^3_{i,j=1}$ and $\mathcal{A}^1 = (A^1_{ij})^3_{i,j=1}$ have the following components

(see [34]):

$$
\begin{aligned}
&C^0_{1111} = 48\,GPa, \quad C^0_{2211} = 40\,GPa, \quad C^0_{2222} = 48\,GPa,\\
&C^0_{3311} = 40\,GPa, \quad C^0_{3322} = 40\,GPa, \quad C^0_{3333} = 54\,GPa,\\
&C^0_{1211} = C^0_{1222} = C^0_{1233} = 0\,GPa,\\
&C^0_{1311} = C^0_{1322} = C^0_{1333} = C^0_{1312} = 0\,GPa,\\
&C^0_{2311} = C^0_{2322} = C^0_{2333} = C^0_{2312} = C^0_{2313} = 0\,GPa,\\
&C^0_{1212} = 4\,GPa, \quad C^0_{1313} = 4\,GPa, \quad C^0_{2323} = 7\,GPa,\\
&C^1_{1111} = 90.816\,GPa, \quad C^1_{2211} = 75.68\,GPa, \quad C^1_{2222} = 90.816\,GPa,\\
&C^1_{3311} = 75.68\,GPa, \quad C^1_{3322} = 75.68\,GPa, \quad C^1_{3333} = 102.17\,GPa,\\
&C^1_{1211} = C^1_{1222} = C^1_{1233} = 0\,GPa,\\
&C^1_{1311} = C^1_{1322} = C^1_{1333} = C^1_{1312} = 0\,GPa,\\
&C^1_{2311} = C^1_{2322} = C^1_{2333} = C^1_{2312} = C^1_{2313} = 0\,GPa,\\
&C^1_{1212} = 7.5680\,GPa, \quad C^1_{1313} = 7.5680\,GPa, \quad C^1_{2323} = 13.244\,GPa,\\
&A^0_{11} = 216\,(100\text{days})^{-1}, \quad A^0_{22} = 216\,(100\text{days})^{-1}, \quad A^0_{33} = -216\,(100\text{days})^{-1},\\
&A^1_{11} = 216\,(100\text{days})^{-1}, \quad A^1_{22} = 216\,(100\text{days})^{-1}, \quad A^1_{33} = -216\,(100\text{days})^{-1},\\
&A^0_{ij} = A^1_{ij} = 0 \quad if \quad i \neq j.
\end{aligned}
$$

Taking $k = 0.01$ as the time discretization parameter, in Figures 2.15 and 2.16 we plot the displacement field (multiplied by 10^3), at initial time and at final time, and the bone remodeling function at final time. Again, we observe that the material is stronger at final time, because of the bone remodeling, and the deformation decreases. Moreover, as in the previous examples, the bone remodeling function takes the bigger values where the body bends and the smaller ones where there is an extension.

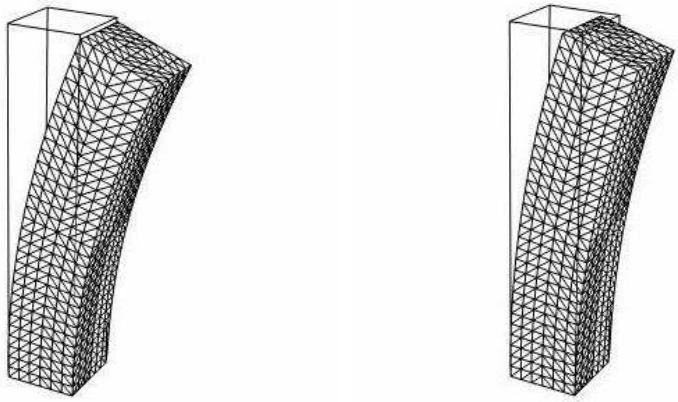

Figure 2.15: Example **P1-3D-1**: Initial configuration and displacements ($\times 10^3$) at initial time (left) and after 114 days (right).

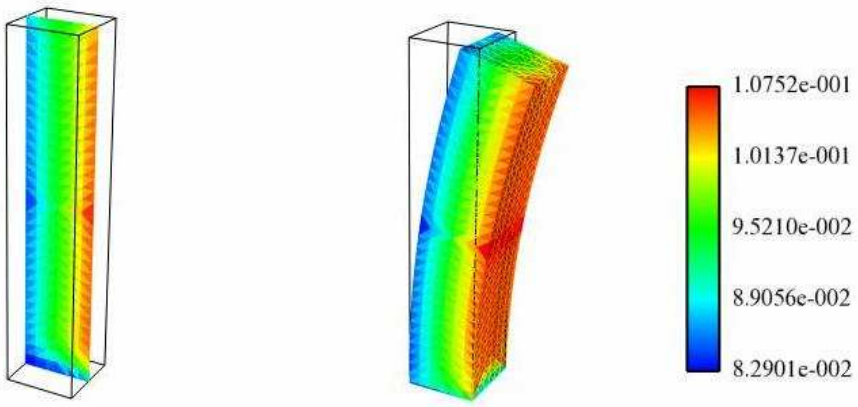

Figure 2.16: Example **P1-3D-1**: Bone remodeling function at final time.

2.3 A contact problem in a bone remodeling model

Considering the constitutive laws described in the previous section to model the behavior of a bone, a contact problem between a bone and an obstacle is numerically studied in this section. We note that this situation could model, for instance, the case when a bone like the femur is in contact with an orthopedic prosthesis. Thus, the so-called obstacle would represent such prosthesis.

We will consider two different problems, in the first one the obstacle is deformable and in the second one it is rigid. To model these two situations we use the normal compliance condition and the classical Signorini condition, respectively.

Our aim in this final section is to prove the convergence of the solution to the problem with normal compliance contact law to the solution to the Signorini problem, to provide the numerical analysis of a fully discrete algorithm for both problems and to perform some numerical simulations.

2.3.1 Mechanical and variational problems

Following the notation of the previous section, let us denote by $\Omega \subset \mathbb{R}^d$, $d = 1, 2, 3$, an open bounded domain and let $\Gamma = \partial\Omega$ be its outer surface which is assumed to be Lipschitz continuous and it is divided into three disjoint parts Γ_D, Γ_N and Γ_C. The body is being acted upon by a volume force of density $\boldsymbol{f}$, it is clamped on Γ_D and surface tractions with density $\boldsymbol{g}$ act on Γ_N. Finally, we assume that the body may come in contact with an obstacle (deformable or rigid) on the boundary part Γ_C which is located at a distance s, measured along the outward unit normal vector $\boldsymbol{\nu}$ (see Figure 2.17).

We turn now to the description of the contact conditions. First, we assume that the contact is produced with a deformable obstacle, and the well-known normal compliance contact condition is employed (see [52, 54]); that is, the normal stress $\sigma_\nu = \boldsymbol{\sigma\nu} \cdot \boldsymbol{\nu}$ on Γ_C is given by

$$-\sigma_\nu = p_\nu(u_\nu - s),$$

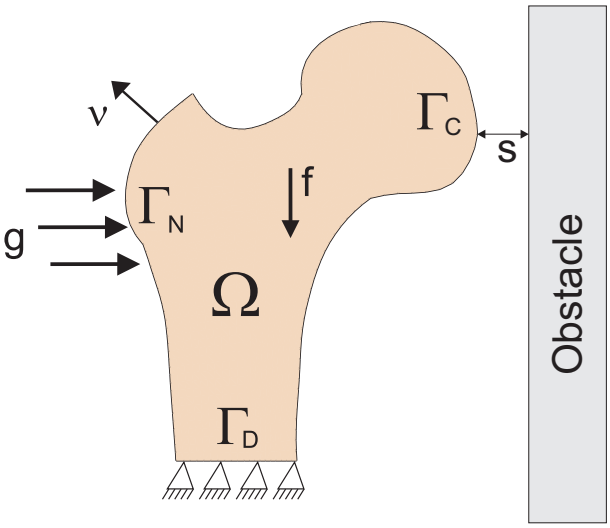

Figure 2.17: A contact problem including bone remodeling.

where $u_\nu = \boldsymbol{u}\cdot\boldsymbol{\nu}$ denotes the normal displacement in such a way that, when $u_\nu > s$, the difference $u_\nu - s$ represents the interpenetration of the body's asperities into those of the foundation. The normal compliance function p_ν is prescribed and satisfies $p_\nu(r) = 0$ for $r \leq 0$, since then there is no contact. As an example, one may consider

$$p_\nu(r) = \frac{1}{\mu}\, r_+, \tag{2.32}$$

where $\mu > 0$ represents a deformability constant (that is, it denotes the stiffness of the obstacle), and $r_+ = \max\{0, r\}$.

Secondly, we assume now that the contact is produced with a rigid obstacle, and the classical Signorini contact conditions are employed (see [51]); that is,

$$u_\nu \leq s, \quad \sigma_\nu \leq 0, \quad (u_\nu - s)\sigma_\nu = 0.$$

We remark that the Signorini contact conditions can be understood as the limit of the normal compliance contact condition when $\mu \to 0$ in expresion (2.32).

We also assume that the contact is frictionless for both problems, i.e. the tangential component of the stress field, denoted $\boldsymbol{\sigma}_\tau = \boldsymbol{\sigma\nu} - \sigma_\nu\boldsymbol{\nu}$, vanishes on the contact surface.

Again, the model is assumed quasistatic and therefore, the inertia effects are neglected. Moreover, let $e_\mu^0 = e_\mu(t=0)$ denote the initial bone remodeling function at time $t = 0$ for the normal compliance problem and $e_0 = e(t=0)$ for the Signorini problem.

Keeping in mind the notation and constitutive laws presented in the previous section for Problem P1, if we suppose that the obstacle is deformable, then the strong formulation of the contact problem is the following.

Problem P1$_\mu^{cont}$. *Find the displacement field* $\boldsymbol{u}_\mu : \Omega \times (0,T) \to \mathbb{R}^d$*, the stress field* $\boldsymbol{\sigma}_\mu : \Omega \times (0,T) \to \mathbb{S}^d$ *and the bone remodeling function* $e_\mu : \Omega \times (0,T) \to \mathbb{R}$ *such that* $e_\mu(0) = e_\mu^0$ *and for a.e.* $t \in (0,T)$*,*

$$\boldsymbol{\sigma}_\mu(t) = (\xi_0 + e_\mu(t))\mathcal{C}(e_\mu(t))\boldsymbol{\varepsilon}(\boldsymbol{u}_\mu(t)) \quad in \quad \Omega, \tag{2.33}$$

$$\dot{e}_\mu(t) = a(e_\mu(t)) + \mathcal{A}(e_\mu(t)) : \boldsymbol{\varepsilon}(\boldsymbol{u}_\mu(t)) \quad in \quad \Omega, \tag{2.34}$$

$$-\mathrm{Div}\,\boldsymbol{\sigma}_\mu(t) = \gamma(\xi_0 + \Phi_L(e_\mu(t)))\boldsymbol{f}(t) \quad in \quad \Omega, \tag{2.35}$$

$$\boldsymbol{u}_\mu(t) = \boldsymbol{0} \quad on \quad \Gamma_D, \tag{2.36}$$

$$\boldsymbol{\sigma}_\mu(t)\boldsymbol{\nu} = \boldsymbol{g}(t) \quad on \quad \Gamma_N, \tag{2.37}$$

$$(\boldsymbol{\sigma}_\mu)_\tau(t) = \boldsymbol{0}, \quad (\sigma_\mu)_\nu(t) = -p_\nu((u_\mu)_\nu(t) - s) \quad on \quad \Gamma_C. \tag{2.38}$$

We recall that $\gamma > 0$ is assumed to be constant, for the sake of simplicity, and it represents the density of the full elastic material presented in the bone.

If we assume that the obstacle is rigid and within exactly the same framework of the previous problem, the strong formulation of the problem with the Signorini contact conditions is the following.

Problem P1^{cont}. *Find the displacement field* $\boldsymbol{u} : \Omega \times (0,T) \to \mathbb{R}^d$*, the stress field* $\boldsymbol{\sigma} : \Omega \times (0,T) \to \mathbb{S}^d$ *and the bone remodeling function* $e : \Omega \times (0,T) \to \mathbb{R}$ *such that*

$e(0) = e_0$ *and for a.e.* $t \in (0,T)$,

$$\boldsymbol{\sigma}(t) = (\xi_0 + e(t))\mathcal{C}(e(t))\boldsymbol{\varepsilon}(\boldsymbol{u}(t)) \quad in \quad \Omega, \tag{2.39}$$

$$\dot{e}(t) = a(e(t)) + \mathcal{A}(e(t)) : \boldsymbol{\varepsilon}(\boldsymbol{u}(t)) \quad in \quad \Omega, \tag{2.40}$$

$$-\mathrm{Div}\,\boldsymbol{\sigma}(t) = \gamma(\xi_0 + \Phi_L(e(t)))\boldsymbol{f}(t) \quad in \quad \Omega, \tag{2.41}$$

$$\boldsymbol{u}(t) = \boldsymbol{0} \quad on \quad \Gamma_D, \tag{2.42}$$

$$\boldsymbol{\sigma}(t)\boldsymbol{\nu} = \boldsymbol{g}(t) \quad on \quad \Gamma_N, \tag{2.43}$$

$$\boldsymbol{\sigma}_\tau(t) = \boldsymbol{0}, \quad u_\nu(t) \leq s, \quad \sigma_\nu(t) \leq 0, \quad (u_\nu - s)\sigma_\nu = 0 \quad on \quad \Gamma_C. \tag{2.44}$$

We observe that in the two equilibrium equations (2.35) and (2.41) the truncation operator Φ_L was applied on the respective bone remodeling functions. This is done from the mathematical point of view since these functions will be proved to be bounded (see Theorems 2.4 and 2.5), and so we will can remove it.

We turn now to obtain a variational formulation of both problems $\mathrm{P1}_\mu^{cont}$ and $\mathrm{P1}^{cont}$. First, recall that we denote by $Y = L^2(\Omega)$ and $H = [L^2(\Omega)]^d$, and the definition of the variational spaces

$$V = \{\boldsymbol{v} \in [H^1(\Omega)]^d \,;\, \boldsymbol{v} = \boldsymbol{0} \quad \text{on} \quad \Gamma_D\},$$

$$Q = \{\boldsymbol{\tau} = (\tau_{ij})_{i,j=1}^d \in [L^2(\Omega)]^{d\times d} \,;\, \tau_{ij} = \tau_{ji}, \quad 1 \leq i,j \leq d\}.$$

Let U be the admissible mechanical displacement convex set given by

$$U = \{\boldsymbol{w} \in V \,;\, w_\nu = \boldsymbol{w}\cdot\boldsymbol{\nu} \leq s \quad \text{on} \quad \Gamma_C\}.$$

Let assumptions (2.6)-(2.9) be hold, and assume that the initial values of the bone remodeling functions e_0 and e_μ^0 verify that

$$e_0,\, e_\mu^0 \in C(\overline{\Omega}), \tag{2.45}$$

and moreover the normal compliance function $p_\nu : \Gamma_C \times \mathbb{R} \longrightarrow \mathbb{R}_+$ satisfies:

$$
\begin{aligned}
&\text{(a) There exists } L_\nu > 0 \text{ such that} \\
&\quad |p_\nu(\boldsymbol{x}, r_1) - p_\nu(\boldsymbol{x}, r_2)| \leq L_\nu \, |r_1 - r_2| \quad \forall\, r_1, r_2 \in \mathbb{R}, \text{ a.e. } \boldsymbol{x} \in \Gamma_C. \\
&\text{(b) The mapping } \boldsymbol{x} \mapsto p_\nu(\boldsymbol{x}, r) \text{ is Lebesgue measurable on } \Gamma_C \quad \forall r \in \mathbb{R}. \\
&\text{(c) } (p_\nu(\boldsymbol{x}, r_1) - p_\nu(\boldsymbol{x}, r_2)) \cdot (r_1 - r_2) \geq 0 \quad \forall\, r_1, r_2 \in \mathbb{R}, \text{ a.e. } \boldsymbol{x} \in \Gamma_C. \\
&\text{(d) The mapping } \boldsymbol{x} \mapsto p_\nu(\boldsymbol{x}, r) = 0 \quad \text{for all } r \leq 0.
\end{aligned}
\tag{2.46}
$$

Let us obtain the variational formulation of Problem $\mathrm{P1}_\mu^{cont}$. Multiplying the equilibrium equation (2.35) by a test function $\boldsymbol{v} \in V$, integrating in Ω and applying the Green's formula we obtain

$$\int_\Omega \boldsymbol{\sigma} : \boldsymbol{\varepsilon}(\boldsymbol{v}) d\boldsymbol{x} = \int_\Omega \gamma(\xi_0 + \Phi_L(e)) \boldsymbol{f} \cdot \boldsymbol{v} d\boldsymbol{x} + \int_\Gamma \boldsymbol{\sigma\nu} \cdot \boldsymbol{v} d\Gamma.$$

Keeping in mind the boundary conditions (2.36) and (2.37) we deduce the relation

$$\int_\Omega \boldsymbol{\sigma} : \boldsymbol{\varepsilon}(\boldsymbol{v}) d\boldsymbol{x} = \int_\Omega \gamma(\xi_0 + \Phi_L(e)) \boldsymbol{f} \cdot \boldsymbol{v} d\boldsymbol{x} + \int_{\Gamma_C} \boldsymbol{\sigma\nu} \cdot \boldsymbol{v} d\Gamma + \int_{\Gamma_N} \boldsymbol{g} \cdot \boldsymbol{v} d\Gamma.$$

Since on the contact boundary Γ_C we have $\boldsymbol{\sigma\nu} \cdot \boldsymbol{v} = \sigma_\nu v_\nu$ ($\boldsymbol{\sigma}_\tau = \boldsymbol{0}$), where $v_\nu = \boldsymbol{v} \cdot \boldsymbol{\nu}$, we obtain the following variational equation

$$\int_\Omega \boldsymbol{\sigma} : \boldsymbol{\varepsilon}(\boldsymbol{v}) d\boldsymbol{x} = \int_\Omega \gamma(\xi_0 + \Phi_L(e)) \boldsymbol{f} \cdot \boldsymbol{v} d\boldsymbol{x} + \int_{\Gamma_C} \sigma_\nu v_\nu d\Gamma + \int_{\Gamma_N} \boldsymbol{g} \cdot \boldsymbol{v} d\Gamma.$$

When the normal compliance condition is assumed, we have $-\sigma_\nu = p_\nu(u_\nu - s)$ and then, we deduce

$$\int_{\Gamma_C} \sigma_\nu v_\nu d\Gamma = -\int_{\Gamma_C} p_\nu(u_\nu - s) v_\nu d\Gamma.$$

Let us define the contact functional $j : V \times V \to \mathbb{R}$ as,

$$j(\boldsymbol{u}, \boldsymbol{v}) = \int_{\Gamma_C} p_\nu(u_\nu - s) \, v_\nu \, d\Gamma \qquad \forall \boldsymbol{u}, \boldsymbol{v} \in V.$$

Keeping in mind the definition of the bilinear form $c(e;\cdot,\cdot) : V \times V \to \mathbb{R}$,

$$c(e;\boldsymbol{u},\boldsymbol{v}) = \int_\Omega (\xi_0 + e)\mathcal{C}(e)\boldsymbol{\varepsilon}(\boldsymbol{u}) \,:\, \boldsymbol{\varepsilon}(\boldsymbol{v})\, d\boldsymbol{x} \quad \forall \boldsymbol{u},\boldsymbol{v} \in V,$$

and the linear form $L(e;\cdot) : V \to \mathbb{R}$,

$$L(e;\boldsymbol{v}) = \int_\Omega \gamma(\xi_0 + \Phi_L(e))\boldsymbol{f}\cdot\boldsymbol{v}\, d\boldsymbol{x} + \int_{\Gamma_N} \boldsymbol{g}\cdot\boldsymbol{v}\, d\Gamma \quad \forall \boldsymbol{v} \in V$$

introduced in Section 2.2.1, we then derive the following variational formulation of Problem $\mathrm{P1}_\mu^{cont}$.

Problem $\mathbf{VP1}_\mu^{cont}$. *Find a displacement field $\boldsymbol{u}_\mu : [0,T] \to V$ and a bone remodeling function $e_\mu : [0,T] \to L^\infty(\Omega)$ such that $e_\mu(0) = e_\mu^0$ and for a.e. $t \in (0,T)$,*

$$\dot{e}_\mu(t) = a(e_\mu(t)) + \mathcal{A}(e_\mu(t)) \,:\, \boldsymbol{\varepsilon}(\boldsymbol{u}_\mu(t)), \tag{2.47}$$

$$c(e_\mu(t);\boldsymbol{u}_\mu(t),\boldsymbol{v}) + j(\boldsymbol{u}_\mu(t),\boldsymbol{v}) = L(e_\mu(t);\boldsymbol{v}) \quad \forall \boldsymbol{v} \in V. \tag{2.48}$$

In order to obtain the variational formulation of Problem $\mathrm{P1}^{cont}$, we argue in the same way but now, we multiply equation (2.41) by $\boldsymbol{v}-\boldsymbol{u}$, where $\boldsymbol{v} \in U$, and we deduce the equality

$$\begin{aligned}\int_\Omega \boldsymbol{\sigma} : (\boldsymbol{\varepsilon}(\boldsymbol{v}) - \boldsymbol{\varepsilon}(\boldsymbol{u}))d\boldsymbol{x} \quad &= \int_\Omega \gamma(\xi_0 + \Phi_L(e))\boldsymbol{f}\cdot(\boldsymbol{v}-\boldsymbol{u})d\boldsymbol{x} \\ &+ \int_{\Gamma_N} \boldsymbol{g}\cdot(\boldsymbol{v}-\boldsymbol{u})d\Gamma + \int_{\Gamma_C} \boldsymbol{\sigma}\boldsymbol{\nu}(\boldsymbol{v}-\boldsymbol{u})d\Gamma.\end{aligned}$$

Moreover, taking into account that $\boldsymbol{\sigma}_\tau = \mathbf{0}$ on the contact boundary Γ_C, we have $\boldsymbol{\sigma}\boldsymbol{\nu}\cdot(\boldsymbol{v}-\boldsymbol{u}) = \sigma_\nu(v_\nu - u_\nu)$. Hence, we obtain the following

$$\begin{aligned}\int_\Omega \boldsymbol{\sigma} : (\boldsymbol{\varepsilon}(\boldsymbol{v}) - \boldsymbol{\varepsilon}(\boldsymbol{u}))d\boldsymbol{x} \quad &= \int_\Omega \gamma(\xi_0 + \Phi_L(e))\boldsymbol{f}\cdot(\boldsymbol{v}-\boldsymbol{u})d\boldsymbol{x} \\ &+ \int_{\Gamma_N} \boldsymbol{g}\cdot(\boldsymbol{v}-\boldsymbol{u})d\Gamma + \int_{\Gamma_C} \sigma_\nu(v_\nu - u_\nu)d\Gamma.\end{aligned}$$

Using the boundary conditions (2.44) we deduce

$$\int_{\Gamma_C} \sigma_\nu(v_\nu - u_\nu) d\Gamma \geq 0,$$

and obtain the following variational problem.

Problem VP1^{cont}. *Find a displacement field $\boldsymbol{u} : [0,T] \to U$ and a bone remodeling function $e : [0,T] \to L^\infty(\Omega)$ such that $e(0) = e_0$ and for a.e. $t \in (0,T)$,*

$$\dot{e}(t) = a(e(t)) + \mathcal{A}(e(t)) \,:\, \boldsymbol{\varepsilon}(\boldsymbol{u}(t)), \tag{2.49}$$

$$c(e(t); \boldsymbol{u}(t), \boldsymbol{v} - \boldsymbol{u}(t)) \geq L(e(t); \boldsymbol{v} - \boldsymbol{u}(t)) \quad \forall \boldsymbol{v} \in U. \tag{2.50}$$

The following result states the existence of a unique solution to Problem VP1^{cont}. It can be proved by using similar arguments to those employed in [32] for the case of an asymptotic bone remodeling rod model with Signorini contact conditions (see also [57]).

Theorem 2.4 *Let the assumptions (2.6)-(2.9) and (2.45) hold. Assume that, for any given function $e \in C^1([0,T]; C(\overline{\Omega}))$, the unique solution to the following problem:*

$$\boldsymbol{u}(t) \in U, \quad c(e(t); \boldsymbol{u}(t), \boldsymbol{v} - \boldsymbol{u}(t)) \geq L(e(t); \boldsymbol{v} - \boldsymbol{u}(t)) \quad \forall \boldsymbol{v} \in U, \tag{2.51}$$

has the regularity

$$\boldsymbol{u} \in C([0,T]; [H^3(\Omega)]^d) \text{ for } d = 2, 3$$

or the regularity

$$u \in C([0,T]; H^2(\Omega)) \text{ for } d = 1.$$

Then, there exists a unique solution to Problem VP1^{cont} with the following regularity:

$$\boldsymbol{u} \in C([0,T]; [C^1(\overline{\Omega})]^d), \quad e \in C^1([0,T]; C(\overline{\Omega})).$$

Arguing in an analogous way, we also have.

Theorem 2.5 *Let the assumptions (2.6)-(2.9), (2.45) and (2.46) hold. Assume that, for any given function $e_\mu \in C^1([0,T];C(\overline{\Omega}))$, the unique solution to the following problem:*

$$\boldsymbol{u}_\mu(t) \in V, \quad c(e_\mu(t);\boldsymbol{u}_\mu(t),\boldsymbol{v}) + j(\boldsymbol{u}_\mu(t),\boldsymbol{v}) = L(e_\mu(t);\boldsymbol{v}) \quad \forall \boldsymbol{v} \in V, \tag{2.52}$$

has the regularity

$$\boldsymbol{u}_\mu \in C([0,T];[H^3(\Omega)]^d) \text{ for } d = 2,3$$

or the regularity

$$u \in C([0,T];H^2(\Omega)) \text{ for } d = 1.$$

Then, there exists a unique solution to Problem $VP1_\mu^{cont}$ with the following regularity:

$$\boldsymbol{u}_\mu \in C([0,T];[C^1(\overline{\Omega})]^d), \quad e_\mu \in C^1([0,T];C(\overline{\Omega})).$$

Remark 2.2 *We notice that these two existence and uniqueness results, Theorems 2.4 and 2.5, are obtained by assuming that the variational inequality (2.51) or the variational equation (2.52) have a unique solution with the required regularity $\boldsymbol{u}, \boldsymbol{u}_\mu \in C([0,T];[H^3(\Omega)]^d)$ for $d = 2,3$ or $\boldsymbol{u}, \boldsymbol{u}_\mu \in C([0,T];H^2(\Omega))$ for $d = 1$. The proof of both results, detailed in [60], is based on the existence and uniqueness result stated in [57] in the study of bone remodeling problems without contact (see Theorem 2.1). Anyway, the proof of both theorems, without such assumptions, is not done yet and it remains as an open problem.*

The aim of this section is to prove the convergence of the solution to Problem $\mathrm{VP1}_\mu^{cont}$ to the solution to Problem $\mathrm{VP1}^{cont}$ when the deformability coefficient μ tends to zero, considering the normal compliance function p_ν given by (2.32). Notice that this function p_ν satisfies the properties (2.46). This convergence is established in the following

theorem.

Theorem 2.6 *Let the assumptions (2.6)-(2.9), (2.45) and (2.46) hold. Then, the solution* $(\boldsymbol{u}_\mu, e_\mu)$ *to Problem* $VP1_\mu^{cont}$ *converges to the solution* $(\boldsymbol{u}, e)$ *to Problem* $VP1^{cont}$*, in the space* $C([0,T]; V \times Y)$*, when the normal compliance function is given by (2.32) and the deformability coefficient* μ *tends to zero; that is,*

$$\max_{0\le t\le T}\{\|\boldsymbol{u}_\mu(t)-\boldsymbol{u}(t)\|_V + \|e_\mu(t)-e(t)\|_Y\} \to 0 \quad \textit{when} \quad \mu \to 0. \tag{2.53}$$

Proof In order to simplify the writing and the calculations we assume that $s = 0$ and that the initial conditions coincide (i.e. $e_\mu^0 = e_0$ for all $\mu > 0$). Clearly, it is straightforward to extend the results presented below to more general situations.

First, let us estimate the error on the bone remodeling function. Integrating in time both differential equations (2.47) and (2.49) we have,

$$\begin{aligned} e(t) &= \int_0^t \Big[a(e(s)) + \mathcal{A}(e(s)) \,:\, \boldsymbol{\varepsilon}(\boldsymbol{u}(s))\Big]\, ds + e_0, \\ e_\mu(t) &= \int_0^t \Big[a(e_\mu(s)) + \mathcal{A}(e_\mu(s)) \,:\, \boldsymbol{\varepsilon}(\boldsymbol{u}_\mu(s))\Big]\, ds + e_0. \end{aligned}$$

Subtracting both expressions we find that

$$\begin{aligned} \|e(t)-e_\mu(t)\|_Y \le \int_0^t \Big(&\|a(e(s)) - a(e_\mu(s))\|_Y \\ &+ \|\mathcal{A}(e(s)) \,:\, \boldsymbol{\varepsilon}(\boldsymbol{u}(s)) - \mathcal{A}(e_\mu(s)) \,:\, \boldsymbol{\varepsilon}(\boldsymbol{u}_\mu(s))\|_Y\Big)\, ds. \end{aligned}$$

Using now properties (2.7) it follows that

$$\begin{aligned} &\|a(e(s)) - a(e_\mu(s))\|_Y \le L_a \|e(s) - e_\mu(s)\|_Y, \\ &\|\mathcal{A}(e(s)) \,:\, \boldsymbol{\varepsilon}(\boldsymbol{u}(s)) - \mathcal{A}(e_\mu(s)) \,:\, \boldsymbol{\varepsilon}(\boldsymbol{u}_\mu(s))\|_Y \\ &\qquad \le \|\mathcal{A}(e_\mu(s)) \,:\, \boldsymbol{\varepsilon}(\boldsymbol{u}(s)) - \mathcal{A}(e_\mu(s)) \,:\, \boldsymbol{\varepsilon}(\boldsymbol{u}_\mu(s))\|_Y \\ &\qquad\quad + \|\mathcal{A}(e(s)) \,:\, \boldsymbol{\varepsilon}(\boldsymbol{u}(s)) - \mathcal{A}(e_\mu(s)) \,:\, \boldsymbol{\varepsilon}(\boldsymbol{u}(s))\|_Y \\ &\qquad \le C(\|\boldsymbol{u}(s) - \boldsymbol{u}_\mu(s)\|_V + \|e_\mu(s) - e(s)\|_Y), \end{aligned}$$

where C, in what follows, is a generic positive constant which depends on the problem data and, here, it is linearly dependent on the norm $\|\boldsymbol{\varepsilon}(\boldsymbol{u})\|_{[C(\overline{\Omega})]^{d\times d}}$. Moreover, the regularity provided in Theorem 2.4 has been used.

Thus, we obtain that

$$\|e(t)-e_\mu(t)\|_Y \leq C\int_0^t \Big(\|\boldsymbol{u}(s)-\boldsymbol{u}_\mu(s)\|_V + \|e_\mu(s)-e(s)\|_Y\Big)\,ds, \tag{2.54}$$

where C is independent of μ, t and e.

We proceed now with the mechanical displacement fields. In what follows, we suppress the dependence on time to simplify the writing. Taking $\boldsymbol{v}=\boldsymbol{u}-\boldsymbol{u}_\mu\in V$ in the nonlinear variational equation (2.48) we have

$$c(e_\mu;\boldsymbol{u}_\mu,\boldsymbol{u}-\boldsymbol{u}_\mu)+j(\boldsymbol{u}_\mu,\boldsymbol{u}-\boldsymbol{u}_\mu)=L(e_\mu;\boldsymbol{u}-\boldsymbol{u}_\mu),$$

and using $c(e;\boldsymbol{u},\boldsymbol{v}-\boldsymbol{u}_\mu+\boldsymbol{u}_\mu-\boldsymbol{u})$ instead of $c(e;\boldsymbol{u},\boldsymbol{v}-\boldsymbol{u})$ in (2.50), it follows that

$$c(e;\boldsymbol{u},\boldsymbol{u}_\mu-\boldsymbol{u})\geq L(e;\boldsymbol{v}-\boldsymbol{u})-c(e;\boldsymbol{u},\boldsymbol{v}-\boldsymbol{u}_\mu)\quad\forall\boldsymbol{v}\in U.$$

We observe that we can not take $\boldsymbol{v}=\boldsymbol{u}-\boldsymbol{u}_\mu\in U$ in (2.50) because, in general, we can not guarantee that $\boldsymbol{u}_\mu\in U$.

Since $u_\nu\leq 0$ on Γ_C it is easy to check that

$$j(\boldsymbol{u}_\mu,\boldsymbol{u}-\boldsymbol{u}_\mu)=j(\boldsymbol{u}_\mu,\boldsymbol{u})-j(\boldsymbol{u}_\mu,\boldsymbol{u}_\mu)\leq 0,$$

and the previous equations can be rewritten as

$$\begin{aligned}&c(e_\mu;-\boldsymbol{u}_\mu,\boldsymbol{u}-\boldsymbol{u}_\mu)\leq -L(e_\mu;\boldsymbol{u}-\boldsymbol{u}_\mu),\\ &c(e;\boldsymbol{u},\boldsymbol{u}-\boldsymbol{u}_\mu)\leq L(e;\boldsymbol{u}-\boldsymbol{v})+c(e;\boldsymbol{u},\boldsymbol{v}-\boldsymbol{u}_\mu)\quad\forall\boldsymbol{v}\in U.\end{aligned}$$

Keeping in mind that

$$-L(e_\mu;\boldsymbol{u}-\boldsymbol{u}_\mu)+L(e;\boldsymbol{u}-\boldsymbol{v})=L(e;\boldsymbol{u}-\boldsymbol{u}_\mu)-L(e_\mu;\boldsymbol{u}-\boldsymbol{u}_\mu)$$
$$+L(e;\boldsymbol{u}-\boldsymbol{v})-L(e;\boldsymbol{u}-\boldsymbol{u}_\mu)\quad\forall\boldsymbol{v}\in U,$$

and

$$c(e_\mu;-\boldsymbol{u}_\mu,\boldsymbol{u}-\boldsymbol{u}_\mu)+c(e;\boldsymbol{u},\boldsymbol{u}-\boldsymbol{u}_\mu)=c(e_\mu;\boldsymbol{u}-\boldsymbol{u}_\mu,\boldsymbol{u}-\boldsymbol{u}_\mu)$$
$$+c(e;\boldsymbol{u},\boldsymbol{u}-\boldsymbol{u}_\mu)-c(e_\mu;\boldsymbol{u},\boldsymbol{u}-\boldsymbol{u}_\mu),$$

adding the previous inequalities and using properties (2.6) and (2.9) we obtain

$$\begin{aligned}
&c(e_\mu;\boldsymbol{u}-\boldsymbol{u}_\mu,\boldsymbol{u}-\boldsymbol{u}_\mu)+c(e;\boldsymbol{u},\boldsymbol{u}-\boldsymbol{u}_\mu)-c(e_\mu;\boldsymbol{u},\boldsymbol{u}-\boldsymbol{u}_\mu)\\
&\qquad\le L(e;\boldsymbol{u}-\boldsymbol{u}_\mu)-L(e_\mu;\boldsymbol{u}-\boldsymbol{u}_\mu)+L(e;\boldsymbol{u}-\boldsymbol{v})\\
&\qquad -L(e;\boldsymbol{u}-\boldsymbol{u}_\mu)+c(e;\boldsymbol{u},\boldsymbol{v}-\boldsymbol{u}_\mu),\\
&c(e_\mu;\boldsymbol{u}-\boldsymbol{u}_\mu,\boldsymbol{u}-\boldsymbol{u}_\mu)\ge C\|\boldsymbol{u}-\boldsymbol{u}_\mu\|_V^2,\\
&c(e;\boldsymbol{u},\boldsymbol{u}-\boldsymbol{u}_\mu)-c(e_\mu;\boldsymbol{u},\boldsymbol{u}-\boldsymbol{u}_\mu)\le C\|e-e_\mu\|_Y^2\|\boldsymbol{u}-\boldsymbol{u}_\mu\|_V^2,\\
&L(e;\boldsymbol{u}-\boldsymbol{u}_\mu)-L(e_\mu;\boldsymbol{u}-\boldsymbol{u}_\mu)+L(e;\boldsymbol{u}-\boldsymbol{v})-L(e;\boldsymbol{u}-\boldsymbol{u}_\mu)\\
&\qquad\le C\Big(\|e-e_\mu\|_Y\|\boldsymbol{u}-\boldsymbol{u}_\mu\|_H+\|\boldsymbol{u}_\mu-\boldsymbol{v}\|_{[L^2(\Gamma_N)]^d}\Big).
\end{aligned}$$

Using the inequality (2.22) we find that

$$\|\boldsymbol{u}-\boldsymbol{u}_\mu\|_V^2\le C\Big(\|e-e_\mu\|_Y^2+\|\boldsymbol{v}-\boldsymbol{u}_\mu\|_H+\|\boldsymbol{v}-\boldsymbol{u}_\mu\|_{[L^2(\Gamma_N)]^d}$$
$$+c(e;\boldsymbol{u},\boldsymbol{v}-\boldsymbol{u}_\mu)\Big)\quad\forall\boldsymbol{v}\in U.$$

Therefore, we obtain the following estimates for the displacement field

$$\begin{aligned}
\|\boldsymbol{u}-\boldsymbol{u}_\mu\|_V\le\ & C\Big(\|e-e_\mu\|_Y+\|\boldsymbol{v}-\boldsymbol{u}_\mu\|_H^{1/2}+\|\boldsymbol{v}-\boldsymbol{u}_\mu\|_{[L^2(\Gamma_N)]^d}^{1/2}\\
&+|c(e;\boldsymbol{u},\boldsymbol{v}-\boldsymbol{u}_\mu)|^{1/2}\Big)\quad\forall\boldsymbol{v}\in U.
\end{aligned}\tag{2.55}$$

Combining now estimates (2.54) and (2.55) and using Gronwall's inequality we conclude

that

$$\max_{0\le t\le T}\Big\{\|\boldsymbol{u}(t)-\boldsymbol{u}_\mu(t)\|_V+\|e(t)-e_\mu(t)\|_Y\Big\}\le C\max_{0\le t\le T}\Big(\|\boldsymbol{v}(t)-\boldsymbol{u}_\mu(t)\|_H^{1/2} +\|\boldsymbol{v}(t)-\boldsymbol{u}_\mu(t)\|^{1/2}_{[L2(\Gamma_N)]^d}+|c(e(t);\boldsymbol{u}(t),\boldsymbol{v}(t)-\boldsymbol{u}_\mu(t))|^{1/2}\Big) \tag{2.56}$$

for all $\boldsymbol{v}\in C([0,T];U)$.

Taking into account that $j(\boldsymbol{u}_\mu(t),\boldsymbol{u}_\mu(t))\ge 0$, using property (2.6)(d) we find that

$$m_{\mathcal{C}}\|\boldsymbol{u}_\mu(t)\|_V^2\le c(e_\mu(t);\boldsymbol{u}_\mu(t),\boldsymbol{u}_\mu(t))\le L(e_\mu(t);\boldsymbol{u}_\mu(t))\le C\|\boldsymbol{u}_\mu(t)\|_V,$$

and therefore, there exists $M>0$, independent of μ, such that

$$\|\boldsymbol{u}_\mu(t)\|_V\le M\quad\forall\mu>0.$$

Hence, there exists a subsequence of $\big(\boldsymbol{u}_\mu(t)\big)$, denoted by $\big(\boldsymbol{u}_{\mu_k}(t)\big)$, which is weakly convergent to an element $\tilde{\boldsymbol{u}}(t)$ belonging to V (since V is a closed space). Let us prove that $\tilde{\boldsymbol{u}}(t)\in U$, i.e. we shall verify that $\tilde{u}_\nu(t)=\tilde{\boldsymbol{u}}(t)\cdot\boldsymbol{\nu}\le 0$ on Γ_C.

Using again properties (2.6) it follows that $c(e_{\mu_k}(t);\boldsymbol{u}_{\mu_k}(t),\boldsymbol{u}_{\mu_k}(t))\ge 0$, and thus we have,

$$0\le j(\boldsymbol{u}_{\mu_k}(t),\boldsymbol{u}_{\mu_k}(t))\le L(e_{\mu_k}(t);\boldsymbol{u}_{\mu_k}(t))\le C\|\boldsymbol{u}_{\mu_k}(t)\|_V\le CM,$$

where C is a positive constant independent of t, μ_k, $\boldsymbol{u}$ and e.

Taking limits it follows that

$$0\le\lim_{\mu_k\to 0}\frac{1}{\mu_k}\int_{\Gamma_C}[(\boldsymbol{u}_{\mu_k}(t))_\nu]_+(\boldsymbol{u}_{\mu_k}(t))_\nu\,d\Gamma\le CM=\text{constant},$$

and, by Fatou's lemma, we have

$$0\le\int_{\Gamma_C}\lim_{\mu_k\to 0}\Big\{[(\boldsymbol{u}_{\mu_k}(t))_\nu]_+(\boldsymbol{u}_{\mu_k}(t))_\nu\Big\}\,d\Gamma\le\lim_{\mu_k\to 0}\int_{\Gamma_C}[(\boldsymbol{u}_{\mu_k}(t))_\nu]_+(\boldsymbol{u}_{\mu_k}(t))_\nu\,d\Gamma=0.$$

Since $\boldsymbol{u}_{\mu_k}(t)$ converges strongly to $\tilde{\boldsymbol{u}}(t)$ on Γ_C (the trace operator from V into $[L^2(\Gamma_C)]^d$

is compact), we find that $\displaystyle\int_{\Gamma_C} [\tilde{u}_\nu(t)]_+ \tilde{u}_\nu(t)\, d\Gamma = 0$, which implies that $\tilde{u}_\nu(t) \leq 0$ on Γ_C. Therefore we have proved that $\tilde{\boldsymbol{u}}(t) \in U$.

Keeping in mind that V is compactly embedded in H (Rellich-Kondrachov theorem) and that the trace operator is also compact from V into $[L^2(\Gamma_N)]^d$, the subsequence $\big(\boldsymbol{u}_{\mu_k}(t)\big)$ is also strongly convergent to $\tilde{\boldsymbol{u}}(t)$ in H and its trace is strongly convergent to the trace of $\tilde{\boldsymbol{u}}(t)$ in $[L^2(\Gamma_N)]^d$. Moreover, since $\boldsymbol{u}_{\mu_k}(t) \rightharpoonup \tilde{\boldsymbol{u}}(t)$ in V, we have

$$|c(e(t); \boldsymbol{u}(t), \tilde{\boldsymbol{u}}(t) - \boldsymbol{u}_{\mu_k}(t))|^{1/2} \to 0 \quad \text{as} \quad \mu_k \to 0,$$

and taking again $\boldsymbol{v}(t) = \tilde{\boldsymbol{u}}(t)$ in (2.56) for $\mu = \mu_k$ we conclude that

$$\max_{0\leq t\leq T} \Big\{ \|\boldsymbol{u}(t) - \boldsymbol{u}_{\mu_k}(t)\|_V + \|e(t) - e_{\mu_k}(t)\|_Y \Big\} \to 0 \quad \text{as} \quad \mu_k \to 0. \tag{2.57}$$

Finally, for any other subsequence $\big(\boldsymbol{u}_{\mu_i}(t)\big)$ of $\big(\boldsymbol{u}_\mu(t)\big)$ weakly convergent to another element $\hat{\boldsymbol{u}}(t) \in V$, we can repeat these arguments and we again obtain that $\hat{\boldsymbol{u}}(t) \in U$ and so, the limits are equal to zero as in (2.57). Thus we can conclude that (2.57) is verified for every sequence $\big(\boldsymbol{u}_\mu(t)\big)$. □

In addition to the mathematical importance of this result, it is interesting to remark that, in applications, from this theorem we can conclude that the solution to the contact problem with a rigid obstacle may be then approached by the solution to the contact problem with a deformable foundation, for small obstacle's deformability coefficients. This is very important for the applications, since contact problems with normal compliance give much better results than Signorini problems due to the loss of the regularity of its solution and they are easier to be solved.

2.3.2 Numerical analysis of a fully discrete scheme

We now introduce a finite element algorithm for approximating solutions of both variational problems VP1^{cont} and VP1$_\mu^{cont}$ and derive an error estimate on them.

The discretization of the two variational problems is done in two steps. First, we consider two finite dimensional spaces $V^h \subset V$ and $B^h \subset L^\infty(\Omega) \subset Y$, approximating the spaces V and $L^\infty(\Omega)$, respectively. Here, $h > 0$ denotes the spatial discretization parameter. Moreover, we define the discrete admissible displacement convex set $U^h = U \cap V^h$; that is,

$$U^h = \{\boldsymbol{w}^h \in V^h\,;\, w_\nu^h = \boldsymbol{w}^h \cdot \boldsymbol{\nu} \leq s^h \quad \text{on} \quad \Gamma_C\},$$

where s^h is an appropriate approximation of the gap function s.

Secondly, the time derivatives are discretized by using a uniform partition of the time interval $[0, T]$, denoted by $0 = t_0 < t_1 < \ldots < t_N = T$, and let k be the time step size, $k = T/N$. Moreover, for a continuous function $f(t)$ we let $f_n = f(t_n)$.

In this section, no summation is assumed over a repeated index, and C denotes a positive constant which depends on the problem data, but it is independent of the discretization parameters h and k.

Using the forward Euler scheme, the fully discrete approximations of problems VP1^{cont} and VP1$_\mu^{cont}$ are as follows.

Problem VP1^{cont,hk}. *Find a discrete displacement field* $\boldsymbol{u}^{hk} = \{\boldsymbol{u}_n^{hk}\}_{n=0}^N \subset U^h$ *and a discrete bone remodeling function* $e^{hk} = \{e_n^{hk}\}_{n=0}^N \subset B^h$ *such that* $e_0^{hk} = e_0^h$ *and for* $n = 1, \ldots, N$,

$$c(e_n^{hk}; \boldsymbol{u}_n^{hk}, \boldsymbol{v}^h - \boldsymbol{u}_n^{hk}) \geq L(e_n^{hk}; \boldsymbol{v}^h - \boldsymbol{u}_n^{hk}) \quad \forall \boldsymbol{v}^h \in U^h, \tag{2.58}$$

$$\frac{e_n^{hk} - e_{n-1}^{hk}}{k} = a(e_{n-1}^{hk}) + \mathcal{A}(e_{n-1}^{hk}) \,:\, \boldsymbol{\varepsilon}(\boldsymbol{u}_{n-1}^{hk}), \tag{2.59}$$

where e_0^h is an appropriate approximation of the initial condition e_0 and $\boldsymbol{u}_0^{hk}$ is defined

as the solution to the following problem,

$$\boldsymbol{u}_0^{hk} \in U^h, \quad c(e_0^h; \boldsymbol{u}_0^{hk}, \boldsymbol{v}^h - \boldsymbol{u}_0^{hk}) \geq L(e_0^h; \boldsymbol{v}^h - \boldsymbol{u}_0^{hk}) \quad \forall \boldsymbol{v}^h \in U^h. \tag{2.60}$$

Problem VP1$_\mu^{cont,hk}$. *Find a discrete displacement field* $\boldsymbol{u}_\mu^{hk} = \{(\boldsymbol{u}_\mu)_n^{hk}\}_{n=0}^N \subset V^h$ *and a discrete function* $e_\mu^{hk} = \{(e_\mu)_n^{hk}\}_{n=0}^N \subset B^h$ *such that* $(e_\mu)_0^{hk} = e_0^h$ *and for* $n = 1, \ldots, N$,

$$c((e_\mu)_n^{hk}; (\boldsymbol{u}_\mu)_n^{hk}, \boldsymbol{v}^h) + j((\boldsymbol{u}_\mu)_n^{hk}, \boldsymbol{v}^h) = L((e_\mu)_n^{hk}; \boldsymbol{v}^h) \quad \forall \boldsymbol{v}^h \in V^h, \tag{2.61}$$

$$\frac{(e_\mu)_n^{hk} - (e_\mu)_{n-1}^{hk}}{k} = a((e_\mu)_{n-1}^{hk}) + \mathcal{A}((e_\mu)_{n-1}^{hk}) : \boldsymbol{\varepsilon}((\boldsymbol{u}_\mu)_{n-1}^{hk}), \tag{2.62}$$

where e_0^h is an appropriate approximation of the initial condition e_0 (which we assumed, as in the previous section, equal to the initial condition for the Signorini's problem) and $(\boldsymbol{u}_\mu)_0^{hk}$ is the solution to the following problem,

$$(\boldsymbol{u}_\mu)_0^{hk} \in V^h, \quad c((e_\mu)_0^h; (\boldsymbol{u}_\mu)_0^{hk}, \boldsymbol{v}^h) + j((\boldsymbol{u}_\mu)_0^{hk}, \boldsymbol{v}^h) = L((e_\mu)_0^h; \boldsymbol{v}^h) \quad \forall \boldsymbol{v}^h \in V^h.$$

From the properties (2.6), using classical results on nonlinear variational equations and elliptic variational inequalities (see [44]), it is straightforward to obtain the existence and uniqueness of solution to both fully discrete problems.

The aim of this section is to derive a priori error estimates on the numerical errors $\|\boldsymbol{u}_n - \boldsymbol{u}_n^{hk}\|_V$ and $\|e_n - e_n^{hk}\|_Y$, in the Problem VP1^{cont,hk}, and $\|(\boldsymbol{u}_\mu)_n - (\boldsymbol{u}_\mu)_n^{hk}\|_V$ and $\|(e_\mu)_n - (e_\mu)_n^{hk}\|_Y$ in the Problem VP1$_\mu^{cont,hk}$. Therefore, we have first the following.

Theorem 2.7 *Let assumptions (2.6)-(2.10) and (2.46) hold and denote by* $(\boldsymbol{u}, e)$ *and* $(\boldsymbol{u}^{hk}, e^{hk})$ *the respective solutions to problems VP1^{cont} and VP1^{cont,hk}. Then we have, for all* $\{\boldsymbol{v}_n^h\}_{n=0}^N \subset U^h$,

$$\max_{0\leq n\leq N}\{\|e_n - e_n^{hk}\|_Y^2 + \|\boldsymbol{u}_n - \boldsymbol{u}_n^{hk}\|_V^2\} \leq C\Big(\|e_0 - e_0^h\|_Y^2 + \|\boldsymbol{u}_0 - \boldsymbol{u}_0^{hk}\|_V^2$$

$$+k\sum_{j=1}^{N}\Big[\|\dot{e}_j-\delta e_j\|_Y^2+\|\boldsymbol{u}_j-\boldsymbol{u}_{j-1}\|_V^2\Big]+k^2+\max_{0\le n\le N}\|\boldsymbol{u}_n-\boldsymbol{v}_n^h\|_V$$
$$+\max_{0\le n\le N}\|\boldsymbol{u}_n-\boldsymbol{v}_n^h\|_V^2\Big), \tag{2.63}$$

where the notation $\delta e_j=(e_j-e_{j-1})/k$ is employed.

Proof First, we recall that an error estimates on the function e were already established in the previous section (see Theorem 2.3). It was proved the following:

$$\|e_n-e_n^{hk}\|_Y\le\|e_0-e_0^h\|_Y+Ck+Ck\sum_{j=1}^{n}\Big[\|e_{j-1}-e_{j-1}^{hk}\|_Y \\ +\|\dot{e}_j-\delta e_j\|_Y+\|\boldsymbol{u}_{j-1}-\boldsymbol{u}_{j-1}^{hk}\|_V+\|\boldsymbol{u}_j-\boldsymbol{u}_{j-1}\|_V\Big]. \tag{2.64}$$

Next, let us estimate the numerical errors on the displacement field. Thus, we write variational inequality (2.50) at time $t=t_n$ for $\boldsymbol{v}=\boldsymbol{u}_n^{hk}\in U^h\subset U$ to obtain,

$$c(e_n;\boldsymbol{u}_n,\boldsymbol{u}_n^{hk}-\boldsymbol{u}_n)\ge L(e_n;\boldsymbol{u}_n^{hk}-\boldsymbol{u}_n). \tag{2.65}$$

Then, we rewrite variational inequality (2.58) in the form,

$$c(e_n^{hk};\boldsymbol{u}_n^{hk},\boldsymbol{u}_n-\boldsymbol{u}_n^{hk})\ge L(e_n^{hk};\boldsymbol{v}^h-\boldsymbol{u}_n^{hk})+c(e_n^{hk};\boldsymbol{u}_n^{hk},\boldsymbol{u}_n-\boldsymbol{v}^h)\quad\forall\boldsymbol{v}^h\in U^h. \tag{2.66}$$

Subtracting (2.65) and (2.66), we find that

$$c(e_n;\boldsymbol{u}_n,\boldsymbol{u}_n-\boldsymbol{u}_n^{hk})-c(e_n^{hk};\boldsymbol{u}_n^{hk},\boldsymbol{u}_n-\boldsymbol{u}_n^{hk})\le L(e_n;\boldsymbol{u}_n-\boldsymbol{u}_n^{hk})+L(e_n^{hk};\boldsymbol{u}_n^{hk}-\boldsymbol{v}^h)$$
$$+c(e_n^{hk};\boldsymbol{u}_n^{hk},\boldsymbol{v}^h-\boldsymbol{u}_n).$$

Using property (2.6) it follows that

$$c(e_n^{hk};\boldsymbol{u}_n-\boldsymbol{u}_n^{hk},\boldsymbol{u}_n-\boldsymbol{u}_n^{hk})\ge C\|\boldsymbol{u}_n-\boldsymbol{u}_n^{hk}\|_V^2,$$
$$c(e_n;\boldsymbol{u}_n,\boldsymbol{u}_n-\boldsymbol{u}_n^{hk})-c(e_n^{hk};\boldsymbol{u}_n^{hk},\boldsymbol{u}_n-\boldsymbol{u}_n^{hk})=c(e_n^{hk};\boldsymbol{u}_n-\boldsymbol{u}_n^{hk},\boldsymbol{u}_n-\boldsymbol{u}_n^{hk})$$
$$+c(e_n;\boldsymbol{u}_n,\boldsymbol{u}_n-\boldsymbol{u}_n^{hk})-c(e_n^{hk};\boldsymbol{u}_n,\boldsymbol{u}_n-\boldsymbol{u}_n^{hk}),$$

$$
\begin{aligned}
&c(e_n;\boldsymbol{u}_n,\boldsymbol{u}_n-\boldsymbol{u}_n^{hk})-c(e_n^{hk};\boldsymbol{u}_n,\boldsymbol{u}_n-\boldsymbol{u}_n^{hk})\leq C\|e_n-e_n^{hk}\|_Y\|\boldsymbol{u}_n-\boldsymbol{u}_n^{hk}\|_V,\\
&L(e_n;\boldsymbol{u}_n-\boldsymbol{u}_n^{hk})+L(e_n^{hk};\boldsymbol{u}_n^{hk}-\boldsymbol{v}^h)=L(e_n;\boldsymbol{u}_n-\boldsymbol{u}_n^{hk})-L(e_n^{hk};\boldsymbol{u}_n-\boldsymbol{u}_n^{hk})\\
&\qquad\qquad +L(e_n^{hk};\boldsymbol{u}_n-\boldsymbol{u}_n^{hk})+L(e_n^{hk};\boldsymbol{u}_n^{hk}-\boldsymbol{v}^h)\\
&\qquad\qquad \leq C\|e_n-e_n^{hk}\|_Y\|\boldsymbol{u}_n-\boldsymbol{u}_n^{hk}\|_H+C\|\boldsymbol{u}_n-\boldsymbol{v}^h\|_H\\
&c(e_n^{hk};\boldsymbol{u}_n^{hk},\boldsymbol{v}^h-\boldsymbol{u}_n)=c(e_n^{hk};\boldsymbol{u}_n,\boldsymbol{v}^h-\boldsymbol{u}_n)+c(e_n^{hk};\boldsymbol{u}_n^{hk}-\boldsymbol{u}_n,\boldsymbol{v}^h-\boldsymbol{u}_n)\\
&\qquad\qquad \leq C\left(\|\boldsymbol{u}_n-\boldsymbol{v}^h\|_V+\|\boldsymbol{u}_n-\boldsymbol{u}_n^{hk}\|_V\|\boldsymbol{u}_n-\boldsymbol{v}^h\|_V\right),
\end{aligned}
$$

and applying several times the inequality (2.22) it yields

$$
\|\boldsymbol{u}_n-\boldsymbol{u}_n^{hk}\|_V^2\leq C\left(\|e_n-e_n^{hk}\|_Y^2+\|\boldsymbol{u}_n-\boldsymbol{v}^h\|_V+\|\boldsymbol{u}_n-\boldsymbol{v}^h\|_V^2\right)\quad\forall\boldsymbol{v}^h\in U^h. \tag{2.67}
$$

Combining (2.64) and (2.67) we have, for all $\boldsymbol{v}_n^h\in U^h$,

$$
\begin{aligned}
\|\boldsymbol{u}_n-\boldsymbol{u}_n^{hk}\|_V^2+\|e_n-e_n^{hk}\|_Y^2\leq C\Big(&\|\boldsymbol{u}_n-\boldsymbol{v}_n^h\|_V+\|\boldsymbol{u}_n-\boldsymbol{v}_n^h\|_V^2+\|e_0-e_0^h\|_Y^2\\
&+k^2+\sum_{j=1}^n k\left[\|\dot e_j-\delta e_j\|_Y^2+\|e_{j-1}-e_{j-1}^{hk}\|_Y^2+\|\boldsymbol{u}_{j-1}-\boldsymbol{u}_{j-1}^{hk}\|_V^2+\|\boldsymbol{u}_j-\boldsymbol{u}_{j-1}\|_V^2\right]\Big),
\end{aligned}
$$

and using now a discrete version of Gronwall's inequality (see Lemma 2.1) with

$$
\begin{aligned}
&E_n=\|\boldsymbol{u}_n-\boldsymbol{u}_n^{hk}\|_V^2+\|e_n-e_n^{hk}\|_Y^2,\\
&E_0=g_0=\|\boldsymbol{u}_0-\boldsymbol{u}_0^{hk}\|_V^2+\|e_0-e_0^h\|_Y^2\\
&g_n=\|e_0-e_0^h\|_Y^2+k^2+\sum_{j=1}^n k\left[\|\dot e_j-\delta e_j\|_Y^2+\|\boldsymbol{u}_j-\boldsymbol{u}_{j-1}\|_V^2\right]\\
&\qquad\qquad +\|\boldsymbol{u}_n-\boldsymbol{v}_n^h\|_V+\|\boldsymbol{u}_n-\boldsymbol{v}_n^h\|_V^2,
\end{aligned}
$$

we conclude error estimates (2.20). □

We prove now an error estimates result for the solutions to problems $\mathrm{VP1}_\mu^{cont}$ and $\mathrm{VP1}_\mu^{cont,hk}$.

Theorem 2.8 *Let assumptions (2.6)-(2.9), (2.45) and (2.46) hold. Let* $((\boldsymbol{u}_\mu),(e_\mu))$

and $((\boldsymbol{u}_\mu)^{hk}, (e_\mu)^{hk})$ *denote the respective solutions to problems* $VP1_\mu^{cont}$ *and* $VP1_\mu^{cont,hk}$. *Then we have, for all* $\{\boldsymbol{v}_n^h\}_{n=0}^N \subset V^h$,

$$\begin{aligned}\max_{0\le n\le N}\{\|(e_\mu)_n-(e_\mu)_n^{hk}\|_Y^2+\|(\boldsymbol{u}_\mu)_n-(\boldsymbol{u}_\mu)_n^{hk}\|_V^2\}&\le C\|(e_\mu)_0-(e_\mu)_0^h\|_Y^2\\&+C\Big(k\sum_{j=1}^N\Big[\|(\dot e_\mu)_j-\delta(e_\mu)_j\|_Y^2+\|(\boldsymbol{u}_\mu)_j-(\boldsymbol{u}_\mu)_{j-1}\|_V^2\Big]\\&+k^2+\max_{1\le n\le N}\|(\boldsymbol{u}_\mu)_n-\boldsymbol{v}_n^h\|_V^2+\|(\boldsymbol{u}_\mu)_0-(\boldsymbol{u}_\mu)_0^{hk}\|_V^2\Big),\end{aligned}\tag{2.68}$$

where the notation $\delta(e_\mu)_j=((e_\mu)_j-(e_\mu)_{j-1})/k$ *is employed.*

Proof Again, we recall that an error estimates on the function e_μ were already established:

$$\begin{aligned}\|(e_\mu)_n-(e_\mu)_n^{hk}\|_Y\le C\|(e_\mu)_0-(e_\mu)_0^h\|_Y+Ck+Ck\sum_{j=1}^n\Big[&\|(e_\mu)_{j-1}-(e_\mu)_{j-1}^{hk}\|_Y\\&+\|(\dot e_\mu)_j-\delta(e_\mu)_j\|_Y+\|(\boldsymbol{u}_\mu)_{j-1}-(\boldsymbol{u}_\mu)_{j-1}^{hk}\|_V+\|(\boldsymbol{u}_\mu)_j-(\boldsymbol{u}_\mu)_{j-1}\|_V\Big].\end{aligned}\tag{2.69}$$

Next, let us estimate the numerical errors on the displacement field. Thus, we write equation (2.48) at time $t=t_n$ for all $\boldsymbol{v}=\boldsymbol{v}^h\in V^h\subset V$ and we subtract it to equation (2.61) to obtain,

$$\begin{aligned}&c((e_\mu)_n;(\boldsymbol{u}_\mu)_n,\boldsymbol{v}^h)+j((\boldsymbol{u}_\mu)_n,\boldsymbol{v}^h)-L((e_\mu)_n;\boldsymbol{v}^h)\\&\quad-c((e_\mu)_n^{hk};(\boldsymbol{u}_\mu)_n^{hk},\boldsymbol{v}^h)-j((\boldsymbol{u}_\mu)_n^{hk},\boldsymbol{v}^h)+L((e_\mu)_n^{hk};\boldsymbol{v}^h)=0.\end{aligned}$$

Therefore, we find that, for all $\boldsymbol{v}^h\in V^h$,

$$\begin{aligned}&c((e_\mu)_n;(\boldsymbol{u}_\mu)_n,(\boldsymbol{u}_\mu)_n-(\boldsymbol{u}_\mu)_n^{hk})+j((\boldsymbol{u}_\mu)_n,(\boldsymbol{u}_\mu)_n-(\boldsymbol{u}_\mu)_n^{hk})\\&\quad-L((e_\mu)_n;(\boldsymbol{u}_\mu)_n-(\boldsymbol{u}_\mu)_n^{hk})-c((e_\mu)_n^{hk};(\boldsymbol{u}_\mu)_n^{hk},(\boldsymbol{u}_\mu)_n-(\boldsymbol{u}_\mu)_n^{hk})\\&\quad-j((\boldsymbol{u}_\mu)_n^{hk},(\boldsymbol{u}_\mu)_n-(\boldsymbol{u}_\mu)_n^{hk})+L((e_\mu)_n^{hk};(\boldsymbol{u}_\mu)_n-(\boldsymbol{u}_\mu)_n^{hk})\\&\quad=c((e_\mu)_n;(\boldsymbol{u}_\mu)_n,(\boldsymbol{u}_\mu)_n-\boldsymbol{v}^h)+j((\boldsymbol{u}_\mu)_n,(\boldsymbol{u}_\mu)_n-\boldsymbol{v}^h)-L((e_\mu)_n;(\boldsymbol{u}_\mu)_n-\boldsymbol{v}^h)\\&\quad-c((e_\mu)_n^{hk};(\boldsymbol{u}_\mu)_n^{hk},(\boldsymbol{u}_\mu)_n-\boldsymbol{v}^h)-j((\boldsymbol{u}_\mu)_n^{hk},(\boldsymbol{u}_\mu)_n-\boldsymbol{v}^h)+L((e_\mu)_n^{hk};(\boldsymbol{u}_\mu)_n-\boldsymbol{v}^h).\end{aligned}$$

Since

$$\begin{aligned}
&c((e_\mu)_n;(\boldsymbol{u}_\mu)_n,(\boldsymbol{u}_\mu)_n-\boldsymbol{v}^h)-c((e_\mu)_n^{hk};(\boldsymbol{u}_\mu)_n^{hk},(\boldsymbol{u}_\mu)_n-\boldsymbol{v}^h)\\
&\quad=c((e_\mu)_n^{hk};(\boldsymbol{u}_\mu)_n-(\boldsymbol{u}_\mu)_n^{hk},(\boldsymbol{u}_\mu)_n-\boldsymbol{v}^h)+c((e_\mu)_n;(\boldsymbol{u}_\mu)_n,(\boldsymbol{u}_\mu)_n-\boldsymbol{v}^h)\\
&\quad-c((e_\mu)_n^{hk};(\boldsymbol{u}_\mu)_n,(\boldsymbol{u}_\mu)_n-\boldsymbol{v}^h)\quad\forall\boldsymbol{v}^h\in V^h,
\end{aligned}$$

from assumption (2.6)(d) it follows that

$$c((e_\mu)_n^{hk};(\boldsymbol{u}_\mu)_n-(\boldsymbol{u}_\mu)_n^{hk},(\boldsymbol{u}_\mu)_n-(\boldsymbol{u}_\mu)_n^{hk})\geq m_C\|(\boldsymbol{u}_\mu)_n-(\boldsymbol{u}_\mu)_n^{hk}\|_V^2.$$

Moreover, taking into account that (see (2.46)),

$$\begin{aligned}
&j((\boldsymbol{u}_\mu)_n,(\boldsymbol{u}_\mu)_n-(\boldsymbol{u}_\mu)_n^{hk})-j((\boldsymbol{u}_\mu)_n^{hk},(\boldsymbol{u}_\mu)_n-(\boldsymbol{u}_\mu)_n^{hk})\geq 0,\\
&j((\boldsymbol{u}_\mu)_n,(\boldsymbol{u}_\mu)_n-\boldsymbol{v}^h)-j((\boldsymbol{u}_\mu)_n^{hk},(\boldsymbol{u}_\mu)_n-\boldsymbol{v}^h)\leq C\|(\boldsymbol{u}_\mu)_n-(\boldsymbol{u}_\mu)_n^{hk}\|_V\|(\boldsymbol{u}_\mu)_n-\boldsymbol{v}^h\|_V,
\end{aligned}$$

keeping in mind properties (2.6) and (2.9) we obtain for all $\boldsymbol{v}^h\in V^h$,

$$\begin{aligned}
m_C\|(\boldsymbol{u}_\mu)_n-(\boldsymbol{u}_\mu)_n^{hk}\|_V^2&\leq\|\boldsymbol{f}_n\|_{[C(\overline{\Omega})]^d}\|(e_\mu)_n-(e_\mu)_n^{hk}\|_Y\|(\boldsymbol{u}_\mu)_n-(\boldsymbol{u}_\mu)_n^{hk}\|_V\\
&+\|(\boldsymbol{u}_\mu)_n\|_{[C^1(\overline{\Omega})]^d}\|(e_\mu)_n-(e_\mu)_n^{hk}\|_Y\|(\boldsymbol{u}_\mu)_n-(\boldsymbol{u}_\mu)_n^{hk}\|_V\\
&+M_C\|(\boldsymbol{u}_\mu)_n-(\boldsymbol{u}_\mu)_n^{hk}\|_V\|(\boldsymbol{u}_\mu)_n-\boldsymbol{v}^h\|_V\\
&+\|(\boldsymbol{u}_\mu)_n\|_{[C^1(\overline{\Omega})]^d}\|(e_\mu)_n-(e_\mu)_n^{hk}\|_Y\|(\boldsymbol{u}_\mu)_n-\boldsymbol{v}^h\|_V\\
&+\|\boldsymbol{f}_n\|_{[C(\overline{\Omega})]^d}\|(e_\mu)_n-(e_\mu)_n^{hk}\|_Y\|(\boldsymbol{u}_\mu)_n-\boldsymbol{v}^h\|_V.
\end{aligned}$$

Using again several times the inequality (2.22), we have the following error estimates for the displacement field,

$$\|(\boldsymbol{u}_\mu)_n-(\boldsymbol{u}_\mu)_n^{hk}\|_V^2\leq C(\|(e_\mu)_n-(e_\mu)_n^{hk}\|_Y^2+\|(\boldsymbol{u}_\mu)_n-\boldsymbol{v}^h\|_V^2)\qquad\forall\boldsymbol{v}^h\in V^h.\quad(2.70)$$

Combining (2.69) and (2.70), we find that

$$\begin{aligned}\|(e_\mu)_n-(e_\mu)_n^{hk}\|_Y^2+\|(\boldsymbol{u}_\mu)_n-(\boldsymbol{u}_\mu)_n^{hk}\|_V^2 &\le C\|(e_\mu)_0-(e_\mu)_0^h\|_Y^2+C\|(\boldsymbol{u}_\mu)_0-(\boldsymbol{u}_\mu)_0^{hk}\|_V^2\\ &+Ck^2+Ck\sum_{j=1}^{n}\Big[\|(e_\mu)_{j-1}-(e_\mu)_{j-1}^{hk}\|_Y^2+\|(\boldsymbol{u}_\mu)_j-(\boldsymbol{u}_\mu)_{j-1}\|_V^2+\|\dot{(e_\mu)}_j-\delta(e_\mu)_j\|_Y^2\\ &+\|(\boldsymbol{u}_\mu)_{j-1}-(\boldsymbol{u}_\mu)_{j-1}^{hk}\|_V^2\Big]+C\|(\boldsymbol{u}_\mu)_n-\boldsymbol{v}_n^h\|_V^2\quad\forall\boldsymbol{v}_n^h\in V^h.\end{aligned}$$

Finally, using a discrete version of Gronwall's inequality (see Lemma 2.1), it leads to (2.68). □

Error estimates (2.63) and (2.68) are the basis for the convergence rate of the algorithm.

Let Ω be a polyhedral domain and denote by $\mathcal{T}^h$ a triangulation of $\overline{\Omega}$ compatible with the partition of the boundary $\Gamma=\partial\Omega$ into Γ_D, Γ_N and Γ_C.

Let V^h and B^h consist of continuous and piecewise affine functions and piecewise constant functions; that is,

$$V^h=\{\boldsymbol{v}^h\in[C(\overline{\Omega})]^d\ ;\ \boldsymbol{v}^h_{|_{Tr}}\in[P_1(Tr)]^d,\ Tr\in\mathcal{T}^h,\quad \boldsymbol{v}^h=\boldsymbol{0}\quad\text{on}\quad\Gamma_D\},\tag{2.71}$$

$$B^h=\{\xi^h\in L^\infty(\Omega)\ ;\ \xi^h_{|_{Tr}}\in P_0(Tr),\quad Tr\in\mathcal{T}^h\},\tag{2.72}$$

and define the discrete initial condition by $e_0^h=\pi^h e_0$ and $(e_\mu)_0^h=\pi^h(e_\mu)_0$, where $\pi^h: C(\overline{\Omega})\to B^h$ is the standard finite element interpolation operator (see, e.g., [13]). Assume the additional regularity conditions

$$\begin{aligned}&e,e_\mu\in C([0,T];H^1(\Omega))\cap H^2(0,T;Y),\\ &\boldsymbol{u},\boldsymbol{u}_\mu\in C^1([0,T];V)\cap C([0,T];[H^2(\Omega)]^d).\end{aligned}\tag{2.73}$$

We have the following corollary which states the linear convergence of the solution to Problem VP1^{cont,hk} under adequate regularity conditions.

Corollary 2.2 *Let the assumptions of Theorem 2.7 hold. Under the additional regularity condition (2.73), the solution to the discrete scheme VP1^{cont,hk} verifies*

$$\max_{0\leq n\leq N}\{\|\boldsymbol{u}_n-\boldsymbol{u}_n^{hk}\|_V+\|e_n-e_n^{hk}\|_Y\}\leq C(h^{1/2}+k), \tag{2.74}$$

where $C>0$ is a positive constant independent of h and k.

Moreover, if we also assume that

$$\sigma_\nu\in L^\infty(0,T;L^2(\Gamma_C)),\quad u_\nu\in L^\infty(0,T;H^2(\Gamma_C)),$$

the fully discrete scheme is linearly convergent; that is, we derive the optimal error order estimate

$$\max_{0\leq n\leq N}\{\|\boldsymbol{u}_n-\boldsymbol{u}_n^{hk}\|_V+\|e_n-e_n^{hk}\|_Y\}\leq C(h+k). \tag{2.75}$$

The proof of Corollary 2.2 is done taking into account the well-known approximation properties of the finite element space V^h (see [13]),

$$\max_{1\leq n\leq N}\inf_{v_n^h\in V^h}\|\boldsymbol{u}_n-\boldsymbol{v}_n^h\|_V\leq Ch\|\boldsymbol{u}\|_{C([0,T];[H^2(\Omega)]^d)},$$

the straighforward estimates

$$k\sum_{j=1}^{N}\left[\|\dot{e}_j-\delta e_j\|_Y^2+\|\boldsymbol{u}_j-\boldsymbol{u}_{j-1}\|_V^2\right]\leq Ck^2\left(\|e\|_{H^2(0,T;Y)}^2+\|\boldsymbol{u}\|_{C^1([0,T];V)}^2\right),$$

and the definition of the discrete initial condition e_0^h,

$$\|e_0-e_0^h\|_Y^2\leq Ch^2\|e\|_{C([0,T];H^1(\Omega))}^2.$$

Finally, proceeding as in (2.67) we easily find that

$$\|\boldsymbol{u}_0-\boldsymbol{u}_0^{hk}\|_V^2\leq C\left(\|e_0-e_0^h\|_Y^2+\|\boldsymbol{u}_0-\boldsymbol{v}^h\|_V+\|\boldsymbol{u}_0-\boldsymbol{v}^h\|_V^2\right)\quad\forall\boldsymbol{v}^h\in U^h,$$

and, from the previous estimates, we deduce (2.74).

The second part of Corollary 2.2, the linear convergence stated in (2.75), is obtained remaining the term on the contact boundary in the variational problem. Then, the variational inequality (2.65) is replaced by

$$c(e_n;\boldsymbol{u}_n,\boldsymbol{u}_n^{hk}-\boldsymbol{u}_n)=L(e_n;\boldsymbol{u}_n^{hk}-\boldsymbol{u}_n)+\int_{\Gamma_C}\sigma_\nu((\boldsymbol{u}_n^{hk})_\nu-(\boldsymbol{u}_n)_\nu)d\Gamma,$$

and taking into account the regularity $\sigma_\nu\in L^\infty(0,T;L^2(\Gamma_C))$ we obtain

$$\int_{\Gamma_C}\sigma_\nu((\boldsymbol{u}_n^{hk})_\nu-(\boldsymbol{u}_n)_\nu)d\Gamma\leq\|\sigma_\nu\|_{L^2(\Gamma_C)}\|((\boldsymbol{u}_n^{hk})_\nu-(\boldsymbol{u}_n)_\nu)\cdot\boldsymbol{\nu}\|_{L^2(\Gamma_C)}.$$

Finally applying the estimate (see again [13]),

$$\max_{1\leq n\leq N}\inf_{v_n^h\in V^h}\|(\boldsymbol{u}_n-\boldsymbol{v}_n^h)\cdot\boldsymbol{\nu}\|_{L^2(\Gamma_C)}\leq Ch^2\|\boldsymbol{u}\|_{L^\infty(0,T;H^2(\Gamma_C))}$$

we obtain (2.75). □

Arguing in a analogous way, we also have the following corollary for Theorem 2.8.

Corollary 2.3 *Let the assumptions of Theorem 2.8 hold. Under the additional regularity condition (2.73), the fully discrete scheme $VP1_\mu^{hk}$ is linearly convergent, that is, there exist a positive constant C, independent of h and k, such that*

$$\max_{0\leq n\leq N}\{\|(\boldsymbol{u}_\mu)_n-(\boldsymbol{u}_\mu)_n^{hk}\|_V+\|(e_\mu)_n-(e_\mu)_n^{hk}\|_Y\}\leq C(h+k). \tag{2.76}$$

Its proof is obtained proceeding as for Corollary 2.2.

2.3.3 Numerical results

In this section we first describe shortly the numerical scheme which we have implemented to solve both contact problems, and then we present some numerical examples

to exhibit its accuracy and its performance in one, two and three dimensions.

Numerical scheme

To approximate the spaces V and $L^\infty(\Omega)$ we use the finite element spaces V^h and B^h defined by (2.71) and (2.72), respectively.

First, for Problem $\mathrm{VP1}_\mu^{cont,hk}$, $(\boldsymbol{u}_\mu)_n^{hk}$ is obtained solving the following nonlinear variational equation,

$$(\boldsymbol{u}_\mu)_n^{hk} \in V^h, \quad c((e_\mu)_n^{hk}; (\boldsymbol{u}_\mu)_n^{hk}, \boldsymbol{v}^h) + j((\boldsymbol{u}_\mu)_n^{hk}, \boldsymbol{v}^h) = L((e_\mu)_n^{hk}; \boldsymbol{v}^h) \quad \forall \boldsymbol{v}^h \in V^h.$$

This leads to a nonlinear variational equation which was solved by using a penalty-duality algorithm introduced in [9] and already applied in other contact problems.

Next, let $n \in \{1, \ldots, N\}$ and assume that $(\boldsymbol{u}_\mu)_{n-1}^{hk}$ and $(e_\mu)_{n-1}^{hk}$ are known. The discrete bone remodeling function $(e_\mu)_n^{hk}$ is given by

$$(e_\mu)_n^{hk} = (e_\mu)_{n-1}^{hk} + ka((e_\mu)_{n-1}^{hk}) + k\mathcal{A}((e_\mu)_{n-1}^{hk}) \,:\, \boldsymbol{\varepsilon}((\boldsymbol{u}_\mu)_{n-1}^{hk}).$$

Problem $\mathrm{VP1}^{cont,hk}$ was solved in an analogous way. The discrete displacement field $\boldsymbol{u}_n^{hk}$ is obtained solving the following elliptic variational inequality,

$$\boldsymbol{u}_n^{hk} \in U^h, \quad c(e_n^{hk}; \boldsymbol{u}_n^{hk}, \boldsymbol{v}^h - \boldsymbol{u}_n^{hk}) \geq L(e_n^{hk}; \boldsymbol{v}^h - \boldsymbol{u}_n^{hk}) \quad \forall \boldsymbol{v}^h \in U^h.$$

Again, the above penalty-duality algorithm was applied for solving it.

Next, let $n \in \{1, \ldots, N\}$ and assume that $\boldsymbol{u}_{n-1}^{hk}$ and e_{n-1}^{hk} are known. The discrete bone remodeling function is given by

$$e_n^{hk} = e_{n-1}^{hk} + ka(e_{n-1}^{hk}) + k\mathcal{A}(e_{n-1}^{hk}) \,:\, \boldsymbol{\varepsilon}(\boldsymbol{u}_{n-1}^{hk}).$$

A one-dimensional example: the numerical convergence

As a first one-dimensional example, the following problem is considered.

Problem P1^{cont}-1D. *Find a displacement field* $u : [0,1] \times [0,1] \to \mathbb{R}$ *and a bone remodeling function* $e : [0,1] \times [0,1] \to \mathbb{R}$ *such that*

$$
\begin{aligned}
&-\frac{\partial}{\partial x}\left(e\frac{\partial u}{\partial x}\right)(x,t) = \frac{1740}{2}\,(\frac{1}{2}+e(x,t)) \\
&\qquad\qquad \times\frac{-4xt\,e^{2t}-2e^{2t}(2xt+1)}{870+1740e^{t}(2xt+1)} \quad x\in(0,1),\, t\in(0,1),\\
&\dot{e}(x,t) = e(x,t)+\frac{\partial u}{\partial x}(x,t) \quad x\in[0,1],\, t\in[0,1],\\
&u(0,t) = 0 \quad t\in(0,1),\\
&\left(e\frac{\partial u}{\partial x}\right)(1,t) = -1000\,\max\{u(1,t),0\} \quad t\in(0,1),\\
&e(1,t)\frac{\partial u}{\partial x}(1,t) = 2\,e^{2t}(2t+1) \quad t\in(0,1),\\
&e(x,0) = 1 \quad x\in[0,1],
\end{aligned}
$$

which corresponds to consider Problem P1$^{cont}_{\mu}$ with the following data:

$$
\begin{aligned}
&\Omega=(0,1),\quad \Gamma_D=\{0\},\quad \Gamma_N=\emptyset,\quad \Gamma_C=\{1\},\quad T=1\,s,\quad \mathcal{C}(e)=\frac{e}{\xi_0+e},\\
&a(e)=e,\quad \mathcal{A}(e)=1,\quad \xi_0=\frac{1}{2},\quad \gamma=1740,\\
&f(x,t)=\frac{1740}{2}\,(\frac{1}{2}+e(x,t))\frac{-4xt\,e^{2t}-2e^{2t}(2xt+1)}{870+1740e^{t}(2xt+1)} \quad x\in[0,1],\, t\in[0,1],\\
&p_\nu(r)=\frac{1}{\mu}\max\{r,0\},\quad \mu=10^{-3},\quad s=0\,m.
\end{aligned}
$$

We notice that coefficients $\mathcal{C}(e)$ and $a(e)$ do not satisfy properties (2.6) and (2.7) since they are not bounded. However, this is easily done by using truncation operator Φ_L. Anyway, we assume that constant L is large enough ($L = 10^6$), and the truncation does not modify the results presented below.

Our aim here is to show the numerical convergence of the algorithm. Therefore, several uniform partitions of both the time interval and the domain, dividing $\Omega = (0,1)$ into n segments, have been performed. We note that the spatial discretization

parameter h equals to $\frac{1}{n}$, and we used the solution obtained with $h = \frac{1}{4096}$ and $k = 0.0001$ as the "exact solution".

The numerical errors, given by

$$E^{hk} = \max_{0 \le n \le N} \left\{ \|(\boldsymbol{u}_\mu)_n - (\boldsymbol{u}_\mu)_n^{hk}\|_V + \|(e_\mu)_n - (e_\mu)_n^{hk}\|_Y \right\}$$

and obtained for different discretization parameters h and k, are depicted in Table 2.2. Moreover, the evolution of the error depending on $h + k$ is plotted in Figure 2.18. We notice that the convergence of the algorithm is clearly observed, and the linear convergence, stated in Corollary 2.3, is also achieved.

$n \downarrow k \rightarrow$	0.1	0.05	0.01	0.005	0.001	0.0005	0.0001
2	0.954803	0.911805	0.899980	0.900148	0.900290	0.900192	0.900152
4	0.663977	0.599267	0.580571	0.580788	0.580943	0.580802	0.580754
8	0.505779	0.416137	0.388340	0.388659	0.388843	0.388636	0.388569
16	0.423963	0.306701	0.266201	0.266647	0.266883	0.266581	0.266486
32	0.382092	0.243081	0.185913	0.185691	0.185992	0.185558	0.185421
64	0.361165	0.206235	0.131184	0.130510	0.130847	0.130224	0.130028
128	0.352379	0.186833	0.093746	0.092400	0.092719	0.091829	0.091547

Table 2.2: Example **P1**^{cont}**-1D**: Numerical errors for some h and k.

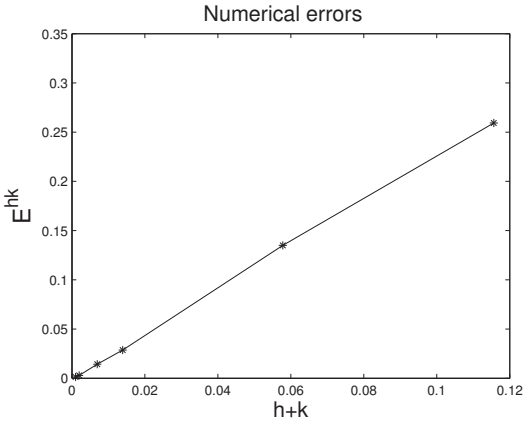

Figure 2.18: Example **P1**^{cont}**-1D**: Asymptotic constant of error.

Numerical results in two-dimensional problems: a compression force

As a two-dimensional example, we consider the domain $\Omega = (0, 6) \times (0, 1.2)$ which is clamped on the boundary part $\Gamma_D = \{0\} \times [0, 1.2]$. No volume forces are supposed to act in the body, a linearly increasing surface force acts on the boundary part $[0, 6] \times \{1.2\}$ and, finally, the body is supposed to be in contact with a rigid obstacle on the contact boundary $\Gamma_C = [0, 6] \times \{0\}$ (see Figure 2.19).

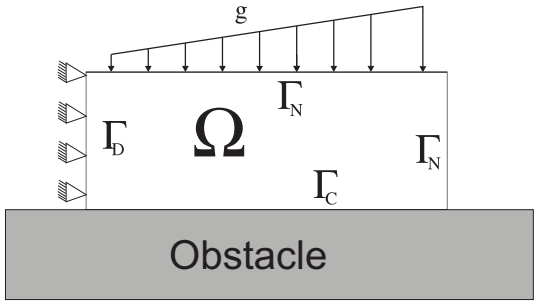

Figure 2.19: Example **P1**^{cont}**-2D**: Physical setting.

The following data were employed in this example:

$$T = 78\,\text{days}, \quad \mu = 0, \quad s = 0\,m, \quad \gamma = 1740\,Kg/m^3,$$
$$\boldsymbol{f} = \mathbf{0}\,N/m^3, \quad \boldsymbol{g}(x, y, t) = (0, -5x)\,N/m^2.$$

The bone remodeling coefficients and elasticity parameters can be seen in Section 2.2.3. Moreover, we assume that the initial bone remodeling function is given by

$$e_0(x, y) = 0.01 sin(\frac{\pi y}{3}) \quad \forall (x, y) \in (0, 6) \times (0, 1.2).$$

Taking $k = 0.01$ as the time discretization parameter, the displacements field (multiplied by 10) and the reference configuration are plotted in Figure 2.20 at initial time (left) and after 78 days (right). We observe that the deformation has decreased and that no penetration into the obstacle has been produced, because we are considering a rigid obstacle. Moreover, in Figure 2.21 the bone remodeling function is shown at initial time (left) and at final time (right). As can be seen, the bone remodeling func-

Figure 2.20: Example **P1**^{cont}**-2D**: Initial configuration and displacements at initial time (left) and after 78 days (right).

tion is positive on the right part which caused that the stiffness increases and so the displacements decrease there.

Figure 2.21: Example **P1**^{cont}**-2D**: Bone remodeling function at initial time (left) and after 78 days (right).

In order to show the differences when the obstacle is assumed deformable or rigid, we have plotted in Figure 2.22 the displacement field, multiplied by 10 (left), and the bone remodeling function (right) for a deformable obstacle with a deformability coefficient $\mu = 0.5$ at final time. We notice that, if we assume that the obstacle is deformable, a clear penetration is produced into the obstacle and the bone remodeling function reaches smaller values on the left part.

Figure 2.22: Example **P1**^{cont}**-2D**: Displacements at final time (left) and the bone remodeling function (right) for a deformable obstacle.

Moreover, the transverse mechanical displacement of the contact boundary is plotted in Figure 2.23 at final time for different values of μ. As can be seen, the displacements on the left node is zero because of the Dirichlet condition and on the others nodes converges to zero when $\mu \to 0$.

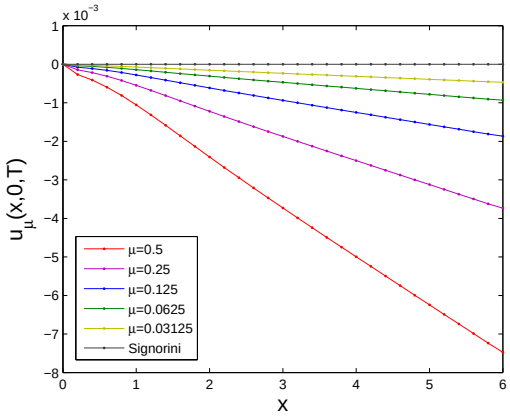

Figure 2.23: Example **P1**^{cont}**-2D**: Displacements of the contact boundary depending on μ.

Finally, in Figure 2.24 we depict the convergence of the bone remodeling function, assuming the contact with a deformable obstacle for different deformability coefficients. For this function, the differences are located on the left part. As can be seen, if the obstacle is assumed deformable, then the bone remodeling function has smaller values, even negative. We can also observe the convergence to the solution of the Signorini

problem.

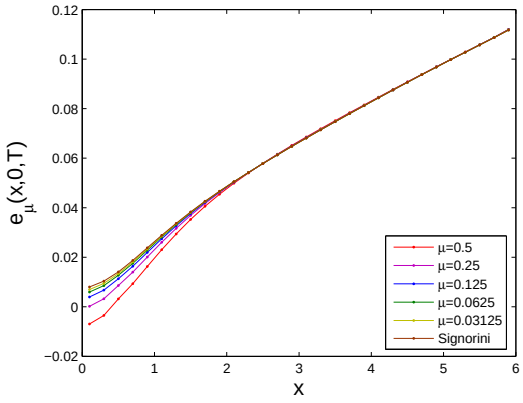

Figure 2.24: Example **P1**^{cont}**-2D**: Bone remodeling function, on the contact boundary, depending on μ.

Chapter 3

Bone remodeling induced by a local stimulus

In this chapter, we use the bone remodeling model analyzed in [66] by Weinans, Huiskes and Grootenboer in 1992, which is based on the principle that bone remodeling is induced by a local mechanical signal which activates the regulating cells (osteoblasts and osteoclasts); that is, the bone has sensors, which can detect a mechanical stimulus, and, depending on its magnitude, cause local bone adaptations. The main idea of this model is to use the apparent density as the characterization of the internal morphology.

Here, our aim is to continue [66], providing the numerical analysis of a fully discrete algorithm, proving an error estimate result, establishing its linear convergence under some regularity conditions and performing some numerical simulations. Moreover, we notice that the results provided below have been published in [23] and, although we did not include it in this Ph.D. thesis for the clarity of presentation, the numerical analysis of a contact problem between a bone modeled with this law and a deformable obstacle was recently submitted (see [29]).

3.1 The model

According to [66], the rate of change of the apparent density in a bone, is given by a function $\rho = \rho(\boldsymbol{x}, t)$ and described as an objective function which depends on a particular stimulus at point $\boldsymbol{x}$.

In the previous chapter it was assumed a relationship in which the adaptation of the bone was coupled directly to deviations of the strain tensor. This implicates that the normal stimulus distribution must be known or be determined from a normal equilibrium density distribution. However, the original ideas of Wolff implied more issues than just this notion of bone remodeling due to deviations in its normal stress environment. Therefore, following the ideas of Fyhrie and Carter (see [40]), a different definition for the mechanical stimulus is considered by Weinans et al. in [66]. They postulate that this stimulus is related to the Strain Energy Density (SED) and the bone would adopt its apparent density locally for any loading environment, in order to normalize a predestined effective stress value.

The SED value in the trabeculae was approximated by U/ρ, where U is the apparent SED in the bone when it is assumed continuous and ρ, as mentioned above, is the apparent density. Hence, U/ρ represents the strain energy per unit of bone mass. Moreover, since this function is a remodeling objective, it is assumed that this goal is only valid for $\rho_a \leq \rho \leq \rho_b$, where ρ_a represents the minimal density corresponding to the reabsorved bone and ρ_b is the maximal density of cortical bone. We notice that in all the examples presented in Section 3.4, we have used the values $\rho_a = 0.01\, g/cm^3$ and $\rho_b = 1.74\, g/cm^3$ (see [66]). Thus, such a remodeling objective is incorporated into the time-dependent equation for the apparent density and it leads to the following nonlinear first-order ODE for the apparent density (see [8, 47, 49, 65]):

$$\dot{\rho} = B\left(\frac{U(\boldsymbol{\sigma}(\boldsymbol{u}), \boldsymbol{\varepsilon}(\boldsymbol{u}))}{\rho} - S_r\right), \quad \rho_a \leq \rho \leq \rho_b,$$

where B and S_r are given constants and U is the mechanical stimulus given by

$$U(\boldsymbol{\sigma}(\boldsymbol{u}), \boldsymbol{\varepsilon}(\boldsymbol{u})) = \frac{1}{2}\boldsymbol{\sigma}(\boldsymbol{u}) \,:\, \boldsymbol{\varepsilon}(\boldsymbol{u}).$$

This equation means that the points in which the density reaches the minimum or maximum value, the remodeling process stops. On the other points, the system is in equilibrium when the stimulus reaches the reference value S_r.

According to [66], the bone is assumed elastic and the constitutive law is written as follows,

$$\boldsymbol{\sigma} = \boldsymbol{\sigma}(\boldsymbol{u}) = 2\,\mu(\rho)\boldsymbol{\varepsilon}(\boldsymbol{u}) + \lambda(\rho)\mathrm{Div}\,(\boldsymbol{u})\mathcal{I},$$

where $\mathcal{I}$ denotes the identity operator in $\mathbb{S}^d$, Div represents the divergence operator and $\mu(\rho)$ and $\lambda(\rho)$ are Lame's coefficients of the material, which are assumed to depend on the apparent density of the bone ρ. We recall that these coefficients are related to Young's modulus $E(\rho)$ and Poisson's ratio $\kappa(\rho)$ through the relations:

$$\mu(\rho) = \frac{E(\rho)}{2(1+\kappa(\rho))},$$

and

$$\lambda(\rho) = \frac{\kappa(\rho)E(\rho)}{1-\kappa^2(\rho)}$$

if the plane stress hypothesis is assumed, or

$$\lambda(\rho) = \frac{\kappa(\rho)E(\rho)}{(1+\kappa(\rho))(1-2\kappa(\rho))}$$

if the plane strain hypothesis is used or if the three-dimensional case is considered. Notice that we are using the constitutive law for elastic materials but, in this case, we assume the Poisson's ratio is independent of ρ, $\kappa(\rho) = \kappa$, and the following equation is used for Young's modulus depending on the apparent density:

$$E(\rho) = M\rho^{\gamma},$$

where M and γ are positive constants which characterize the bone behavior.

Finally, as usual in bone remodeling models, the process is assumed quasistatic and therefore, the inertia effects are neglected. Moreover, let ρ_0 denote the initial apparent density function.

3.2 Mechanical and variational problems

From the constitutive laws introduced in the previous section, we obtain the following mechanical problem, derived from the continuum mechanics laws in the framework of the small displacements theory (see [66]).

Problem P2. *Find a displacement field* $\boldsymbol{u} : \overline{\Omega} \times [0,T] \to \mathbb{R}^d$ *and an apparent density function* $\rho : \overline{\Omega} \times [0,T] \to [\rho_a, \rho_b]$ *such that* $\rho(0) = \rho_0$ *and,*

$$\dot{\rho} = B\left(\frac{U(\boldsymbol{\sigma}(\boldsymbol{u}), \boldsymbol{\varepsilon}(\boldsymbol{u}))}{\rho} - S_r\right) \quad in \quad \Omega \times (0,T), \tag{3.1}$$

$$-\mathrm{Div}\,\boldsymbol{\sigma}(\boldsymbol{u}) = \boldsymbol{f} \quad in \quad \Omega \times (0,T), \tag{3.2}$$

$$\boldsymbol{u} = \boldsymbol{0} \quad on \quad \Gamma_D \times (0,T), \tag{3.3}$$

$$\boldsymbol{\sigma\nu} = \boldsymbol{g} \quad on \quad \Gamma_N \times (0,T), \tag{3.4}$$

where Lame's coefficients $\lambda(\rho)$ *and* $\mu(\rho)$ *were defined above and the stress field* $\boldsymbol{\sigma}(\boldsymbol{u}) : \overline{\Omega} \times [0,T] \to \mathbb{S}^d$ *is given by*

$$\boldsymbol{\sigma}(\boldsymbol{u}) = 2\,\mu(\rho)\boldsymbol{\varepsilon}(\boldsymbol{u}) + \lambda(\rho)\mathrm{Div}\,(\boldsymbol{u})\mathcal{I} \quad in \quad \overline{\Omega} \times [0,T]. \tag{3.5}$$

We turn now to obtain a variational formulation of Problem P2. As in the previous chapter, let us denote $Y = L^2(\Omega)$ and $H = [L^2(\Omega)]^d$, and define the following spaces

equipped with the product norms derived from usual norms in Sobolev spaces:

$$V = \{\boldsymbol{v} = (v_i)_{i=1}^d \in [H^1(\Omega)]^d \ ; \ \boldsymbol{v} = \boldsymbol{0} \quad \text{on} \quad \Gamma_D\},$$

$$Q = \{\boldsymbol{\tau} = (\tau_{ij})_{i,j=1}^d \in [L^2(\Omega)]^{d\times d} \ ; \ \tau_{ij} = \tau_{ji}, \quad 1 \le i,j \le d\}.$$

The following assumptions are required on the problem data.

(i) The density forces have the regularity:

$$\boldsymbol{f} \in C([0,T];[C(\overline{\Omega})]^d), \quad \boldsymbol{g} \in C([0,T];[C(\overline{\Gamma_N})]^d). \tag{3.6}$$

(ii) The initial apparent density ρ_0 satisfies the following conditions:

$$\rho_0 \in C(\overline{\Omega}), \quad \rho_a \le \rho_0(\boldsymbol{x}) \le \rho_b \quad \text{for all} \quad \boldsymbol{x} \in \overline{\Omega}. \tag{3.7}$$

For every $\rho \in L^\infty(\Omega)$, let us define the following bilinear form $c(\rho;\cdot,\cdot) : V \times V \to \mathbb{R}$ given by

$$c(\rho;\boldsymbol{u},\boldsymbol{v}) = \int_\Omega 2\mu(\rho)\boldsymbol{\varepsilon}(\boldsymbol{u}) \ : \boldsymbol{\varepsilon}(\boldsymbol{v}) + \lambda(\rho)\mathrm{Tr}(\boldsymbol{\varepsilon}(\boldsymbol{u}))\mathrm{Tr}(\boldsymbol{\varepsilon}(\boldsymbol{v}))\, d\boldsymbol{x}, \quad \forall \boldsymbol{u},\boldsymbol{v} \in V,$$

where Tr denotes the trace operator defined as $\mathrm{Tr}(\boldsymbol{\tau}) = \sum_{i=1}^d \tau_{ii}$ for all $\boldsymbol{\tau} = (\tau_{ij})_{i,j=1}^d$.

Also we introduce the linear form $L : V \to \mathbb{R}$ given by

$$L(\boldsymbol{v}) = \int_\Omega \boldsymbol{f}\cdot\boldsymbol{v}\, d\boldsymbol{x} + \int_{\Gamma_N} \boldsymbol{g}\cdot\boldsymbol{v}\, d\Gamma, \quad \forall \boldsymbol{v} \in V.$$

Applying Green's formula, we derive the following variational equation for the displacement field:

$$\boldsymbol{u} \in V \quad c(\rho(t);\boldsymbol{u}(t),\boldsymbol{v}) = L(\boldsymbol{v}), \quad \forall \boldsymbol{v} \in V.$$

Now, we will try to obtain an equivalent expression for equation (3.1), incorporating

the restriction $\rho_a \leq \rho \leq \rho_b$. In order to do so, we recall the following definition (see [45]).

Definition 3.1 *Let X be a Hilbert space and $\psi : X \to (-\infty, \infty]$. The function ψ is said to be subdifferentiable in $\boldsymbol{u} \in X$ if $\psi(\boldsymbol{u}) < +\infty$ and there exists $G(\boldsymbol{u}) \in X$ such that*

$$\psi(\boldsymbol{v}) \geq \psi(\boldsymbol{u}) + (G(\boldsymbol{u}), \boldsymbol{v} - \boldsymbol{u})_X \qquad \forall \boldsymbol{v} \in X.$$

The element $G(\boldsymbol{u})$ is known as the subgradient of ψ in $\boldsymbol{u}$. The set of subgradients of ψ in $\boldsymbol{u} \in X$ is named the subdifferential of ψ in $\boldsymbol{u}$, and it is denoted by $\partial\psi(\boldsymbol{u})$.

Denoting by $\partial I_{[\rho_a,\rho_b]}$ the subdifferential of the indicator function $I_{[\rho_a,\rho_b]}$ of the interval $[\rho_a, \rho_b]$ we can write equation (3.1) in the following weak form,

$$\dot{\rho} - B\left(\frac{U(\boldsymbol{\sigma}(\boldsymbol{u}), \boldsymbol{\varepsilon}(\boldsymbol{u}))}{\rho} - S_r\right) + \partial I_{[\rho_a,\rho_b]}(\rho) \ni 0.$$

In order to simplify the writing, we define the function $\Phi : Y \times Q \times Q \to Y$ given by

$$\Phi(\rho, \boldsymbol{\sigma}, \boldsymbol{\tau}) = B\left(\frac{U(\boldsymbol{\sigma}, \boldsymbol{\tau})}{\rho} - S_r\right),$$

where we recall that $U(\boldsymbol{\sigma}, \boldsymbol{\tau}) = \dfrac{1}{2}\boldsymbol{\sigma} : \boldsymbol{\tau}$.

Since this function has a quadratic behavior with respect to $\boldsymbol{\tau}$, a truncation operator should be employed and therefore, this function must be redefined in the form,

$$\Phi(\rho, \boldsymbol{\sigma}, \boldsymbol{\tau}) = B\left(\frac{U(\boldsymbol{\sigma}, \mathcal{L}(\boldsymbol{\tau}))}{\rho} - S_r\right), \tag{3.8}$$

where the truncation operator $\mathcal{L} : \mathbb{S}^d \to \mathbb{S}^d$ is defined in the following form, where $L > 0$ is a given positive constant,

$$(\mathcal{L}(\boldsymbol{\tau}))_{ij} = \begin{cases} L & \text{if} \quad \tau_{ij} > L, \\ \tau_{ij} & \text{if} \quad \tau_{ij} \in [-L, L], \\ -L & \text{if} \quad \tau_{ij} < -L. \end{cases}$$

Indeed, we need to control the bounds of $\boldsymbol{\varepsilon}(\boldsymbol{u})$ and this formulation does not pose any practical limitations on the applicability of the model. Moreover, it seems to be reasonable from the physical point of view because this problem is considered within the small displacement theory.

Finally, let us define the convex set of admissible apparent density functions,

$$K = \{\xi \in Y \,;\, \rho_a \leq \xi \leq \rho_b, \text{ a.e. in } \Omega\}.$$

From the definition of the subdifferential operator, we obtain the following elliptic variational inequality:

$$\rho \in [\rho_a, \rho_b] \quad (\dot{\rho}(t), \xi - \rho(t))_Y \geq (\Phi(\rho(t), \boldsymbol{\sigma}(\boldsymbol{u}(t)), \boldsymbol{\varepsilon}(\boldsymbol{u}(t))), \xi - \rho(t))_Y \quad \forall \xi \in K.$$

Gathering the variational equation obtained for the displacement field and the variational inequality for the apparent density function, we derive the following variational formulation for the mechanical Problem P2.

Problem VP2. *Find a displacement field* $\boldsymbol{u} : [0,T] \to V$ *and an apparent density function* $\rho : [0,T] \to K$ *such that* $\rho(0) = \rho_0$ *and for a.e.* $t \in (0,T)$,

$$c(\rho(t); \boldsymbol{u}(t), \boldsymbol{v}) = L(\boldsymbol{v}), \quad \forall \boldsymbol{v} \in V, \tag{3.9}$$

$$(\dot{\rho}(t), \xi - \rho(t))_Y \geq (\Phi(\rho(t), \boldsymbol{\sigma}(\boldsymbol{u}(t)), \boldsymbol{\varepsilon}(\boldsymbol{u}(t))), \xi - \rho(t))_Y, \quad \forall \xi \in K, \tag{3.10}$$

where the function Φ *is given in (3.8) and the stress field* $\boldsymbol{\sigma}(\boldsymbol{u}(t))$ *is obtained from (3.5).*

We notice that the existence of a unique solution to Problem VP2 has not been proved yet. Although we observe that there is a clear similarity between this kind of problems and the damage problem considered, for instance, in [12], we remark that such result is not straightforward because of the absence of the diffusion term. This makes the problem more difficult. We think that similar results to those applied in [57] for another bone remodeling problem could be used here; however, this problem

remains still open. Recently, Fernández and Kuttler proved in [24] an existence and uniqueness result for a related problem, obtained by using convolution operators, but the arguments applied there can not be extended to the analysis of Problem VP2.

3.3 Numerical analysis of a fully discrete scheme

In this section, we introduce a finite element algorithm for approximating solutions to variational problem VP2. Its discretization is done in two steps. First, we consider the finite element spaces $V^h \subset V$, $Q^h \subset Q$ and $B^h \subset Y$ given by

$$V^h = \{\boldsymbol{w}^h \in [C(\overline{\Omega})]^d \,;\, \boldsymbol{w}^h_{|_T} \in [P_1(T)]^d,\, T \in \mathcal{T}^h, \quad \boldsymbol{w}^h = \boldsymbol{0} \text{ on } \Gamma_D\}, \tag{3.11}$$

$$Q^h = \{\boldsymbol{\tau}^h \in [L^2(\Omega)]^{d\times d} \,;\, \boldsymbol{\tau}^h_{|_T} \in [P_0(T)]^{d\times d},\, T \in \mathcal{T}^h\}, \tag{3.12}$$

$$B^h = \{\xi^h \in Y \,;\, \xi^h_{|_T} \in P_0(T), \quad T \in \mathcal{T}^h\}, \tag{3.13}$$

where Ω is assumed to be a polyhedral domain, $\mathcal{T}^h$ denotes a triangulation of $\overline{\Omega}$ compatible with the partition of the boundary $\Gamma = \partial\Omega$ into Γ_D and Γ_N, and $P_q(T)$, $q = 0, 1$, represents the space of polynomials of global degree less or equal to q in T. Here, $h > 0$ denotes the spatial discretization parameter. Moreover, we define the discrete convex set of admissible apparent density functions $K^h = K \cap B^h$; that is,

$$K^h = \{\xi^h \in B^h \,;\, \rho_a \leq \xi^h \leq \rho_b \quad \text{in} \quad \Omega\}.$$

Secondly, the time derivatives are discretized by using a uniform partition of the time interval $[0, T]$, denoted by $0 = t_0 < t_1 < \ldots < t_N = T$, and let k be the time step size, $k = T/N$. Moreover, for a continuous function $f(t)$ we denote $f_n = f(t_n)$.

Using the forward Euler scheme, the fully discrete approximation of Problem VP2 is the following.

Problem VP2^{hk}. *Find a discrete displacement field* $\boldsymbol{u}^{hk} = \{\boldsymbol{u}^{hk}_n\}_{n=0}^N \subset V^h$ *and a discrete apparent density function* $\rho^{hk} = \{\rho^{hk}_n\}_{n=0}^N \subset K^h$ *such that for all* $\boldsymbol{v}^h \in V^h$ *and*

$\xi^h \in K^h$,

$$c(\rho_n^{hk}; \boldsymbol{u}_n^{hk}, \boldsymbol{v}^h) = L(\boldsymbol{v}^h), \quad n = 0, 1, \ldots, N, \tag{3.14}$$

$$\left(\frac{\rho_n^{hk} - \rho_{n-1}^{hk}}{k}, \xi^h - \rho_n^{hk}\right)_Y \geq \left(\Phi(\rho_{n-1}^{hk}, \boldsymbol{\sigma}_{n-1}^{hk}, \boldsymbol{\varepsilon}(\boldsymbol{u}_{n-1}^{hk})), \xi^h - \rho_n^{hk}\right)_Y, \quad n = 1, 2, \ldots, N, \tag{3.15}$$

where ρ_0^{hk} denotes an appropriate approximation of the initial condition ρ_0 and the discrete stress field $\boldsymbol{\sigma}_n^{hk} = (\boldsymbol{\sigma}_n^{hk})_{n=0}^N \subset Q^h$ is given by

$$\boldsymbol{\sigma}_n^{hk} = 2\,\mu(\rho_n^{hk})\boldsymbol{\varepsilon}(\boldsymbol{u}_n^{hk}) + \lambda(\rho_n^{hk})\mathrm{Div}\,(\boldsymbol{u}_n^{hk})\mathcal{I}, \quad n = 0, 1, \ldots, N. \tag{3.16}$$

Using classical results on elliptic linear variational inequalities (see [44]), the existence of a unique solution to discrete problem VP2^{hk} is deduced.

In this section, our aim is to provide an error estimate on the numerical errors $\|\boldsymbol{u}_n - \boldsymbol{u}_n^{hk}\|_V$ and $\|\rho_n - \rho_n^{hk}\|_Y$ which we state in the following.

Theorem 3.1 *Assume that Problem VP2 has a unique solution $(\boldsymbol{u}, \rho)$ with regularity*

$$\boldsymbol{u} \in C^1([0,T]; V) \cap C([0,T]; [W^{1,\infty}(\overline{\Omega})]^d), \quad \rho \in C^1([0,T]; Y), \tag{3.17}$$

and denote by $(\boldsymbol{u}^{hk}, \rho^{hk})$ the solution to Problem VP2^{hk}. Then, there exists a positive constant $C > 0$, independent of the discretization parameters h and k but depending on the continuous solution $(\boldsymbol{u}, \rho)$ and the problem data, such that, for all $\{\boldsymbol{v}_n^h\}_{n=0}^N \subset V^h$ and $\{\xi_n^h\}_{n=0}^N \subset K^h$,

$$\begin{aligned}\max_{0\leq n\leq N} \left\{\|\boldsymbol{u}_n - \boldsymbol{u}_n^{hk}\|_V^2 + \|\rho_n - \rho_n^{hk}\|_Y^2\right\} \leq C\Big(k\sum_{j=1}^N \Big\{\|\rho_j - \xi_j^h\|_Y^2 \\ + \left\|\frac{\rho_j - \rho_{j-1}}{k} - \dot{\rho}_j\right\|_Y^2 + \left\|\Phi_j - \frac{\rho_j - \rho_{j-1}}{k}\right\|_Y \|\rho_j - \xi_j^h\|_Y\Big\} + k^2 \\ + \max_{0\leq n\leq N}\|\rho_n - \xi_n^h\|_Y^2 + \max_{0\leq n\leq N}\|\boldsymbol{u}_n - \boldsymbol{v}_n^h\|_V^2 + \|\boldsymbol{u}_0 - \boldsymbol{u}_0^{hk}\|_V^2 + \|\rho_0 - \rho_0^h\|_Y^2 \\ + \frac{1}{k}\sum_{j=1}^{N-1}\|\rho_j - \xi_j^h - (\rho_{j+1} - \xi_{j+1}^h)\|_Y^2\Big).\end{aligned} \tag{3.18}$$

Proof First, we will obtain an error estimate on the displacement fields. Subtracting variational equation (3.9) at time $t = t_n$ for $\boldsymbol{v} = \boldsymbol{v}^h \in V^h$ and variational equation (3.14) we find that

$$c(\rho_n; \boldsymbol{u}_n, \boldsymbol{v}^h) - c(\rho_n^{hk}; \boldsymbol{u}_n^{hk}, \boldsymbol{v}^h) = 0 \quad \forall \boldsymbol{v}^h \in V^h.$$

Therefore,

$$\begin{aligned} &c(\rho_n; \boldsymbol{u}_n, \boldsymbol{u}_n - \boldsymbol{u}_n^{hk}) - c(\rho_n^{hk}; \boldsymbol{u}_n^{hk}, \boldsymbol{u}_n - \boldsymbol{u}_n^{hk}) \\ &\qquad = c(\rho_n; \boldsymbol{u}_n, \boldsymbol{u}_n - \boldsymbol{v}^h) - c(\rho_n^{hk}; \boldsymbol{u}_n^{hk}, \boldsymbol{u}_n - \boldsymbol{v}^h) \quad \forall \boldsymbol{v}^h \in V^h. \end{aligned}$$

Since $\rho_n^{hk} \in K^h$, we have $\rho_n^{hk} \geq \rho_a > 0$ and we immediately get

$$\begin{aligned} &c(\rho_n; \boldsymbol{u}_n, \boldsymbol{u}_n - \boldsymbol{u}_n^{hk}) - c(\rho_n^{hk}; \boldsymbol{u}_n^{hk}, \boldsymbol{u}_n - \boldsymbol{u}_n^{hk}) \\ &\qquad = c(\rho_n^{hk}; \boldsymbol{u}_n - \boldsymbol{u}_n^{hk}, \boldsymbol{u}_n - \boldsymbol{u}_n^{hk}) \\ &\qquad\quad + c(\rho_n; \boldsymbol{u}_n, \boldsymbol{u}_n - \boldsymbol{u}_n^{hk}) - c(\rho_n^{hk}; \boldsymbol{u}_n, \boldsymbol{u}_n - \boldsymbol{u}_n^{hk}), \\ &c(\rho_n; \boldsymbol{u}_n, \boldsymbol{u}_n - \boldsymbol{v}^h) - c(\rho_n^{hk}; \boldsymbol{u}_n^{hk}, \boldsymbol{u}_n - \boldsymbol{v}^h) \\ &\qquad = c(\rho_n^{hk}; \boldsymbol{u}_n - \boldsymbol{u}_n^{hk}, \boldsymbol{u}_n - \boldsymbol{v}^h) \\ &\qquad\quad + c(\rho_n; \boldsymbol{u}_n, \boldsymbol{u}_n - \boldsymbol{v}^h) - c(\rho_n^{hk}; \boldsymbol{u}_n, \boldsymbol{u}_n - \boldsymbol{v}^h), \\ &c(\rho_n^{hk}; \boldsymbol{u}_n - \boldsymbol{u}_n^{hk}, \boldsymbol{u}_n - \boldsymbol{u}_n^{hk}) \geq \alpha \|\boldsymbol{u}_n - \boldsymbol{u}_n^{hk}\|_V^2. \end{aligned}$$

From the regularity $\boldsymbol{u} \in C([0,T]; [W^{1,\infty}(\overline{\Omega})]^{d\times d})$, keeping in mind that $\rho_n, \rho_n^{hk} \in [\rho_a, \rho_b]$ it follows that

$$\begin{aligned} &c(\rho_n; \boldsymbol{u}_n, \boldsymbol{u}_n - \boldsymbol{u}_n^{hk}) - c(\rho_n^{hk}; \boldsymbol{u}_n, \boldsymbol{u}_n - \boldsymbol{u}_n^{hk}) \leq C \|\rho_n - \rho_n^{hk}\|_Y \|\boldsymbol{u}_n - \boldsymbol{u}_n^{hk}\|_V, \\ &c(\rho_n; \boldsymbol{u}_n, \boldsymbol{u}_n - \boldsymbol{v}^h) - c(\rho_n^{hk}; \boldsymbol{u}_n^{hk}, \boldsymbol{u}_n - \boldsymbol{v}^h) \\ &\qquad \leq C \|\boldsymbol{u}_n - \boldsymbol{u}_n^{hk}\|_V \|\boldsymbol{u}_n - \boldsymbol{v}^h\|_V + C \|\rho_n - \rho_n^{hk}\|_Y \|\boldsymbol{u}_n - \boldsymbol{v}^h\|_V, \\ &c(\rho_n^{hk}; \boldsymbol{u}_n - u_n^{hk}, \boldsymbol{u}_n - \boldsymbol{v}^h) \leq C \|\boldsymbol{u}_n - \boldsymbol{u}_n^{hk}\|_V \|\boldsymbol{u}_n - \boldsymbol{v}^h\|_V, \end{aligned}$$

where, here and in what follows, C denotes a generic positive constant which depends on the continuous solution but it is independent of the discretization parameters h and k, and whose value may change from line to line.

Hence, using several times the inequality

$$ab \leq \epsilon a^2 + \frac{1}{4\epsilon} b^2, \quad a, b, \epsilon \in \mathbb{R},\ \epsilon > 0, \tag{3.19}$$

it leads to the following estimates for the displacement fields:

$$\|\boldsymbol{u}_n - \boldsymbol{u}_n^{hk}\|_V^2 \leq C(\|\boldsymbol{u}_n - \boldsymbol{v}^h\|_V^2 + \|\rho_n - \rho_n^{hk}\|_Y^2) \quad \forall \boldsymbol{v}^h \in V^h. \tag{3.20}$$

Next, let us obtain an error estimate for the apparent density function. In order to simplify the writing, we use the notations $\Phi_j = \Phi(\rho_j, \boldsymbol{\sigma}(\boldsymbol{u}_j), \boldsymbol{\varepsilon}(\boldsymbol{u}_j))$ and $\Phi_j^{hk} = \Phi(\rho_j^{hk}, \boldsymbol{\sigma}_j^{hk}, \boldsymbol{\varepsilon}(\boldsymbol{u}_j^{hk}))$. First, we rewrite the discrete variational inequality (3.15) in the following form,

$$\left(\frac{\rho_n^{hk} - \rho_{n-1}^{hk}}{k}, \rho_n - \rho_n^{hk}\right)_Y \geq (\Phi_{n-1}^{hk}, \xi^h - \rho_n^{hk})_Y + \left(\frac{\rho_n^{hk} - \rho_{n-1}^{hk}}{k}, \rho_n - \xi^h\right)_Y$$

for all $\xi^h \in K^h$. Taking now the variational inequality (3.10) at time $t = t_n$ and for $\xi = \rho_n^{hk} \in B^h \subset Y$, by subtracting the two inequalities with $\xi^h = \xi_n^h \in K^h$ we conclude that

$$\begin{aligned}\left(\dot\rho_n - \frac{\rho_n^{hk} - \rho_{n-1}^{hk}}{k}, \rho_n - \rho_n^{hk}\right)_Y &\leq (\Phi_n, \rho_n - \rho_n^{hk})_Y - (\Phi_{n-1}^{hk}, \xi_n^h - \rho_n^{hk})_Y \\ &\quad - \left(\frac{\rho_n^{hk} - \rho_{n-1}^{hk}}{k}, \rho_n - \xi_n^h\right)_Y \quad \forall \xi_n^h \in K^h,\end{aligned}$$

and thus,

$$\begin{aligned}&\left(\frac{\rho_n - \rho_{n-1}}{k} - \frac{\rho_n^{hk} - \rho_{n-1}^{hk}}{k}, \rho_n - \rho_n^{hk}\right)_Y \\ &\quad \leq \left(\Phi_n - \Phi_{n-1}^{hk}, \xi_n^h - \rho_n^{hk}\right)_Y + (\Phi_n, \rho_n - \xi_n^h)_Y \\ &\qquad + \left(\frac{\rho_n - \rho_{n-1}}{k} - \dot\rho_n, \rho_n - \rho_n^{hk}\right)_Y - \left(\frac{\rho_n - \rho_{n-1}}{k}, \rho_n - \xi_n^h\right)_Y \\ &\qquad + \left(\frac{\rho_n - \rho_{n-1}}{k} - \frac{\rho_n^{hk} - \rho_{n-1}^{hk}}{k}, \rho_n - \xi_n^h\right)_Y.\end{aligned}$$

Taking into account that

$$\left(\frac{\rho_n-\rho_{n-1}}{k}-\frac{\rho_n^{hk}-\rho_{n-1}^{hk}}{k},\rho_n-\rho_n^{hk}\right)_Y \geq \frac{1}{k}\left(\|\rho_n-\rho_n^{hk}\|_Y^2-\|\rho_{n-1}-\rho_{n-1}^{hk}\|_Y\|\rho_n-\rho_n^{hk}\|_Y\right)$$
$$\geq \frac{1}{2k}\left(\|\rho_n-\rho_n^{hk}\|_Y^2-\|\rho_{n-1}-\rho_{n-1}^{hk}\|_Y^2\right),$$

and, applying several times inequality (3.19), we find that for $n=1,2,\ldots,N$,

$$\|\rho_n-\rho_n^{hk}\|_Y^2 \leq Ck\Big\{\|\Phi_n-\Phi_{n-1}^{hk}\|_Y^2+\|\rho_n-\xi_n^h\|_Y^2+\left\|\Phi_n-\frac{\rho_n-\rho_{n-1}}{k}\right\|_Y\|\rho_n-\xi_n^h\|_Y$$
$$+\|\rho_n-\rho_n^{hk}\|_Y^2+\left\|\frac{\rho_n-\rho_{n-1}}{k}-\dot\rho_n\right\|_Y^2\Big\}+\|\rho_{n-1}-\rho_{n-1}^{hk}\|_Y^2$$
$$+C\left(\rho_n-\rho_{n-1}-(\rho_n^{hk}-\rho_{n-1}^{hk}),\rho_n-\xi_n^h\right)_Y \quad \forall \xi_n^h\in K^h.$$

By induction in n, we then obtain

$$\|\rho_n-\rho_n^{hk}\|_Y^2 \leq Ck\sum_{j=1}^n\Big\{\|\Phi_j-\Phi_{j-1}^{hk}\|_Y^2+\|\rho_j-\xi_j^h\|_Y^2+\left\|\Phi_j-\frac{\rho_j-\rho_{j-1}}{k}\right\|_Y\|\rho_j-\xi_j^h\|_Y$$
$$+\|\rho_j-\rho_j^{hk}\|_Y^2+\left\|\frac{\rho_j-\rho_{j-1}}{k}-\dot\rho_j\right\|_Y^2\Big\}+\|\rho_0-\rho_0^{hk}\|_Y^2$$
$$+C\sum_{j=1}^n\left(\rho_j-\rho_{j-1}-(\rho_j^{hk}-\rho_{j-1}^{hk}),\rho_j-\xi_j^h\right)_Y \quad \forall\{\xi_j^h\}_{j=1}^n\subset K^h.$$

From the definition of Φ_j and Φ_j^{hk} (see also (3.8)) it follows that

$$\begin{aligned}\|\Phi_j-\Phi_{j-1}^{hk}\|_Y^2 &\leq C\|\rho_{j-1}^{hk}\boldsymbol{\sigma}_j:\mathcal{L}(\boldsymbol{\varepsilon}(\boldsymbol{u}_j))-\rho_j\boldsymbol{\sigma}_{j-1}^{hk}:\mathcal{L}(\boldsymbol{\varepsilon}(\boldsymbol{u}_{j-1}^{hk}))\|_Y^2\\ &\leq C\Big(\|\rho_{j-1}^{hk}\boldsymbol{\sigma}_j:\mathcal{L}(\boldsymbol{\varepsilon}(\boldsymbol{u}_j))-\rho_j\boldsymbol{\sigma}_j:\mathcal{L}(\boldsymbol{\varepsilon}(\boldsymbol{u}_j))\|_Y^2\\ &\quad+\|\rho_j\boldsymbol{\sigma}_j:\mathcal{L}(\boldsymbol{\varepsilon}(\boldsymbol{u}_j))-\rho_j\boldsymbol{\sigma}_j:\mathcal{L}(\boldsymbol{\varepsilon}(\boldsymbol{u}_{j-1}^{hk}))\|_Y^2\\ &\quad+\|\rho_j\boldsymbol{\sigma}_j:\mathcal{L}(\boldsymbol{\varepsilon}(\boldsymbol{u}_{j-1}^{hk}))-\rho_j\boldsymbol{\sigma}_{j-1}^{hk}:\mathcal{L}(\boldsymbol{\varepsilon}(\boldsymbol{u}_{j-1}^{hk}))\|_Y^2\Big)\\ &\leq C\Big(\|\rho_j-\rho_{j-1}^{hk}\|_Y^2+\|\boldsymbol{\sigma}_j-\boldsymbol{\sigma}_{j-1}^{hk}\|_Q^2+\|\boldsymbol{u}_j-\boldsymbol{u}_{j-1}^{hk}\|_V^2\Big),\end{aligned}$$

and, keeping in mind (3.5) and (3.16), it yields

$$\begin{aligned}\|\Phi_j-\Phi_{j-1}^{hk}\|_Y^2 &\leq C\Big(\|\rho_j-\rho_{j-1}\|_Y^2+\|\rho_{j-1}-\rho_{j-1}^{hk}\|_Y^2+\|\boldsymbol{u}_j-\boldsymbol{u}_{j-1}\|_V^2\\ &\quad+\|\boldsymbol{u}_{j-1}-\boldsymbol{u}_{j-1}^{hk}\|_V^2\Big).\end{aligned}$$

After simple calculations we deduce the following relation

$$\begin{aligned}
&\sum_{j=1}^{n}\big(\rho_j-\rho_{j-1}-(\rho_j^{hk}-\rho_{j-1}^{hk}),\rho_j-\xi_j^h\big)_Y\\
&\qquad=(\rho_n-\rho_n^{hk},\rho_n-\xi_n^h)_Y-(\rho_0-\rho_0^{hk},\rho_1-\xi_1^h)_Y\\
&\qquad\quad+\sum_{j=1}^{n-1}(\rho_j-\rho_j^{hk},\rho_j-\xi_j^h-(\rho_{j+1}-\xi_{j+1}^h))_Y\\
&\qquad\le\epsilon\|\rho_n-\rho_n^{hk}\|_Y^2+C\Big(\|\rho_n-\xi_n^h\|_Y^2+\|\rho_0-\rho_0^{hk}\|_Y^2+\|\rho_1-\xi_1^h\|_Y^2\\
&\qquad\quad+k\sum_{j=1}^{n}\|\rho_j-\rho_j^{hk}\|_Y^2+\frac{1}{k}\sum_{j=1}^{n-1}\|\rho_j-\xi_j^h-(\rho_{j+1}-\xi_{j+1}^h)\|_Y^2\Big),
\end{aligned}$$

where we have used three times inequality (3.19) and $\epsilon>0$ is a parameter assumed small enough.

Using the previous inequalities, we deduce the following estimates for the apparent density function,

$$\begin{aligned}
\|\rho_n-\rho_n^{hk}\|_Y^2\le Ck\sum_{j=1}^{n}\Big\{&\|\boldsymbol{u}_j-\boldsymbol{u}_j^{hk}\|_V^2+\|\rho_j-\rho_j^{hk}\|_Y^2+\|\rho_j-\xi_j^h\|_Y^2\\
&+\left\|\Phi_j-\frac{\rho_j-\rho_{j-1}}{k}\right\|_Y\|\rho_j-\xi_j^h\|_Y+\|\rho_j-\rho_{j-1}\|_Y^2\\
&+\|\boldsymbol{u}_j-\boldsymbol{u}_{j-1}\|_V^2+\left\|\frac{\rho_j-\rho_{j-1}}{k}-\dot\rho_j\right\|_Y^2\Big\}+C\|\rho_n-\xi_n^h\|_Y^2\\
&+\frac{C}{k}\sum_{j=1}^{n-1}\|\rho_j-\xi_j^h-(\rho_{j+1}-\xi_{j+1}^h)\|_Y^2+C\|\rho_1-\xi_1^h\|_Y^2\\
&+C\|\rho_0-\rho_0^{hk}\|_Y^2+C\|\boldsymbol{u}_0-\boldsymbol{u}_0^{hk}\|_V^2\quad\forall\{\xi_j^h\}_{j=1}^n\subset K^h,
\end{aligned}\tag{3.21}$$

and combining estimates (3.20) and (3.21) we obtain the following estimates for the numerical errors:

$$\begin{aligned}
\|\boldsymbol{u}_n-\boldsymbol{u}_n^{hk}\|_V^2+\|\rho_n-\rho_n^{hk}\|_Y^2\le Ck\sum_{j=1}^{n}\Big\{&\|\boldsymbol{u}_j-\boldsymbol{u}_j^{hk}\|_V^2+\|\rho_j-\rho_j^{hk}\|_Y^2\\
&+\left\|\Phi_j-\frac{\rho_j-\rho_{j-1}}{k}\right\|_Y\|\rho_j-\xi_j^h\|_Y+\|\rho_j-\rho_{j-1}\|_Y^2
\end{aligned}$$

$$+\|\boldsymbol{u}_j-\boldsymbol{u}_{j-1}\|_V^2+\|\rho_j-\xi_j^h\|_Y^2+\left\|\frac{\rho_j-\rho_{j-1}}{k}-\dot{\rho}_j\right\|_Y^2\Big\}+C\|\rho_n-\xi_n^h\|_Y^2$$
$$+C\|\boldsymbol{u}_n-\boldsymbol{v}_n^h\|_V^2+\frac{C}{k}\sum_{j=1}^{n-1}\|\rho_j-\xi_j^h-(\rho_{j+1}-\xi_{j+1}^h)\|_Y^2+C\|\rho_1-\xi_1^h\|_Y^2$$
$$+C\|\rho_0-\rho_0^{hk}\|_Y^2+C\|\boldsymbol{u}_0-\boldsymbol{u}_0^{hk}\|_V^2\quad\forall\{\xi_j^h\}_{j=1}^n\subset K^h,\ \forall\boldsymbol{v}_n^h\in V^h.$$

From the previous estimates, keeping in mind the regularities $\boldsymbol{u}\in C^1([0,T];V)$ and $\rho\in C^1([0,T];Y)$ which implied the estimate

$$k\sum_{j=1}^{n}\left\{\|\rho_j-\rho_{j-1}\|_Y^2+\|\boldsymbol{u}_j-\boldsymbol{u}_{j-1}\|_V^2\right\}\leq Ck^2,$$

and using Lemma 2.1 with

$$e_n=\|\boldsymbol{u}_n-\boldsymbol{u}_n^{hk}\|_V^2+\|\rho_n-\rho_n^{hk}\|_Y^2,$$
$$g_0=e_0=\|\boldsymbol{u}_0-\boldsymbol{u}_0^{hk}\|_V^2+\|\rho_0-\rho_0^h\|_Y^2$$

and g_n the remaining terms, we obtain the result. □

We notice that the above error estimates are the basis for the analysis of the convergence rate of the algorithm. Hence, under additional regularity assumptions we obtain the linear convergence of the algorithm that we state in the following corollary.

Corollary 3.1 *Let assumptions of Theorem 3.1 hold. Define the initial condition for the apparent density function as follows,*

$$\rho_0^{hk}=\mathcal{P}^h\rho_0,$$

where $\mathcal{P}^h$ is the $L^2(\Omega)$-projection operator onto B^h. Under the additional regularity conditions

$$\boldsymbol{u}\in L^\infty(0,T;[H^2(\Omega)]^d),\quad\rho\in H^2(0,T;Y)\cap H^1([0,T];H^1(\Omega)),$$

the algorithm is linearly convergent; that is, there exists a positive constant $C > 0$, independent of the discretization parameters h and k, such that

$$\max_{0\le n\le N}\left\{\|\boldsymbol{u}_n-\boldsymbol{u}_n^{hk}\|_V+\|\rho_n-\rho_n^{hk}\|_Y\right\}\le c(h+k). \tag{3.22}$$

Proof The proof of the above corollary is obtained in several steps. First, by using the well-known result on the approximations by finite elements and the projection operator $\mathcal{P}^h$, we have (see [13]):

$$\begin{aligned}
&\inf_{v_n^h\in V^h}\|\boldsymbol{u}_n-\boldsymbol{v}_n^h\|_V\le ch\|\boldsymbol{u}_n\|_{[H^2(\Omega)]^d}\le ch\|\boldsymbol{u}\|_{C([0,T];[H^2(\Omega)]^d)},\\
&\inf_{\xi_n^h\in K^h}\|\rho_n-\xi_n^h\|_Y\le ch\|\rho_n\|_{H^1(\Omega)}\le ch\|\rho\|_{C([0,T];H^1(\Omega))},\\
&\|\rho_0-\rho_0^{hk}\|_Y\le ch\|\rho_0\|_{H^1(\Omega)}\le ch\|\rho\|_{C([0,T];H^1(\Omega))}.
\end{aligned}$$

Using estimates (3.20) with $n=0$ we find that

$$\|\boldsymbol{u}_0-\boldsymbol{u}_0^{hk}\|_V^2\le C\left(\|\boldsymbol{u}_0-\boldsymbol{v}^h\|_V^2+\|\rho_0-\rho_0^{hk}\|_Y^2\right)\quad\forall\boldsymbol{v}^h\in V^h,$$

and the previous result on the approximation of ρ_0 leads to the following estimate,

$$\|\boldsymbol{u}_0-\boldsymbol{u}_0^{hk}\|_V^2\le Ch^2(\|\rho\|^2_{C([0,T];H^1(\Omega))}+\|\boldsymbol{u}\|^2_{C([0,T];[H^2(\Omega)]^d)}).$$

An straightforward estimate implies that

$$k\sum_{j=1}^N\left\|\frac{\rho_j-\rho_{j-1}}{k}-\dot\rho_j\right\|_Y^2\le Ck^2\|\rho\|^2_{H^2(0,T;Y)},$$

and we also have

$$\begin{aligned}
k\sum_{j=1}^N\left\|\Phi_j-\frac{\rho_j-\rho_{j-1}}{k}\right\|_Y\|\rho_j-\xi_j^h\|_Y\le k\sum_{j=1}^N\Big\{&\|\Phi_j-\dot\rho_j\|_Y\|\rho_j-\xi_j^h\|_Y\\
&+\left\|\dot\rho_j-\frac{\rho_j-\rho_{j-1}}{k}\right\|_Y\|\rho_j-\xi_j^h\|_Y\Big\}
\end{aligned}$$

$$\leq C \max_{1\leq j\leq N} \|\rho_j - \xi_j^h\|_Y + C\sum_{j=1}^{N} k\Big\{ \Big\| \dot{\rho}_j - \frac{\rho_j - \rho_{j-1}}{k} \Big\|_Y^2 + \|\rho_j - \xi_j^h\|_Y^2 \Big\}.$$

Finally, applying the following estimate (see [5])

$$\frac{1}{k}\sum_{n=1}^{N-1} \|\rho_n - \xi_n^h - (\rho_{n+1} - \xi_{n+1}^h)\|_Y^2 \leq ch^2 \|\rho\|^2_{H^1(0,T;H^1(\Omega))},$$

and combining the previous results and error estimates (3.18), we conclude (3.22). □

3.4 Numerical results

In this section we first describe shortly the numerical scheme implemented, and then we present some numerical examples to exhibit its accuracy and its performance in one- and two-dimensional examples.

Numerical scheme

To approximate the spaces V, Q and B and the convex subset K, we use the finite element spaces V^h, Q^h and B^h defined by (3.11), (3.12) and (3.13), respectively. Moreover, we recall that $K^h = K \cap B^h$.

We notice that, in (3.14), for $n = 0$ the discrete initial apparent density ρ_0^{hk} is given and, for $n = 1, 2, \ldots, N$, ρ_n^{hk} is known. Hence, we obtain the discrete displacement field $\boldsymbol{u}_n^{hk}$ solving the discrete linear variational equation,

$$\boldsymbol{u}_n^{hk} \in V^h, \quad c(\rho_n^{hk}; \boldsymbol{u}_n^{hk}, \boldsymbol{v}^h) = L(\boldsymbol{v}^h) \quad \forall \boldsymbol{v}^h \in V^h.$$

This is a linear problem equivalent to a linear system and Cholesky's method is employed for its resolution.

Next, the discrete stress field is updated using the equation

$$\boldsymbol{\sigma}_n^{hk} = 2\,\mu(\rho_n^{hk})\boldsymbol{\varepsilon}(\boldsymbol{u}_n^{hk}) + \lambda(\rho_n^{hk})\mathrm{Div}\,(\boldsymbol{u}_n^{hk})\mathcal{I}.$$

Now, for $n = 1, 2, \ldots, N$ in (3.15) $\boldsymbol{u}_{n-1}^{hk}$, $\boldsymbol{\sigma}_{n-1}^{hk}$ and ρ_{n-1}^{hk} are known. The discrete apparent density function ρ_n^{hk} is then obtained from (3.15),

$$\begin{aligned}\rho_n^{hk} \in K^h, \quad \left(\rho_n^{hk}, \xi^h - \rho_n^{hk}\right)_Y \geq \;& k\left(\Phi(\rho_{n-1}^{hk}, \boldsymbol{\sigma}_{n-1}^{hk}, \boldsymbol{\varepsilon}(\boldsymbol{u}_{n-1}^{hk})), \xi^h - \rho_n^{hk}\right)_Y \\ & + \left(\rho_{n-1}^{hk}, \xi^h - \rho_n^{hk}\right)_Y \quad \forall \xi^h \in K^h.\end{aligned}$$

This leads to a discrete elliptic linear variational inequality which is solved using a penalty-duality algorithm introduced in [9] and that can be also seen, for instance, in [68].

The numerical scheme was implemented on a 3.2Ghz PC using MATLAB, and a typical 1D run ($h = k = 0.01$) took about 3 seconds of CPU time and a run for the 2D example spent about 17 seconds for each time iteration.

A one-dimensional example: the numerical convergence

As a one-dimensional example, the following problem is considered:

Problem P2-1D. *Find a displacement field* $u : [0,1] \times [0,1] \to \mathbb{R}$ *and an apparent density function* $\rho : [0,1] \times [0,1] \to [0.01, 1.74]$ *such that*

$$\begin{aligned}
&-\frac{\partial \sigma}{\partial x}(x,t) = 0 \quad x \in (0,1),\, t \in (0,1),\\
&\dot{\rho}(x,t) = \left(\frac{\sigma(x,t)\frac{\partial u}{\partial x}(x,t)}{2\rho(x,t)} - 0.25\right) \quad x \in [0,1],\, t \in [0,1],\\
&u(0,t) = 0 \quad t \in (0,1),\\
&\sigma(1,t) = -10^{-7}e^{10t} \quad t \in (0,1),\\
&\rho(x,0) = 0.8 \quad x \in [0,1],
\end{aligned}$$

where the stress field $\sigma : [0,1] \times [0,1] \to \mathbb{R}$ *is given by*

$$\sigma(x,t) = 100(\rho(x,t))^2 \frac{\partial u}{\partial x}(x,t) \quad x \in (0,1),\, t \in (0,1).$$

Problem **P2-1D** corresponds to Problem P2 with the following data, keeping in mind that the area of the cross section is $A = 1m^2$:

$$\Omega = (0,1), \quad T = 1\,day, \quad E(\rho) = M\rho^\gamma, \quad M = 100\,Nm^2/kg^2, \quad \gamma = 2,$$
$$B = 1, \quad \rho_a = 0.01\,Kg/m, \quad \rho_b = 1.74\,Kg/m, \quad S_r = 0.25\,Kg/ms,$$
$$\rho_0 = 0.8\,Kg/m, \quad f = 0\,N/m, \quad g(t) = -10^{-7}e^{10t}\,N \quad \text{for} \quad t \in [0,1].$$

Our aim here is to show the numerical convergence of the algorithm. Therefore, several uniform partitions of both the time interval and the domain, dividing $\Omega = (0,1)$ into n segments, have been performed. We note that the spatial discretization parameter h equals to $\dfrac{1}{n}$, and we used the solution obtained with $n = 2^{12}$ and $k = 0.0001$ as the "exact solution".

The numerical errors, given by

$$E^{hk} = \max_{0 \le n \le N} \left\{ \|\boldsymbol{u}_n - \boldsymbol{u}_n^{hk}\|_V + \|\rho_n - \rho_n^{hk}\|_Y \right\},$$

and obtained for different discretization parameters h and k, are depicted (multiplied by 100) in Table 3.1. Moreover, the evolution of the error depending on $h+k$ is plotted in Figure 3.1. We notice that the convergence of the algorithm is clearly observed, and the linear convergence, stated in Corollary 3.1, seems to be achieved.

$n \downarrow k \rightarrow$	0.01	0.005	0.001	0.0005	0.0001
16	1.21145e-1	1.70817e-4	1.64500e-4	1.63712e-4	1.63081e-4
32	8.90414e-5	8.50916e-5	8.19398e-5	8.15464e-5	8.12317e-5
64	4.41993e-5	4.22266e-5	4.06524e-5	4.04559e-5	4.02987e-5
128	2.17794e-5	2.07936e-5	2.00069e-5	1.99087e-5	1.98302e-5
256	1.05697e-5	1.00769e-5	9.68371e-6	9.63467e-6	9.59540e-6
512	4.96499e-6	4.71853e-6	4.52201e-6	4.49752e-6	4.47781e-6
1024	2.16260e-6	2.03944e-6	1.94086e-6	1.92894e-6	1.91910e-6

Table 3.1: Example **P2-1D**: Numerical errors for some h and k.

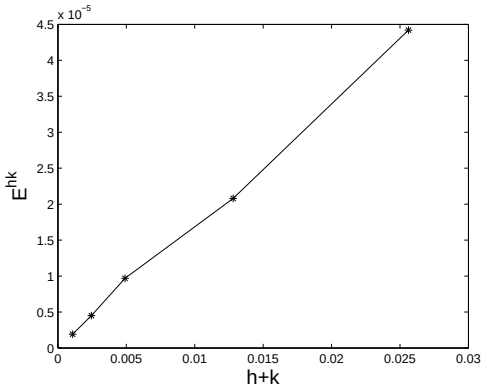

Figure 3.1: Example **P2-1D**: Asymptotic constant error.

Numerical results for two-dimensional problems

A plate model

As a first two-dimensional example, we consider a similar problem to that introduced in [59, 66]. The two-dimensional body occupies a square domain $\Omega = (0, 100) \times (0, 100)$ which is assumed to be fixed on its lower horizontal boundary $\Gamma_D = [0, 100] \times \{0\}$ (the left lower node is completely clamped, whereas the rest of the boundary has only its vertical displacements fixed). Moreover, the body is being acted by a linearly increasing compression force on the boundary part $[0, 100] \times \{1\}$ with maximum magnitude $10\, MPa$. No volume forces are given in Ω (see Figure 3.2).

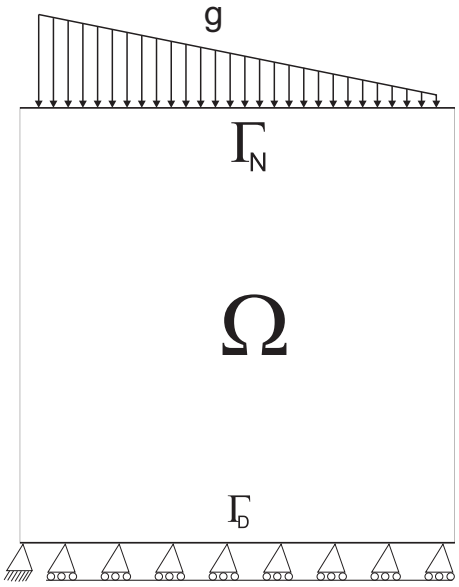

Figure 3.2: Example **P2-2D-1**: Plate of 100x100mm.

The following data have been employed in this example:

$$
\begin{aligned}
&T = 25\,days, \quad E(\rho) = M\rho^{\gamma}, \quad M = 100\,Pa/(Kg\,m^{-3})^2,\\
&B = 1\,(g\,cm^{-3})^2, \quad \rho_a = 0.010\,g/cm^3, \quad \rho_b = 1.740\,g/cm^3,\\
&S_r = 0.25\,J/g, \quad \rho_0 = 0.8\,g/cm^3, \quad \gamma = 0.5, \quad \kappa = 0.3,\\
&\boldsymbol{f} = \mathbf{0}\,N/m^2, \quad \boldsymbol{g}(x,y,t) = \begin{cases} (0, 0.1x - 10)\,MPa & \text{if} \quad y = 1,\\ \mathbf{0}\,MPa & \text{otherwise.} \end{cases}
\end{aligned}
$$

Therefore, using the time discretization parameter $k = 0.01$, in Figure 3.3 the apparent density function is plotted at final time and over the deformed mesh. As can be seen, the apparent density concentrates on the left part, where maximum forces are applied, and decrease from left to right. Moreover, since γ is less than one, the continuous solution has become stable; that is, in this case, the stimulus U/ρ has reached exactly the reference stimulus value of $0.25\,J/g$ in all elements.

As a second example, we consider a similar situation than in the previous one.

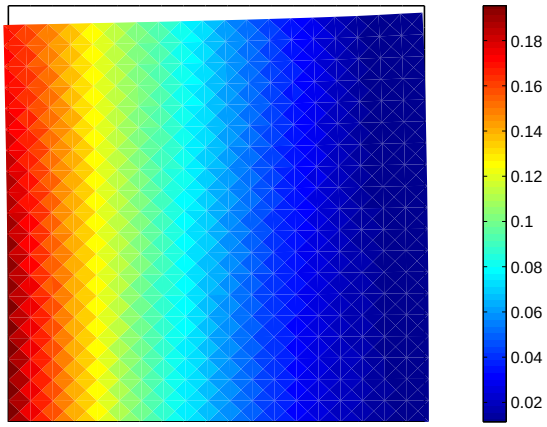

Figure 3.3: Example **P2-2D-1**: The apparent density at final time over the deformed configuration.

Therefore, a plate model is used again with the following data:

$$
\begin{aligned}
&T = 25\,days, \quad E(\rho) = M\rho^{\gamma}, \quad M = 100\,Pa/(Kg\,m^{-3})^2,\\
&B = 1\,(g\,cm^{-3})^2, \quad \rho_a = 0.01\,g/cm^3, \quad \rho_b = 1.740\,g/cm^3,\\
&S_r = 0.25\,J/g, \quad \rho_0 = 0.8\,g/cm^3, \quad \gamma = 2, \quad \kappa = 0.3,\\
&\boldsymbol{f} = \mathbf{0}\,N/m^2, \quad \boldsymbol{g}(x,y,t) = \begin{cases} (0, 0.1x - 10)\,MPa & \text{if} \quad y = 1,\\ \mathbf{0}\,MPa & \text{otherwise.} \end{cases}
\end{aligned}
$$

The difference is that the power index γ is greater than 1, which makes the solution unstable.

Using now the time discretization parameter $k = 0.01$, the evolution of the apparent density is plotted in Figure 3.4 and over the deformed configuration. As expected, the classical "checkerboard pattern" is clearly observed (like it was also shown in [66]). We can observe that in the left boundary, where the compression force reaches its maximum intensity, the bone density also takes the biggest value, in order to increase the resistance of the bone. As a consequence, the displacements in this area decrease with respect to time and they increase in the right part where the compression load takes small values.

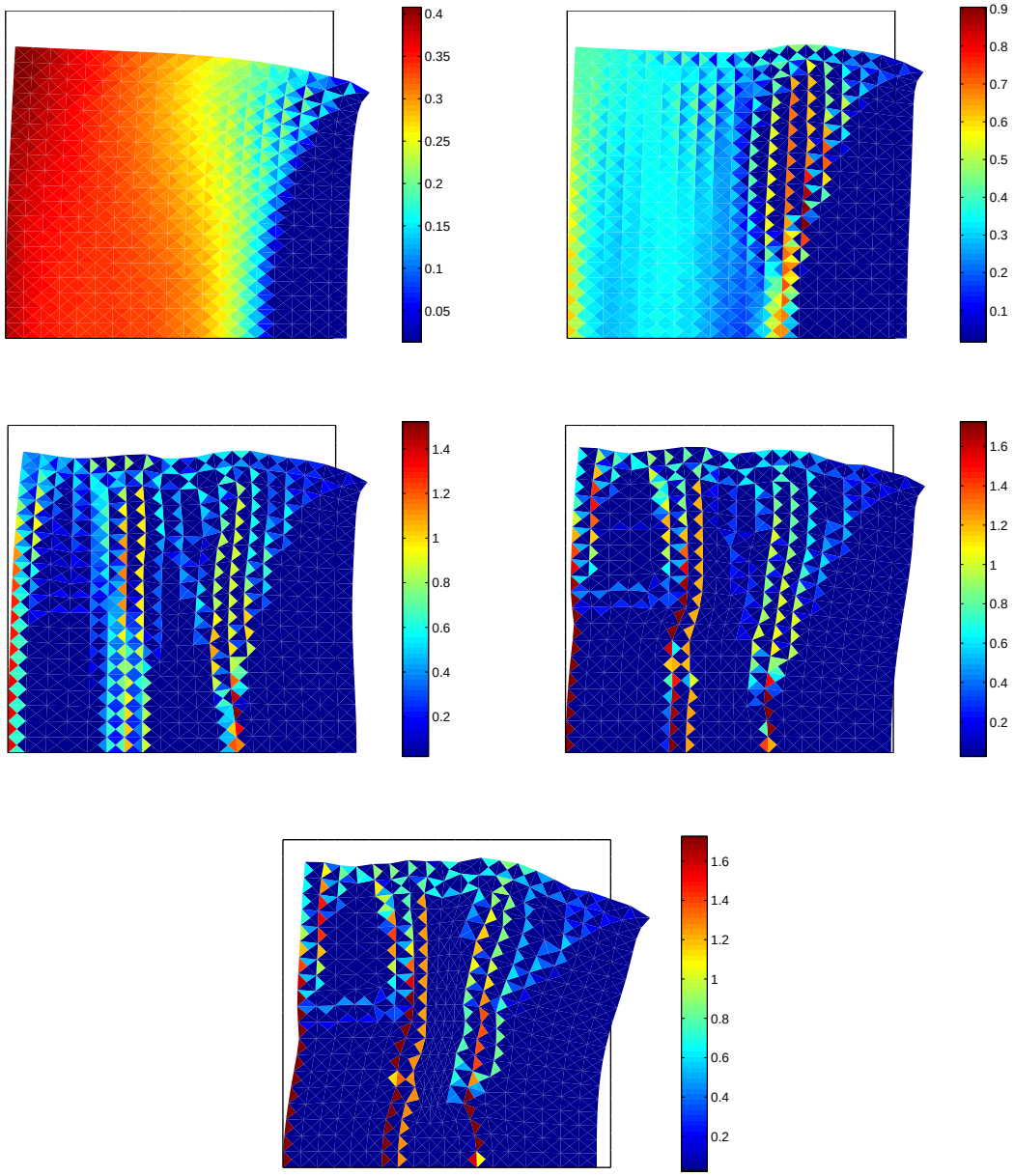

Figure 3.4: Example **P2-2D-2**: The evolution of the apparent density over the deformed configuration (t=5, 10, 15, 20 and 25).

Due to the construction of the finite element spaces, the discrete apparent density is discontinuous (it is assumed constant for each element). However, this solution is usually represented in a continuous way by using an interpolation post-processor

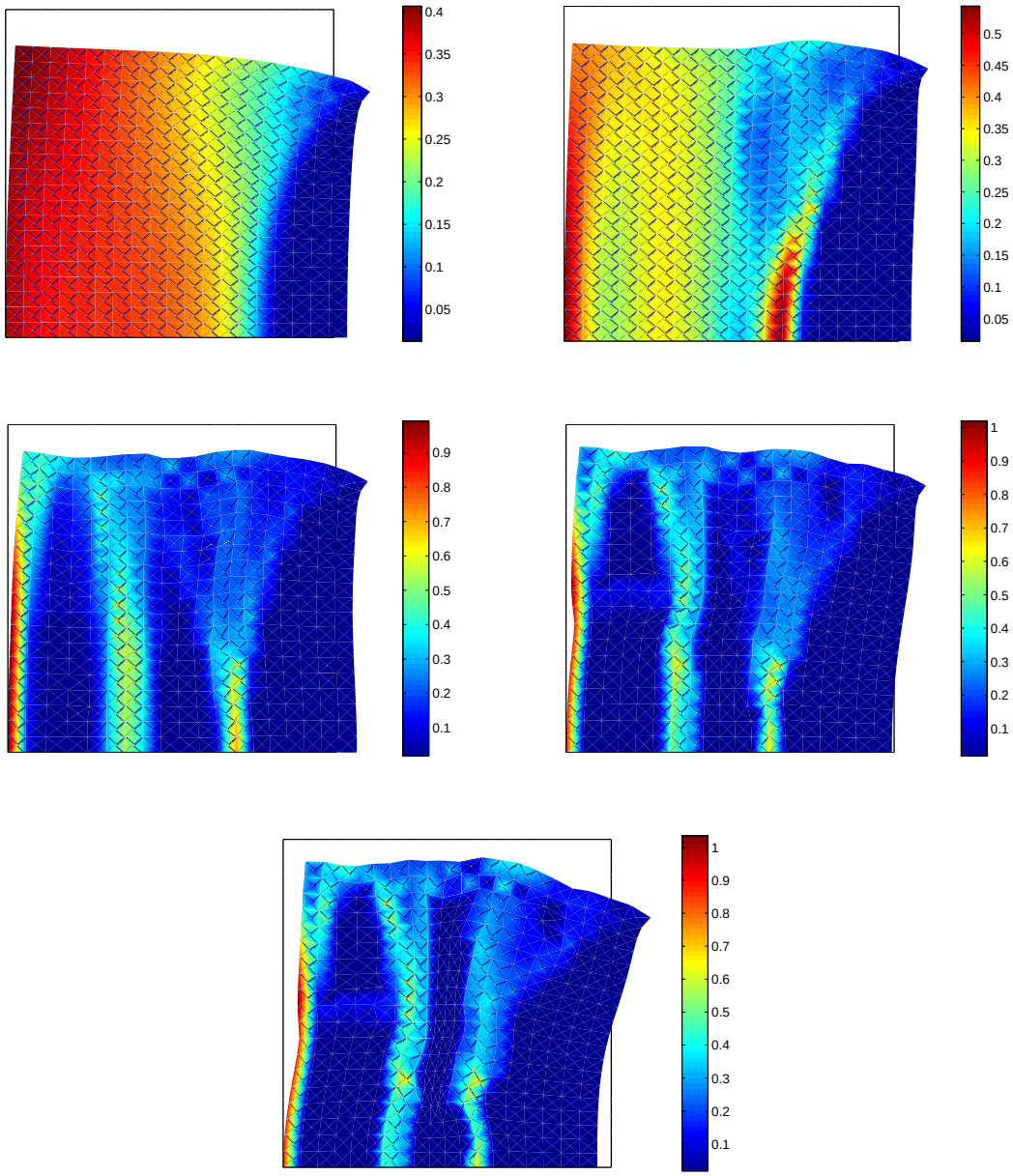

Figure 3.5: Example **P2-2D-2**: The evolution of the apparent density over the deformed configuration after an interpolation post-processing.

(see [59] for details). Therefore, in Figure 3.5 this continuous apparent density is also depicted over the deformed mesh. We notice that, due to the interpolation process, its values have changed although the behavior is very similar.

A femur model

As a final two-dimensional example we have considered a proximal femur model like that described in [19] or [66]. The setting is depicted in Figure 3.6 where, in order to describe the bone dimensions, we have plotted some points. . The distance between points A and B (the diameter of the diaphysis) is 30mm and the distance between points C and D is 57.76mm. The finite element mesh of the proximal femur has 1144 nodes and 2139 elements. A clear limitation of this 2D model is the lack of connection between the two cortical layers of the diaphysis. Here, we have followed the solution used by several authors that included an additional side plate joining both layers (see [8, 48]). This side plate is a new body which represents the cortical side of the femur, it is determined by the four points A, B, C and D and its finite element mesh is made by 1119 elements and 609 nodes. Moreover, in order to assure the rigidity of this part of the femur, we assume that the Young modulus E for the side plate is 17000MPa and that no bone remodeling takes place here.

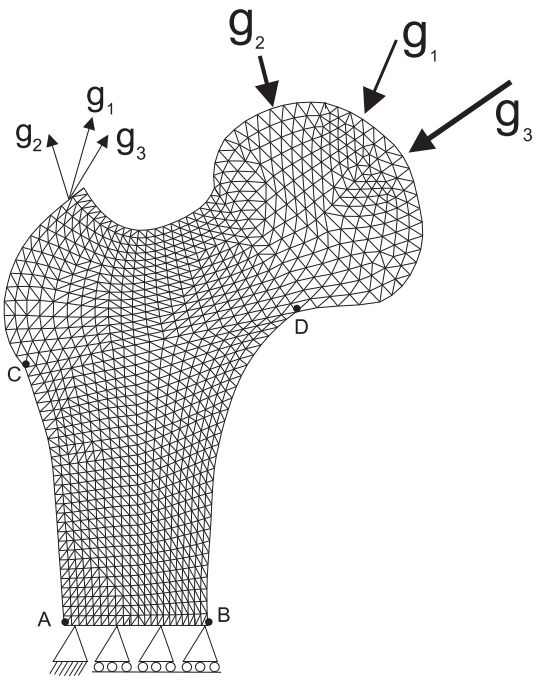

Figure 3.6: Example **P2-2D-3**: Physical setting and finite element mesh.

We assume that the lower horizontal boundary is clamped (the left lower point is

fixed whereas the rest of this boundary is fixed only through the vertical direction). According to [50, 66], the daily load history was represented using three loading cases. Each of them consists in two distributed loads acting on the femoral head plus the reaction forces induced in the abductor muscle (Table 3.2). These loads are applied sequentially (see Figure 3.7).

Case	Load at the femoral head		Reaction at the abductor	
	Load (N)	Direction (°)	Load (N)	Direction (°)
1	2317	24	703	28
2	1158	-15	351	-8
3	1548	56	468	35

Table 3.2: Moduli and orientation of the resultant forces. Orientations are referred to the vertical direction.

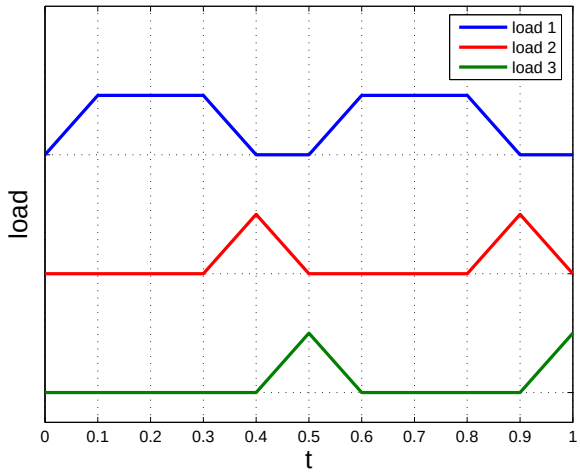

Figure 3.7: Loads applied sequentially

The following data have been used in this simulation:

$$T = 310\,days, \quad E(\rho) = M\rho^{\gamma}, \quad M = 3790\,Pa/(Kg\,m^{-2})^2, \quad \gamma = 3,$$
$$\boldsymbol{f} = \mathbf{0}\,N/m^2, \quad B = 1\,(g\,cm^{-3})^2(MPa\,day)^{-1}, \quad S_r = 0.004\,J/g, \quad \kappa = 0.3,$$
$$\rho_a = 0.01\,g/cm^3, \quad \rho_b = 1.740\,g/cm^3, \quad \rho_0 = 0.8\,g/cm^3.$$

We are assuming a plane strain hypothesis. The proximal femur has a uniform thickness

of 10mm and the side plate 1mm. Using the time step $k = 0.1$, the evolution of the apparent density is plotted in Figure 3.8. We can observe that the side plate plays the role of the cortical bone in the diaphysis and how the model predicts the formation of the marrow cavity from a initial homogeneous apparent density. The end configuration also predicts a reasonably accurate density distribution with a intramedullary canal. As it was also noticed in [66], Ward's triangle and the typical cancellous density patterns in this femoral head.

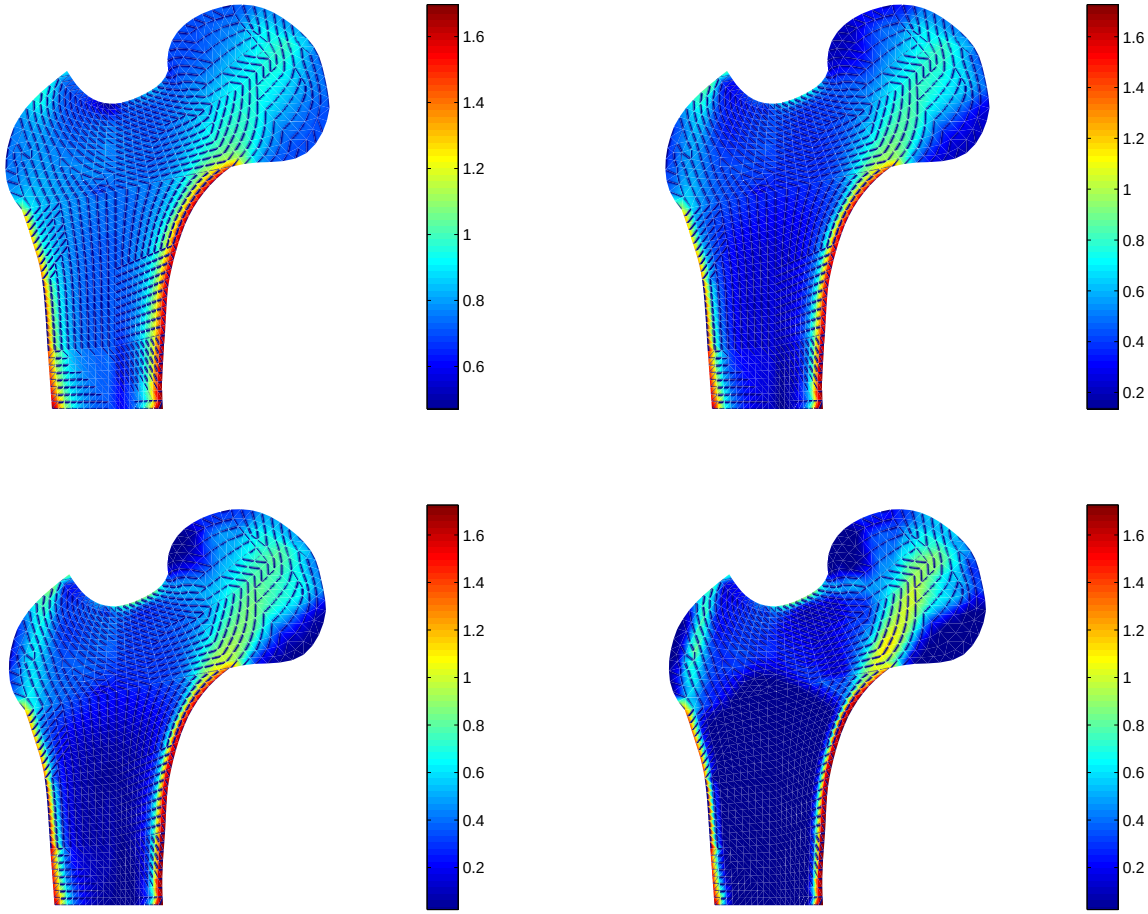

Figure 3.8: Example **P2-2D-3**: The evolution of the apparent density at several times (t=100, 150, 200 and 310).

Chapter 4

A piezoelectric bone remodeling model

4.1 Piezoelectricity as responsible of bone formation and resorption

Although it is widely accepted that mechanical loading can regulate bone adaptation and that osteocytes are the mechanosensor cells, it is unclear how actuator cells, osteoclasts and osteoblasts, are able to control bone resorption and formation in function of mechanical conditions.

The problem that has been widely analyzed to understand bone adaptation capacity is the self-straightening of a fractured bone, when it has healed in an angulated position. This fact motivated that several authors (see [6, 7]) proposed that tensile stress on the convex surface causes bone resorption, while compressive stress on the concave surface produce bone formation. However, Frost (see [37]) proposed that bone response on the surface depends on the relative curvature of the surface, where increased surface convexity produces bone resorption, whereas a decreased surface convexity causes bone formation.

In spite of all the studies developed since Wolff proposed that the bone adapts its structure in response to the mechanical loads, how cells are able to sense this mechanical environment is a current research issue. One possible mechanism that could justify that osteoclasts and osteoblasts tend to work in some bone surfaces instead of others, could be the different electric charge in each surface. Fukada and Yasuda showed in 1957 that dry bone is piezoelectric in the classic sense, that is, mechanical stress produces polarization (direct effect) and application of an electric field produces strain (converse effect) (see [38, 39]). Since then, the electrical properties of bone tissue have been widely investigated. It is believed that electric signals play an important role in the bone remodeling process and therefore, the piezoelectric properties of bone could help to understand the behavior of the bone cells.

Recently, a renovated interest has appeared to show the importance of bone piezoelectricity in bone responsiveness to mechanical environment (see [2, 63]). Although, this interest appeared in the 1960s, when bone piezoelectricity was invoked as a potential mechanism to explain mechanical bone adaptation (see [3, 6, 7]). However and despite of piezoelectricity relevance, it has not been normally used to understand bone remodeling and, currently, there are not many models that justify bone remodeling based on bone piezoelectricity (see [61, 62, 63]).

In this chapter, our aim is to propose a hypothesis in which we demonstrate, through a computational approach, that only bone matrix piezoelectricity is able to explain how bone is selectively deposited or removed at different periosteal surfaces.

We propose to use the bone remodeling model analyzed in the previous chapter to characterize the mechanical properties of the bone. Recall that in this model the bone is considered as an elastic solid assuming that the Poisson's ratio ν is independent of the apparent density ρ whereas the Young's modulus is given by $E(\rho) = M\rho^{\gamma}$, where M and γ are positive constants which characterize the bone behavior.

Since no results are found in the literature, from the numerical tests, in order to introduce the piezoelectricity in the model, we extend the classical electro-mechanical dependence adding a function $\alpha(\rho) = \rho^{\gamma}$, which regulates the coupling between the mechanical and electric field. This function guarantees that the electric field increases with the density of the bone. Hence, as a first approach, the constitutive law for the stress tensor $\boldsymbol{\sigma}$ and the electric displacement $\mathbf{D}$ are the following:

$$\boldsymbol{\sigma} = 2\,\mu(\rho)\boldsymbol{\varepsilon}(\boldsymbol{u}) + \lambda(\rho)\mathrm{Div}\,(\boldsymbol{u})\mathcal{I} - \alpha(\rho)\mathcal{E}^{*}\mathbf{E}(\varphi), \tag{4.1}$$

$$\mathbf{D} = \mathbf{D}_{\boldsymbol{\varepsilon}} + \mathbf{D}_{\mathbf{E}} = \alpha(\rho)\mathcal{E}\boldsymbol{\varepsilon}(\boldsymbol{u}) + \alpha(\rho)\beta\mathbf{E}(\varphi), \tag{4.2}$$

where $\boldsymbol{u}$ is the displacement field, $\boldsymbol{\varepsilon}$ is the strain tensor, $\mathbf{E}(\varphi) = (E_i(\varphi))_{i=1}^{d}$ represents the electric field defined by

$$E_i(\varphi) = -\frac{\partial\varphi}{\partial x_i}, \quad i = 1, \ldots, d,$$

and $\mathcal{E}^{*} = (e^{*}_{ijk})_{i,j,k=1}^{d}$ denotes the transpose of the third-order piezoelectric tensor $\mathcal{E} = (e_{ijk})_{i,j,k=1}^{d}$. We recall that

$$e^{*}_{ijk} = e_{kij}, \quad \text{for all} \quad i, j, k = 1, \ldots, d.$$

Moreover, β is the electric permittivity tensor, $\mathcal{I}$ denotes the identity operator, Div represents the divergence operator and $\mu(\rho)$ and $\lambda(\rho)$ are Lame's coefficients of the material, assumed to depend on the apparent density of the bone.

Equations (4.1) and (4.2) can be written as a matrix expression, considering that $\boldsymbol{\sigma} = \{\sigma_{xx}, \sigma_{yy}, \sigma_{zz}, \sigma_{yz}, \sigma_{zx}, \sigma_{xy}\}$ is the stress tensor, $\boldsymbol{\varepsilon} = \{\varepsilon_{xx}, \varepsilon_{yy}, \varepsilon_{zz}, \varepsilon_{yz}, \varepsilon_{zx}, \varepsilon_{xy}\}$, is the strain tensor, $\mathbf{D} = \{D_x, D_y, D_z\}$ is the electric displacement, $E = \{E_x, E_y, E_z\}$ is the electric field, $\mathcal{E}$ is the piezoelectric matrix and β is the permittivity matrix.

Assuming as several authors (see [35, 42, 61, 63]) that the bone behaves in the same way as a crystal with hexagonal symmetry, the piezoelectric tensor $\mathcal{E}$ is defined with

four values and the dielectric tensor β is represented as a diagonal matrix given by two constants. These tensors take the following matrix expression:

$$\mathcal{E} = \begin{pmatrix} 0 & 0 & 0 & e_{14} & e_{15} & 0 \\ 0 & 0 & 0 & e_{15} & -e_{14} & 0 \\ e_{31} & e_{31} & e_{33} & 0 & 0 & 0 \end{pmatrix} \qquad \text{and} \qquad \beta = \begin{pmatrix} \beta_{11} & 0 & 0 \\ 0 & \beta_{11} & 0 \\ 0 & 0 & \beta_{33} \end{pmatrix},$$

where we have assumed that the coordinate system is orientated in such a way that the third axis coincides with the material direction.

Our aim is to numerically show that bone formation and resorption may be related with electrical charges in the bone surfaces due to contributions produced by mechanical loading $\mathbf{D}_{\boldsymbol{\varepsilon}}$, following the works of Gjelsvik (see [42, 43]). The mechanical polarization is related to the strain through a matrix equation:

$$(\mathbf{D}_{\boldsymbol{\varepsilon}})_i = \alpha(\rho)\mathcal{E}_{ij}\boldsymbol{\varepsilon}_j(\boldsymbol{u}) \qquad for \quad i = 1, 2, 3 \qquad j = 1, 2, \ldots, 6$$

According to [35] we consider the following piezoelectric and dielectric coefficients:

$$\begin{aligned} e_{31} &= 1.50765 \times 10^{-9} C/mm^2, \quad e_{33} = 1.87209 \times 10^{-9} C/mm^2, \\ e_{15} &= 3.57643 \times 10^{-9} C/mm^2, \quad e_{14} = 17.88215 \times 10^{-}9 C/mm^2 \\ \beta_{11} &= 88.54 \times 10^{-12} F/mm, \quad \beta_{33} = 106.248 \times 10^{-12} F/mm, \end{aligned}$$

where C and F denote the units Coulomb and Faraday, respectively.

We have to keep in mind that the conclusions that we present along this chapter have been obtained with the piezoelectric tensor provided above. We have to remark that other authors consider that this piezoelectric tensor is defined by non-zero constants in the normal components (see [2, 3]). However, shear components were not evaluated in this study. Therefore and despite of having found some parameter values in the literature, bone piezoelectricity is a research field that has hardly been considered rel-

evant in bone adaptation and regeneration mechanisms. This fact has motivated that the number of biomechanical works in this field has been reduced dramatically since the 1960 to 2000, being really difficult to find experiments to validate models of the electro-mechanical behavior of the bone. However, an increasing number of works dealing with this topic has been published during the last ten years. Therefore, a strong effort should be done in this direction in order to unravel the multiphysics character of bone physiology. Moreover, the piezoelectric constants will need to be determined accurately; otherwise, the model cannot be a useful tool to understand the effect of piezoelectricity on bone mechanics.

We recall that the evolution of the apparent density function is obtained from the following first-order ordinary differential equation (see the previous chapter for details), where we still assume that the rate of bone remodeling is regulated by a mechanical-based stimulus

$$\dot{\rho} = B\left(\frac{U(\boldsymbol{\sigma}, \boldsymbol{\varepsilon}(\boldsymbol{u}))}{\rho} - S_r\right) \quad \text{in} \quad \Omega \times (0, T),$$

where B and S_r are experimental constants and $U(\boldsymbol{\sigma}, \boldsymbol{\varepsilon}(\boldsymbol{u}))$ is the strain energy density given by

$$U(\boldsymbol{\sigma}, \boldsymbol{\varepsilon}(\boldsymbol{u})) = \frac{1}{2}\boldsymbol{\sigma} \,:\, \boldsymbol{\varepsilon}(\boldsymbol{u}).$$

In order to obtain a real apparent density we have to assume again that this function is bounded as

$$\rho_a \leq \rho \leq \rho_b,$$

where value ρ_a represents the minimal density corresponding to the reabsorbed bone and value ρ_b is the maximal density of cortical bone.

The parameters which characterize the mechanical properties of the bone matrix and the experimental constants which determine the evolution of the bone density were proposed by [66] and already employed in the previous chapter.

In the next sections we study, from the mathematical point of view, this piezoelectric bone remodeling model. We will write the variational problem as a coupled system of a two non-linear variational equations for the displacement field and the electric potencial and a nonlinear parabolic variational inequality for the apparent density.

Then, fully discrete approximations are provided by using the finite element method to approximate the spatial variable and the explicit Euler scheme to discretize the time derivatives. Error estimates are proved, from which, under adequate regularity conditions, the linear convergence of the algorithm is derived. Finally, some numerical simulations, involving one, two and three dimensional examples, are presented to demonstrate the accuracy of the approximation and the behavior of the solution. Moreover, we notice that the results presented in this chapter have been recently submitted (see [21, 22]).

4.2 Mechanical and variational problem

Let us denote by $\mathbb{S}^d$ the space of second order symmetric tensors on $\mathbb{R}^d$, or equivalently, the space of symmetric matrices of order d, and let : be its inner product and $|\cdot|$ its norm.

Denote by $\Omega \subset \mathbb{R}^d$, $d = 1, 2, 3$, an open bounded domain and let $\Gamma = \partial\Omega$ be its boundary, assumed to be Lipschitz continuous and divided into two disjoint parts Γ_D and Γ_N. Let $[0, T]$, $T > 0$, be the time interval of interest, denote by $\boldsymbol{x} = (x_i)_{i=1}^d$ a generic point of $\overline{\Omega} = \Omega \cup \Gamma$, and for $\boldsymbol{x} \in \Gamma$, let $\boldsymbol{\nu}(\boldsymbol{x}) = (\nu_i(\boldsymbol{x}))_{i=1}^d$ be the outward unit normal vector to Γ at point $\boldsymbol{x}$. Volume forces of density $\boldsymbol{f}_B$ act in $\Omega \times (0, T)$, volume electric charges of density q_B are present in $\Omega \times (0, T)$, traction forces of density $\boldsymbol{f}_N$ are applied on $\Gamma_N \times (0, T)$ and surface electric charges of density q_N are found on $\Gamma_N \times (0, T)$. Finally, we assume that the body is clamped on $\Gamma_D \times (0, T)$ and a prescribed electric potential φ_D is applied there (see Figure 4.1).

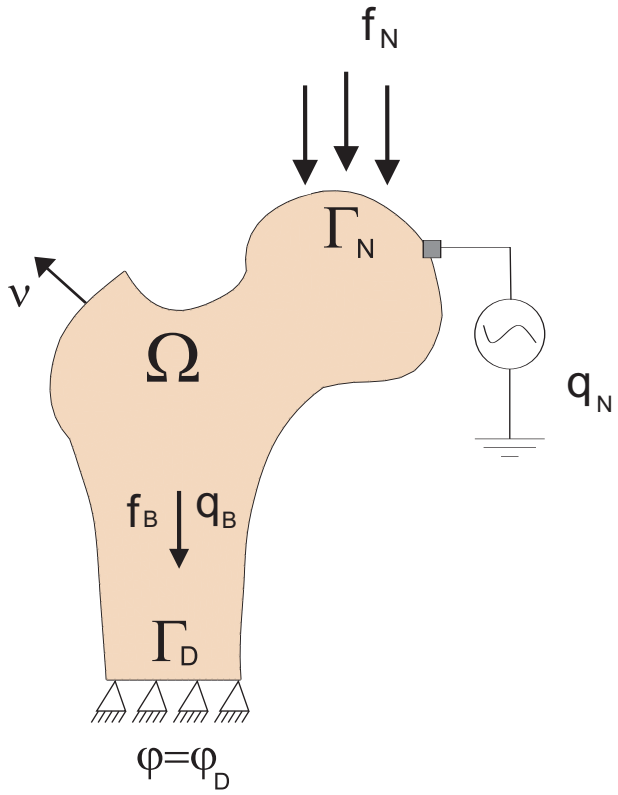

Figure 4.1: A bone remodeling problem.

Remark 4.1 *We notice that we have used the same decomposition of the boundary to impose the boundary conditions for the displacements and the electric potential. It is straightforward to extend the results presented in this section, and in the following one, to more general situations.*

As we explain in the previous section, the constitutive laws for the stress tensor $\boldsymbol{\sigma}$ and the electric displacement $\mathbf{D}$ are written as follows,

$$\boldsymbol{\sigma} = 2\,\mu(\rho)\boldsymbol{\varepsilon}(\boldsymbol{u}) + \lambda(\rho)\mathrm{Div}\,(\boldsymbol{u})\mathcal{I} - \alpha(\rho)\mathcal{E}^*\mathbf{E}(\varphi) \quad \text{in} \quad \overline{\Omega}\times[0,T],$$

$$\mathbf{D} = \alpha(\rho)\mathcal{E}\boldsymbol{\varepsilon}(\boldsymbol{u}) + \alpha(\rho)\beta\mathbf{E}(\varphi) \quad \text{in} \quad \overline{\Omega}\times[0,T].$$

Let us assume that the process is quasistatic and therefore, the inertia effects are neglected. Moreover, let ρ_0 denote the initial apparent density function. The mechani-

cal problem, derived from the continuum mechanics laws in the framework of the small displacements theory, is the following.

Problem P3. *Find a displacement field* $\boldsymbol{u} : \overline{\Omega} \times [0,T] \to \mathbb{R}^d$*, an electric potential field* $\varphi : \overline{\Omega} \times (0,T) \to \mathbb{R}$ *and an apparent density function* $\rho : \overline{\Omega} \times [0,T] \to [\rho_a, \rho_b]$ *such that* $\rho(0) = \rho_0$ *and,*

$$\dot{\rho} = B\left(\frac{U(\boldsymbol{\sigma}, \boldsymbol{\varepsilon}(\boldsymbol{u}))}{\rho} - S_r\right) \quad in \quad \Omega \times (0,T), \tag{4.3}$$

$$-\mathrm{Div}\,\boldsymbol{\sigma} = \boldsymbol{f}_B \quad in \quad \Omega \times (0,T), \tag{4.4}$$

$$\mathrm{div}\,\mathbf{D} = q_B \quad in \quad \Omega \times (0,T), \tag{4.5}$$

$$\boldsymbol{u} = \mathbf{0} \quad on \quad \Gamma_D \times (0,T), \tag{4.6}$$

$$\varphi = \varphi_D \quad on \quad \Gamma_D \times (0,T), \tag{4.7}$$

$$\boldsymbol{\sigma}\boldsymbol{\nu} = \boldsymbol{f}_N \quad on \quad \Gamma_N \times (0,T), \tag{4.8}$$

$$\mathbf{D} \cdot \boldsymbol{\nu} = q_N \quad on \quad \Gamma_N \times (0,T), \tag{4.9}$$

where $\lambda(\rho)$ *and* $\mu(\rho)$ *are the Lame's coefficients and the stress field* $\boldsymbol{\sigma} : \overline{\Omega} \times [0,T] \to \mathbb{S}^d$ *and the electric displacement field* $\mathbf{D} : \overline{\Omega} \times (0,T) \to \mathbb{R}^d$ *are given by*

$$\boldsymbol{\sigma} = 2\,\mu(\rho)\boldsymbol{\varepsilon}(\boldsymbol{u}) + \lambda(\rho)\mathrm{Div}\,(\boldsymbol{u})\mathcal{I} - \rho^\gamma \mathcal{E}^*\mathbf{E}(\varphi) \quad in \quad \Omega \times [0,T], \tag{4.10}$$

$$\mathbf{D} = \rho^\gamma \mathcal{E}\boldsymbol{\varepsilon}(\boldsymbol{u}) + \rho^\gamma \beta \mathbf{E}(\varphi) \quad in \quad \Omega \times (0,T). \tag{4.11}$$

We turn now to obtain a variational formulation of Problem P3. Let us denote again $Y = L^2(\Omega)$ and $H = [L^2(\Omega)]^d$, and define the following spaces equipped with the product norms derived from usual norms in Sobolev spaces:

$$W = \{\psi \in H^1(\Omega)\ ;\ \psi = 0 \quad \text{on} \quad \Gamma_D\},$$
$$V = \{\boldsymbol{v} = (v_i)_{i=1}^d \in [H^1(\Omega)]^d\ ;\ \boldsymbol{v} = \mathbf{0} \quad \text{on} \quad \Gamma_D\},$$
$$Q = \{\boldsymbol{\tau} = (\tau_{ij})_{i,j=1}^d \in [L^2(\Omega)]^{d\times d}\ ;\ \tau_{ij} = \tau_{ji}, \quad 1 \le i,j \le d\}.$$

In order to develop the numerical analysis, the following assumptions on the problem

data are required.

The density of mechanical and electrical forces have the regularity:

$$\begin{aligned} &\boldsymbol{f}_B \in C([0,T];[C(\overline{\Omega})]^d), \quad \boldsymbol{f}_N \in C([0,T];[C(\overline{\Gamma_N})]^d), \\ &q_B \in C([0,T];C(\overline{\Omega})), \quad q_N \in C([0,T];C(\overline{\Gamma_N})). \end{aligned} \tag{4.12}$$

The initial apparent density ρ_0 satisfies the following conditions:

$$\rho_0 \in C(\overline{\Omega}), \quad \rho_a \leq \rho_0(\boldsymbol{x}) \leq \rho_b \quad \text{for all} \quad \boldsymbol{x} \in \overline{\Omega}. \tag{4.13}$$

The piezoelectric tensor $\boldsymbol{\mathcal{E}}(\boldsymbol{x}) = (e_{ijk}(\boldsymbol{x}))_{i,j,k=1}^d : \boldsymbol{\tau} \in \mathbb{S}^d \to \boldsymbol{\mathcal{E}}(\boldsymbol{x})(\boldsymbol{\tau}) \in \mathbb{R}^d$ satisfies:

$$\begin{aligned} &\text{(a) } e_{ijk} = e_{ikj} \quad \text{for} \quad i,j,k = 1,\ldots,d. \\ &\text{(b) } e_{ijk} \in L^\infty(\Omega) \quad \text{for} \quad i,j,k = 1,\ldots,d. \end{aligned} \tag{4.14}$$

The permittivity tensor $\beta(\boldsymbol{x}) = (\beta_{ij}(\boldsymbol{x}))_{i,j=1}^d : \boldsymbol{w} \in \mathbb{R}^d \to \beta(\boldsymbol{x})(\boldsymbol{w}) \in \mathbb{R}^d$ satisfies:

$$\begin{aligned} &\text{(a) } \beta_{ij} = \beta_{ji} \quad \text{for} \quad i,j = 1,\ldots,d. \\ &\text{(b) } \beta_{ij} \in L^\infty(\Omega) \quad \text{for} \quad i,j = 1,\ldots,d. \\ &\text{(c) There exists } m_\beta > 0 \text{ such that } \beta(\boldsymbol{x})\boldsymbol{w}\cdot\boldsymbol{w} \geq m_\beta\,|\boldsymbol{w}|^2 \\ &\qquad \forall\, \boldsymbol{w} \in \mathbb{R}^d, \text{ a.e. } \boldsymbol{x} \in \Omega. \end{aligned} \tag{4.15}$$

For every $\rho \in L^\infty(\Omega)$, let us define the following bilinear form $c(\rho;\cdot,\cdot) : V \times V \to \mathbb{R}$ given by, for all $\boldsymbol{u}, \boldsymbol{v} \in V$,

$$c(\rho;\boldsymbol{u},\boldsymbol{v}) = \int_\Omega 2\mu(\rho)\boldsymbol{\varepsilon}(\boldsymbol{u}) \,:\boldsymbol{\varepsilon}(\boldsymbol{v}) + \lambda(\rho)\mathrm{Tr}(\boldsymbol{\varepsilon}(\boldsymbol{u}))\mathrm{Tr}(\boldsymbol{\varepsilon}(\boldsymbol{v}))\,d\boldsymbol{x},$$

where Tr denotes the trace operator defined as $\mathrm{Tr}(\boldsymbol{\tau}) = \sum_{i=1}^d \tau_{ii}$ for all $\boldsymbol{\tau} = (\tau_{ij})_{i,j=1}^d$.

Also we introduce the linear mappings $\boldsymbol{f} : [0,T] \to V$ and $q : [0,T] \to W$ given by

$$(\boldsymbol{f}(t), \boldsymbol{v})_V = \int_\Omega \boldsymbol{f}_B(t) \cdot \boldsymbol{v}\, d\boldsymbol{x} + \int_{\Gamma_N} \boldsymbol{f}_N(t) \cdot \boldsymbol{v}\, d\Gamma \quad \forall \boldsymbol{v} \in V,$$
$$(q(t), \boldsymbol{v})_W = \int_\Omega q_B(t)\psi\, d\boldsymbol{x} + \int_{\Gamma_N} q_N(t)\psi\, d\Gamma \quad \forall \psi \in W.$$

Applying Green's formula, we easily obtain the following variational equations for the displacement and electric potential fields:

$$c(\rho(t); \boldsymbol{u}(t), \boldsymbol{v}) = (\boldsymbol{f}(t), \boldsymbol{v})_V - (\rho(t)^\gamma \mathcal{E}^* \nabla\varphi(t), \boldsymbol{\varepsilon}(\boldsymbol{v}))_Q \quad \forall \boldsymbol{v} \in V,$$
$$(\rho(t)^\gamma[\beta\nabla\varphi(t) - \mathcal{E}\boldsymbol{\varepsilon}(\boldsymbol{u}(t))], \nabla\psi)_H = (q(t), \psi)_W \quad \forall \psi \in W.$$

Now, we need an equivalent expression for equation (4.3), incorporating the restriction $\rho_a \leq \rho \leq \rho_b$. In order to do so, we write this equation in the following form (see Chapter 3 for details),

$$\dot{\rho} - B\left(\frac{U(\boldsymbol{\sigma}, \boldsymbol{\varepsilon}(\boldsymbol{u}))}{\rho} - S_r\right) + \partial I_{[\rho_a,\rho_b]}(\rho) \ni 0,$$

where $\partial I_{[\rho_a,\rho_b]}$ denotes the subdifferential of the indicator function $I_{[\rho_a,\rho_b]}$ of the interval $[\rho_a, \rho_b]$.

We recall the definition of the function $\Phi : Y \times Q \times Q \to Y$ given by

$$\Phi(\rho, \boldsymbol{\sigma}, \boldsymbol{\tau}) = B\left(\frac{U(\boldsymbol{\sigma}, \boldsymbol{\tau})}{\rho} - S_r\right),$$

where $U(\boldsymbol{\sigma}, \boldsymbol{\tau}) = \dfrac{1}{2}\boldsymbol{\sigma} : \boldsymbol{\tau}$.

Since this function has a quadratic behavior with respect to $\boldsymbol{\tau}$, a truncation operator should be employed and therefore, this function must be redefined in the form:

$$\Phi(\rho, \boldsymbol{\sigma}, \boldsymbol{\tau}) = B\left(\frac{U(\boldsymbol{\sigma}, \mathcal{L}(\boldsymbol{\tau}))}{\rho} - S_r\right), \tag{4.16}$$

where the truncation operator $\mathcal{L} : \mathbb{S}^d \to \mathbb{S}^d$ is defined in the following form, where

$L > 0$ is a given positive constant,

$$(\mathcal{L}(\boldsymbol{\tau}))_{ij} = \begin{cases} L & \text{if} \quad \tau_{ij} > L, \\ \tau_{ij} & \text{if} \quad \tau_{ij} \in [-L, L], \\ -L & \text{if} \quad \tau_{ij} < -L. \end{cases}$$

Finally, let us recall the definition of the convex set of admissible apparent density functions,

$$K = \{\xi \in Y \,;\, \rho_a \leq \xi \leq \rho_b, \text{ a.e. in } \Omega\},$$

and, in order to simplify the calculations and the writing, we assume in this section, and also in the following one, that $\varphi_D = 0$.

By definition of the subdifferential operator, we obtain the following parabolic variational inequality:

$$\rho \in [\rho_a, \rho_b] \quad (\dot{\rho}(t), \xi - \rho(t))_Y \geq (\Phi(\rho(t), \boldsymbol{\sigma}(\boldsymbol{u}(t)), \boldsymbol{\varepsilon}(\boldsymbol{u}(t))), \xi - \rho(t))_Y \quad \forall \xi \in K.$$

Gathering this variational inequality with the variational equations obtained for the displacement and electric potential fields we derive the following variational formulation for the mechanical Problem P3.

Problem VP3. *Find a displacement field $\boldsymbol{u} : [0,T] \to V$, an electric potential field $\varphi : [0,T] \to W$ and an apparent density function $\rho : [0,T] \to K$ such that $\rho(0) = \rho_0$ and for a.e. $t \in (0,T)$,*

$$c(\rho(t); \boldsymbol{u}(t), \boldsymbol{v}) = (\boldsymbol{f}(t), \boldsymbol{v})_V - (\rho(t)^\gamma \mathcal{E}^* \nabla\varphi(t), \boldsymbol{\varepsilon}(\boldsymbol{v}))_Q \quad \forall \boldsymbol{v} \in V, \tag{4.17}$$

$$(\rho(t)^\gamma [\beta \nabla\varphi(t) - \mathcal{E}\boldsymbol{\varepsilon}(\boldsymbol{u}(t))], \nabla\psi)_H = (q(t), \psi)_W \quad \forall \psi \in W, \tag{4.18}$$

$$(\dot{\rho}(t), \xi - \rho(t))_Y \geq (\Phi(\rho(t), \boldsymbol{\sigma}(t), \boldsymbol{\varepsilon}(\boldsymbol{u}(t))), \xi - \rho(t))_Y \quad \forall \xi \in K, \tag{4.19}$$

where function Φ and stress field $\boldsymbol{\sigma}(t)$ are given in (4.16) and (4.10), respectively.

We notice that the existence of a unique solution to Problem VP3 has not been proved yet. Although we observe that there is a clear similarity between this kind of problems and the elasto-piezoelectric problem with damage considered in [25], we remark that such result is not straightforward because of the absence of the diffusion term. This makes the problem more difficult. However, we hope that related results to those applied in [57] for another bone remodeling problem could be used here.

4.3 Numerical analysis

In this section, we introduce a finite element algorithm for approximating solutions to variational problem VP3. Its discretization is done in two steps. First, we consider the finite element spaces $V^h \subset V$, $Q^h \subset Q$, $W^h \subset W$ and $B^h \subset Y$ given by

$$V^h = \{\boldsymbol{v}^h \in [C(\overline{\Omega})]^d \,;\, \boldsymbol{v}^h_{|_T} \in [P_1(T)]^d,\, T \in \mathcal{T}^h, \quad \boldsymbol{v}^h = \mathbf{0} \text{ on } \Gamma_D\}, \tag{4.20}$$

$$Q^h = \{\boldsymbol{\tau}^h \in [L^2(\Omega)]^{d\times d} \,;\, \boldsymbol{\tau}^h_{|_T} \in [P_0(T)]^{d\times d},\, T \in \mathcal{T}^h\}, \tag{4.21}$$

$$W^h = \{\psi^h \in C(\overline{\Omega}) \,;\, \psi^h_{|_T} \in P_1(T),\, T \in \mathcal{T}^h, \quad \psi^h = 0 \text{ on } \Gamma_D\}, \tag{4.22}$$

$$B^h = \{\xi^h \in Y \,;\, \xi^h_{|_T} \in P_0(T), \quad T \in \mathcal{T}^h\}, \tag{4.23}$$

where Ω is assumed to be a polyhedral domain, $\mathcal{T}^h$ denotes a triangulation of $\overline{\Omega}$ compatible with the partition of the boundary $\Gamma = \partial\Omega$ into Γ_D and Γ_N, and $P_q(T)$, $q = 0, 1$, represents the space of polynomials of global degree less or equal to q in T. Here, $h > 0$ denotes the spatial discretization parameter. Moreover, we define the discrete convex set of admissible apparent density functions as $K^h = K \cap B^h$; that is,

$$K^h = \{\xi^h \in B^h \,;\, \rho_a \leq \xi^h \leq \rho_b \quad \text{in} \quad \Omega\}.$$

Secondly, the time derivatives are discretized by using a uniform partition of the time interval $[0, T]$, denoted by $0 = t_0 < t_1 < \ldots < t_N = T$, and let k be the time step size, $k = T/N$. Moreover, for a continuous function $f(t)$ we denote $f_n = f(t_n)$.

Using the forward Euler scheme, the fully discrete approximation of Problem VP3 is the following.

Problem VP3^{hk}. *Find a discrete displacement field* $\boldsymbol{u}^{hk} = \{\boldsymbol{u}_n^{hk}\}_{n=0}^N \subset V^h$, *a discrete electric potential field* $\varphi^{hk} = \{\varphi_n^{hk}\}_{n=0}^N \subset W^h$ *and a discrete apparent density function* $\rho^{hk} = \{\rho_n^{hk}\}_{n=0}^N \subset K^h$ *such that for all* $\boldsymbol{v}^h \in V^h$, $\psi^h \in W^h$ *and* $\xi^h \in K^h$,

$$c(\rho_n^{hk}; \boldsymbol{u}_n^{hk}, \boldsymbol{v}^h) = (\boldsymbol{f}_n, \boldsymbol{v}^h)_V - ((\rho_n^{hk})^\gamma \mathcal{E}^* \nabla \varphi_n^{hk}, \boldsymbol{\varepsilon}(\boldsymbol{v}^h))_Q, \ n = 0, 1, \ldots, N, \quad (4.24)$$

$$((\rho_n^{hk})^\gamma [\beta \nabla \varphi_n^{hk} - \mathcal{E}\boldsymbol{\varepsilon}(\boldsymbol{u}_n^{hk})], \nabla \psi^h)_H = (q_n, \psi^h)_W, \quad n = 0, 1, \ldots, N, \quad (4.25)$$

$$\left(\frac{\rho_n^{hk} - \rho_{n-1}^{hk}}{k}, \xi^h - \rho_n^{hk}\right)_Y \geq \left(\Phi(\rho_{n-1}^{hk}, \boldsymbol{\sigma}_{n-1}^{hk}, \boldsymbol{\varepsilon}(\boldsymbol{u}_{n-1}^{hk})), \xi^h - \rho_n^{hk}\right)_Y, \quad n = 1, 2, \ldots, N, \quad (4.26)$$

where ρ_0^{hk} denotes an appropriate approximation of the initial condition ρ_0 and the discrete stress field $\boldsymbol{\sigma}^{hk} = (\boldsymbol{\sigma}_n^{hk})_{n=0}^N \subset Q^h$ is given by

$$\begin{aligned} \boldsymbol{\sigma}_n^{hk} = 2\,\mu(\rho_n^{hk})\boldsymbol{\varepsilon}(\boldsymbol{u}_n^{hk}) + \lambda(\rho_n^{hk})\mathrm{Div}\,(\boldsymbol{u}_n^{hk})\mathcal{I} \\ +(\rho_n^{hk})^\gamma \mathcal{E}^* \nabla \varphi_n^{hk}, \quad n = 0, 1, \ldots, N. \end{aligned} \quad (4.27)$$

Using classical results on linear variational inequalities and nonlinear variational equations (see [44]), the existence of a unique solution to discrete problem VP3^{hk} is easily deduced.

In this section, our aim is to provide an error estimate on the numerical errors $\|\boldsymbol{u}_n - \boldsymbol{u}_n^{hk}\|_V$, $\|\varphi_n - \varphi_n^{hk}\|_W$ and $\|\rho_n - \rho_n^{hk}\|_Y$. Thus, we have to make the following assumption on the regularity of the continuous solution:

$$\begin{aligned} &\boldsymbol{u} \in C^1([0,T]; V) \cap C([0,T]; [W^{1,\infty}(\overline{\Omega})]^d), \quad \rho \in C^1([0,T]; Y), \\ &\varphi \in C^1([0,T]; W) \cap C([0,T]; W^{1,\infty}(\overline{\Omega})). \end{aligned} \quad (4.28)$$

Theorem 4.1 *Let assumptions (4.12)-(4.15) hold. Assume that Problem VP3 has a unique solution* $(\boldsymbol{u}, \varphi, \rho)$ *with regularity (4.28) and denote by* $(\boldsymbol{u}^{hk}, \varphi^{hk}, \rho^{hk})$ *the unique solution to Problem VP3*^{hk}. *Then, there exists a positive constant* $C > 0$, *independent of the discretization parameters* h *and* k *but depending on the continuous solution*

$(\boldsymbol{u},\varphi,\rho)$ and the problem data, such that, for all $\{\boldsymbol{v}_n^h\}_{n=0}^N \subset V^h$, $\{\psi_n^h\}_{n=0}^N \subset W^h$ and $\{\xi_n^h\}_{n=0}^N \subset K^h$,

$$\begin{aligned}\max_{0\le n\le N}\{\|\boldsymbol{u}_n-\boldsymbol{u}_n^{hk}\|_V^2+\|\varphi_n-\varphi_n^{hk}\|_W^2+\|\rho_n-\rho_n^{hk}\|_Y^2\}\le C\Big(k\sum_{j=1}^N\Big\{\|\rho_j-\xi_j^h\|_Y^2\\ +\Big\|\frac{\rho_j-\rho_{j-1}}{k}-\dot\rho_j\Big\|_Y^2+\Big\|\Phi_j-\frac{\rho_j-\rho_{j-1}}{k}\Big\|_Y\|\rho_j-\xi_j^h\|_Y\Big\}+\|\varphi_0-\varphi_0^{hk}\|_W^2\\ +\max_{0\le n\le N}\|\rho_n-\xi_n^h\|_Y^2+\max_{0\le n\le N}\|\boldsymbol{u}_n-\boldsymbol{v}_n^h\|_V^2+\|\boldsymbol{u}_0-\boldsymbol{u}_0^{hk}\|_V^2+\|\rho_0-\rho_0^h\|_Y^2\\ +k^2+\max_{0\le n\le N}\|\varphi_n-\psi_n^h\|_W^2+\frac{1}{k}\sum_{j=1}^{N-1}\|\rho_j-\xi_j^h-(\rho_{j+1}-\xi_{j+1}^h)\|_Y^2\Big).\end{aligned}\tag{4.29}$$

Proof First, the error estimates for the apparent density functions were already derived in the previous chapter (see Theorem 3.1) for the case without piezoelectric effects. Proceeding in an analogous way, the following estimates are proved for all $\{\xi_j^h\}_{j=1}^n \subset K^h$:

$$\begin{aligned}&\|\rho_n-\rho_n^{hk}\|_Y^2\\ &\le Ck\sum_{j=1}^n\Big\{\|\boldsymbol{u}_j-\boldsymbol{u}_j^{hk}\|_V^2+\|\rho_j-\rho_j^{hk}\|_Y^2+\|\rho_j-\xi_j^h\|_Y^2+\|\varphi_j-\varphi_j^{hk}\|_W^2\\ &\quad+\Big\|\Phi_j-\frac{\rho_j-\rho_{j-1}}{k}\Big\|_Y\|\rho_j-\xi_j^h\|_Y+\|\rho_j-\rho_{j-1}\|_Y^2+\|\boldsymbol{u}_j-\boldsymbol{u}_{j-1}\|_V^2\\ &\quad+\|\varphi_j-\varphi_{j-1}\|_W^2+\Big\|\frac{\rho_j-\rho_{j-1}}{k}-\dot\rho_j\Big\|_Y^2\Big\}+C\|\rho_n-\xi_n^h\|_Y^2\\ &\quad+\frac{C}{k}\sum_{j=1}^{n-1}\|\rho_j-\xi_j^h-(\rho_{j+1}-\xi_{j+1}^h)\|_Y^2+C\|\rho_1-\xi_1^h\|_Y^2\\ &\quad+C\|\rho_0-\rho_0^{hk}\|_Y^2+C\|\boldsymbol{u}_0-\boldsymbol{u}_0^{hk}\|_V^2+C\|\varphi_0-\varphi_0^{hk}\|_W^2,\end{aligned}\tag{4.30}$$

where we used the notation $\Phi_j=\Phi(\rho_j,\boldsymbol{\sigma}(\boldsymbol{u}_j),\boldsymbol{\varepsilon}(\boldsymbol{u}_j))$ and, here and in what follows, C denotes a generic positive constant which depends on the continuous solution but it is independent of the discretization parameters h and k, and whose value may change from line to line. Moreover, we note that these error estimates depend on the electric potential because the stress field does it too.

Secondly, we turn to estimate the numerical errors on the electric potential and the

displacement field simultaneously. Hence, subtracting variational equation (4.18) at time $t = t_n$ for $\psi = \psi^h \in W^h$ and variational equation (4.25) we find that

$$(\rho_n^\gamma[\beta\nabla\varphi_n - \mathcal{E}\boldsymbol{\varepsilon}(\boldsymbol{u}_n)] - (\rho_n^{hk})^\gamma[\beta\nabla\varphi_n^{hk} - \mathcal{E}\boldsymbol{\varepsilon}(\boldsymbol{u}_n^{hk})], \nabla\psi^h)_H = 0 \qquad \forall\psi^h \in W^h,$$

and therefore,

$$\begin{aligned}(\rho_n^\gamma[\beta\nabla\varphi_n - \mathcal{E}\boldsymbol{\varepsilon}(\boldsymbol{u}_n)] - (\rho_n^{hk})^\gamma[\beta\nabla\varphi_n^{hk} - \mathcal{E}\boldsymbol{\varepsilon}(\boldsymbol{u}_n^{hk})], \nabla(\varphi_n - \varphi_n^{hk}))_H \\ = (\rho_n^\gamma[\beta\nabla\varphi_n - \mathcal{E}\boldsymbol{\varepsilon}(\boldsymbol{u}_n)] - (\rho_n^{hk})^\gamma[\beta\nabla\varphi_n^{hk} - \mathcal{E}\boldsymbol{\varepsilon}(\boldsymbol{u}_n^{hk})], \nabla(\varphi_n - \psi^h))_H\end{aligned}$$

for all $\psi^h \in W^h$.

Taking into account that

$$\begin{aligned}(\rho_n^\gamma[\beta\nabla\varphi_n - \mathcal{E}\boldsymbol{\varepsilon}(\boldsymbol{u}_n)] - (\rho_n^{hk})^\gamma[\beta\nabla\varphi_n^{hk} - \mathcal{E}\boldsymbol{\varepsilon}(\boldsymbol{u}_n^{hk})], \nabla\psi)_H \\ = ((\rho_n^{hk})^\gamma[\beta\nabla(\varphi_n - \varphi_n^{hk}) - \mathcal{E}\boldsymbol{\varepsilon}(\boldsymbol{u}_n - \boldsymbol{u}_n^{hk})], \nabla\psi)_H \\ +((\rho_n^\gamma - (\rho_n^{hk})^\gamma)[\beta\nabla\varphi_n - \mathcal{E}\boldsymbol{\varepsilon}(\boldsymbol{u}_n)], \nabla\psi)_H \quad \forall\psi \in W,\end{aligned}$$

we have

$$\begin{aligned}-((\rho_n^{hk})^\gamma\mathcal{E}\boldsymbol{\varepsilon}(\boldsymbol{u}_n - \boldsymbol{u}_n^{hk}), \nabla(\varphi_n - \varphi_n^{hk}))_H \\ = ((\rho_n^\gamma - (\rho_n^{hk})^\gamma)\mathcal{E}\boldsymbol{\varepsilon}(\boldsymbol{u}_n), \nabla(\varphi_n - \varphi_n^{hk}))_H \\ -((\rho_n^\gamma - (\rho_n^{hk})^\gamma)\beta\nabla\varphi_n, \nabla(\varphi_n - \varphi_n^{hk}))_H \\ -((\rho_n^{hk})^\gamma\beta\nabla(\varphi_n - \varphi_n^{hk}), \nabla(\varphi_n - \varphi_n^{hk}))_H \\ +((\rho_n^{hk})^\gamma\beta\nabla(\varphi_n - \varphi_n^{hk}), \nabla(\varphi_n - \psi^h))_H \\ +((\rho_n^\gamma - (\rho_n^{hk})^\gamma\beta\nabla\varphi_n, \nabla(\varphi_n - \psi^h))_H \\ -((\rho_n^{hk})^\gamma\mathcal{E}\boldsymbol{\varepsilon}(\boldsymbol{u}_n - \boldsymbol{u}_n^{hk}), \nabla(\varphi_n - \psi^h))_H \\ -((\rho_n^\gamma - (\rho_n^{hk})^\gamma)\mathcal{E}\boldsymbol{\varepsilon}(\boldsymbol{u}_n), \nabla(\varphi_n - \psi^h))_H \quad \forall\psi^h \in W^h. \qquad (4.31)\end{aligned}$$

Next, subtracting variational equation (4.17) at time $t = t_n$ for $\boldsymbol{v} = \boldsymbol{v}^h \in V^h$ and

variational equation (4.24) we find that

$$c(\rho_n;\boldsymbol{u}_n,\boldsymbol{v}^h)-c(\rho_n^{hk};\boldsymbol{u}_n^{hk},\boldsymbol{v}^h)+(\rho_n^{\gamma}\mathcal{E}^*\nabla\varphi_n-(\rho_n^{hk})^{\gamma}\mathcal{E}^*\nabla\varphi_n^{hk},\boldsymbol{\varepsilon}(\boldsymbol{v}^h))_Q=0,$$

for all $\boldsymbol{v}^h\in V^h$. Therefore,

$$\begin{aligned}
&c(\rho_n;\boldsymbol{u}_n,\boldsymbol{u}_n-\boldsymbol{u}_n^{hk})-c(\rho_n^{hk};\boldsymbol{u}_n^{hk},\boldsymbol{u}_n-\boldsymbol{u}_n^{hk})\\
&\qquad+(\rho_n^{\gamma}\mathcal{E}^*\nabla\varphi_n-(\rho_n^{hk})^{\gamma}\mathcal{E}^*\nabla\varphi_n^{hk},\boldsymbol{\varepsilon}(\boldsymbol{u}_n-\boldsymbol{u}_n^{hk}))_Q\\
&=c(\rho_n;\boldsymbol{u}_n,\boldsymbol{u}_n-\boldsymbol{v}^h)-c(\rho_n^{hk};\boldsymbol{u}_n^{hk},\boldsymbol{u}_n-\boldsymbol{v}^h)\\
&\qquad+(\rho_n^{\gamma}\mathcal{E}^*\nabla\varphi_n-(\rho_n^{hk})^{\gamma}\mathcal{E}^*\nabla\varphi_n^{hk},\boldsymbol{\varepsilon}(\boldsymbol{u}_n-\boldsymbol{v}^h))_Q\quad\forall\boldsymbol{v}^h\in V^h.
\end{aligned}$$

From the regularity $\boldsymbol{u}\in C([0,T];[W^{1,\infty}(\overline{\Omega})]^{d\times d})$ (which implies that $\boldsymbol{\varepsilon}(\boldsymbol{u}_n)\in[L^\infty(\overline{\Omega})]^{d\times d}$) and keeping in mind that $\rho_n,\rho_n^{hk}\in[\rho_a,\rho_b]$, after easy algebraic manipulations it follows that

$$\begin{aligned}
&c(\rho_n;\boldsymbol{u}_n,\boldsymbol{u}_n-\boldsymbol{u}_n^{hk})-c(\rho_n^{hk};\boldsymbol{u}_n^{hk},\boldsymbol{u}_n-\boldsymbol{u}_n^{hk})=c(\rho_n;\boldsymbol{u}_n,\boldsymbol{u}_n-\boldsymbol{u}_n^{hk})\\
&\qquad-c(\rho_n^{hk};\boldsymbol{u}_n,\boldsymbol{u}_n-\boldsymbol{u}_n^{hk})+c(\rho_n^{hk};\boldsymbol{u}_n,\boldsymbol{u}_n-\boldsymbol{u}_n^{hk})-c(\rho_n^{hk};\boldsymbol{u}_n^{hk},\boldsymbol{u}_n-\boldsymbol{u}_n^{hk})\\
&c(\rho_n^{hk};\boldsymbol{u}_n,\boldsymbol{u}_n-\boldsymbol{u}_n^{hk})-c(\rho_n^{hk};\boldsymbol{u}_n^{hk},\boldsymbol{u}_n-\boldsymbol{u}_n^{hk})\geq C\|u_n-u_n^{hk}\|_V^2\\
&c(\rho_n;\boldsymbol{u}_n,\boldsymbol{u}_n-\boldsymbol{u}_n^{hk})-c(\rho_n^{hk};\boldsymbol{u}_n,\boldsymbol{u}_n-\boldsymbol{u}_n^{hk})\leq C\|\rho_n-\rho_n^{hk}\|_Y\|\boldsymbol{u}_n-\boldsymbol{u}_n^{hk}\|_V,\\
&c(\rho_n;\boldsymbol{u}_n,\boldsymbol{u}_n-\boldsymbol{v}^h)-c(\rho_n^{hk};\boldsymbol{u}_n^{hk},\boldsymbol{u}_n-\boldsymbol{v}^h)\\
&\quad\leq C\|\boldsymbol{u}_n-\boldsymbol{u}_n^{hk}\|_V\|\boldsymbol{u}_n-\boldsymbol{v}^h\|_V+C\|\rho_n-\rho_n^{hk}\|_Y\|\boldsymbol{u}_n-\boldsymbol{v}^h\|_V.
\end{aligned}$$

Keeping in mind that $\rho_n,\rho_n^{hk}\in[\rho_a,\rho_b]$, properties (4.14)-(4.15) and equation (4.31), taking into account that

$$\begin{aligned}
&(\rho_n^{\gamma}\mathcal{E}^*\nabla\varphi_n-(\rho_n^{hk})^{\gamma}\mathcal{E}^*\nabla\varphi_n^{hk},\boldsymbol{\varepsilon}(\boldsymbol{v}))_Q=((\rho_n^{hk})^{\gamma}\mathcal{E}^*\nabla(\varphi_n-\varphi_n^{hk}),\boldsymbol{\varepsilon}(\boldsymbol{v}))_Q\\
&\qquad+((\rho_n^{\gamma}-(\rho_n^{hk})^{\gamma})\mathcal{E}^*\nabla\varphi_n,\boldsymbol{\varepsilon}(\boldsymbol{v}))_Q,\\
&((\rho_n^{hk})^{\gamma}\mathcal{E}^*\nabla(\varphi_n-\varphi_n^{hk}),\boldsymbol{\varepsilon}(\boldsymbol{u}_n-\boldsymbol{u}_n^{hk}))_Q=((\rho_n^{hk})^{\gamma}\mathcal{E}\boldsymbol{\varepsilon}(\boldsymbol{u}_n-\boldsymbol{u}_n^{hk}),\nabla(\varphi_n-\varphi_n^{hk}))_H,
\end{aligned}$$

and the regularity $\varphi\in C([0,T];W^{1,\infty}(\overline{\Omega}))$ (which implies that $\nabla\varphi_n\in[L^\infty(\overline{\Omega})]^d$), using several times the inequality (3.19), it leads to the following estimates for the electric

potential and the displacement field, for all $\boldsymbol{v}^h \in V^h$ and $\psi^h \in W^h$,

$$\begin{aligned} &\|\boldsymbol{u}_n - \boldsymbol{u}_n^{hk}\|_V^2 + \|\varphi_n - \varphi_n^{hk}\|_W^2 \\ &\qquad \leq C\left(\|\boldsymbol{u}_n - \boldsymbol{v}^h\|_V^2 + \|\rho_n - \rho_n^{hk}\|_Y^2 + \|\varphi_n - \psi^h\|_W^2\right). \end{aligned} \tag{4.32}$$

Combining now estimates (4.30) and (4.32) we obtain the following estimates for the numerical errors:

$$\begin{aligned} &\|\boldsymbol{u}_n - \boldsymbol{u}_n^{hk}\|_V^2 + \|\rho_n - \rho_n^{hk}\|_Y^2 + \|\varphi_n - \varphi_n^{hk}\|_W^2 \\ &\quad \leq Ck \sum_{j=1}^{n} \Big\{ \|\boldsymbol{u}_j - \boldsymbol{u}_j^{hk}\|_V^2 + \|\varphi_j - \varphi_j^{hk}\|_W^2 + \|\rho_j - \rho_j^{hk}\|_Y^2 \\ &\qquad + \left\| \Phi_j - \frac{\rho_j - \rho_{j-1}}{k} \right\|_Y \|\rho_j - \xi_j^h\|_Y + \|\rho_j - \rho_{j-1}\|_Y^2 + \|\boldsymbol{u}_j - \boldsymbol{u}_{j-1}\|_V^2 \\ &\qquad + \|\varphi_j - \varphi_{j-1}\|_W^2 + \|\rho_j - \xi_j^h\|_Y^2 + \left\| \frac{\rho_j - \rho_{j-1}}{k} - \dot{\rho}_j \right\|_Y^2 \Big\} + C\|\boldsymbol{u}_n - \boldsymbol{v}_n^h\|_V^2 \\ &\qquad + \frac{C}{k} \sum_{j=1}^{n-1} \|\rho_j - \xi_j^h - (\rho_{j+1} - \xi_{j+1}^h)\|_Y^2 + C\|\rho_1 - \xi_1^h\|_Y^2 + C\|\rho_n - \xi_n^h\|_Y^2 \\ &\qquad + C\|\varphi_n - \psi_n^h\|_W^2 + C\|\rho_0 - \rho_0^{hk}\|_Y^2 + C\|\boldsymbol{u}_0 - \boldsymbol{u}_0^{hk}\|_V^2 + C\|\varphi_0 + \varphi_0^{hk}\|_W^2 \end{aligned}$$

for all $\{\xi_j^h\}_{j=1}^n \subset K^h$, $\boldsymbol{v}_n^h \in V^h$ and $\psi_n^h \in W^h$.

Keeping in mind the regularities $\boldsymbol{u} \in C^1([0,T];V)$, $\varphi \in C^1([0,T];W)$ and $\rho \in C^1([0,T];Y)$ we easily find that

$$k \sum_{j=1}^{n} \left\{ \|\rho_j - \rho_{j-1}\|_Y^2 + \|\varphi_j - \varphi_{j-1}\|_W^2 + \|\boldsymbol{u}_j - \boldsymbol{u}_{j-1}\|_V^2 \right\} \leq Ck^2.$$

Finally, using a discrete version of Gronwall's inequality (see Lemma 2.1) with

$$e_0 = g_0 = \|\boldsymbol{u}_0 - \boldsymbol{u}_0^{hk}\|_V^2 + \|\rho_0 - \rho_0^{hk}\|_Y^2 + \|\varphi_0 - \varphi_0^{hk}\|_W^2,$$

$$e_n = \|\boldsymbol{u}_n - \boldsymbol{u}_n^{hk}\|_V^2 + \|\rho_n - \rho_n^{hk}\|_Y^2 + \|\varphi_n - \varphi_n^{hk}\|_W^2$$

and g_n the remaining terms, we obtain the desired result. □

We notice that the above error estimates are the basis for the analysis of the convergence rate of the algorithm. Hence, under additional regularity assumptions we obtain the linear convergence of the algorithm that we state in the following corollary.

Corollary 4.1 *Let assumptions of Theorem 4.1 hold. Define the initial condition for the apparent density function as follows,*

$$\rho_0^{hk} = \mathcal{P}^h \rho_0,$$

where $\mathcal{P}^h$ is the $L^2(\Omega)$-projection operator onto B^h (see [13]). Under the additional regularity conditions

$$\begin{aligned}
&\boldsymbol{u} \in L^\infty(0,T;[H^2(\Omega)]^d), \quad \varphi \in L^\infty(0,T;H^2(\Omega)),\\
&\rho \in H^2(0,T;Y) \cap H^1([0,T];H^1(\Omega)) \cap C([0,T];H^2(\Omega)),
\end{aligned}$$

the algorithm is linearly convergent; that is, there exists a positive constant $C > 0$, independent of the discretization parameters h and k, such that

$$\max_{0\le n\le N} \left\{ \|\boldsymbol{u}_n - \boldsymbol{u}_n^{hk}\|_V + \|\varphi_n - \varphi_n^{hk}\|_W + \|\rho_n - \rho_n^{hk}\|_Y \right\} \le C(h+k). \tag{4.33}$$

Proof Using the well-known result on the approximations by finite elements and the projection operator $\mathcal{P}^h$, we have (see [13]),

$$\begin{aligned}
&\inf_{v_n^h \in V^h} \|\boldsymbol{u}_n - \boldsymbol{v}_n^h\|_V \le Ch\|\boldsymbol{u}_n\|_{[H^2(\Omega)]^d} \le Ch\|\boldsymbol{u}\|_{C([0,T];[H^2(\Omega)]^d)},\\
&\inf_{\psi_n^h \in W^h} \|\varphi_n - \psi_n^h\|_W \le Ch\|\varphi_n\|_{H^2(\Omega)} \le Ch\|\varphi\|_{C([0,T];H^2(\Omega))},\\
&\inf_{\xi_n^h \in K^h} \|\rho_n - \xi_n^h\|_Y \le Ch\|\rho_n\|_{H^1(\Omega)} \le Ch\|\rho\|_{C([0,T];H^1(\Omega))},\\
&\|\rho_0 - \rho_0^{hk}\|_Y \le Ch\|\rho_0\|_{H^1(\Omega)} \le Ch\|\rho\|_{C([0,T];H^1(\Omega))}.
\end{aligned}$$

Using estimates (4.32) with $n = 0$ we find that

$$\begin{aligned}
&\|\boldsymbol{u}_0 - \boldsymbol{u}_0^{hk}\|_V^2 + \|\varphi_0 - \varphi_0^{hk}\|_W^2\\
&\qquad \le C\left(\|\boldsymbol{u}_0 - \boldsymbol{v}^h\|_V^2 + \|\rho_0 - \rho_0^{hk}\|_Y^2 + \|\varphi_0 - \psi^h\|_W^2\right),
\end{aligned}$$

for all $\boldsymbol{v}^h \in V^h$ and $\psi^h \in W^h$, and the previous result on the approximation of ρ_0 leads to the following estimate,

$$\begin{aligned}\|\boldsymbol{u}_0 - \boldsymbol{u}_0^{hk}\|_V^2 + \|\varphi_0 - \varphi_0^{hk}\|_W^2 \\ \leq Ch^2 \left(\|\rho\|^2_{C([0,T];H^1(\Omega))} + \|\boldsymbol{u}\|^2_{C([0,T];[H^2(\Omega)]^d)} + \|\varphi\|^2_{C([0,T];H^2(\Omega))} \right).\end{aligned}$$

An straightforward estimate implies that

$$k \sum_{j=1}^{N} \left\| \frac{\rho_j - \rho_{j-1}}{k} - \dot{\rho}_j \right\|_Y^2 \leq Ck^2 \|\rho\|^2_{H^2(0,T;Y)},$$

and we also have

$$\begin{aligned}k \sum_{j=1}^{N} \left\| \Phi_j - \frac{\rho_j - \rho_{j-1}}{k} \right\|_Y \|\rho_j - \xi_j^h\|_Y \leq k \sum_{j=1}^{N} \Big\{ \|\Phi_j - \dot{\rho}_j\|_Y \|\rho_j - \xi_j^h\|_Y \\ + \left\| \dot{\rho}_j - \frac{\rho_j - \rho_{j-1}}{k} \right\|_Y \|\rho_j - \xi_j^h\|_Y \Big\} \\ \leq C \max_{1 \leq j \leq N} \|\rho_j - \xi_j^h\|_Y + C \sum_{j=1}^{N} k \Big\{ \left\| \dot{\rho}_j - \frac{\rho_j - \rho_{j-1}}{k} \right\|_Y^2 + \|\rho_j - \xi_j^h\|_Y^2 \Big\}.\end{aligned}$$

Finally, applying the following estimate (proved in [5]):

$$\frac{1}{k} \sum_{n=1}^{N-1} \|\rho_n - \xi_n^h - (\rho_{n+1} - \xi_{n+1}^h)\|_Y^2 \leq Ch^2 \|\rho\|^2_{H^1(0,T;H^1(\Omega))},$$

taking into account that

$$\inf_{\xi_j^h \in K^h} \|\rho_j - \xi_j^h\|_Y \leq Ch^2 \|\rho_j\|_{H^2(\Omega)} \leq Ch^2 \|\rho\|_{C([0,T];H^2(\Omega))},$$

and combining the previous results and error estimates (4.29), we conclude (4.33). □

4.4 Numerical results

In this section we first describe shortly the numerical scheme implemented, and then we present some numerical examples to exhibit its accuracy and its performance and behavior in one-, two- and three-dimensional examples.

Numerical scheme

First, we recall that variational spaces V, Q, W and B are approximated using the finite element spaces V^h, Q^h, W^h and B^h defined by (4.20), (4.21), (4.22) and (4.23), respectively. Moreover, the discrete convex set K^h is given by $K^h = K \cap B^h$.

We notice that, in (4.24) and (4.25), for $n = 0$ the discrete initial apparent density ρ_0^{hk} is given and, for $n = 1, 2, \ldots, N$, ρ_n^{hk} is known. Hence, we obtain the discrete displacement field $\boldsymbol{u}_n^{hk}$ and the discrete electric potential φ_n^{hk} solving the equations:

$$\begin{aligned}
&\boldsymbol{u}_n^{hk} \in V^h, \quad c(\rho_n^{hk}; \boldsymbol{u}_n^{hk}, \boldsymbol{v}^h) = (\boldsymbol{f}_n, \boldsymbol{v}^h)_V - ((\rho_n^{hk})^\gamma \mathcal{E}^* \nabla \varphi_n^{hk}, \boldsymbol{\varepsilon}(\boldsymbol{v}^h))_Q \ \ \forall \boldsymbol{v}^h \in V^h, \\
&\varphi_n^{hk} \in W^h, \quad ((\rho_n^{hk})^\gamma [\beta \nabla \varphi_n^{hk} - \mathcal{E} \boldsymbol{\varepsilon}(\boldsymbol{u}_n^{hk})], \nabla \psi^h)_H = (q_n, \psi^h)_W \ \ \forall \psi^h \in W^h.
\end{aligned}$$

These two coupled discrete linear variational equations lead to a nonsymmetric linear system in terms of a product variable $\boldsymbol{x}_n = (\boldsymbol{u}_n^{hk}, \varphi_n^{hk})$, which is solved by using the LU decomposition method. Next, the discrete stress field is updated by using the equation,

$$\boldsymbol{\sigma}_n^{hk} = 2\,\mu(\rho_n^{hk}) \boldsymbol{\varepsilon}(\boldsymbol{u}_n^{hk}) + \lambda(\rho_n^{hk}) \mathrm{Div}\,(\boldsymbol{u}_n^{hk}) \mathcal{I} + (\rho_n^{hk})^\gamma \mathcal{E}^* \nabla \varphi_n^{hk}.$$

Now, for $n = 1, 2, \ldots, N$, in (4.26) $\boldsymbol{u}_{n-1}^{hk}$, $\boldsymbol{\sigma}_{n-1}^{hk}$ and ρ_{n-1}^{hk} are known. The discrete apparent density function ρ_n^{hk} is then obtained from (4.26):

$$\begin{aligned}
\rho_n^{hk} \in K^h, \quad \left(\rho_n^{hk}, \xi^h - \rho_n^{hk}\right)_Y \geq \ & k \left(\Phi(\rho_{n-1}^{hk}, \boldsymbol{\sigma}_{n-1}^{hk}, \boldsymbol{\varepsilon}(\boldsymbol{u}_{n-1}^{hk})), \xi^h - \rho_n^{hk}\right)_Y \\
& + \left(\rho_{n-1}^{hk}, \xi^h - \rho_n^{hk}\right)_Y \quad \forall \xi^h \in K^h.
\end{aligned}$$

This leads to a variational inequality of the first kind which is solved using a penalty-duality algorithm that can be seen, for instance, in [68].

A one-dimensional example: the numerical convergence

As a one-dimensional example, the following problem is considered.

Problem P3-1D. *Find a displacement field* $u : [0,1] \times [0,1] \to \mathbb{R}$*, an electric potential field* $\varphi : [0,1] \times [0,1] \to \mathbb{R}$ *and an apparent density function* $\rho : [0,1] \times [0,1] \to [0.01, 1.74]$ *such that:*

$$
\begin{aligned}
&-\frac{\partial \sigma}{\partial x}(x,t) = 0 \quad x \in (0,1),\, t \in (0,1),\\
&-\frac{\partial D}{\partial x}(x,t) = 0 \quad x \in (0,1),\, t \in (0,1),\\
&\dot{\rho}(x,t) = \left(\frac{\sigma(x,t)\frac{\partial u}{\partial x}(x,t)}{2\rho(x,t)} - 0.004 \right) \quad x \in [0,1],\, t \in [0,1],\\
&u(0,t) = 0 \quad t \in (0,1),\\
&\varphi(0,t) = 0 \quad t \in (0,1),\\
&\sigma(1,t) = -10^{-4}\, e^{t} \quad t \in (0,1),\\
&\rho(x,0) = 0.8 \quad x \in [0,1],
\end{aligned}
$$

where the stress field $\sigma : [0,1] \times [0,1] \to \mathbb{R}$ *and the electric displacement field* $D : [0,1] \times [0,1] \to \mathbb{R}$ *are given by*

$$
\begin{aligned}
&\sigma(x,t) = M(\rho(x,t))^3 \frac{\partial u}{\partial x}(x,t) - 2 \times 10^{-9} (\rho(x,t))^3 \frac{\partial \varphi}{\partial x}(x,t) \quad x \in (0,1),\, t \in (0,1),\\
&D(x,t) = 2 \times 10^{-9} (\rho(x,t))^3 \frac{\partial u}{\partial x}(x,t)\\
&\qquad\qquad +190 \times 10^{-15} (\rho(x,t))^3 \frac{\partial \varphi}{\partial x}(x,t) \quad x \in (0,1),\, t \in (0,1).
\end{aligned}
$$

Problem **P3-1D** corresponds to Problem P3 with the following data, keeping in mind that the area of the cross-section is $A = 1m^2$:

$$
\Omega = (0,1), \quad T = 1\, day, \quad E(\rho) = M\rho^{\gamma}, \quad M = 3790\, Nm^2/Kg^2, \quad \gamma = 3,
$$

$$
B = 1, \quad S_r = 0.004\, Kg/ms, \quad \beta = 190 \times 10^{-15}\, F/mm \quad \mathcal{E} = 2 \times 10^{-9}\, C/mm^2,
$$

$$\rho_a = 0.01\, g/cm^3, \quad \rho_b = 1.740\, g/cm^3, \quad \rho_0 = 0.8\, g/cm^3,$$

$$f = 0\, N/m, \quad g(t) = -10^{-4} e^t\, N \quad \text{for} \quad t \in [0,1].$$

Our aim here is to show the numerical convergence of the algorithm. Therefore, several uniform partitions of both the time interval and the domain, dividing $\Omega = (0,1)$ into n segments, have been performed. We note that the spatial discretization parameter h equals to $\dfrac{1}{n}$, and we used the solution obtained with $n = 2^{12}$ and $k = 10^{-4}$ as the "exact solution".

The numerical errors, given by

$$E^{hk} = \max_{0 \le n \le N} \Big\{ \|\boldsymbol{u}_n - \boldsymbol{u}_n^{hk}\|_V + \|\rho_n - \rho_n^{hk}\|_Y + \|\varphi_n - \varphi_n^{hk}\|_W \Big\},$$

and obtained for different discretization parameters h and k, are depicted (multiplied by 100) in Table 4.1. Moreover, the evolution of the error depending on $h+k$ is plotted in Figure 4.2. We notice that the convergence of the algorithm is clearly observed, and

$n \downarrow \; k \rightarrow$	0.1	0.05	0.01	0.005	0.001	0.0005	0.0001
16			0.473426	0.473064	0.472774	0.472738	0.472709
32	157.9005	76.30889	0.235741	0.235561	0.235416	0.235398	0.235383
64	124.1726	0.117657	0.116933	0.116842	0.116771	0.116761	0.116754
128	0.058353	0.057899	0.057537	0.057492	0.057456	0.057451	0.057448
256	0.028249	0.028022	0.027841	0.027819	0.027801	0.027798	0.027797
512	0.013198	0.013084	0.012994	0.012983	0.012974	0.012972	0.012972
1024	0.005672	0.005615	0.005571	0.005565	0.005561	0.005559	0.005559

Table 4.1: Example **P3-1D**: Numerical errors (x100) for some h and k.

the linear convergence, stated in Corollary 4.1, seems to be achieved.

Numerical results for two and three dimensional problems: predicting bone formation and resorption

Our aim here is to numerically show that bone formation and resorption may be related to electrical charges in the bone surfaces due to contributions produced by the mechanical loading $\mathbf{D}_{\boldsymbol{\varepsilon}}$. Hence, we consider a diaphysis of a long bone and an osteon under

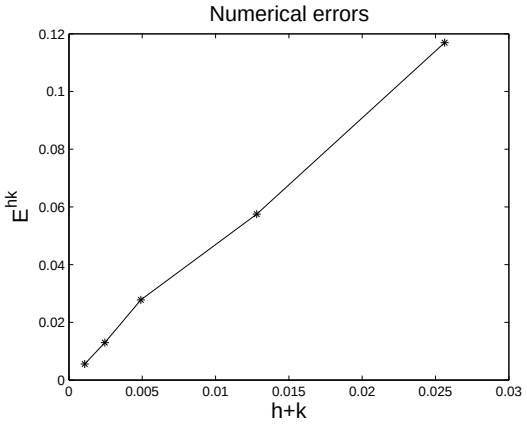

Figure 4.2: Example **P3-1D**: Asymptotic constant error.

compressive and torsional loads, in order to understand its mechano-electric behavior. For these two examples, we will only consider one time step, because our study reflects the bone formation and resorption on bone surface.

Diaphysis of a long bone with a malaligned fracture

In the first example, we consider a diaphysis of a fractured long bone which is healed in an angulated position, forming 10° with the vertical direction. It is known that in this situation, the bone tends to become straighter and bone formation occurs on concave surface while bone resorption takes place on convex surfaces.

We will assume that the length of the diaphysis is 150mm and the diameter 27mm (see [18]). Moreover, it has an internal part formed by cancellous bone, with a density of 0.8 g/cm^3 and two layers of 7mm thickness of cortical bone with a higher density of 1.6 g/cm^3. We apply a compression force on the upper boundary, with a maximum value of 5MPa. We have chosen this load in order to obtain a maximum deformation between 2000 and 3000$\mu\varepsilon$ (see [53]). Finally we have fixed the potential and displacement fields on the lower boundary (see Figure 4.3). As a first approach, we model this example using a plane strain hypothesis. We consider that the horizontal direction is

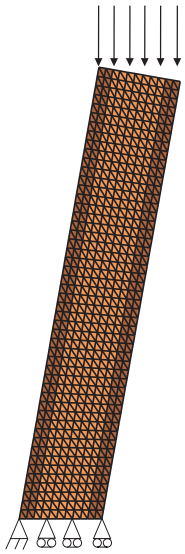

Figure 4.3: Diaphysis of a long bone.

the number 1 and the vertical direction number 3, according to the notation introduced in Section 4.1. Then, considering the two dimensional case, on the piezoelectric tensor only appear the components e_{31}, e_{33} and e_{15}.

In order to show the behavior of the electric displacement we have analyzed in Figure 4.4 the normal electric displacement due to mechanical conditions ($\mathbf{D}_{\boldsymbol{\varepsilon}} \cdot \boldsymbol{\nu} = \alpha(\rho)\mathcal{E}\boldsymbol{\varepsilon}(\boldsymbol{u}) \cdot \boldsymbol{\nu}$) on the boundaries of both cortical layers. We have plotted in blue the curves corresponding to the left cortical and in red for the right cortical. We can observe that the concave surfaces, marked with circles, where the bone is forming, takes positive electrical values, whereas the convex surfaces, marked with cross, takes negative electrical values because the bone is resorbed. This result is obtained due to the expression of the piezoelectric tensor $\mathcal{E}$ and the distribution of the strains in the cortex. Since the normal vector to the surfaces is perpendicular to 3, then the normal strains have no effect on the electrical displacement which is regulated by the shear strains on the bone surfaces (see Figure 4.5) that occur as a consequence of the inclination of the load with respect to the bone axis.

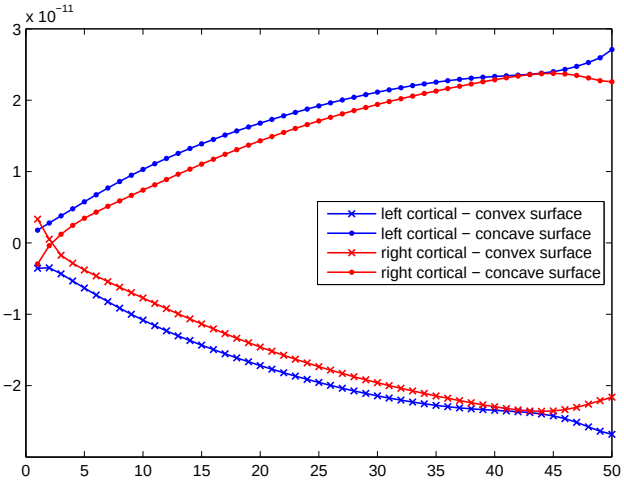

Figure 4.4: The normal electric displacement due to mechanical effects ($\mathbf{D}_{\boldsymbol{\varepsilon}}$).

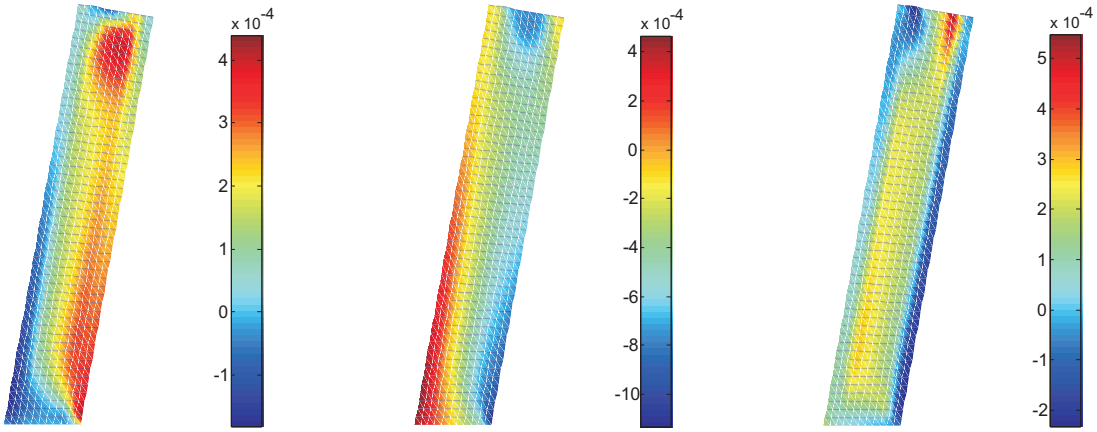

(a) (b) (c)

Figure 4.5: Shear strain distribution on the bone: (a) x-component (b) y-component and (c) xy-component

Analysis of one osteon in progression

In the second example, we analyze the bone remodeling in an osteon. In Figure 4.6 we can see the 3D finite element mesh of this osteon. The cylindrical tunnel and the spherical cutting cone have a diameter of 200μm, which is representative for a resorption cavity in human cortical bone. The outer diameter of the piece of bone in the model is 700μm. The bone is assumed to be loaded in compression along its longitudinal

direction at maximum load during a walking cycle and a torsional load is also applied (see [4]). Moreover, we have fixed the electric potential field on the outer boundary. In order to simulate a piece of cortical bone, we assume that the density is 1.6 g/cm^3.

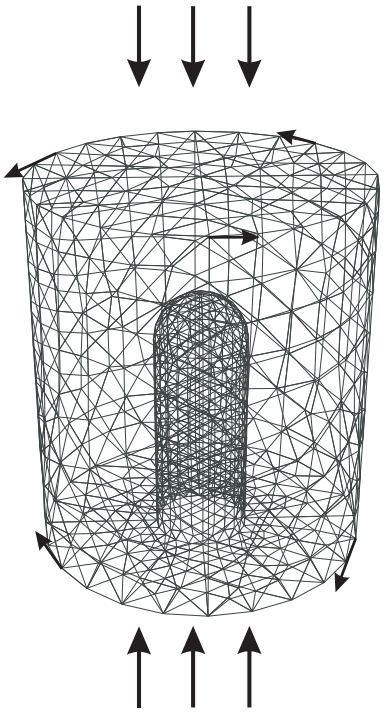

Figure 4.6: Osteon under compressive and torsional loads.

It is known that bone remodeling occurs in local groups of osteoblasts and osteoclasts called bone multicellular units (BMU), where each unit is organized into "cutting cone" of osteoclasts reabsorbing bone followed by osteoblasts refilling the bone defect left by osteoclasts [36]. In order to understand this behavior in function of the electromechanical behavior of the bone we have analyzed the normal electric displacement due to mechanical effects ($\mathbf{D}_{\boldsymbol{\varepsilon}}$) on the cylindrical tunnel and the spherical cutting cone. In Figure 4.7 we can observe these values on a vertical section of the osteon. When we apply the compressive and torsional loads we can observe that this value is positive in the cylindrical part, where normally osteoblasts deposit bone matrix and is negative at the tip of the cutting cone. Moreover, the normal vector to the surface coincides

there with the direction 3 and therefore, the normal strains contribute to the electrical displacement, mainly the strain in the direction 3 (z direction) (see Figure 4.8). However, in the cylindrical surface of the osteon, the normal to the surface is perpendicular to the direction 3 and therefore, only the shear strains influence on the electrical displacement. In the transition zone between the cutting zone and the cylindrical zone the normal is changing and there is a coupled contribution of the normal and shear strains.

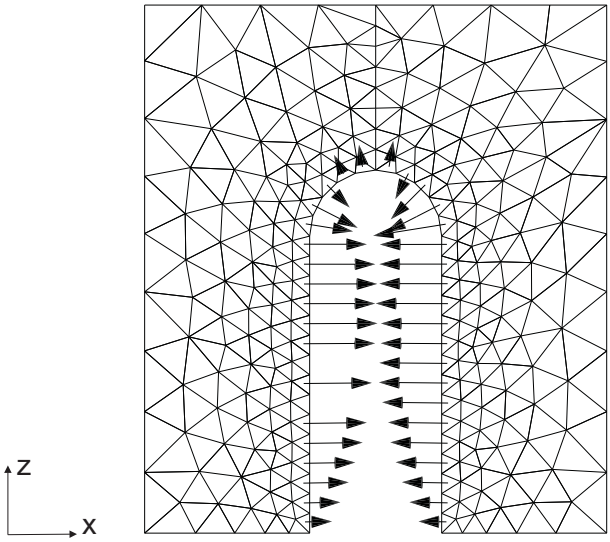

Figure 4.7: Normal electric displacement due to mechanical effects under compressive and torsional loads.

Then, we have to remark the importance of the torsional load, because if we only consider the compressive load, we can see in Figure 4.9 how only negative electrical displacements occur in the cutting cone. Meanwhile, in the cylindrical tunnel of the osteon these electrical displacements are zero. It is due to the fact that, under compression loads, shear strains are zero in this zone. However, with torsional loads, shear strains are different from zero producing an electrical displacement perpendicular to the bone surface.

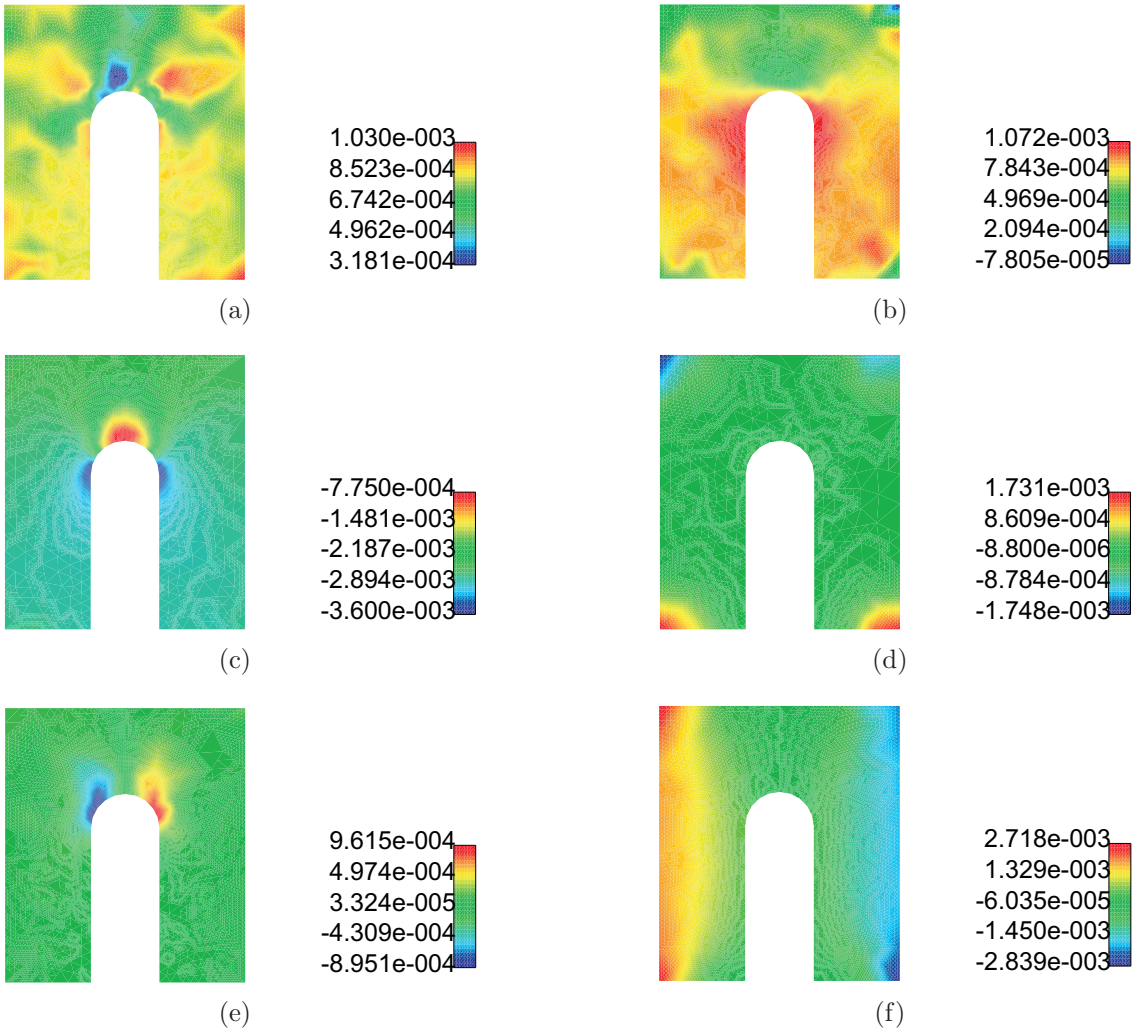

Figure 4.8: Strain distribution around the osteon: (a) x-component, (b) y-component, (c) z-component, (d) xy-component, (e) xz-component and (f) yz-component

A femur model

As a final example, we will consider a complete bone remodeling process in a proximal femur. Our aim here is, first, to reproduce the simulation performed in the previous chapter considering the piezoelectric model. Hence, now we will obtain electrical effects

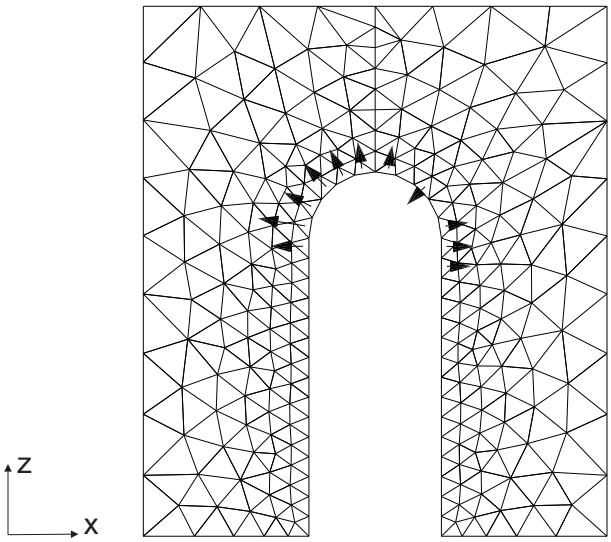

Figure 4.9: Normal electric displacement due to mechanical effects under compressive loads.

due to the mechanical loads that are acting on the bone. As we explain there, the daily load history is represented using three loading cases acting sequentially. Each load consists in one compressive load acting on the femoral head plus the reaction force induced in the abductor muscle. In order to avoid the lack of connection between the cortical layers of the diaphysis, we include a side plate joining both layers (see Section 3.4 for more details). We assume that the lower horizontal boundary is fixed through the vertical direction meanwhile the left point is clamped. Moreover, in this point the potential field is equal to zero. We consider a plain strain hypothesis in which the proximal femur has a uniform thickness of 10mm and the side plate 1mm.

The following data have been used in this simulation:

$$T = 300\,days, \quad E(\rho) = M\rho^{\gamma}, \quad M = 3790\,Pa/(Kg\,m^{-2})^2, \quad \gamma = 3,$$
$$\boldsymbol{f} = \mathbf{0}\,N/m^2, \quad B = 1\,(g\,cm^{-3})^2(MPa\,day)^{-1}, \quad S_r = 0.004\,J/g,$$
$$\kappa = 0.3, \quad \rho_a = 0.01\,g/cm^3, \quad \rho_b = 1.740\,g/cm^3, \quad \rho_0 = 0.8\,g/cm^3,$$

$$\beta_{11} = 88.54 \times 10^{-12} F/mm, \quad \beta_{33} = 106.248 \times 10^{-12} F/mm,$$
$$e_{31} = 1.50765 \times 10^{-9} C/mm^2, \quad e_{33} = 1.87209 \times 10^{-9} C/mm^2,$$
$$e_{15} = 3.57643 \times 10^{-9} C/mm^2.$$

In Figure 4.10 we can observe the final configuration of the bone density after 300 days. The end configuration predicts a reasonable accurate density distribution with an intramedullary canal. As it was also noticed in the previous chapter, Ward's triangle and the typical cancellous density patterns in this femoral head are shown. Comparing these results with those obtained in the previous chapter for the model without piezoelectricity, we can observe that, in this example, the electrical field does not have an important influence on the distribution of the bone density, maybe because the potential field generated by these mechanical loads is small. In Figure 4.11 the electric potential is plotted at different instants of the 215 day. We can observe several varia-

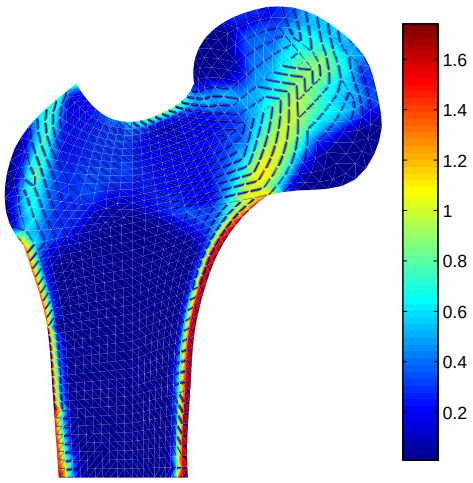

Figure 4.10: Bone density after 300 days.

tions in the distribution of electric charges and in its values, caused by the application of the different mechanical loads.

Then, we will assume that between day 300 and day 400 the physical activity is re-

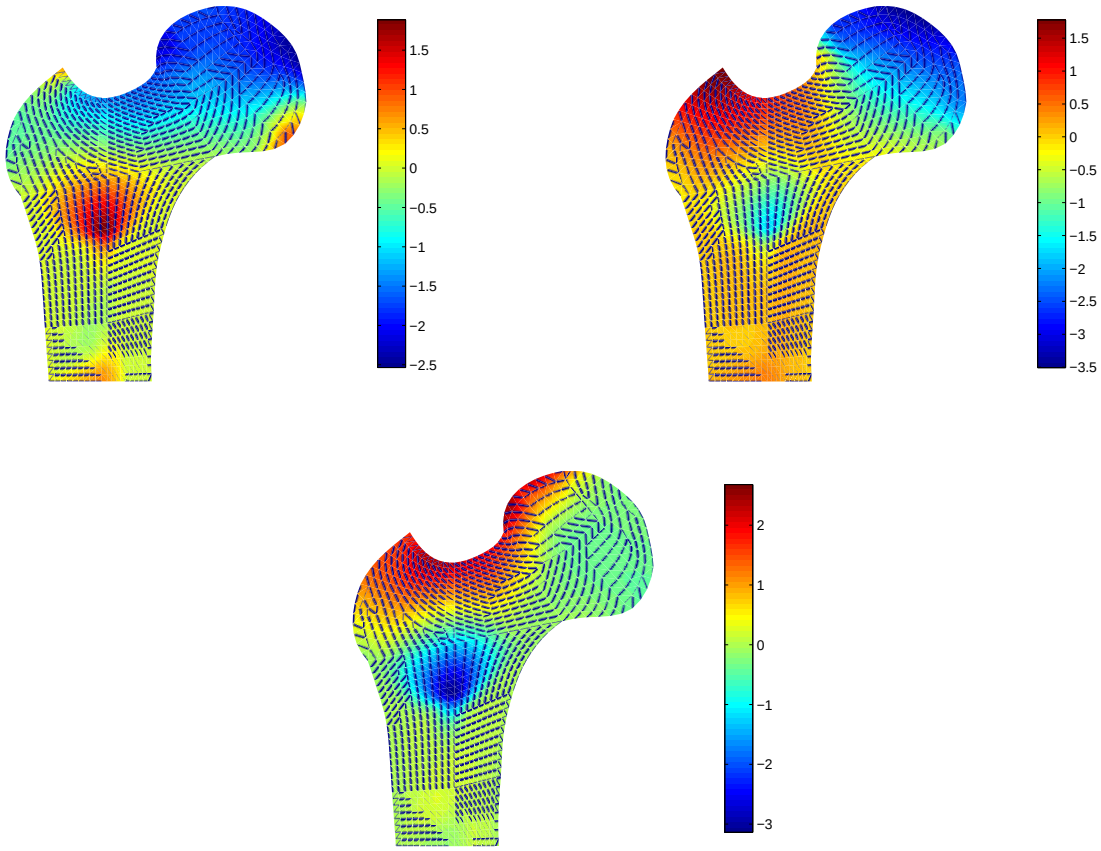

Figure 4.11: The potential field at several times (t=215, 215.2 and 215.4).

duced and the mechanical loads are applied one of each three days. As we can observe in Figure 4.12, the bone density in the femoral head at time T=400 days is lower than at time T=300 days.

Probably, the most important advantage of considering the piezoelectric effects in bone remodeling is the ability to change the bone density applying electric charges. As we explained along this Ph.D. thesis, the mechanical loads are the responsible of the changes in the internal structure of the bone. Moreover, when we apply an electric charge in a piezoelectric material, we obtain an associated mechanical displacement and, in a bone, we obtain a change in the bone density. In the following simulations we will try to show how an electrical charge can change the bone density distribution.

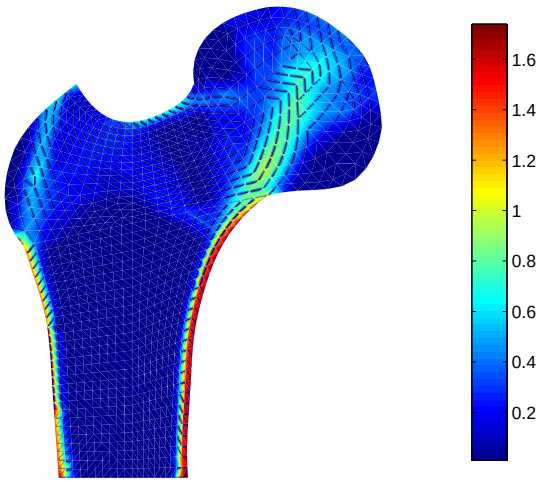

Figure 4.12: Bone density after a period of reduce physical activity (T=400 days).

Then, we will assume the configuration obtained after 300 days and we will consider that an electric charge is applied, on three different parts of the bone, during a period of reduced physical activity (see Figure 4.13). Moreover, we will compare the bone density corresponding to each case with that previously obtained when no electrical forces were applied (Figure 4.12).

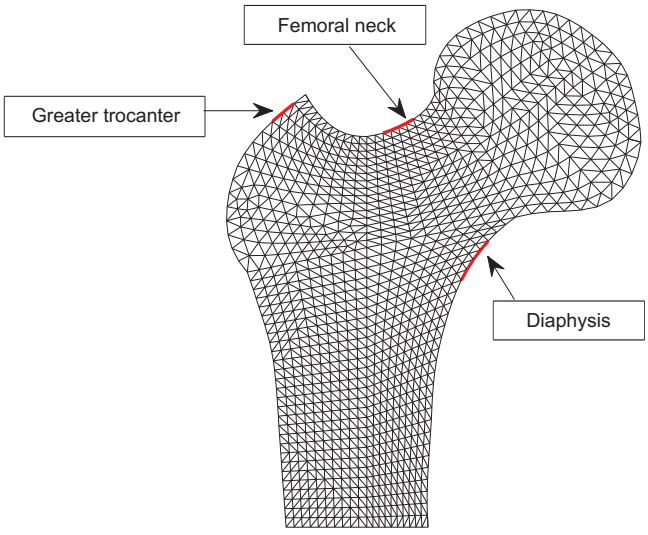

Figure 4.13: Boundaries for the electric charge.

An electric charge on the greater trocanter.

In this first case, an electric load is applied in the greater trocanter (see Figure 4.13) between days 300 and 400. During this time, the mechanical loads are applied only one of each three days. Applying the electrical surface charge of $2 \times 10^{-9} C/mm^2$ we obtain a negative potential field with a maximum intensity of $-50V$ (see Figure 4.14). In order to show the variation of the bone density, we have plotted in Figure 4.15 the

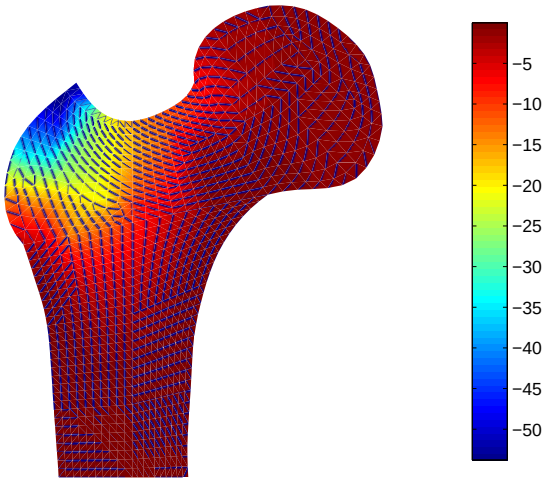

Figure 4.14: Electric potential after a period of reduced physical activity (T=400 days) in which an electric charge is acting on the greater trocanter.

difference between the bone density, when an electric charge is applied and the bone density when only the mechanical loads are acting. In spite of the small differences obtained, we can observe that in the areas in red an increment in the bone density has been produced. However, in the areas in blue the bone density has decreased when the electric charge has been applied.

An electric charge on the diaphysis.

In the second example we will apply an electric load on the upper part of the diaphysis (see Figure 4.13). In this case an electrical surface charge of $5 \times 10^{-8} C/mm^2$ is applied.

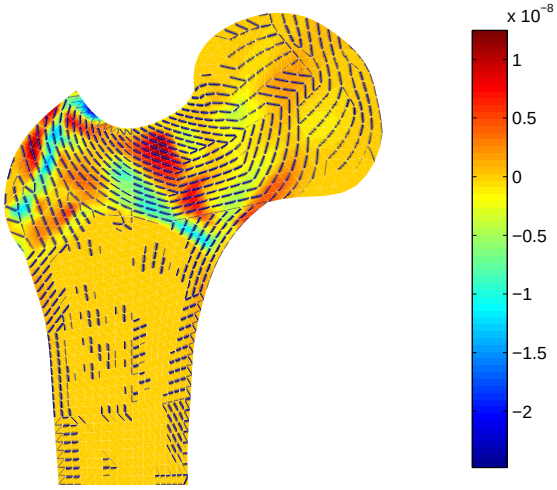

Figure 4.15: Differences between the bone density when an electric charge is applied and the bone density when only the mechanical loads are acting (T=400 days).

In Figure 4.16 we can see that the electric charge produces a potential field with a maximum intensity of $-40V$.

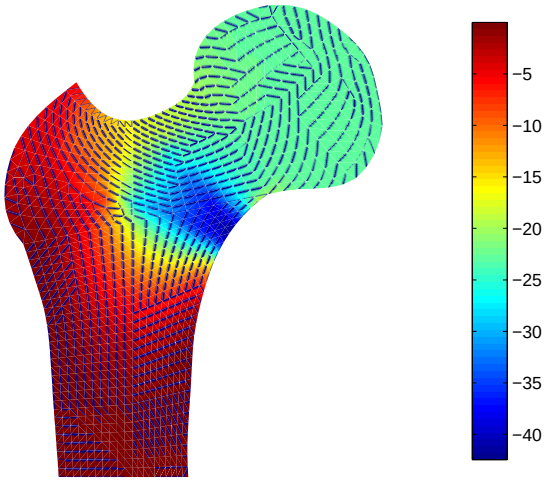

Figure 4.16: Electric potential after a period of reduced physical activity (T=400 days) in which an electric charge is acting on the diaphysis.

The differences between the bone density, when only the mechanical loads are acting, and when an electric charge is applied are plotted in Figure 4.17. In this case, the electric charge affects, mainly, to the closer area of the application point, producing an increase of the bone density near of the cortical bone.

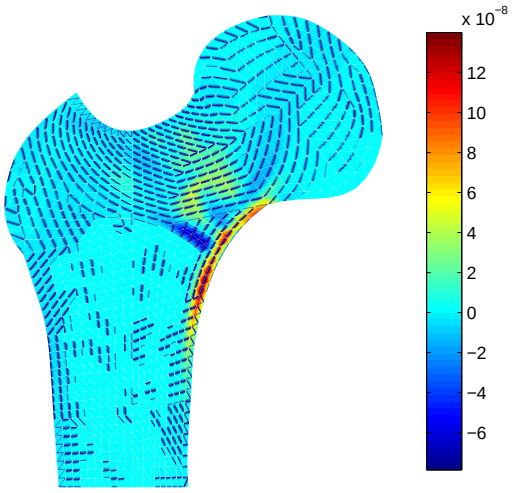

Figure 4.17: Differences between the bone density when an electric charge is applied and the bone density when only the mechanical loads are acting (T=400 days).

An electric charge on the femoral neck.

As a final example, we will consider an electrical charge of $2 \times 10^{-9} C/mm^2$ acting on the upper part of the femoral neck (see Figure 4.13). The potential field at 400 days is plotted in Figure 4.18. In this case, the porosity decreases in several areas, remarking those areas with higher density (see Figure 4.19).

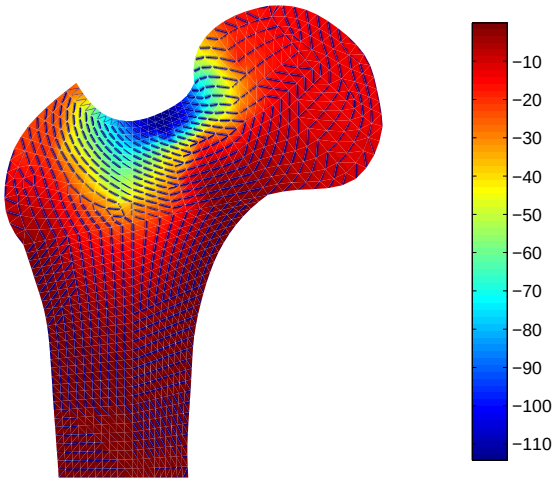

Figure 4.18: Electric potential after a period of reduced physical activity (T=400 days) in which an electric charge is applied.

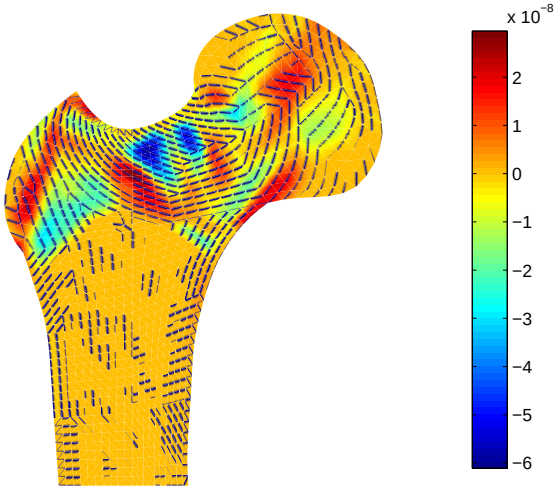

Figure 4.19: Differences between the bone density when an electric charge is applied and the bone density when only the mechanical loads are acting (T=400 days).

Conclusions

In the course of this Ph.D. thesis we studied several bone remodeling models, trying to develop a complete study from the mathematical and physical points of view.

In Chapter 2, the Cowin and Hegedus model was introduced. In this model, the bone is considered as an elastic material. A variational formulation was provided, obtaining an elliptic variational equation for the displacement field and an ordinary differential equation which describes the evolution of the bone density. Applying the finite element method and an Euler scheme to approximate the spatial variable and the time derivatives, respectively, we obtained a fully discrete problem and we proved an error estimates result. Moreover, under additional regularity assumptions, we derived the linear convergence of the algorithm. Numerical simulations in one, two and three dimensions were presented to show the accuracy and the behavior of the approximations.

In the second part of this chapter, we considered a similar problem assuming now that the bone may come into contact with a rigid or a deformable obstacle. In order to model these two contact conditions, we used the classical Signorini condition and the normal compliance contact law, respectively. The variational formulation was obtained for both problems and the convergence of the solution to the contact problem with a deformable obstacle, when the deformability coefficient tends to zero, to the solution of the Signorini's problem was established. We introduced fully discrete aproximations and we proved an error estimates result for both problems. Finally, under additional regularity assumptions, we obtained the linear convergence of the algorithm and some simulations were also presented.

The third chapter dealt with the numerical analysis, including numerical simulations in one and two dimensions, of a bone remodeling model introduced by Weinans, Huiskes and Grootenboer in [66]. A numerical algorithm for the variational problem, based on the finite element method to approximate the spatial variable and an Euler scheme to discretize the time derivatives, was proposed, an error estimate on its solutions was obtained and its linear convergence was established under suitable regularity assumptions. The numerical simulations demonstrated the accuracy of the approximations and some properties related to the behavior of the solution.

Finally, in the last chapter, we proposed a new bone remodeling model in which we considered the bone as an piezoelectric material. This property of the bone tissue was suggested in 1957. However, it was not normally used to understand bone remodeling and there are not many models that justify bone remodeling based on bone piezoelectricity. We continued the work developed in the previous chapter, using this model to characterize the evolution of the bone density and the mechanical properties of the bone. Then, we extended the classical electro-mechanical dependence adding a function $\alpha(\rho) = \rho^\gamma$, which regulates the coupling between the mechanical and electric fields. This function guarantees that the electric field increases with the density of the bone. The variational formulation for this model was derived and a numerical algorithm was proposed, coupling the electric and displacement fields. Finally, error estimates were proved and the linear convergence was established under adequate regularity conditions. Again, the numerical results shown the accuracy of the approximations as well as the behavior of the solution, giving also a numerical justification of the electro-mechanical bone remodeling model.

All the algorithms proposed in this Ph.D. thesis were implemented using MATLAB code and a good number of examples were computed. First, the one-dimensional examples were chosen in such a way as to show the numerical convergence of the algorithms and also their linear convergence. Then, two- or three-dimensional examples were per-

formed in order to show the behavior of the models.

The existence and uniqueness of weak solutions for the discrete problems were obtained applying classical results on linear variational equations or nonlinear variational inequalities (see [44]). However, we remark that the existence and uniqueness results of weak solutions for the continuous variational formulations are open problems. In the Cowin and Hegedus model, this result was obtained for a similar variational formulation in which stronger assumptions were made over the data. Recently, Fernández and Kuttler dealt with the model proposed by Weinans, Huiskes and Grootenboer obtaining an existence and uniqueness result for a regularized problem.

Bibliography

[1] R.A. Adams, *Sobolev spaces*, 1^{st} edition, Pure and applied mathematics, Academic Press (1975).

[2] A.C. Ahn and A.J. Grodzinsky, Relevance of collagen piezoelectricity to "Wolff's Law": A critical review, *Medical Engineering and Physics* **31** (2009) 733-741.

[3] J.C. Anderson and C. Eriksson, Piezoelectric properties of dry and wet bone, *Nature* **227** (1970) 491-492.

[4] V. Báca, D. Kachlík, Z. Horák and J. Stingl, The course of osteons in the compact bone of the human proximal femur with clinical and biomechanical significance, *Surg. Radiol. Anat.* **29**(2007) 201-207.

[5] M. Barboteu, J.R. Fernández and T.-V. Hoarau-Mantel, A class of evolutionary variational inequalities with applications in viscoelasticity, *Math. Models Methods Appl. Sci.* **15**(10) (2005) 1595–1617.

[6] C.A. Basset and R.O. Becker, Generation of electric potentials by bone in response to mechanical stress, *Science* **137** (1962) 1063-1064.

[7] C.A. Basset and R.J. Pawluk and R.O. Becker, Effects of electric currents on bone in vivo, *Nature* **204** (1964) 652-654.

[8] G.S. Beaupré, T.E. Orr and D.R. Carter, An approach for time-dependent bone modeling and remodeling-theoretical development, *J. Orthop. Res.* **8** (1990) 651–661.

[9] A. Bermúdez and C. Moreno, Duality methods for solving variational inequalities, *Comp. Math. Appl.* **7**

[10] J.A. Buckwater, M.J. Glimcher, R.R. Cooper and R. Recker, Bone biology. Part I, *J. Bone Joint Surg. Am.* **77** (1995) 1256–1275

[11] J.A. Buckwater, M.J. Glimcher, R.R. Cooper and R. Recker, Bone biology. Part II, *J. Bone Joint Surg. Am.* **77** (1995) 1276–1289

[12] M. Campo, J.R. Fernández, K.L. Kuttler and M. Shillor, Quasistatic evolution of damage in an elastic body: numerical analysis and computational experiments, *Appl. Numer. Math.* **57** (9) (2007) 975–988.

[13] P.G. Ciarlet, *The Finite Element Method for Elliptic Problems,* in Handbook of Numerical Analysis, Volume II, Part 1, Eds. P.G. Ciarlet and J.L. Lions, North Holland (1991), 17–352.

[14] S.C. Cowin, The exact stimulus for the strain adaptation of bone tissue is unknown, *J. Biomech. Sci. Engrg.* **1** (1) (2006), 16–28.

[15] S.C. Cowin and D.H. Hegedus, Bone remodeling I: theory of adaptive elasticity, *J. Elasticity* **6** (3) (1976) 313–326.

[16] S.C. Cowin and R.R. Nachlinger, Bone remodeling III: uniqueness and stability in adaptive elasticity theory, *J. Elasticity* **8** (3) (1978) 285–295.

[17] S.C. Cowin and W.C. Van Buskirk, Internal bone remodeling induced by a medullary pin, *J. Biomech* **11** (1978) 269–275.

[18] S.L. Croker, J.G. Clement and D. Donlon, A comparison of cortical bone thickness in the femoral midshaft of humans and two non-human mammals, *Journal of Comparative Human Biology* **60** (2009) 551–565.

[19] M. Doblaré and J.M. García-Aznar, Application of an anisotropic bone-remodelling model based on a damage-repair theory to the analysis of the proximal femur before and after total hip replacement, *J. Biomech.* **34** (9) (2001) 1157-1170.

[20] J.R. Fernández, I.N. Figueiredo and R. Martínez, A convergence result in the study of bone remodeling contact problems, *J. Math. Anal. Appl.* **343**(2) (2008) 951–964.

[21] J.R. Fernández, J.M. García-Aznar and R. Martínez, Piezoelectricity could predict sites of formation/resorption in bone modelling, *Preprint* (2010).

[22] J.R. Fernández, J.M. García-Aznar and R. Martínez, Numerical analysis of a piezoelectric bone remodeling problem. *Preprint* (2010).

[23] J.R. Fernández, J.M. García-Aznar, R. Martínez and J.M. Viaño, Numerical analysis of a strain-adaptive bone remodelling problem, *Comput. Methods Appl. Mech. Engrg.* **199** (2010) 1549–1557.

[24] J.R. Fernández and K.L. Kuttler, An existence and uniqueness result for an elasto-piezoelectric problem with damage, *Math. Models Methods Appl. Sci.* **19**(1) (2009) 31–50.

[25] J.R. Fernández and K.L. Kuttler, An existence and uniqueness result for a bone remodeling problem, *Nonlinear Anal. Real World Appl.* (in press).

[26] J.R. Fernández and R. Martínez, Numerical analysis of a contact problem including bone remodeling, *J. Comput. Appl. Math.* (in press).

[27] J.R. Fernández and R. Martínez, Numerical analysis of a bone remodelling contact problem, *Proceedings of the CMIS 2009 Conference*, Springer (to appear).

[28] J.R. Fernández, R. Martínez and J.M. Viaño, Analysis of a bone remodeling model, *Commun. Pure Appl. Anal.* **8**(1) (2009) 255–274.

[29] J.R. Fernández, R. Martínez and J.M. Viaño, Numerical analysis of a strain-adaptive bone remodelling process including contact, *Preprint* (2009).

[30] I.N. Figueiredo, Approximation of bone remodeling models, *J. Math. Pures Appl.* **84** (2005) 1794–1812.

[31] I.N. Figueiredo, C. Leal and C.S. Pinto, Shape analysis of an adaptive elastic rod model, *SIAM J. Appl. Math.* **66**(1) (2005) 153–173.

[32] I.N. Figueiredo, C. Leal and C.S. Pinto, Conical differentiability for bone remodeling contact rod models, ESAIM: *Control, Optimisation and Calculus of Variations* **11**(3) (2005) 382–400.

[33] I.N. Figueiredo and L. Trabucho, Asymptotic model of a nonlinear adaptive elastic rod, *Math. Mech. Solids* **9**(4) (2004) 331–354.

[34] K. Firoozbakhsh and S.C. Cowin, Devolution of inhomogeneities in bone structure-predictions of adaptive elaticiy thory, *J. Biomech. Engrg.* **102** (1980) 287–293.

[35] D.I. Fotiadis, G. Foutsitzi and C.V. Massalas, Wave propagation modeling in human long bones, *Acta Mechanica* **137** (1999) 65–81.

[36] H.M. Frost, Tetracycline-based histological analysis of bone remodelling, *Calcif. Tissue Res.* **2** (1969) 211–237.

[37] H.M. Frost, *The laws of bone structure*, Springfield (1964).

[38] E. Fukada and I. Yasuda, On the piezoelectric effect of bone, *J. Phys. Soc. Japan* **12**(10) (1957) 1158–1162.

[39] E. Fukada and I. Yasuda, Piezoelectric effects in collagen, *Jpn. J. Appl. Phys.* **3**(2) (1964) 117–121.

[40] D.P. Fyhrie and D.R. Carter, A unifying principle relating stress to trabecular bone morphology, *J. Orthop. Res.* **4** (1986) 304–317.

[41] J.M. García Aznar, *Modelos de remodelación ósea: análisis numérico y aplicaciones al diseño de fijaciones de fracturas del fémur proximal,* Tesis, Universidad de Zaragoza (1999).

[42] A. Gjelsvik, Bone remodeling and piezoelectricity I, *J. Biomech.* **6** (1973) 69–77.

[43] A. Gjelsvik, Bone remodeling and piezoelectricity II, *J. Biomech.* **6** (1973) 187–193.

[44] R. Glowinski, *Numerical methods for nonlinear variational problems.* Springer-Verlag, New York (1984).

[45] W. Han and M. Sofonea, *Quasistatic contact problems in viscoelasticity and viscoplasticity,* AMS-IP, Providence, 2002.

[46] D.H. Hegedus and S.C. Cowin, Bone remodeling II: small strain adaptive elasticity, *J. Elasticity* **6**(4) (1976) 337–352.

[47] R. Huiskes, H. Weinans and M. Dalstra, Adaptive bone remodeling and biomechanical design considerations for noncemented total hip arthroplasty, *Orthopedics* **12** (1989) 1255–1267.

[48] R. Huiskes, H. Weinans, H.J. Grootenboer, M. Dalstra, B. Fudala and T.J. Sloof, Adaptive bone-remodeling theory applied to prosthetic-design analysis, *J. Biomech.* **20** (1987) 1135–1150.

[49] R. Huiskes, H. Weinans, D.R. Summer, N. Fudala, T.M. Turner, H.J. Grootenboer and J. Galante, Stress-shielding, stress-bypassing and bone resorption around "press-fit" and bone ingrowth THA, *Trans. 35th Orthop. Res. Soc.* **14** (1989) 529.

[50] C.R. Jacobs, Numerical simulation of bone adaptation to mechanical loading, Dissertation for the Degree of Doctor of Philosophy, Stanford University, 1994.

[51] N. Kikuchi and J.T. Oden, *Contact problems in elasticity: a study of variational inequalities and finite element methods,* SIAM Studies in Applied Mathematics, 8. Society for Industrial and Applied Mathematics (SIAM), Philadelphia, 1988.

[52] A. Klarbring, A. Mikelić and M. Shillor, Frictional contact problems with normal compliance, *Internat. J. Engrg. Sci.* **26** (1988) 811–832.

[53] R. Martin, D. Burr and N. Sharkey, *Skeletal tissue mechanics*, Springer-Verlag (1998).

[54] J.A.C. Martins and J. T. Oden, Existence and uniqueness results for dynamic contact problems with nonlinear normal and friction interface laws, *Nonlinear Anal.* **11** (1987) 407–428.

[55] Y. Matsuura, Mathematical models of bone remodeling phenomena and numerical simulations. II. Algorithm and numerical methods, *Adv. Math. Sci. Appl.* **13**(2) (2003) 755–779.

[56] Y. Matsuura and S. Oharu, Mathematical models of bone remodeling phenomena and numerical simulations. I. Modeling and computer simulations, *Adv. Math. Sci. Appl.* **13**(2) (2003) 401–422.

[57] J. Monnier and L. Trabucho, Existence and uniqueness of a solution to an adaptive elasticity model, *Math. Mech. Solids* **3** (1998) 217–228.

[58] J. Monnier and L. Trabucho, An existence and uniqueness result in bone remodeling theory, *Comput. Methods. Appl. Mech. Engrg.* **151** (1998) 539–544.

[59] M.G. Mullender, R. Huiskes and H. Weinans, A physiological approach to the simulation of bone remodeling as a self-organizational control process, *J. Biomech.* **27**(11) (1994) 1389–1394.

[60] C.S. Pinto, *"Análise de sensibilidades em elasticidade adaptativa,"* PhD Thesis, Departamento de Matemática, Universidade de Coimbra, Portugal, 2007.

[61] Q. Qin and J. Ye, Thermoelectroelastic solutions for internal bone remodeling under axial transverse loads, *Int. J. Solids Struct.* **41** (2004) 2447–2460.

[62] C. Qu, Q. Qin and Y. Kang, A hypothetical mechanism of bone remodeling and modeling under electromagnetic loads, *Biomaterials* **27** (2006) 4050–4057.

[63] S. Ramtani, Electro-mechanics of bone remodelling, *Internat. J. Engrg. Sci.* **46** (2008) 1173–1182.

[64] L. Trabucho, Non-linear bone remodeling: an existence and uniqueness result, *Math. Methods Appl. Sci.* **23** (2000) 1331–1346.

[65] H. Weinans, R. Huiskes and H.J. Grootenboer, Convergence and uniqueness of adaptive bone remodeling, *Trans. 35th Orthop. Res. Soc.* **14** (1989) 310.

[66] H. Weinans, R. Huiskes and H.J. Grootenboer, The behaviour of adaptive bone-remodeling simulation models, *J. Biomech.* **25**(12) (1992) 1425–1441.

[67] J. Wolff, Das gesetz der transformation der knochen, A. Hirschwald, Berlin, 1892. Translated by P.G.J. Maquet and R. Furlong. The law of bone remodelling (1986) Springer-Verlag in Berlin, New York.

[68] J.M. Viaño, Análisis de un método numérico con elementos finitos para problemas de contacto unilateral sin rozamiento en elasticidad. Parte II: Aproximación y resolución de los problemas discretos, *Rev. Internac. Métod. Numér. Cálc. Diseñ. Ingr.* **2** (1986) 63–86.